

**STABILITY OF COUPLED
SEMICONDUCTOR DIODE LASERS**

David J. Bossert

B.S., University of Portland, 1986

A dissertation submitted to the faculty of the
Oregon Graduate Institute of Science & Technology
in partial fulfillment of the
requirements for the degree
Doctor of Philosophy
in
Applied Physics

April, 1992

The dissertation "Stability of Coupled Semiconductor Diode Lasers" by David J. Bossert has been examined and approved by the following Examination Committee:

Richard K. DeFrez, Advisor
Associate Professor

Paul R. Davis
Professor

Gregory C. Dente
G.C.D. Associates

Reinhart W. H. Engelmann
Professor

ACKNOWLEDGMENTS

I would like to thank my research advisor Dr. Richard DeFreez for his support and encouragement during my studies at the Oregon Graduate Institute. I am also greatly indebted to Dr. Greg Dente for all that he has done for me. His guidance on this project was invaluable to its success. I further wish to acknowledge the late Dr. Richard Elliott for providing me a solid start in graduate school.

My deepest appreciation is extended to the people of the Pilot program at the Air Force Phillips Laboratory. The time I spent researching there was very enjoyable due to their friendship and cooperation. I would particularly like to thank Dr. Dave Depatie, Chuck Moeller and Dave Gallant, who offered abundant assistance with technical as well as administrative problems. Sponsorship of this study from the Air Force Office of Scientific Research is gratefully acknowledged.

The staff and students of the Oregon Graduate Institute have also helped me in innumerable ways during my graduate work. I would like to thank John Hunt, Pete Carleson and Jeff Irland for their expert technical assistance. My fellow students Geoff Wilson, Nu Yu, Marc Felisky, Raghu Ranganathan and others truly deserve my thanks for their support and friendship.

This work is dedicated to my family. It is always a comfort to know that they are there for me.

Table of Contents

ACKNOWLEDGEMENTS	iii
LIST OF FIGURES	vii
LIST OF TABLES	xii
LIST OF SYMBOLS	xiii
ABSTRACT	xvi
1. INTRODUCTION	1
2. THEORY	7
2.1 Rate Equations	9
2.2 Coupled Rate Equations	16
2.3 Stationary Solutions	24
2.4 Stability Analysis	37
2.5 Coupling Coefficients	53
2.5.1 Self-Coupling	57
2.5.2 Cross-Coupling	60
2.5.3 Power Coupling Ratio	61
3. SELF COUPLING (FEEDBACK)	65
3.1 Delayed Self-Coupling	66
3.1.1 Steady-State Operation	67
3.1.2 Linewidth	71

3.2 Experiment	74
3.3 Single Mode Operation	80
3.4 Multimode Operation	86
3.5 Modal Stability	93
3.6 Mode Selection	99
3.7 Coherence Collapse	109
4. MUTUAL COUPLING	134
4.1 Delayed Mutual Coupling	135
4.1.1 Steady-State Operation	137
4.1.2 Stability	139
4.2 Experiment	143
4.3 Resonant Locking	153
4.4 Non-resonant Locking	170
4.5 Overcoupling	184
5. CONCLUSIONS	206
REFERENCES	211
APPENDIX A	230
A.1 Resonant Susceptibility	230
A.2 Definition of α	233
A.3 Discussion	235
APPENDIX B	237
B.1 Measurement of Coupling Coefficients	237

B.2 Self-Coupling Calibration	240
B.3 Mutual Coupling Calibration	245
APPENDIX C	247
C.1 Visibility	247
C.2 Measuring Visibility	248
C.3 Visibility From Time Series	257
APPENDIX D	260
D.1 Stochastic Rate Equations	260
D.2 Numerical Simulation of Phase Noise	264
APPENDIX E	272
E.1 Parameter Measurements	272
APPENDIX F	285
APPENDIX G	287
VITA	299

List of Figures

2.1 Stationary solutions for two mutually coupled lasers.	31
2.2 Stationary solutions for two mutually coupled lasers.	32
2.3 Locking bandwidth versus coupling phase.	36
2.4 Stability boundaries for $\alpha = 0$	44
2.5 Stability boundaries for $\alpha = 3$	45
2.6 Eigenvalues of $D(s)$ with $\text{Im}[s] = 0$	49
2.7 Eigenvalues of $D(s)$ with $\text{Im}[s] \neq 0$	50
2.8 Representation of coupling for a passive, lossy gap.	58
3.1 Phasor interpretation of self-coupling.	69
3.2 Optical setup of self-coupling experiment.	75
3.3 Data acquisition setup for self-coupling experiment.	79
3.4 Optical spectra for a -67 dB power coupling ratio.	82
3.5 Stationary solutions for a -67 dB power coupling ratio.	84
3.6 Numerical simulation of mode tuning for a -67 dB power coupling ratio.	85
3.7 Optical spectra for a -58 dB power coupling ratio.	87
3.8 Optical spectra for a -53 dB power coupling ratio.	88
3.9 The transition to multimode operation.	90
3.10 Stationary solutions for a -53 dB power coupling ratio.	92

3.11 Numerical simulation of mode tuning for a -58 dB power coupling ratio.	94
3.12 Graphical solution of the stability criterion for self-coupling.	96
3.13 Experimental measurements of mode hopping.	101
3.14 Optical spectra for a -46 dB power coupling ratio.	103
3.15 Optical spectra for a -44 dB power coupling ratio.	104
3.16 Mode tuning trajectory for a -46 dB power coupling ratio.	106
3.17 Mode hopping versus power coupling ratio.	107
3.18 Experimental optical spectra showing undamping of relaxation oscillations.	112
3.19 Experimental optical spectra showing transition to multiple external cavity mode operation.	113
3.20 Gross spectral features during coherence collapse.	114
3.21 Numerically simulated spectra during coherence collapse.	117
3.22 Numerical simulations of intensity noise spectrum during coherence collapse.	119
3.23 Experimental power spectra during coherence collapse.	121
3.24 Experimental setup used to investigate longitudinal diode mode hopping.	123
3.25 Longitudinal diode mode spectra during coherence collapse.	125
3.26 Resonance frequencies of a self-coupled laser.	127
3.27 Stability boundaries for a self-coupled laser.	129

3.28 Critical coupling level for the onset of self-pulsation.	131
4.1 Graphical solution of mutual coupling stability criterion.	142
4.2 Experimental temperature control setup.	145
4.3 Experimental optical setup for mutual coupling.	147
4.4 Method to insure mutual coupling between lasers.	149
4.5 Data acquisition setup for mutual coupling.	152
4.6 Spectral and coherence measurements for a -70 dB power coupling ratio.	155
4.7 Modes of two mutually coupled lasers at a power coupling ratio of -70 dB.	157
4.8 Spectral and coherence measurements at a -55 dB power coupling ratio.	159
4.9 Spectral and coherence measurements at a -51 dB power coupling ratio.	160
4.10 Modes of two mutually coupled lasers at a power coupling ratio of -55 dB.	162
4.11 Spectral width of phase fluctuations at -55 dB.	165
4.12 Numerical simulations of mode hopping.	167
4.13 Peak visibility versus power coupling ratio.	169
4.14 Experimental spectral and coherence measurements for zero detuning.	171
4.15 Experimental spectral and coherence measurements for 255 MHz detuning.	172

4.16 Experimental spectral and coherence measurements for 470 MHz detuning.	173
4.17 Experimental spectral and coherence measurements for 623 MHz detuning.	174
4.18 Stationary solutions versus detuning.	177
4.19 Numerical simulations of optical spectra versus detuning.	179
4.20 Numerical simulation of phase-locking at lockband edge.	181
4.21 Reduction of visibility near the lockband edge.	183
4.22 Spectral and coherence measurements at a power coupling ratio of -42 dB.	186
4.23 Gross optical spectrum during overcoupling.	188
4.24 Visibility versus power coupling ratio.	189
4.25 Longitudinal diode mode spectra during overcoupling.	192
4.26 Stationary solutions in the overcoupling regime.	194
4.27 Dynamic operation in the overcoupling regime, -45 dB.	197
4.28 Dynamic operation in the overcoupling regime, -30 dB.	199
4.29 Dynamic operation in the overcoupling regime, -15 dB.	200
4.30 Visibility versus coupling delay.	202
4.31 Visibility versus η where $\tau = 0$	204
B.1 Self-coupling calibration curves.	243
C.1 Fourier transform technique to extract visibility.	250
C.2 Visibility versus injection current.	255

D.1 Numerical simulations of natural linewidth.	269
E.1 Gain change and wavelength shift versus current, CSP laser.	275
E.2 Gain change and wavelength shift versus current, TJS laser.	276
E.3 Light versus current characteristics.	278
E.4 Turn-on delay versus excess current.	281

List of Tables

E.1	Compilation of parameters for experimental lasers.	284
-----	---	-----

List of frequently used symbols

Symbol	Description	Page
c	Speed of light in vacuum	9
D_{ij}	Diffusion coefficient	261
$D(s)$	Secular determinant	39
$E(\mathbf{r}, t)$	Electric field	9
$E_m(t)$	Electric field of m th mode	10
$\tilde{E}_m(t)$	Normalized, slowly-varying part of $E_m(t)$	9
$E_m(t)$	Amplitude of $\tilde{E}_m(t)$	9
$\bar{e}(t)$	Dimensionless field amplitude	24
\bar{e}	Dimensionless steady-state field amplitude	27
$F_x(t)$	Langevin noise source for the dynamic variable $X(t)$	66
g	Material gain per unit length	233
g_m	Modal gain per unit length	12
G	Modal rate of gain (linear + nonlinear)	15
G_P	Dimensionless gain compression term	25
h, \hbar	Plank's constant	14
I	Current injection (Coulomb/sec)	273
I_{th}	Threshold current	111
I	Optical intensity	248
$J(t)$	Pump rate (carriers/sec)	24
J_{th}	Threshold pumping rate	24
$\Delta J(t)$	Pump rate relative to threshold	24
L_D	Length of diode laser	55
L_{ext}	Length of external cavity	57
n_{sp}	Inversion factor	263
N	Number of carriers in active region	12
N_{th}	Number of carriers at threshold	12
ΔN	Variation in carrier number from threshold	12
N_o	Number of carriers at transparency	234
$\Delta n(t)$	Dimensionless carrier number relative to threshold	25
$\bar{\Delta n}$	Steady-state carrier number relative to threshold	27
$P(t)$	Optical power	14
$P(\mathbf{r}, t)$	Macroscopic polarization	9
PCR_{cc}	Cross power coupling ratio	62
PCR_{sc}	Self power coupling ratio	62
q	Electronic charge	279
$R_{1,2}$	Facet power reflectivities	57
R_{sp}	Average rate of spontaneous emission into lasing mode	23
r_{sp}	Dimensionless spontaneous emission factor	26
s	Eigenvalue of $D(s)$	38
S_E	Spectral density function of the electric field	265
$S_{\delta P}$	Spectral density function of power fluctuations	118
\tilde{S}_{jk}	Scattering element from laser k to laser j	54
\tilde{S}_{jj}^o	Isolated self-scattering element	55

t	time	9
\hat{t}	Dimensionless time, t/τ_p	25
$u_{j,m}$	m th eigenmode of isolated laser j	9
$v_{c,n}$	n th eigenmode of compound laser cavity	17
v_g	Group velocity	14
V	Volume of active region	19
V	Visibility	248
α	Linewidth enhancement factor	12
α_t	Total loss per unit length	12
α_{mir}	Effective mirror loss per unit length	14
β_o	Free-space propagation constant	233
β_m	Propagation constant of m th mode	10
β_{mn}	Gain suppression coefficient	14
γ	Dimensionless damping constant	41
γ_o	Damping constant of isolated laser	46
$\delta(t)$	Dirac delta function	261
$\Delta_j(t)$	Instantaneous phase difference, $(\omega_{ok} - \omega_{oj})t + \phi_k(t) - \phi_j(t)$	23
ϵ_T	Amplitude transmission coefficient	58
ϵ	Dielectric constant	11
ϵ_m	Modal dielectric constant	11
ϵ_o	Permittivity of free-space	9
η	Dimensionless coupling coefficient $\kappa\tau_p$	66
η_{jk}	Dimensionless coupling coefficient from laser k to laser j	25
η_{sc}	Dimensionless self-coupling coefficient	27
η_{cc}	Dimensionless cross-coupling coefficient	27
κ	Coupling coefficient (rate)	67
κ_{jk}	Coupling coefficient from laser k to laser j	21
λ	Lasing wavelength in air	273
μ	Real refractive index	10
μ_m	Effective modal refractive index	11
μ_g	Group index	10
$\Delta\nu_D$	Longitudinal diode mode spacing	272
$\Delta\nu^o$	Natural linewidth	73
ν_R	Relaxation resonance frequency	48
$\Delta\nu_{cc}$	Resonator cold-cavity half-bandwidth	62
ξ	Amplitude coupling loss	59
$\Delta\rho$	Dimensionless pumping relative to threshold	25
σ	Ratio of carrier and photon lifetimes	25
τ	Coupling delay time	59
$\hat{\tau}$	Dimensionless coupling delay τ/τ_p	66
τ_p	Photon lifetime	15
τ_s	Carrier lifetime	15
τ_D	Round trip time in diode laser	56
$\phi(t)$	Slowly-varying phase of electric field $\vec{E}(t)$	23
$\Delta\phi_L$	Locked phase difference between lasers	27
$\Delta\phi(t, n\tau)$	Delayed phase difference, $\phi(t) - \phi(t - n\tau)$	59

$\Phi(t)$	Instantaneous phase difference between lasers	37
χ	Electric susceptibility	10
ψ	Phase of coupling coefficient	22
ψ_{sc}	Self-coupling phase	27
ψ_{cc}	Cross-coupling phase	27
ω	Angular frequency	20
ω_o	Free-running oscillation frequency	21
$\bar{\omega}_o$	Average free-running frequency of lasers	28
ω_m	Oscillation frequency of mode m	9
ω_L	Oscillation frequency of coupled system	26
$\Delta\omega_o$	Detuning	28
$\Delta\omega_L$	Oscillation frequency relative to ω_o or $\bar{\omega}_o$	28
$\Delta\omega_{LB}$	Phase-locking bandwidth	30
Ω	Dimensionless angular frequency	126
Ω_R	Relaxation frequency of coupled system	41
X_j, X_k	Subscripts j, k reference laser number	
$\delta X(t)$	Fluctuation of the dynamic variable $X(t)$	
\tilde{x}	Explicit notation for complex nature of variable x	
AR	Anti-reflection	
C^3	Cleaved-coupled-cavity	
CSP	Channeled-substrate-planar	
CW	Continuous wave	
HR	High reflectivity	
RHS,LHS	Right-hand side, left-hand side	
TJS	Transverse-junction-stripe	

ABSTRACT

STABILITY OF COUPLED
SEMICONDUCTOR DIODE LASERS

David J. Bossert, Ph.D.

Oregon Graduate Institute, 1992

Supervising Professor: Richard K. DeFreez

This dissertation investigates the stability of self and mutually coupled semiconductor diode lasers. Theoretical analysis is based on coupled rate equations which follow from time-dependent coupled mode theory, including complex coupling coefficients describing optical interactions between the lasers. Phase-locking conditions and small signal stability properties are analyzed for the case of two mutually coupled lasers, including self-coupling. These are found to be strongly influenced by both the linewidth enhancement parameter α and the phase of the coupling coefficient. A wide locking bandwidth and large mode suppression are shown to be incompatible due to a non-zero α . Two different forms of stability are identified.

The model is applied to the cases of one and two diode lasers coupled at a distance. Systematic experiments have been designed to study the stability of

these systems as a function of coupling magnitude and phase. Careful spectral and coherence measurements are compared directly to numerical simulations from the rate equation model, including nonlinear gain compression and spontaneous emission noise. Modes, mode selection and dynamic stability properties are shown to be well accounted for by the rate equation approach. An accurate comparison is enabled through independent measurements of the model parameters for the experimental devices. Further, techniques to reliably determine the level of optical coupling have been developed.

Three distinctive operating regimes are demonstrated with respect to the coupling magnitude. At low coupling levels, mode selection is governed by phase stability. While all oscillating modes are stable, phase-locking is found to be limited by spontaneous emission noise throughout most of this regime. These findings are corroborated through numerical integration of an approximate form of the rate equations. In contrast, at large coupling levels, mode selection and dynamic stability are dominated by threshold gain considerations; where the most stable mode minimizes the population inversion. Here, the effect of α on the stability properties is minimal. Intermediate levels of coupling are characterized by extreme dynamic instability, resulting in spectral broadening and a near total loss of coherence in the coupled system. This regime is interpreted as a transition between phase- and gain-dominated modes of operation, initiated by the system's inability to damp relaxation oscillations.

1. INTRODUCTION

In the last several years, a great deal of research has been devoted toward developing systems of optically coupled semiconductor lasers. Much of the motivation for this effort has been supplied by applications involving coherent communications. Here, transmission and detection schemes are based upon coherence properties of the laser emission, offering potentially much larger optical bandwidths than available from amplitude modulated systems. With this advantage comes stringent requirements on the linewidth and stability of the optical source; requirements which are beyond the capability of conventional Fabry-Perot semiconductor lasers. By properly coupling the output of a single diode laser to another (possibly passive) resonator, however, a narrow linewidth¹, large side-mode suppression ratio²⁻⁷ and dynamic single longitudinal mode operation⁸⁻¹¹ can be achieved.

Optical coupling of semiconductor lasers has also been pursued to increase output power. While the small size of diode lasers makes them attractive in a number of applications, this same property limits the available output power due to catastrophic facet damage¹². One way to avoid this limitation is to phase-lock multiple devices, so that they operate as a single, spatially extended source. Mutual optical coupling of the individual elements is an attractive, convenient method to achieve the desired phase-locking. Numerous schemes have

been attempted, including evanescent field overlap¹³⁻¹⁷, Y-branching^{18,19}, diffraction²⁰⁻²², leaky-waves^{23,24}, external cavities^{25,26}, gratings²⁷, turning mirrors^{28,29}, and combinations thereof³⁰⁻³³. Although each technique has certain advantages and disadvantages, the ultimate goal is the same: to operate the array in its fundamental (in-phase) supermode, while insuring maximum suppression of higher order modes. The result would be a useful single-lobed, diffraction-limited far-field pattern.

Power outputs rivaling large gas or solid-state lasers are conceivable by coupling large numbers of diode lasers. To date, over three watts of continuous power have been obtained from two-dimensional surface-emitting arrays³⁴, although the overall coherence at such power levels is typically rather poor. Diffraction-limited power from semiconductor laser arrays is presently sub-watt³⁵, with fundamental mode operation of only a few hundred milliwatts³⁶. The challenge of maintaining good coherence between large numbers of semiconductor lasers is a formidable one and is a major impetus for the present study.

Coupling oscillators for the purpose of spectral mode control, as well as high power, has by no means been confined to semiconductor lasers. For example, following the pioneering work of van der Pol³⁷, phase-locking of electrical oscillators by externally applied signals has been studied heavily since World War II for applications in microwave communication systems³⁸⁻⁴¹. The injection-locking technique was quickly applied to gas lasers⁴²⁻⁴⁶ shortly after their invention, and eventually found use with semiconductor lasers⁴⁷⁻⁵⁹. Injection-locking utilizes a frequency and mode stabilized master oscillator (MO) to phase-lock one or more slaves. In doing so, the frequency spectrum and

stability of the slave laser(s) are improved. The master, however, becomes redundant if the lasers are allowed to *mutually* couple. In this way, critical optical isolation and stabilization of the MO can be avoided. Mutual interaction, however, is found to profoundly affect the stability of phase-locking between semiconductor lasers, as elucidated in this thesis.

Mutually coupled lasers were first considered theoretically by Spencer and Lamb⁶⁰. Stable phase-locking was predicted by their semiclassical approach⁶¹ as long as the resonance frequencies of the individual lasers were tuned sufficiently close. This was later experimentally verified⁶² using two coupled CO₂ lasers. In contrast, recent experimental investigations of coherent semiconductor laser arrays have revealed that a number of coupling schemes exhibit dynamic instability in the nano- and picosecond temporal regimes⁶³. Y-guided arrays, for example, were found to exhibit severe periodic and quasiperiodic sustained self-pulsations^{64,65} near the relaxation resonance frequency of the semiconducting gain medium and its harmonics. Linear and two-dimensional arrays employing evanescent coupling, on the other hand, have shown a variety of effects from periodic to erratic, possibly chaotic behavior, with power spectra extending well beyond the relaxation resonance frequency⁶⁶⁻⁶⁸. Such instability could limit the usefulness of semiconductor laser arrays toward a number of potential applications, such as free-space communications, where high bit rates are desirable. In fact, only one instance of stable array operation, from a grating surface emitting (GSE) device⁶⁹, has been reported to date. The array was forced to operate in a single stable array mode, although at the expense of output power, by careful adjustment of current to individual gain sections.

Instability has also been observed in simpler systems of optically coupled semiconductor lasers. It is well documented that an injection-locked diode laser self-pulsates over a large part of its phase-locking bandwidth^{49,70-72}. Further, delayed self-coupling (or feedback) is known to induce intensity self-pulsations, followed by an extreme spectral collapse, at moderate coupling levels⁷³⁻⁷⁵. In both cases, instability has been linked to the carrier-dependent refractive index, which is unique to semiconductor gain media and described by the α parameter⁷⁶.

Only recently has the stability of mutually coupled semiconductor lasers been addressed theoretically. Numerical integration of coupled rate equations⁷⁷, similar to those of Spencer and Lamb⁶⁰, has demonstrated that the individual elements in a nearest-neighbor coupled array can exhibit undamped intensity spiking, destabilizing the phase-lock. These simulations are in qualitative agreement with some of the behaviors observed in the previously referenced experimental temporal studies of arrays. By calculating a positive Lyapunov exponent, the unstable time evolution of intensity, in the case of three coupled lasers, has been identified as a manifestation of spatiotemporal optical chaos^{78,79}. Small signal analysis of the coupled rate equations^{80,81} further predicts unstable operation at all but the weakest or strongest coupling levels. Instability, in this work, was again associated with amplitude-phase coupling through the α parameter.

Although a good deal of experimental evidence has been introduced supporting the claim that semiconductor laser arrays are intrinsically unstable, no direct verification of the coupled rate equation predictions has been accomplished. The main reason for this lack of correlation between theory and

experiment is that observations have been limited to large, complicated array structures. While dynamics in such structures can be quite interesting, theoretical simulation is made more difficult due to the large number of nonlinear coupled rate equations to be numerically evaluated. This thesis theoretically and experimentally examines the phase-locking properties of two mutually coupled semiconductor lasers. In particular, regimes of stable phase-locking are identified with respect to the strength and phase of the optical coupling. The causes of instability are further analyzed. By emphasizing correlation between theory and experiment, the applicability of the coupled rate equation approach can also be determined.

The stability of self-coupling also constitutes a sizable portion of this thesis. There are several reasons for its inclusion. First, self-coupling is an inherent part of many mutual coupling schemes. Longitudinally coupled lasers, for example, usually incorporate some sort of feedback, as well as cross-coupling, mechanism. The effect of self-coupling has been ignored in previous stability analyses. Further, in more general terms, self-coupling can be considered the simplest coupled system. Its study, therefore, offers many insights helpful in understanding higher dimensional systems, as is the case in Chapters 3 and 4. On a very practical level, optical elements in experiments inevitably feed back some amount of the laser emission to their source. This becomes especially important in studies of array stability, where outside influences on the array's operation are obviously undesirable. Characterizing low levels of optical feedback is thus also in order.

The thesis is organized as follows: Chapter 2 contains a theoretical development of self and mutually coupled semiconductor lasers based on time-

dependent coupled mode theory. Coupled rate equations are derived which include complex coupling coefficients governing optical interactions. Stationary phase-locking conditions are then determined for two mutually coupled lasers. Stability boundaries with respect to coupling strength and phase are obtained from a small signal analysis, and regimes of optimum phase-locking and stability are identified. Coupling coefficients for the specific case of longitudinally coupled lasers separated by a distance are then derived for future use in numerical simulations and comparison to experiment.

Chapters 3 and 4 present the experimental part of this thesis. The former deals with delayed self-coupling, while the latter investigates two longitudinally coupled semiconductor lasers. Spectral and coherence measurements are primarily used to characterize the stability of the coupled systems. These are directly compared to numerical simulations based on the coupled rate equations, including spontaneous emission noise and nonlinear gain. Mode selection, in particular, is investigated in both stable and unstable operating regimes. Quantum noise, gain compression and the coupling level and phase are all shown to have a significant impact on the stability properties of a self or mutually coupled diode laser.

Chapter 5 sums up the main conclusions of this work.

2. THEORY

This chapter introduces the theoretical model used to describe the operation of mutually coupled lasers throughout this thesis. Since stability of the coupled system is of primary interest, a time-dependent analysis, based on rate equations for the complex optical field and population inversion in the laser cavity, is performed.

Rate equations govern the interaction between carriers and photons in a resonant cavity through spontaneous and stimulated emission processes. In their simplest form^{82,83}, rate equations merely act as conservation equations for the number of carriers and photons inside the laser. In this sense they are very intuitive and can be immediately written in a heuristic manner. In coupled systems of lasers, however, the phase of the optical field is of the utmost importance. Derivation of the rate equations must then proceed from more fundamental principles. Ultimately, of course, Maxwell's equations will govern the behavior of the field in the laser cavity. The second-order partial differential wave equation which follows, however, does not lend itself to solution unless simplifications can be made. This can be accomplished through a proper representation of the optical field. Section 2.1 outlines this procedure, which results in a first-order rate equation for the slowly varying part of the electric field. The derivation is carried out in order to develop a theoretical framework

which can be referenced in later chapters, as well as to point out significant approximations and assumptions inherent in the often used rate equation approach.

Section 2.2 discusses approaches to modeling coupled lasers. Coupled rate equations are shown to follow from the time-dependent wave equation by expanding the field in terms of the actual eigenmodes of the coupled system of lasers. Coupling coefficients are defined which account for the optical interaction of the fields in each laser. Rate equations for two mutually coupled semiconductor lasers directly follow.

Stationary solutions and phase-locking conditions for mutually coupled diode lasers are examined in Section 2.3, while the stability of these equilibria is subsequently analyzed in Section 2.4. The phase of the coupling coefficient is found to significantly affect the locking range, power and stability of the lasers. Those coupling phases which promote dynamical stability and optimum phase-locking are determined. An alternate approach to defining coupling coefficients for longitudinally coupled lasers is derived in Section 2.5. The coupled rate equations are shown to progress naturally from a treatment of the coupling junction as a two-port scattering network. Specific self and cross-coupling coefficients are found from this analysis for the experimental cases examined in Chapters 3 and 4.

2.1 Rate Equations

The electric field $E(\mathbf{r}, t)$ in a laser resonator satisfies Maxwell's equations through the time-dependent wave equation,

$$\nabla^2 E - \frac{\sigma_e}{\epsilon_0 c^2} \frac{\partial E}{\partial t} - \frac{1}{c^2} \frac{\partial^2 E}{\partial t^2} = \frac{1}{\epsilon_0 c^2} \frac{\partial^2 P}{\partial t^2}. \quad (2.1.1)$$

Here $P(\mathbf{r}, t)$ is the induced macroscopic polarization of the medium, c is the speed of light in vacuum, ϵ_0 is the permittivity of free-space, and σ_e is an effective conductivity which accounts for material losses. This form implicitly assumes that the electric field varies slowly in the transverse \hat{y} and lateral \hat{x} directions, so that $\nabla \cdot P \approx 0$. Further, scalar quantities are justified, as semiconductor lasers tend to operate in TE modes linearly polarized in the \hat{x} direction.

The electric field and polarization can be expanded in terms of the resonator eigenmodes u_m as

$$E(\mathbf{r}, t) = \frac{1}{2} \sum_m \left(\tilde{E}_m(t) e^{-i\omega_m t} u_m(z) w(x, y) + c.c. \right), \quad (2.1.2)$$

$$P(\mathbf{r}, t) = \frac{1}{2} \sum_m \left(\tilde{P}_m(t) e^{-i\omega_m t} u_m(z) w(x, y) + c.c. \right). \quad (2.1.3)$$

The key step in the above expansions is the assumption that the temporal and spatial dependences of each resonator mode may be separated. In other words, the modes of the laser cavity are treated as though their spatial profiles are unaffected by the gain and loss mechanisms existing in the laser. Gain and loss are presumed to influence only the time evolution of the amplitudes of the

modes. Further, the time dependence is broken into a sinusoidal oscillation at the optical frequency of the mode ω_m and a complex amplitude \tilde{E}_m , which varies little in an optical period. The laser is also considered to support only the fundamental transverse and lateral modes given by the properly normalized function $w(x,y)$.

Consider a mode with electric field $E_m(\mathbf{r},t)$ oscillating in the laser resonator. E_m will induce the coherent polarization field $P_m(\mathbf{r},t)$ in the gain medium which, in turn, acts as a driving source in the wave equation (2.1.1). The interaction between E_m and P_m is in general found by solving the quantum mechanical density operator equations of motion for the gain medium. The result is well established for an ensemble of two level transitions^{84,85}. Transitions in semiconducting gain media, however, take place both between and within energy bands, further complicating the analysis. It has been shown that intraband transition times characterizing the decay of the polarization occur on the order of 0.1 ps, whereas interband processes, such as radiative and nonradiative recombination, are at least one order of magnitude slower^{86,87}. The response of the semiconductor can then be regarded as instantaneous and the polarization adiabatically eliminated by the equilibrium relation

$$P_m(\mathbf{r}) = \epsilon_o \chi_m(\mathbf{r}) E_m(\mathbf{r}). \quad (2.1.4)$$

Substitution of the expansions (2.1.2) and (2.1.3) without complex conjugates into (2.1.1), using (2.1.4), projecting onto $u_n(z)$, and making use of the slowly varying nature of $\tilde{E}_m(t)$ and $\tilde{P}_m(t)$ results in^{85,87}

$$\left(\nabla_t^2 - \beta_m^2\right) \tilde{E}_m w(x,y) + \frac{\omega_m^2}{c^2} \epsilon_m(x,y) \tilde{E}_m w(x,y) = -\frac{2i\mu\mu_g\omega_m}{c^2} \dot{\tilde{E}}_m w(x,y). \quad (2.1.5)$$

μ_g is the group index associated with the refractive index μ . Both have been considered to be approximately constant over the frequency separation of a few longitudinal modes. A sinusoidal variation of the field profile in the z direction is presumed⁸³, satisfying

$$\frac{d^2 u_m(z)}{dz^2} = -\beta_m^2 u_m(z), \quad (2.1.6)$$

where $\beta_m = \frac{\mu_m \omega_m}{c}$ is the propagation constant of mode m and μ_m is the effective modal index of refraction. A z -independent dielectric constant

$$\epsilon_m(x, y) = 1 + \chi_m(x, y) + i \frac{\sigma_e}{\epsilon_0 \omega_m} \quad (2.1.7)$$

has also been defined in deriving (2.1.5).

The physics of the interaction of the optical field and the semiconducting gain medium are hidden in the dielectric constant ϵ or the electric susceptibility χ . As discussed in Appendix A, the real part of the resonant electric susceptibility describes dispersion (or refractive index change) in the medium, while the imaginary part provides amplification (or gain) for the optical field. Information about the waveguide structure of the laser is also contained in ϵ . In steady-state, the transverse mode profile $w(x, y)$ is assumed to satisfy

$$\left(\nabla_t^2 + \frac{\omega_m^2}{c^2} \epsilon_m^o(x, y) \right) w(x, y) = \beta_m^2 w(x, y) \quad (2.1.8)$$

for an index guided waveguide structure⁸⁷. Therefore β_m is interpreted as the propagation constant of the m th waveguide mode at the lasing threshold.

Variations in the modal dielectric constant about its threshold value are expressed by $\Delta\epsilon$, where $\epsilon \equiv \epsilon^o + \Delta\epsilon$.

The population inversion responsible for optical gain is provided, in a semiconductor laser, by electron-hole pairs in the active layer. A relationship between $\langle\Delta\epsilon\rangle$ (spatially averaged) and the number of carrier pairs, N , can be found from equations (A.5)-(A.7) and (A.11)

$$\langle\Delta\epsilon_m\rangle = -\frac{i\mu_m c}{\omega_m} \frac{\partial g_o}{\partial N} \Delta N (1 - i\alpha), \quad (2.1.9)$$

assuming the linear modal gain

$$g_{L,m} = \frac{\partial g_o}{\partial N} \Delta N + \Delta g_{S,m} + \alpha_t. \quad (2.1.10)$$

Here, $\Delta N \equiv N - N_{th}$ denotes the carrier number variation from threshold, $\frac{\partial g_o}{\partial N}$ is the modal differential gain for the main mode, and α_t is the total loss per unit length as defined by (E.4). Losses are taken to be the same for all modes. $\Delta g_{S,m}$ accounts for spectral gain roll-off, which is approximately parabolic in semiconductor lasers. The gain differential and mode index above are evaluated at threshold.

Substituting (2.1.8) into (2.1.5), averaging over the transverse plane and using (2.1.9) results in

$$\frac{d\tilde{E}_m(t)}{dt} = \frac{1}{2} v_g \frac{\partial g_o}{\partial N} \Delta N (1 - i\alpha) \tilde{E}_m(t), \quad (2.1.11)$$

a rate equation governing the time evolution of the complex field amplitude in

the laser in terms of the carrier number. The refractive index, μ , averaged over the transverse plane, has been approximated as the effective mode index at threshold.

The linear form of gain (2.1.10) used in the derivation of (2.1.11) is, of course, not a valid model in all circumstances. Several phenomena have been identified which contribute to gain nonlinearities. In deriving (2.1.5), for example, the response time of the medium was assumed instantaneous due to the extremely short intraband scattering time ($\tau_{in} \sim 100$ fs) typical of semiconductor lasers. At large circulating powers, however, nonlinear contributions to the induced polarization may become significant. As a result, the gain of all modes within a spectral hole of width $1/\tau_{in}$ is reduced. This static, or spectral hole-burning process is well known⁸⁸⁻⁹¹ and leads to inhomogeneous gain saturation. Other effects result from modulation of the inversion (population pulsations), due to beating of lasing and nonlasing modes^{88, 92}. The interaction of the dominant mode with the modulated inversion causes an additional power dependence of the gain. Further, when modes of the laser are equally spaced, four-wave mixing^{86, 93} can occur in the presence of population pulsations. Nonlinear contributions to the real part of the electric susceptibility (refractive index), on the other hand, are very small compared to the linear variation⁹⁴ resulting from α . They are hereafter neglected.

Nonlinear gain plays an important role in the operation of semiconductor lasers. In particular, gain nonlinearity is known to affect the power distribution⁹⁵⁻⁹⁷ and mode suppression⁹⁸⁻¹⁰⁰ of a laser at high output power. Further, damping of the relaxation resonance is enhanced, significantly affecting the dynamic and modulation responses^{97, 101-107}. Nonlinear gain is often taken

into account through a power-dependent gain compression term^{93,97,103},

$$g_{NL,m} = -g_{L,o} \sum_n \beta_{mn} |\tilde{E}_n|^2, \quad (2.1.12)$$

which specifies the reduction in gain at a given output power. The electric field amplitude in (2.1.11) is considered to be normalized such that $\tilde{E}_m \tilde{E}_m^*$ gives the total number of photons in mode m . This is related to the (total) power output of the mode through¹⁰⁸

$$P_m = \hbar\omega_m \alpha_{mir} v_{g,m} |\tilde{E}_m|^2, \quad (2.1.13)$$

where the mirror loss per unit length α_{mir} is given by (E.9). The dimensionless gain suppression coefficients β_{mn} describe self and cross saturation of the gain, due to the mechanisms described earlier. (2.1.12) has been shown to be theoretically based in the density matrix formalism⁹³ and is valid for laser powers ≤ 10 mW per facet⁹⁴. The values of β_{mn} , however, depend on knowledge of the intraband scattering time constants for the polarization, as well as for carriers in the valence and conduction bands. These are not well-known or easily measurable. The coefficients are better estimated by fitting to spectral measurements⁹⁷, modulation bandwidths¹⁰³ or pulse response¹⁰⁹. Reports vary widely. A value of

$$\frac{\beta_{oo}}{\hbar\omega_o \alpha_{mir} v_g} \sim 1 W^{-1} \quad (2.1.14)$$

describing self-saturation of the main mode (in terms of the power output per facet) has been considered a reasonable estimate for an AlGaAs laser^{109,110}.

InGaAsP values tend to be larger.

Nonlinear gain can be introduced into the rate equation (2.1.11) by defining

$$G_m = v_g(g_{L,m} + g_{NL,m}) \quad (2.1.15)$$

as the modal rate of gain. Hence, with $\frac{\partial G_o}{\partial N} \equiv v_g \frac{\partial g_o}{\partial N}$,

$$\frac{d\bar{E}_m(t)}{dt} = \frac{1}{2} \left(G_m - \frac{1}{\tau_p} \right) \bar{E}_m(t) - i \frac{\alpha}{2} \frac{\partial G_o}{\partial N} \Delta N \bar{E}_m(t). \quad (2.1.16)$$

$\frac{1}{\tau_p} = v_g \alpha_t$ is the total rate of loss, and defines the photon lifetime τ_p in the usual way.

The carrier number N was introduced as a dynamic variable in equation (2.1.9). Its time dependence, although not explicit in (2.1.16), is related to the pumping rate, field strength and recombination mechanisms through the rate equation⁸⁷

$$\frac{dN(t)}{dt} = J(t) - R(N) - \sum_m G_m |\bar{E}_m(t)|^2. \quad (2.1.17)$$

J is the number of electron-hole pairs injected into the active region per second, which may be time dependent. The sum accounts for stimulated transitions over all the lasing modes. $R(N)$ is the carrier recombination rate, which is often written as $\frac{N}{\tau_s}$, with the carrier lifetime, τ_s , given by (E.10). τ_s accounts for all non-stimulated radiative and non-radiative recombination mechanisms.

N is considered to be spatially averaged over the active volume, and carrier diffusion has been neglected. This analysis is therefore most applicable to an index-guided laser structure.

2.2 Coupled Rate Equations

Rate equations (2.1.16) and (2.1.17) constitute the basis for modeling the static and dynamic operation of a single semiconductor diode laser. Coupled lasers are now considered. There are two distinct approaches to model the effect of optical coupling between lasers. In one theory, the lasing field in each resonator is expanded in terms of the individual laser eigenmodes^{60,111}, as was done in Section 2.1 for an isolated laser. With $u_{j,m}(\mathbf{r})$ denoting the m^{th} eigenmode of laser j , the appropriate expansion is

$$E_j(\mathbf{r},t) = \frac{1}{2} \sum_m \left(E_{j,m}(t) u_{j,m}(\mathbf{r}) + c.c. \right). \quad (2.2.1)$$

The $u_{j,m}$ form a complete, orthogonal set over laser cavity j and satisfy the wave equation,

$$\nabla^2 u_{j,m}(\mathbf{r}) + \frac{1}{c^2} \epsilon_{j,m}(\mathbf{r}) \omega_{j,m}^2 u_{j,m}(\mathbf{r}) = 0. \quad (2.2.2)$$

$\epsilon_{j,m}$ denotes the complex modal dielectric constant in the j^{th} laser. This approach is equivalent to taking the electric field amplitude and phase in each resonator as a dynamic variable^{10,77,80}. Coupling between the individual laser resonators is then described in terms of a coefficient characterizing the strength

and phase of the optical interaction.

The coupled system of lasers can also be modeled by considering it as a whole¹¹²⁻¹¹⁶. The lasing field, in this case, is expanded in terms of the eigenmodes of the composite resonator, $v_{c,n}(\mathbf{r})$, which are determined through solution of the resonator boundary value problem. The expansion is

$$E_c(\mathbf{r}, t) = \frac{1}{2} \sum_n \left(E_{c,n}(t) v_{c,n}(\mathbf{r}) + c.c. \right), \quad (2.2.3)$$

where the $v_{c,n}$ satisfy

$$\nabla^2 v_{c,n}(\mathbf{r}) + \frac{1}{c^2} \epsilon_n(\mathbf{r}) \omega_{c,n}^2 v_{c,n}(\mathbf{r}) = 0. \quad (2.2.4)$$

ϵ_n is the dielectric constant throughout the compound laser and is equal to $\epsilon_{j,n}$ in each laser. Here, the electric field amplitudes of the compound cavity modes, as opposed to those of the individual lasers, become the dynamic variables. It is again assumed that the spatial profiles of the composite resonator modes can be treated independently from the temporal dependence. This simplification becomes a bit more tenuous for extended coupling schemes, in which long time delays and local inhomogeneities may become important.

In the latter approach, the lasers are automatically phase-locked in solving for the composite resonator modes. Coupling coefficients become unnecessary. Coupling between the modes may occur, however, through the nonlinear processes described in the last section. The former theoretical approach is adopted in this work, however, since phase-locking conditions and the stability of the phase-lock are both key issues.

One can proceed by substituting an expansion of the form (2.2.1) into the time-dependent wave equation (2.1.1), (one for each resonator j), as was done in the case of an isolated laser. Boundary conditions, however, are also necessary to relate the fields $E_j(\mathbf{r}, t)$ where they overlap. This may consist of requiring continuity of the eigenmodes $u_{j,m}$ or their derivatives. The boundary conditions produce additional source terms in the wave equation of each laser which depend on the field amplitudes in the other lasers. These terms can eventually be defined in terms of coupling coefficients in the resulting rate equations. Unfortunately, the boundary conditions are specific to the particular coupling configuration being considered.

It is desirable, therefore, to have a more general approach to describe coupling coefficients. Two important questions emerge: first, how do coupling coefficients enter the rate equation description of laser operation? Further, what is their form and what dependencies do they possess? These questions can be answered by considering the wave equation for the composite laser resonator. It is required that the decomposition of the field in terms of individual cavity modes yield identical results to the actual field¹¹⁷. This implies that

$$E_j(\mathbf{r}, t) = E_c(\mathbf{r}, t) \quad (2.2.5)$$

in each cavity j . The complete set of modes for the individual cavities, however, may not constitute an adequate basis with which to describe the total field when the lasers are coupled. This is an unavoidable short-coming of treating the coupled system in terms of the individual laser modes. Validity of the model is therefore limited to the case where optical coupling does not perturb the field distribution of each laser resonator too greatly. This statement will be

quantified later in Section 2.5. By substituting the expansions (2.2.1) and (2.2.3) into (2.2.5), exploiting modal orthogonality, the expansion coefficients in the composite resonator description can be written as

$$E_{c,n}(t) = \sum_m \sum_k E_{k,m}(t) \int_{V_k} \epsilon_{k,m} u_{k,m} v_{c,n} dV. \quad (2.2.6)$$

Similarly, the coefficients from the expansion (2.2.1) are

$$E_{j,m}(t) = \sum_n E_{c,n}(t) \int_{V_j} \epsilon_{j,m} u_{j,m} v_{c,n} dV. \quad (2.2.7)$$

The total lasing field in the compound cavity satisfies the wave equation,

$$-\sum_n \omega_{c,n}^2 \epsilon(\mathbf{r}) E_{c,n}(t) v_{c,n}(\mathbf{r}) = \epsilon(\mathbf{r}) \frac{\partial^2 E_c(\mathbf{r}, t)}{\partial t^2}. \quad (2.2.8)$$

Equation (2.2.8) follows from the general time-dependent wave equation (2.1.1) where the equilibrium relation (2.1.4) between the field and induced polarization was again assumed. Further, the dispersive nature of ϵ and the conductivity of the medium were neglected temporarily, since their inclusion is not crucial to the following derivation.

The time evolution of the field in each laser resonator can now be introduced using (2.2.5) and (2.2.1) on the right-hand side of (2.2.8). The composite resonator expansion coefficient of the n^{th} mode, on the left-hand side of the equation, is replaced by (2.2.6). Projecting onto $u_{j,m}(\mathbf{r})$ results in

$$\frac{d^2 E_{j,m}(t)}{dt^2} = -\sum_n \omega_{c,n}^2 \sum_l \sum_k E_{k,l}(t) \int_{V_k} \epsilon_k u_{k,l} v_{c,n} dV \int_{V_j} \epsilon_j u_{j,m} v_{c,n} dV. \quad (2.2.9)$$

The time dependence of $E_{j,m}$ is now broken up into a rapid sinusoidal variation referenced to a convenient optical frequency ω and a slowly varying amplitude,

$$E_{j,m}(t) = \tilde{E}_{j,m}(t)e^{-i\omega t}. \quad (2.2.10)$$

Taking the second time derivative of (2.2.10) and substituting into (2.2.9) gives

$$-2i\omega \frac{d\tilde{E}_{j,m}}{dt} = \omega^2 \tilde{E}_{j,m} - \sum_n \omega_{c,n}^2 \sum_l \sum_k \tilde{E}_{k,l} \int_{V_j} \epsilon_j u_{j,m} v_{c,n} dV \int_{V_k} \epsilon_k u_{k,l} v_{c,n} dV. \quad (2.2.11)$$

The second derivative of the slowly varying amplitude was dropped above. Equation (2.2.11) describes the time evolution of the field in laser j , including the influence of fields in the other lasers. It can be written in a simpler form by replacing $\tilde{E}_{j,m}$ on the right hand side using (2.2.7) and (2.2.6). The rate equation is then

$$\frac{d\tilde{E}_{j,m}}{dt} = i \sum_k \sum_l \mathbf{K}_{m,l}^{j,k} \tilde{E}_{k,l}, \quad (2.2.12)$$

where

$$\mathbf{K}_{m,l}^{j,k} = \sum_n (\omega - \omega_{c,n}) \int_{V_j} \epsilon_j u_{j,m} v_{c,n} dV \int_{V_k} \epsilon_k u_{k,l} v_{c,n} dV. \quad (2.2.13)$$

It was approximated that $(\omega^2 - \omega_{j,m}^2) \approx 2\omega(\omega - \omega_{j,m})$.

(2.2.12) shows that the fields from other lasers k affect the time rate of change of the field in laser j through (cross) coupling coefficients $\mathbf{K}^{j,k}$. When $j=k$ the coupling coefficient describes self-coupling. For the simplest case of two coupled lasers, each consisting of a dominant single mode, the coupled rate

equations are

$$\frac{d\tilde{E}_j(t)}{dt} = i\mathbf{K}^{j,j}\tilde{E}_j(t) + i\mathbf{K}^{j,k}\tilde{E}_k(t) \quad j \neq k = 1,2. \quad (2.2.14)$$

In the general case, modes m and l of each laser are also allowed to self and cross couple. The coupling coefficients are found to involve overlap integrals between the m^{th} mode profile in laser j and the l^{th} mode of the coupled field, with the actual modes of the composite laser. In the limit of no coupling, the spatial profiles of the compound cavity modes approach those of the individual cavities, and all but the self-coupling terms vanish.

Note that since ϵ is generally complex, gain and loss for laser j has been incorporated into the self-coupling coefficient. Gain and loss can be explicitly included through the dielectric constant, as was illustrated in Section 2.1. For coupled lasers, the first term of (2.1.5) is replaced by the right-hand side of (2.2.9). Carrying out the remaining manipulation of the previous section results in rate equations of the form

$$\frac{d\tilde{E}_j(t)}{dt} = \frac{1}{2} \left(G_j - \frac{1}{\tau_{pj}} - i\alpha \frac{\partial G_j}{\partial N} \Delta N_j \right) \tilde{E}_j(t) + \bar{\kappa}_{jj}\tilde{E}_j(t) + \bar{\kappa}_{jk}\tilde{E}_k(t) e^{-i(\omega_{ok} - \omega_{oj})t} \quad j \neq k = 1,2 \quad (2.2.15)$$

for two single-mode coupled semiconductor lasers. In Section 2.5, it is shown that the factor of i in (2.2.12) is conveniently incorporated into the definition of the coupling coefficient for longitudinally coupled lasers. Further, this has become standard notation for describing external cavity lasers and cleaved-coupled-cavity (C^3) lasers^{10,118-120}. Since the experimental portion of this

thesis involves study of axially coupled lasers, the above notation is adopted. In this way, future comparisons between theory and experiment will not be confused by an additional phase shift. In equation (2.2.15), $\bar{\kappa}_{jj}$ denotes the self-coupling coefficient, while cross-coupling is governed by $\bar{\kappa}_{jk}$. The exponential term arises because the amplitudes in this equation and hereafter are referenced to the oscillation frequency of each laser operating in isolation, $\omega_{oj,ok}$.

The concept of modeling the dynamic operation of optically coupled resonators using an isolated rate equation modified by additive coupling terms involving the coupled fields is very appealing. Unfortunately, the coupling coefficients (2.2.13) are not always easily obtained, since the composite resonator eigenmodes are often difficult, if not impossible, to obtain analytically. Further, physical interpretation of the coupling coefficients is unclear from this perspective, and depends on the particular coupling scheme employed. Based on the stationary analysis of Section 2.3, however, the coupling coefficients are readily related to observable quantities, as discussed in Appendix B. For the time being, evaluation and interpretation of the coupling coefficients is left unresolved; they are treated as a parameter characterizing the coupled system. Later, in Section 2.5, coupling coefficients are derived for the specific case of longitudinally coupled lasers, which is investigated experimentally in Chapters 3 and 4.

The complex rate equations (2.2.15) can each be separated into two equations; one for the magnitude of the slowly varying electric field amplitude and one for its phase. With the coupling coefficient defined as

$$\bar{\kappa} \equiv \kappa e^{-i\psi}, \quad (2.2.16)$$

and the electric field amplitude given by

$$\tilde{E}_j(t) \equiv E_j(t)e^{-i\phi_j(t)}, \quad (2.2.17)$$

separation of (2.2.15) into real and imaginary parts results in

$$\begin{aligned} \frac{dE_j(t)}{dt} = \frac{1}{2} \left(G_j - \frac{1}{\tau_{pj}} \right) E_j(t) + \operatorname{Re}[\tilde{\kappa}_{jj}(t)] E_j(t) + \frac{R_{spj}}{2E_j(t)} \\ + \kappa_{jk} E_k(t) \cos[\Delta_j(t) + \psi_{jk}] \end{aligned} \quad (2.2.18)$$

$$\begin{aligned} \frac{d\phi_j(t)}{dt} = \frac{1}{2} \alpha_j \frac{\partial G_j}{\partial N} \Delta N_j + \operatorname{Im}[\tilde{\kappa}_{jj}(t)] \\ + \kappa_{jk} \frac{E_k(t)}{E_j(t)} \sin[\Delta_j(t) + \psi_{jk}] \end{aligned} \quad (2.2.19)$$

$$j \neq k = 1, 2.$$

Here $E_j(t)$, $\phi_j(t)$ and $\Delta N_j(t)$ are real valued dynamic variables, with E denoting the square root of the total number of photons in the lasing mode. Previously defined parameters are subscripted with a j or k to denote the laser to which they belong. The following definition was also incorporated into equations (2.2.18) and (2.2.19) to simplify notation

$$\Delta_j(t) \equiv (\omega_{ok} - \omega_{oj})t + \phi_k(t) - \phi_j(t). \quad (2.2.20)$$

R_{spj} has been added phenomenologically to account for the spontaneous generation of photons¹¹⁰. It is normalized so that its value gives the average number of spontaneously emitted photons per unit time added to the lasing mode.

Equation (2.1.17), describing the time rate of change in the carrier number,

remains essentially unchanged in the coupled situation. However, it will become useful to describe the carrier number relative to threshold. Recalling that $\Delta N_j \equiv N_j - N_{thj}$ for laser j , (2.1.17) can also be written as

$$\Delta \dot{N}_j(t) = \Delta J_j(t) - \frac{\Delta N_j(t)}{\tau_{sj}} - G_j E_j^2(t). \quad (2.2.21)$$

The term $\Delta J_j(t) \equiv J_j(t) - J_{thj}$ denotes the pumping rate with respect to threshold, where the threshold pumping of an isolated laser j is easily shown to be $J_{thj} = \frac{N_{thj}}{\tau_{sj}}$. Rate equations (2.2.18), (2.2.19) and (2.2.21) are the starting point for the investigation of phase-locking and stability properties of mutually coupled semiconductor lasers.

2.3 Stationary Solutions

The stationary solutions for field amplitude, phase and carrier number in each laser are found by solving rate equations (2.2.18),(2.2.19) and (2.2.21) with time derivatives set equal to zero. This will result in a set of coupled nonlinear equations which in general need to be solved numerically. To facilitate numerical solutions, as well as to simplify notation, the rate equations are first rewritten in a dimensionless form by defining the following reduced variables¹²¹:

$$e_j(t) \equiv \left(\frac{1}{2} \tau_s \frac{\partial G}{\partial N} \right)^{\frac{1}{2}} E_j(t) \quad (2.3.1)$$

$$\Delta n_j(t) \equiv \frac{1}{2} \tau_p \frac{\partial G}{\partial N} \Delta N_j(t) \quad (2.3.2)$$

$$\Delta \rho_j(t) \equiv \frac{1}{2} \tau_s \tau_p \frac{\partial G}{\partial N} \Delta J_j(t) \quad (2.3.3)$$

$$\tilde{\eta}_{jk} \equiv \tau_p \tilde{\kappa}_{jk} \quad (2.3.4)$$

$$\sigma \equiv \frac{\tau_s}{\tau_p}. \quad (2.3.5)$$

It is assumed that the lasers are identical in their material and structural related parameters, including $\frac{\partial G}{\partial N}$, τ_s , τ_p , α and R_{sp} . This is the case of interest, since it is usually desirable to couple similar lasers. Semiconductor lasers, in fact, are most often coupled monolithically where the above parameters are indeed nearly identical. In equations (2.3.1)-(2.3.5), $e_j(t)$ is the reduced field amplitude in laser j , while $\Delta n_j(t)$ and $\Delta \rho_j(t)$ are the reduced carrier number and pumping variation from threshold, respectively. A normalized time $\hat{t} \equiv \frac{t}{\tau_p}$ is utilized. All time derivatives are taken with respect to the normalized time. Substituting these definitions into equations (2.2.18), (2.2.19) and (2.2.21) results in the following set of six reduced rate equations:

$$\begin{aligned} \dot{e}_j(\hat{t}) = & \frac{1}{2} \left[(2\Delta n_j(\hat{t}) + 1) G_{Pj} - 1 \right] e_j(\hat{t}) \\ & + \eta_{jj} e_j(\hat{t}) \cos \psi_{jj} + \frac{r_{sp}}{2e_j(\hat{t})} \\ & + \eta_{jk} e_k(\hat{t}) \cos[\tau_p \Delta \omega_{oj} \hat{t} + \phi_k(\hat{t}) - \phi_j(\hat{t}) + \psi_{jk}] \end{aligned} \quad (2.3.6)$$

$$\begin{aligned} \dot{\phi}_j(\hat{t}) = & \alpha \Delta n_j(\hat{t}) + \eta_{jj} \sin \psi_{jj} \\ & + \eta_{jk} \frac{e_k(\hat{t})}{e_j(\hat{t})} \sin[\tau_p \Delta \omega_{oj} \hat{t} + \phi_k(\hat{t}) - \phi_j(\hat{t}) + \psi_{jk}] \end{aligned} \quad (2.3.7)$$

$$\sigma \Delta \dot{n}_j(\hat{t}) = \Delta \rho_j(\hat{t}) - \Delta n_j(\hat{t}) - \left(2 \Delta n_j(\hat{t}) + 1 \right) G_{Pj} e_j^2(\hat{t}). \quad (2.3.8)$$

$$j \neq k = 1, 2.$$

$\Delta \omega_{oj} = \omega_{ok} - \omega_{oj}$ is the uncoupled frequency detuning between the two lasers, referenced to laser j . The dimensionless term G_{Pj} accounts for gain compression, and is given by

$$G_{Pj} = 1 - \frac{2\beta_{oo}^j}{\tau_s \frac{\partial G}{\partial N}} e_j^2(t), \quad (2.3.9)$$

where β_{oo}^j is the self saturation coefficient of the lasing mode in laser j . A dimensionless spontaneous emission rate into the lasing mode has also been defined as

$$r_{sp} \equiv \frac{1}{2} \tau_s \tau_p \frac{\partial G}{\partial N} R_{sp}. \quad (2.3.10)$$

Equations (2.3.6)-(2.3.8) form the basis for the analytical and numerical modeling to be presented in this work.

In phase-locked, steady-state operation, the system will oscillate at a single frequency ω_L , with the phase difference between the lasers remaining constant in time. Here, the steady-state phase of laser j in reduced form is given by

$$\phi_j(t) = \tau_p (\omega_L - \omega_{oj}) t + \phi_{Lj}. \quad (2.3.11)$$

Recalling definition (2.2.20), the locked phase difference $\Delta\phi_{Lj}$ between the lasers can be straightforwardly derived as

$$\begin{aligned}\Delta\phi_{Lj} &\equiv \phi_{Lk} - \phi_{Lj} = \Delta_j(\hat{t}) \\ &= \tau_p \Delta\omega_{oj} \hat{t} + \phi_k(\hat{t}) - \phi_j(\hat{t}).\end{aligned}\quad (2.3.12)$$

Let the stationary values of field amplitude \bar{e}_j , carrier number variation from threshold $\bar{\Delta n}_j$ and pumping parameter $\bar{\Delta\rho}_j$ for laser j be defined as listed, with a bar signifying time independence. Substitution of these, along with (2.3.12), into the reduced rate equations (2.3.6)-(2.3.8) results in the following stationary equations

$$\bar{\Delta n}_j = - \left(\eta_{sc} \cos\psi_{sc} + \eta_{cc} \frac{\bar{e}_k}{\bar{e}_j} \cos(\Delta\phi_{Lj} + \psi_{cc}) \right) \quad (2.3.13)$$

$$\begin{aligned}\tau_p(\omega_L - \omega_{oj}) &= \eta_{sc} \left(\sin\psi_{sc} - \alpha \cos\psi_{sc} \right) \\ &\quad + \eta_{cc} \frac{\bar{e}_k}{\bar{e}_j} \left(\sin(\Delta\phi_{Lj} + \psi_{cc}) - \alpha \cos(\Delta\phi_{Lj} + \psi_{cc}) \right)\end{aligned}\quad (2.3.14)$$

$$\bar{e}_j^2 = \frac{\bar{\Delta\rho}_j - \bar{\Delta n}_j}{1 + 2\bar{\Delta n}_j} \quad (2.3.15)$$

$$j \neq k = 1, 2.$$

The coupling junction has been assumed to be symmetrical in the following analysis, so that $\tilde{\eta}_{12} = \tilde{\eta}_{21} \equiv \tilde{\eta}_{cc} = \eta_{cc} e^{-i\psi_{cc}}$ and $\tilde{\eta}_{11} = \tilde{\eta}_{22} \equiv \tilde{\eta}_{sc} = \eta_{sc} e^{-i\psi_{sc}}$. This is the case in most important coupling schemes. Further, spontaneous emission and gain compression have both been neglected in (2.3.13)-(2.3.15), since they play a negligible role in determining equilibria for a laser operating

CW at moderate output powers.

The preceding set of six nonlinear algebraic equations constitutes the necessary formulae to describe the steady-state operation of mutually coupled semiconductor lasers. There are six unknowns: the field amplitudes $\bar{e}_{j,k}$ and carrier numbers $\bar{n}_{j,k}$ in each laser along with the locked frequency of oscillation ω_L and locked phase difference $\Delta\phi_L$. Their values are dependent upon a number of parameters, including the self and cross-coupling coefficients and the free-running oscillation frequencies of each laser. Absolute frequencies, however, are difficult to obtain precisely. Frequency *differences*, on the other hand, are readily measured. Therefore, equations (2.3.14) (one for each laser j,k) can be rewritten in a more usable form. Subtracting the equations leaves

$$\begin{aligned} \tau_p \Delta\omega_o &= \eta_{cc} \sqrt{1+\alpha^2} \left(\frac{\bar{e}_k}{\bar{e}_j} + \frac{\bar{e}_j}{\bar{e}_k} \right) \sin\Delta\phi_L \cos(\psi_{cc} - \tan^{-1}\alpha) \\ &+ \eta_{cc} \sqrt{1+\alpha^2} \left(\frac{\bar{e}_k}{\bar{e}_j} - \frac{\bar{e}_j}{\bar{e}_k} \right) \cos\Delta\phi_L \sin(\psi_{cc} - \tan^{-1}\alpha). \end{aligned} \quad (2.3.16)$$

The locked phase difference with respect to laser k was eliminated above in favor of $\Delta\phi_L \equiv \Delta\phi_{Lj} = -\Delta\phi_{Lk}$. Similarly, the detuning is defined as $\Delta\omega_o \equiv \Delta\omega_{oj}$. Note that the explicit self-coupling influence has dropped out, due to the assumption of symmetrical coupling. The trigonometric identity $\sin\theta \pm \alpha \cos\theta = \sqrt{1+\alpha^2} \sin(\theta \pm \tan^{-1}\alpha)$ has also been used to simplify (2.3.16).

Further, it is preferable to define the locked frequency of oscillation ω_L with respect to the *average* free-running frequency $\bar{\omega}_o$,

$$\Delta\omega_L \equiv \omega_L - \bar{\omega}_o, \quad (2.3.17)$$

or

$$\Delta\omega_L = \frac{\omega_L - \omega_{oj}}{2} + \frac{\omega_L - \omega_{ok}}{2}. \quad (2.3.18)$$

Substitution of equations (2.3.14) into (2.3.18) then results in an expression for the locked frequency deviation from $\bar{\omega}_o$

$$\begin{aligned} 2\tau_p(\Delta\omega_L - \Delta\omega_{sc}) &= \eta_{cc} \sqrt{1+\alpha^2} \left(\frac{\bar{e}_k}{\bar{e}_j} - \frac{\bar{e}_j}{\bar{e}_k} \right) \sin\Delta\phi_L \cos(\psi_{cc} - \tan^{-1}\alpha) \\ &+ \eta_{cc} \sqrt{1+\alpha^2} \left(\frac{\bar{e}_k}{\bar{e}_j} + \frac{\bar{e}_j}{\bar{e}_k} \right) \cos\Delta\phi_L \sin(\psi_{cc} - \tan^{-1}\alpha). \end{aligned} \quad (2.3.19)$$

The term $\Delta\omega_{sc} = \eta_{sc} \sqrt{1+\alpha^2} \sin(\psi_{sc} - \tan^{-1}\alpha) / \tau_p$ is defined as the angular frequency excursion an exclusively self-coupled laser would experience. (2.3.19) shows that self-coupling manifests as an offset to the locked frequency of oscillation. The direction and magnitude of the frequency shift is determined by the amplitude and phase of the self-coupling coefficient.

The stationary equations can be further simplified by inverting (2.3.15) for $\bar{\Delta n}_j$. Substituting into (2.3.13) leaves

$$\frac{\Delta\bar{\rho}_j - \bar{e}_j^2}{1 + 2\bar{e}_j^2} = -\text{Re}[\tilde{\eta}_{sc}] - \eta_{cc} \frac{\bar{e}_k}{\bar{e}_j} \cos(\Delta\phi_{Lj} + \psi_{cc}), \quad j \neq k = 1, 2. \quad (2.3.20)$$

By considering the locked frequency with respect to the average uncoupled value and making the above substitution, simultaneous solution of only two equations, (2.3.16) and (2.3.20) for $\Delta\phi_L$ and $\bar{e}_{j,k}$, is necessary. The locked frequency deviation $\Delta\omega_L$ and carrier number $\bar{\Delta n}_j$ can be found after the fact from

equations (2.3.19) and (2.3.15) if desired. These are considered in detail through comparisons to experiment in Chapters 3 and 4.

Numerical solutions of (2.3.16) and (2.3.20) are shown in Figures 2.1 and 2.2. The locked phase difference and field amplitudes are plotted as a function of detuning $\Delta\omega_0$ for $\eta_{cc} = 0.1$ at several coupling phases. This coupling magnitude can be considered representative of steady-state operation for $\eta_{cc} \leq 0.1$. The system supports two modes: a symmetric (even) mode with a principal value ($-\pi < \Delta\Phi_L \leq \pi$) of $\Delta\phi_L$ in the range $(-\pi/2, \pi/2)$, and an asymmetric (odd) mode with $\Delta\Phi_L$ elsewhere. Note that the "symmetry" of a mode refers to the phase difference between the field in each laser, and does not pertain in any way to its intensity profile.

Stationary phase locked operation of the mutually coupled system occurs only when the free-running oscillation frequencies of the individual lasers are sufficiently close. As shown in Figure 2.1 a), $\Delta\phi_L$ changes to compensate for the frequency difference when the lasers are detuned. This can only continue up to a point, however. When $\Delta\phi_L$ reaches $(2m+1)\frac{\pi}{2}$, the maximum allowable detuning is reached, after which no stationary solutions exist. The phase difference between the lasers then increases indefinitely. The region of parameter space comprising stationary solutions is termed the *lockband*. Its maximum width with respect to frequency detuning is denoted hereafter as $\Delta\omega_{LB}$. Similar behavior is well known in the operation of injection-locked oscillators^{39, 46}.

For mutual coupling, however, the size of the lockband is in part determined by the cross-coupling phase, ψ_{cc} . This fact has been ignored in previous analyses^{60, 61, 122}. Figures 2.1 and 2.2 illustrate this dependence. The

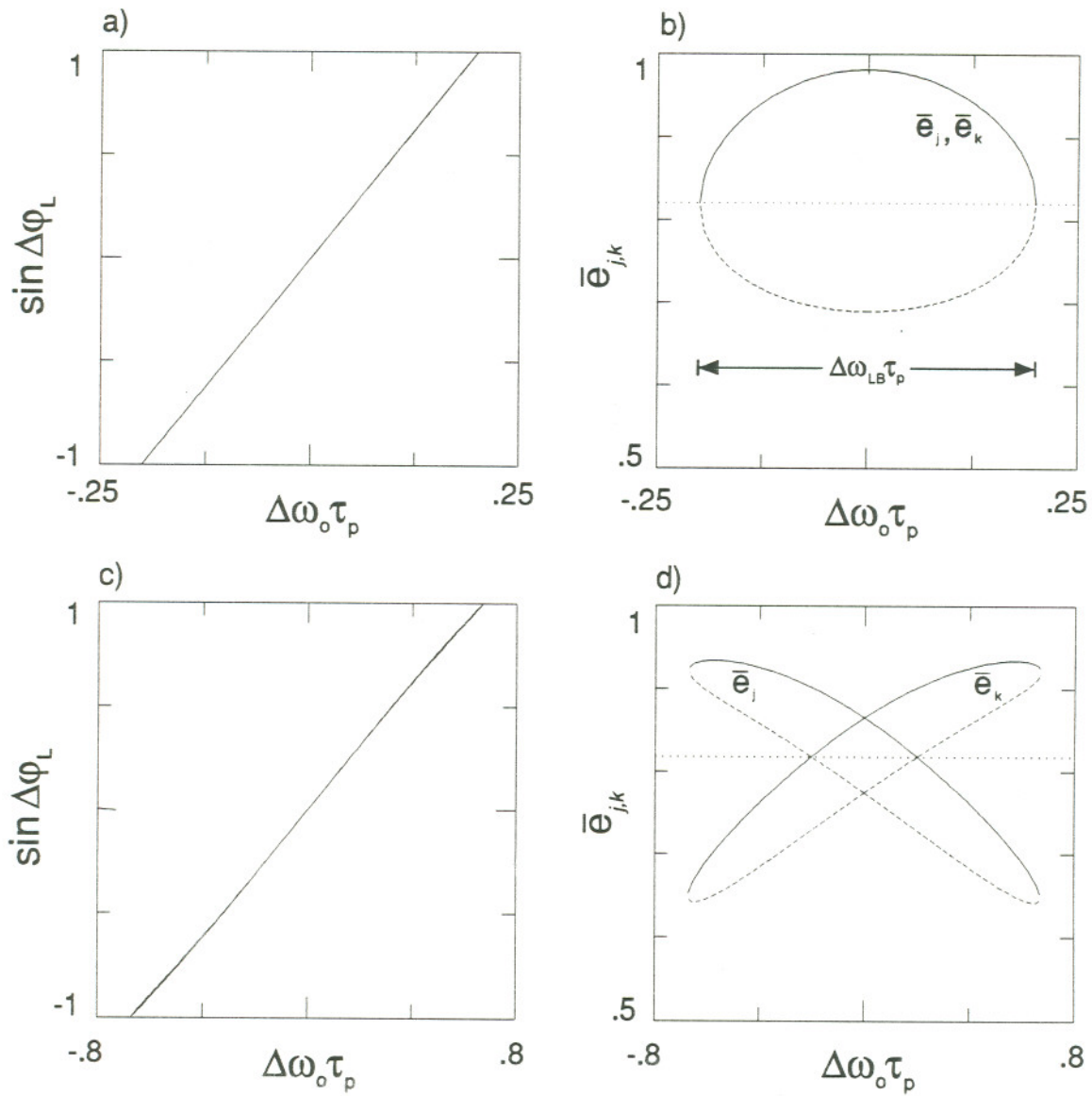


Figure 2.1 Stationary solutions for two mutually coupled semiconductor lasers. $\eta_{\infty} = 0.1$, $\alpha = 3$, $\Delta\rho = 0.67$.
 a),b) maximum mode suppression, $\psi_{\infty} = 0$, c),d) maximum locking range, $\psi_{\infty} = \tan^{-1}\alpha = 1.249$.
 — even mode, - - - - - odd mode, free-running.

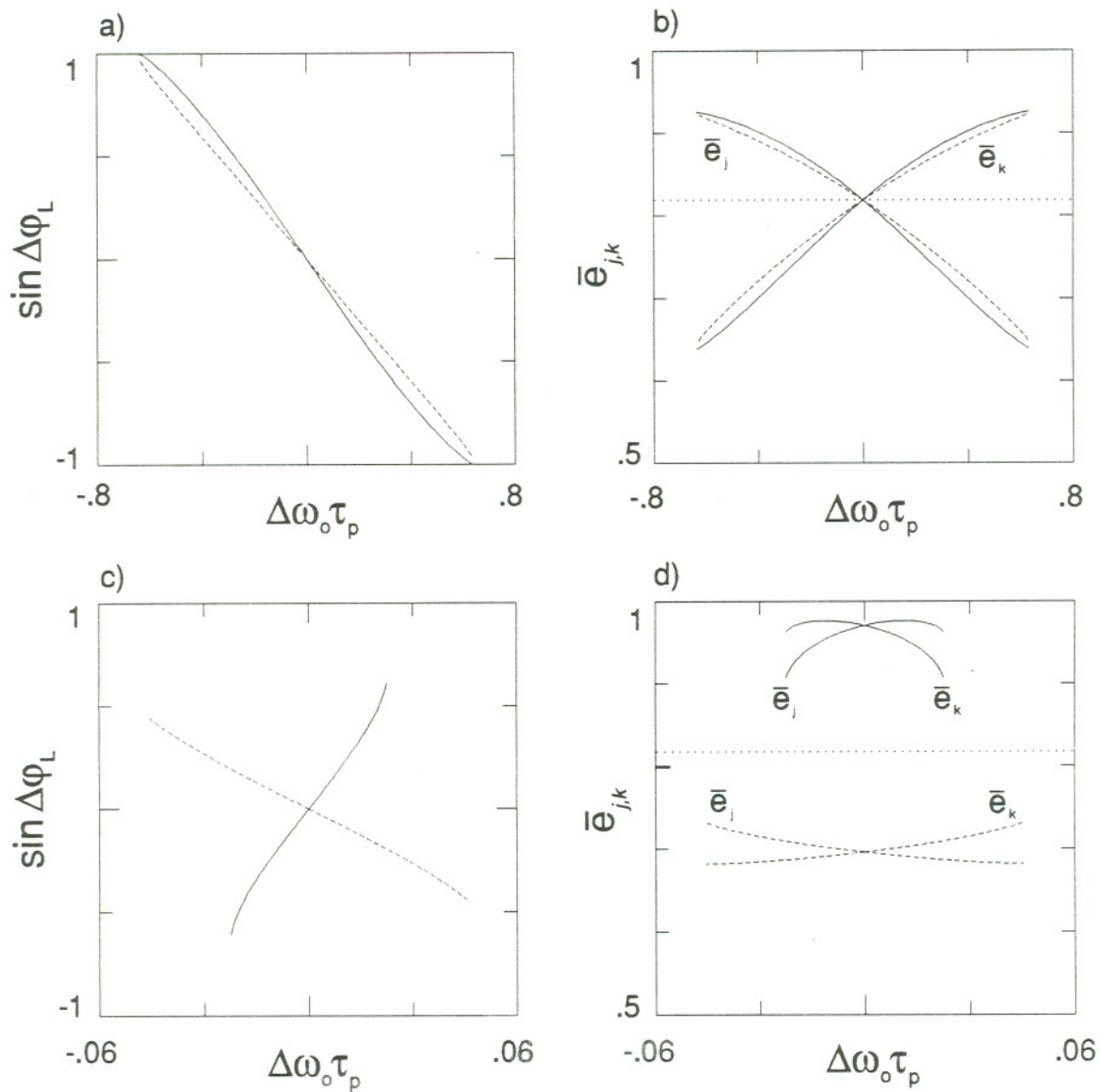


Figure 2.2 Stationary solutions for two mutually coupled semiconductor lasers. $\eta_{\infty} = 0.1$, $\alpha = 3$, $\Delta\rho = 0.67$.
 a), b) minimum mode suppression, $\psi_{cc} = -\pi/2$, c), d) near minimum locking range, $\psi_{cc} = -0.34$.

—— even mode, - - - - - odd mode, free-running.

maximum locking range occurs at $\psi_{cc} = m\pi + \tan^{-1}\alpha$. This location is a consequence of the carrier-dependent refractive index property characteristic of semiconductor lasers (see Appendix A). The α parameter effectively shifts the coupling phase from ψ_{cc} by $-\tan^{-1}\alpha$ as is evident in equation (2.3.16). This phenomenon is crucial to the operation of coupled diode lasers and will appear many times during the course of this study. The minimum lockband, on the other hand, occurs at $\psi_{cc} = (2m+1)\pi/2 + \tan^{-1}\alpha$. Examination of equation (2.3.16) reveals that the lockband would vanish here if not for an imbalance in the field amplitudes with detuning. Figure 2.2 c) displays the locking characteristics at $\psi_{cc} = -0.34$, which is close to $\psi_{cc} = \tan^{-1}\alpha - \pi/2$. The lockband is over an order of magnitude smaller than at $\psi_{cc} = \tan^{-1}\alpha$.

Optical coupling generally creates a difference in amplitudes (or power) between the lasers as they are detuned, as evidenced in Figures 2.1 and 2.2. This power imbalance is greatest at $\psi_{cc} = \pm\pi/2$, whereas the amplitudes in each laser are identical for any detuning only at $\psi_{cc} = 0, \pi$. (Coupling phases separated by π merely have the roles of even and odd modes reversed). The variation in power with detuning relates to a change in threshold gain according to equations (2.3.13) and (2.3.20). Note that for $\psi_{cc} = 0, \pi$, in Figure 2.1 b), the difference in gain between the even and odd modes is maximized. Experimentally, this will be reflected in the mode suppression ratio. Mode suppression, on the other hand, is zero at $\psi_{cc} = \pm\pi/2$.

An approximate analytical expression for the lockband can be found for the case where $\bar{e}_j \approx \bar{e}_k$. This is exactly applicable when $\psi_{cc} = 0, \pi$ and is an excellent approximation for $\eta_{cc} \lesssim 0.1$. The locking range is then given from

(2.3.16) as

$$\Delta\omega_{LB} \approx 2 \frac{\eta_{cc}}{\tau_p} \sqrt{1+\alpha^2} \cos(\psi_{cc} - \tan^{-1}\alpha). \quad (2.3.21)$$

The lockband is therefore directly proportional to the cross-coupling magnitude and depends heavily on its phase as well. For semiconductor lasers, the locking range is increased by a factor of $\sqrt{1+\alpha^2}$ over lasers with $\alpha=0$. The maximum locking range, with $\psi_{cc} = \tan^{-1}\alpha$, is simply

$$\Delta\omega_{LB,max} \approx 2 \frac{\eta_{cc}}{\tau_p} \sqrt{1+\alpha^2}. \quad (2.3.22)$$

Given a typical semiconductor laser photon lifetime of 1 ps, locking ranges of several hundred GHz are expected at strong coupling levels, where $\eta_{cc} \sim 0.1$. It is also notable that the lockband size is very weakly affected by the presence of symmetrical self-coupling; the real part of the self-coupling coefficient, $\text{Re}[\tilde{\eta}_{sc}]$, merely serves to modify the mode suppression ratio through its presence in equation (2.3.20). The shift in the locked frequency due to self-coupling, mentioned earlier, is of no consequence to the lockband.

Obviously, a large lockband is beneficial for coupling lasers optically so that drift, nonuniformities, etc. can be accommodated without adversely affecting the phase-lock. The coupled system should additionally operate in a single mode with adequate side mode suppression. In the interest of beam combining, the symmetric mode, with nearly equal power levels oscillating in each laser, is preferable. The latter conditions are all met for a coupling phase of $\psi_{cc} = 0$. The maximum locking range, however, occurs elsewhere at

$\psi_{cc} = \tan^{-1}\alpha$. Since α is often much larger than one for semiconductor lasers, $\tan^{-1}\alpha$ approaches $\pi/2$ making the lockband at $\psi_{cc}=0$ small. Minimizing α , on the other hand, results in a smaller lockband according to (2.3.22). This behavior is demonstrated in Figure 2.3. The locking range has been plotted for both the even and odd modes as a function of coupling phase with $\eta_{cc} = 0.1$. For $\alpha = 0$ the lockband is smallest at $\psi_{cc} = \pm\pi/2$, whereas for $\alpha = 3$ it nearly vanishes at $\psi_{cc} \approx 0.9\pi, 0.1\pi$. While an enhanced lockband (by a factor of $\sqrt{1+\alpha^2}$) is beneficial in semiconductor lasers possessing large α parameters, a large locking range and good mode suppression appear to be incompatible objectives.

At coupling magnitudes where $\eta_{cc} > 0.1$, the lockband was found to no longer be limited by the condition $\sin\Delta\phi_L \leq 1$, except for ψ_{cc} near 0 or π . Rather, stationary solutions exist for all values of detuning. Stability of the equilibria must then be addressed to determine the locking range⁶⁰. The case in which $\alpha = 0$ and $\psi_{cc} = -\pi/2$, in the present notation, has been previously considered^{61,62} in connection with coupled CO₂ lasers separated by a common coupling mirror. The lockband was found to be linearly dependent on the coupling magnitude, albeit at the expense of a large power imbalance between the lasers. In fact, a large locking range in this circumstance was only possible *because* of the unequal intensities¹²². The threshold gain difference between the even and odd modes, in this situation, is extremely small (zero when the lasers are resonantly tuned). This is due to an absence of supermode selective losses in the compound resonator, which is generally not the case in coupled systems.

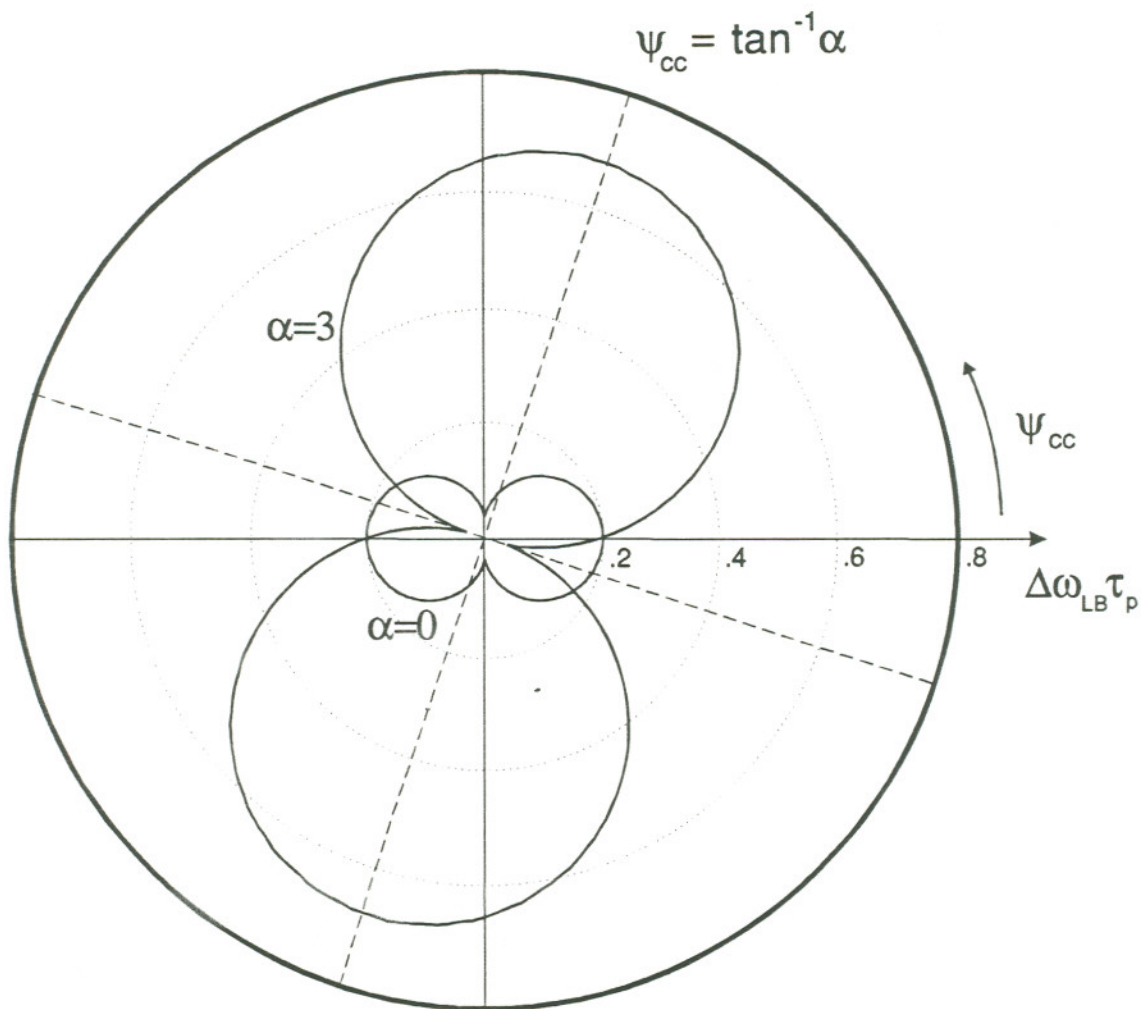


Figure 2.3 Locking bandwidth versus coupling phase for two mutually coupled semiconductor lasers. $\eta = 0.1$, $\Delta\rho = 0.67$.

2.4 Stability Analysis

The phase-locked solutions encountered in Section 2.3 do not necessarily represent dynamically stable states. The usable locking range may therefore be smaller than expected. The stability of a stationary solution can be determined by examining the system's response to infinitesimal fluctuations from the steady-state. In this way, the rate equations (2.3.6)-(2.3.8) are greatly reduced in complexity through linearization. Standard linear systems techniques can then be applied to test stability. Denoting small deviations in field amplitude $\delta e_j(\hat{t})$, phase $\delta\Phi_j(\hat{t})$ and carrier number $\delta n_j(\hat{t})$ as such, the dynamic variables can be written with respect to their stationary values as

$$e_j(\hat{t}) = \bar{e}_j + \delta e_j(\hat{t}) \quad (2.4.1)$$

$$\Phi_j(\hat{t}) = -\tau_p \Delta\omega_{oj} \hat{t} + \Delta\phi_{Lj} + \delta\Phi_j(\hat{t}) \quad (2.4.2)$$

$$\Delta n_j(\hat{t}) = \bar{\Delta n}_j + \delta n_j(\hat{t}). \quad (2.4.3)$$

$\Phi_j \equiv \phi_k(\hat{t}) - \phi_j(\hat{t})$ has been introduced since the phase *difference* between the lasers is the quantity of interest for phase-locking. Additionally, the number of rate equations is reduced from six to five.

Substitution of these expressions (2.4.1)-(2.4.3) into equations (2.3.6)-(2.3.8), retaining terms only to first-order in the deviations, results in the following set of five linearized rate equations:

$$\begin{aligned} \delta \dot{e}_j(\hat{t}) = & -\eta_{jk} \frac{\bar{e}_k}{e_j} \cos(\Delta\phi_{Lj} + \psi_{jk}) \delta e_j(\hat{t}) + \eta_{jk} \cos(\Delta\phi_{Lj} + \psi_{jk}) \delta e_k(\hat{t}) \\ & - \eta_{jk} \bar{e}_k \sin(\Delta\phi_{Lj} + \psi_{jk}) \delta\Phi_j(\hat{t}) + \bar{e}_j \delta n_j(\hat{t}) \end{aligned} \quad (2.4.4)$$

$$\begin{aligned}
\delta\dot{\Phi}_j(\hat{t}) = & \left[\eta_{jk} \frac{\bar{e}_k}{e_j^2} \sin(\Delta\phi_{Lj} + \psi_{jk}) + \eta_{kj} \frac{1}{e_k} \sin(\Delta\phi_{Lk} + \psi_{kj}) \right] \delta e_j(\hat{t}) \\
& - \left[\eta_{jk} \frac{1}{e_j} \sin(\Delta\phi_{Lj} + \psi_{jk}) + \eta_{kj} \frac{\bar{e}_j}{e_k^2} \sin(\Delta\phi_{Lk} + \psi_{kj}) \right] \delta e_k(\hat{t}) \\
& - \left[\eta_{jk} \frac{\bar{e}_k}{e_j} \cos(\Delta\phi_{Lj} + \psi_{jk}) + \eta_{kj} \frac{\bar{e}_j}{e_k} \cos(\Delta\phi_{Lk} + \psi_{kj}) \right] \delta\Phi_j(\hat{t}) \\
& - \alpha \delta n_j(\hat{t}) + \alpha \delta n_k(\hat{t})
\end{aligned} \tag{2.4.5}$$

$$\sigma \delta \dot{n}_j(\hat{t}) = -2\bar{e}_j \left(1 + 2\Delta\bar{n}_j \right) \delta e_j(\hat{t}) - \left(1 + 2\bar{e}_j^2 \right) \delta n_j(\hat{t}) \tag{2.4.6}$$

$$j \neq k = 1, 2.$$

The stationary solutions (2.3.13)-(2.3.15) and the assumption of small fluctuation terms were used to simplify above. Gain compression and spontaneous emission terms were also neglected in this small signal analysis. The latter was found to have a negligible effect on stability boundaries with the lasers biased well above threshold. Gain compression, on the other hand, is later shown to significantly affect the stability properties of a coupled system, and will be incorporated through an effective damping rate. It at first appears that all self-coupling terms have vanished. Note, however, that the real part of each self-coupling coefficient is retained implicitly in the stationary carrier number deviation from threshold $\Delta\bar{n}_{j,k}$ present in (2.4.6).

Equations (2.4.4)-(2.4.6) describe the time evolution of the system to infinitesimal fluctuations about a stationary solution. Since they are linear and homogeneous in the fluctuations $\delta e_{j,k}$, $\delta\Phi_j$ and $\delta n_{j,k}$, solutions proportional to $\exp(s\hat{t})$ can be sought, where s is a complex number describing the rate and frequency of damping for each solution. Substitution of this form into the above

equations results in a system of algebraic equations which can be written as

$$[\mathbf{A} - s\mathbf{I}] \delta \mathbf{x}_0 = 0. \quad (2.4.7)$$

\mathbf{A} is a (Jacobian) matrix containing the coefficients of the fluctuation terms evaluated at the stationary solution, while $\delta \mathbf{x}_0$ is a column vector of the fluctuations evaluated at time zero. For non-trivial solutions to exist, it is required that the secular determinant

$$D(s) \equiv \det[\mathbf{A} - s\mathbf{I}] = 0. \quad (2.4.8)$$

Analytical solutions are, however, only realizable when additional symmetry is introduced. Once again, symmetric coupling is assumed where $\tilde{\eta}_{jk} = \tilde{\eta}_{kj}$ and $\tilde{\eta}_{jj} = \tilde{\eta}_{kk}$. Further, the problem must be restricted to equal pumping and no detuning, resulting in a completely symmetric system. While the general case can be solved numerically, a great deal of insight is achieved by examining the parameter dependence analytically.

Stationary solutions in the symmetric case are greatly simplified. The field amplitudes $\bar{e}_{j,k}$ and carrier numbers $\bar{\Delta n}_{j,k}$ in each laser are equal, as determined in Section 2.3. They are denoted \bar{e} and $\bar{\Delta n}$ hereafter in this section. The locked phase difference $\Delta\phi_L$ between the lasers will assume a value of $m\pi$, with even multiples of π corresponding to the in-phase mode and odd multiples the out-of-phase mode. Equation (2.4.7) becomes

$$\begin{bmatrix} -a_{12}^{-s} & a_{12} & a_{13} & a_{14} & 0 \\ a_{12} & -a_{12}^{-s} & -a_{13} & 0 & a_{14} \\ a_{31} & -a_{31} & -2a_{12}^{-s} & -a_{35} & a_{35} \\ a_{41} & 0 & 0 & a_{44}^{-s} & 0 \\ 0 & a_{41} & 0 & 0 & a_{44}^{-s} \end{bmatrix} \cdot \begin{pmatrix} \delta e_{j0} \\ \delta e_{k0} \\ \delta \Phi_{j0} \\ \delta n_{j0} \\ \delta n_{k0} \end{pmatrix} = 0, \quad (2.4.9)$$

with elements

$$\begin{aligned}
 a_{12} &= \eta_{cc} \cos \psi_{cc} \cos \Delta \phi_L \\
 a_{13} &= -\eta_{cc} \bar{e} \sin \psi_{cc} \cos \Delta \phi_L \\
 a_{14} &= \bar{e} \\
 a_{31} &= 2\eta_{cc} \frac{1}{e} \sin \psi_{cc} \cos \Delta \phi_L \\
 a_{35} &= \alpha \\
 a_{41} &= -\frac{2\bar{e}}{\sigma} (1 + 2\Delta \bar{n}) \\
 a_{44} &= -\frac{1}{\sigma} (1 + 2\bar{e}^2). \tag{2.4.10}
 \end{aligned}$$

η_{cc} is the magnitude of the cross-coupling coefficient and ψ_{cc} is its phase. Expression (2.4.8) then results in a characteristic equation which can be factored into quadratic and cubic terms

$$\begin{aligned}
 D(s) &= [s^2 - a_{44}s - a_{14}a_{41}] \\
 &\cdot [s^3 + (4a_{12} - a_{44})s^2 + (4a_{12}^2 - 2a_{13}a_{31} - a_{14}a_{41} - 4a_{12}a_{44})s \\
 &+ (2a_{13}a_{31}a_{44} - 4a_{12}^2a_{44} + 2a_{13}a_{35}a_{41} - 2a_{12}a_{14}a_{41})] = 0. \tag{2.4.11}
 \end{aligned}$$

Substituting matrix elements (2.4.10) into the second-order term in equation (2.4.11) gives

$$s^2 + \frac{1+2\bar{e}^2}{\sigma}s + \frac{2\bar{e}^2}{\sigma}(1+2\Delta \bar{n}) = 0. \tag{2.4.12}$$

This is merely the equation of a damped harmonic oscillator. Eigenvalues are found from the quadratic equation as

$$s = -\gamma \pm i \sqrt{\Omega_R^2 - \gamma^2}, \quad (2.4.13)$$

where

$$\gamma \equiv \frac{1+2\bar{e}^2}{2\sigma}, \quad \Omega_R^2 \equiv \frac{2\bar{e}^2}{\sigma}(1+2\bar{\Delta n}). \quad (2.4.14)$$

In the limit that the coupling magnitude goes to zero, $\bar{e} = \bar{e}_0$ and $\bar{\Delta n} = 0$. The terms $\frac{\gamma}{\tau_p}$ and $\frac{\Omega_R}{\tau_p}$ can then be identified with the damping rate and the well-known relaxation resonance frequency¹⁰⁸ of an isolated laser. Equation (2.4.12) therefore describes the response associated with the coupled lasers acting as a whole. It differs from a single laser only in that the damping and relaxation resonance are changed due to coupling.

Stability requires that the real part of the eigenvalue s be negative, or that $\gamma > 0$, so that perturbations damp exponentially back to equilibrium. In reality, this condition is always met, since the field amplitude cannot be negative. However, recalling the stationary solution (2.3.15) for field amplitude, stability is violated whenever $\bar{\Delta n} > -1/2$ or

$$\text{Re}[\tilde{\eta}_{sc}] + \text{Re}[\tilde{\eta}_{cc}] \cos \Delta \phi_L < \frac{1}{2}. \quad (2.4.15)$$

(2.4.15) is nearly always met except for strong, in-phase coupling (for $\Delta \phi_L = 0$, or out-of-phase where $\Delta \phi_L = \pi$). As $\bar{\Delta n}$ approaches $-1/2$, the coupled fields are able to offset the total rate of loss in the lasers, effectively reducing the

threshold gain to zero. Therefore, the field amplitude is allowed to grow unbounded, through (2.3.15). This non-physical behavior represents a limitation to the present theoretical approach, which treats the lasers as individual entities. When the limit (2.4.15) is neared, the coupled fields can clearly no longer be considered a perturbation to the circulating field of the isolated laser. A similar problem exists when $\overline{\Delta n} > \overline{\Delta \rho}$.

It is important to note that the same characteristic equation (2.4.12) is obtained in the case of a strictly self-coupled laser (i.e. by dropping all cross-coupling terms). Stability is then expected for this configuration over the whole parameter space spanned by the complex coupling coefficient.

The most interesting stability information is contained in the cubic term of equation (2.4.11), which can also be written

$$\begin{aligned}
 & s^3 + \left(4\eta_{cc} \cos\psi_{cc} \cos\Delta\phi_L + 2\gamma\right) s^2 \\
 & + \left(4\eta_{cc}^2 + \Omega_R^2 + 8\gamma\eta_{cc} \cos\psi_{cc} \cos\Delta\phi_L\right) s \\
 & + \left(8\gamma\eta_{cc}^2 + 2\Omega_R^2\eta_{cc} \cos\Delta\phi_L \sqrt{1+\alpha^2} \cos(\psi_{cc} - \tan^{-1}\alpha)\right) = 0. \quad (2.4.16)
 \end{aligned}$$

The sign of each eigenvalue's real part can be determined, without actually solving for the roots of (2.4.16), by employing the Liénard and Chipart stability test.¹²³ For a third order polynomial,

$$D(s) = a_0 s^3 + a_1 s^2 + a_2 s + a_3 = 0, \quad (2.4.17)$$

the minimum requirement for stability is that the coefficients $a_1 > 0$, $a_3 > 0$ and that the second order Hurwitz determinant

$$\Delta_2 = \begin{vmatrix} a_1 & a_3 \\ a_o & a_2 \end{vmatrix} = a_1 a_2 - a_o a_3 > 0. \quad (2.4.18)$$

It turns out that the coefficient a_2 is always greater than zero when condition (2.4.15) is met. Therefore, the stability criterion $a_1 > 0$ is always contained within (2.4.18). $a_3 > 0$ requires that

$$\eta_{cc} > \frac{1}{4} \frac{\Omega_R^2}{\gamma} \cos \Delta \phi_L \sqrt{1 + \alpha^2} \cos(\psi_{cc} - \tan^{-1} \alpha), \quad (2.4.19)$$

while (2.4.18) results in a complicated expression restricting the coupling magnitude and phase to the region

$$\begin{aligned} & 8\eta_{cc}^3 \cos \psi_{cc} \cos \Delta \phi_L + 8\gamma \eta_{cc}^2 \cos^2 \psi_{cc} \\ & + \eta_{cc} \cos \Delta \phi_L \left(8\gamma^2 \cos \psi_{cc} + \Omega_R^2 \sqrt{1 + \alpha^2} \cos(\psi_{cc} - \tan^{-1} \alpha) \right) + \gamma \Omega_R^2 > 0. \end{aligned} \quad (2.4.20)$$

Figures 2.4 and 2.5 display the stability regions (2.4.19) and (2.4.20) as a function of coupling magnitude and phase. The thick dashed line denotes the limiting case of (2.4.19), whereas the solid line is the boundary of (2.4.20). The radial coordinate in the polar plots gives η_{cc} on a log scale, while the coupling phase ψ_{cc} is the azimuthal coordinate. Concentric dashed circles therefore denote contours of constant coupling magnitude. Regions of unstable operation, where one or both conditions are unsatisfied, have been shaded. In order to avoid confusion, only the symmetric mode $\Delta \phi_L = 0$ has been presented, as boundaries for the asymmetric solution are easily obtained by rotating the plot 180° about the origin. Very few parameters, including σ , $\bar{\Delta p}$ and α , must be specified to evaluate stability in the present model. Boundaries were found to

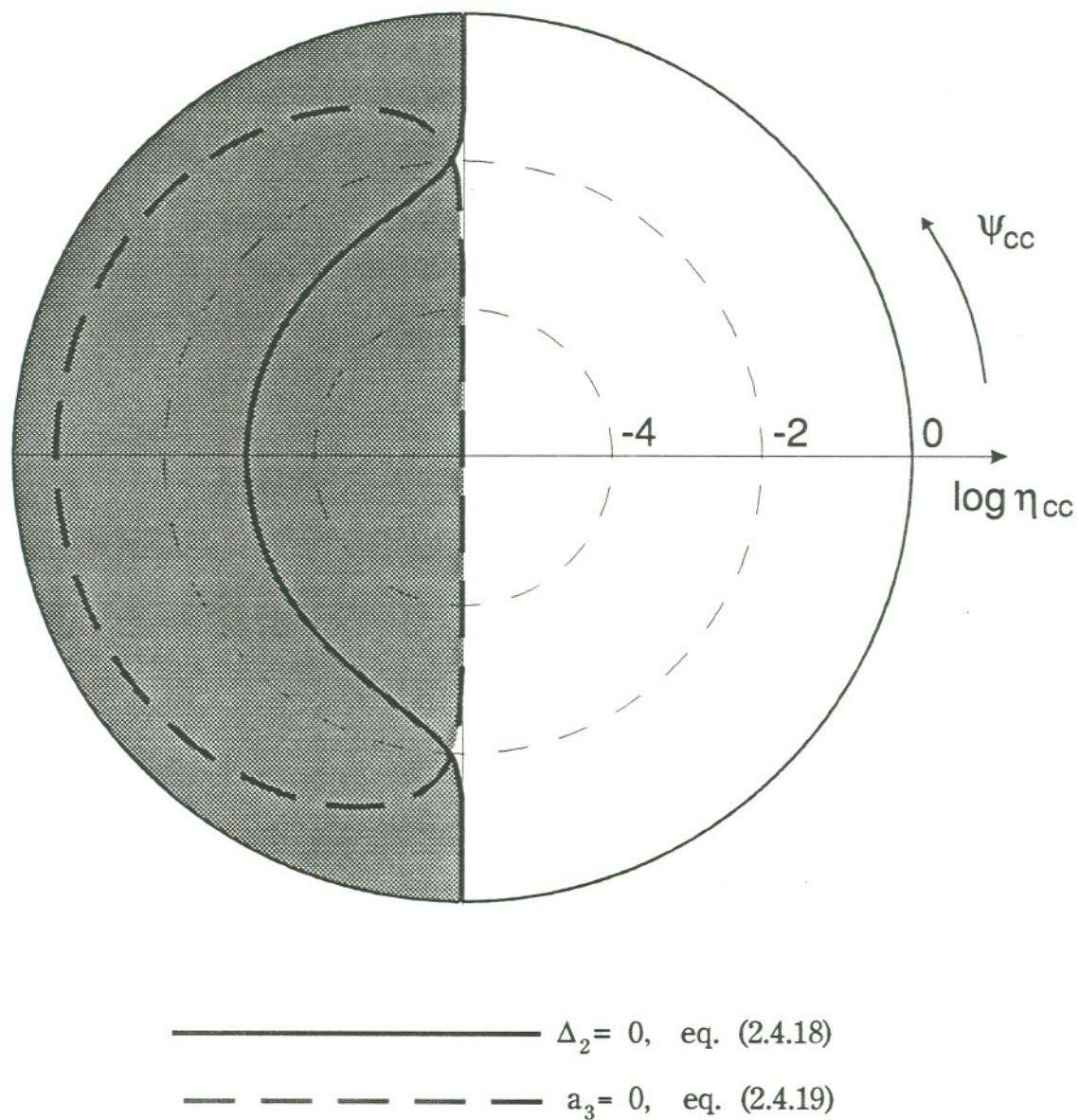


Figure 2.4 Stability boundaries for the symmetric mode of two mutually coupled lasers. $\alpha = 0$, $\sigma = 1500$, $\Delta\rho = 0.67$. Dynamically unstable regions are shaded.

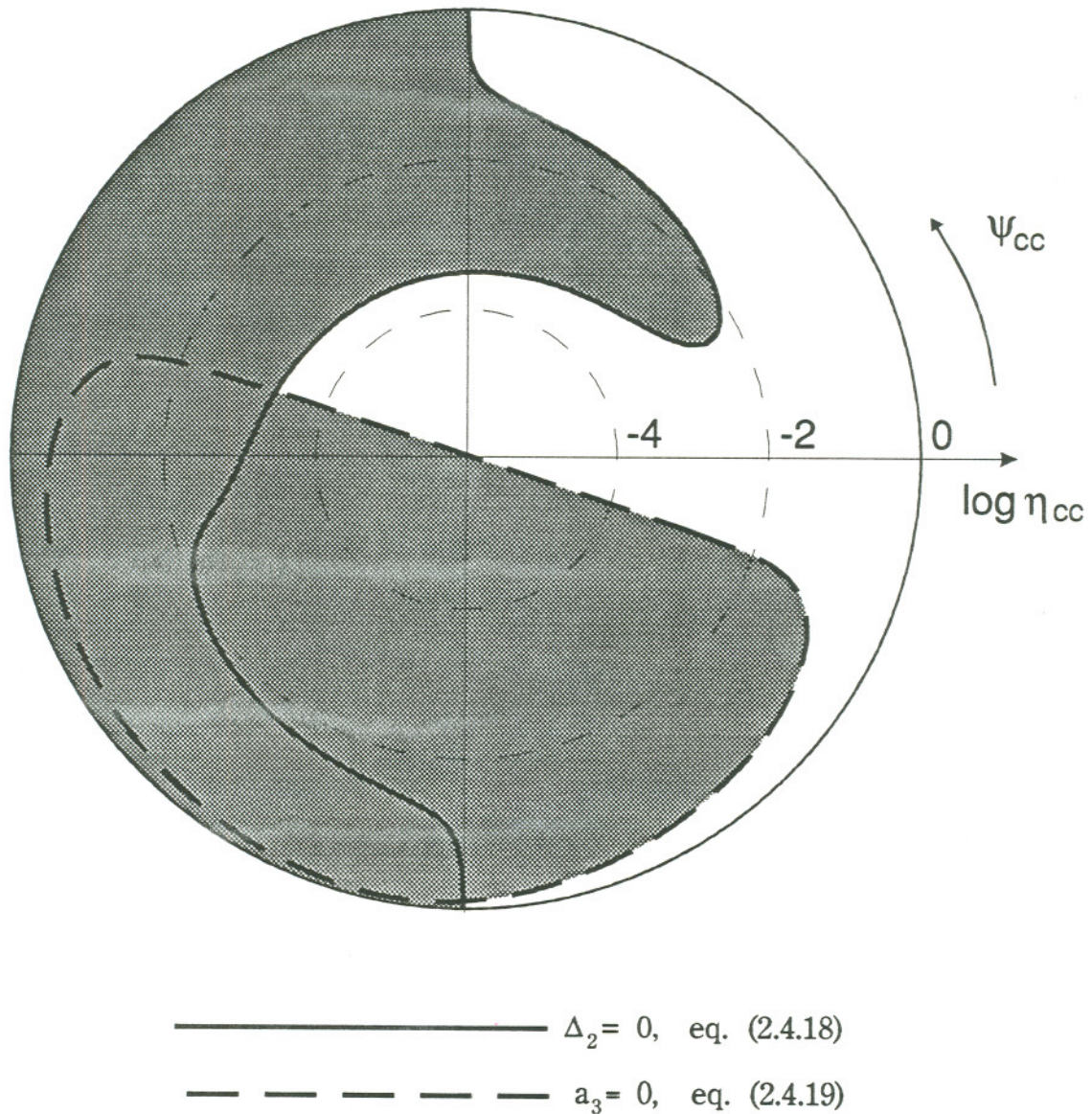


Figure 2.5 Stability boundaries for the symmetric mode of two mutually coupled lasers. $\alpha = 3$, $\sigma = 1500$, $\Delta\rho = 0.67$. Dynamically unstable regions are shaded.

be insensitive to relatively large changes in the former two parameters. These merely affect slight changes to Ω_R and γ through the equilibrium carrier number and field amplitude. Typical values of $\sigma=1500$ and $\overline{\Delta\rho}=0.67$ were chosen for graphical presentation. Self-coupling, for the same reason, also plays a minor role where $\eta_{sc} \lesssim 10^{-1}$ and is therefore neglected in the following.

The α parameter, on the other hand, substantially changes the stability properties of the mutually coupled system. Figure 2.4 first shows the case where $\alpha=0$. The complex plane is divided nearly in half, with the symmetric mode stable where $\text{Re}[\tilde{\eta}_{cc}] > 0$ and the asymmetric mode (not shown) stable for $\text{Re}[\tilde{\eta}_{cc}] < 0$. Therefore, the mutually coupled system operates stably, in one mode or the other, throughout the entire $\tilde{\eta}_{cc}$ plane. With α non-zero, however, the regions of stability become more complicated. Figure 2.5 displays the boundaries for $\alpha=3$. The $\tilde{\eta}_{cc}$ plane remains roughly divided in half by condition (2.4.19), although the dividing line has rotated by $\tan^{-1}\alpha$ about the origin. In the limit of large α , this boundary approaches the real axis, causing the symmetric mode to be stable for $\text{Im}[\tilde{\eta}_{cc}]>0$ and the asymmetric mode elsewhere.

The condition (2.4.20) is also highly dependent on α . Stable operation is predicted for both the symmetric and asymmetric modes at low coupling levels, independent of the coupling phase. The limiting η_{cc} where instability first sets in can be found from (2.4.20). For $\eta_{cc} \lesssim 10^{-2}$, the boundary is given by

$$\eta_{cc} \cos\Delta\phi_L \sqrt{1+\alpha^2} \cos(\psi_{cc} - \tan^{-1}\alpha) = -\gamma_o. \quad (2.4.21)$$

Terms greater than first order in η_{cc} and γ were dropped and γ was approximated as $\gamma_o \equiv (1+2\bar{e}_o^2)/2\sigma$, the reduced damping rate of the isolated laser, in

deriving (2.4.21). The above expression divides the $\tilde{\eta}_{cc}$ plane into stable and unstable halves. In the latter case, fluctuations couple positively, which can offset the inherent damping afforded by gain saturation above a critical coupling level given by

$$\eta_{crit} = \frac{\gamma_o}{\sqrt{1+\alpha^2}}. \quad (2.4.22)$$

In other words, undamped fluctuations may only occur when the coupling rate $\eta_{cc} \sqrt{1+\alpha^2}/\tau_p$ exceeds the intrinsic damping rate γ_o/τ_p . It is important that for $\eta_{cc} \gtrsim 10^{-2}$, stability boundaries approach the $\alpha=0$ condition in Figure 2.5.

Overall stability is decided by the intersection of (2.4.19) and (2.4.20). This is graphically pictured as the unshaded areas in Figure 2.5, for the symmetric mode. These areas do not overlap with the stable operating regions of the asymmetric mode, indicating an absence of bistability, although both solutions are *unstable* over much of the complex η_{cc} plane. With the exception of ψ_{cc} near 0 (for the even mode) or π (odd mode), stable phase-locked operation is expected to be interrupted at coupling magnitudes of about $\eta_{cc} \sim 10^{-3}$. At large coupling levels, stability returns; behavior is that encountered when $\alpha=0$.

Although regions of stable and unstable operation have been identified, it remains to determine where the system should operate for maximum stability. To this end, the three eigenvalues of (2.4.16) were numerically calculated. The limit of stable operation is reached when an eigenvalue s crosses the imaginary axis. It is easily shown that condition (2.4.19) corresponds to a single eigenvalue with $\text{Im}[s]=0$. Except at very large values of η_{cc} , this boundary divides the $\tilde{\eta}_{cc}$ plane in half, with stability confined to the half where interference

between the lasing fields is constructive. In the case $\alpha=0$, this is the right half-plane (for the even mode), as shown in Figure 2.4. When α is non-zero, however, the dividing line rotates by $\tan^{-1}\alpha$, due to the change in refractive index which accompanies a shift in gain or carrier number. The real part of the eigenvalue associated with (2.4.19) is plotted in Figure 2.6 at selected coupling phases which satisfy the stability criterion for the symmetric mode. For $\eta_{cc} \lesssim 10^{-2}$, the best damped mode is at $\psi_{cc} = \tan^{-1}\alpha$ (not shown), where the lockband is maximum. At larger coupling magnitudes, this location shifts to $\psi_{cc}=0$, where Δn is a minimum, even though the stability boundary approaches the real axis for large α . Damping therefore falls off rapidly for ψ_{cc} slightly negative, as evidenced by Figure 2.6 e).

The remaining eigenvalues are complex conjugates, and correspond to the stability criterion (2.4.20). Figure 2.7 displays the real and imaginary parts of the eigenvalue with $\text{Im}[s] \geq 0$, normalized to the free-running condition $(\gamma_o, \omega_R \tau_p)$. Radial slices through Figure 2.5 at constant ψ_{cc} were selected in the right half plane for the even mode. The trajectory of the eigenvalue along each slice as a function of coupling magnitude is plotted in Figure 2.7. Symbols identify three specific coupling levels for reference.

Note that the optical coupling has little effect on the frequency or damping of the eigenvalues where $\eta_{cc} \lesssim 10^{-4}$. They remain near the values $\omega_R \tau_p, \gamma_o$ (solid dot) regardless of the coupling phase. A zero of $D(s)$ first crosses the imaginary axis at $\text{Im}[s]/\tau_p \approx \omega_R$. Hence, instability will initially appear in the optical and intensity spectra as a peak at the relaxation resonance frequency of the isolated laser. Physically, this "undamping" of the relaxation resonance can

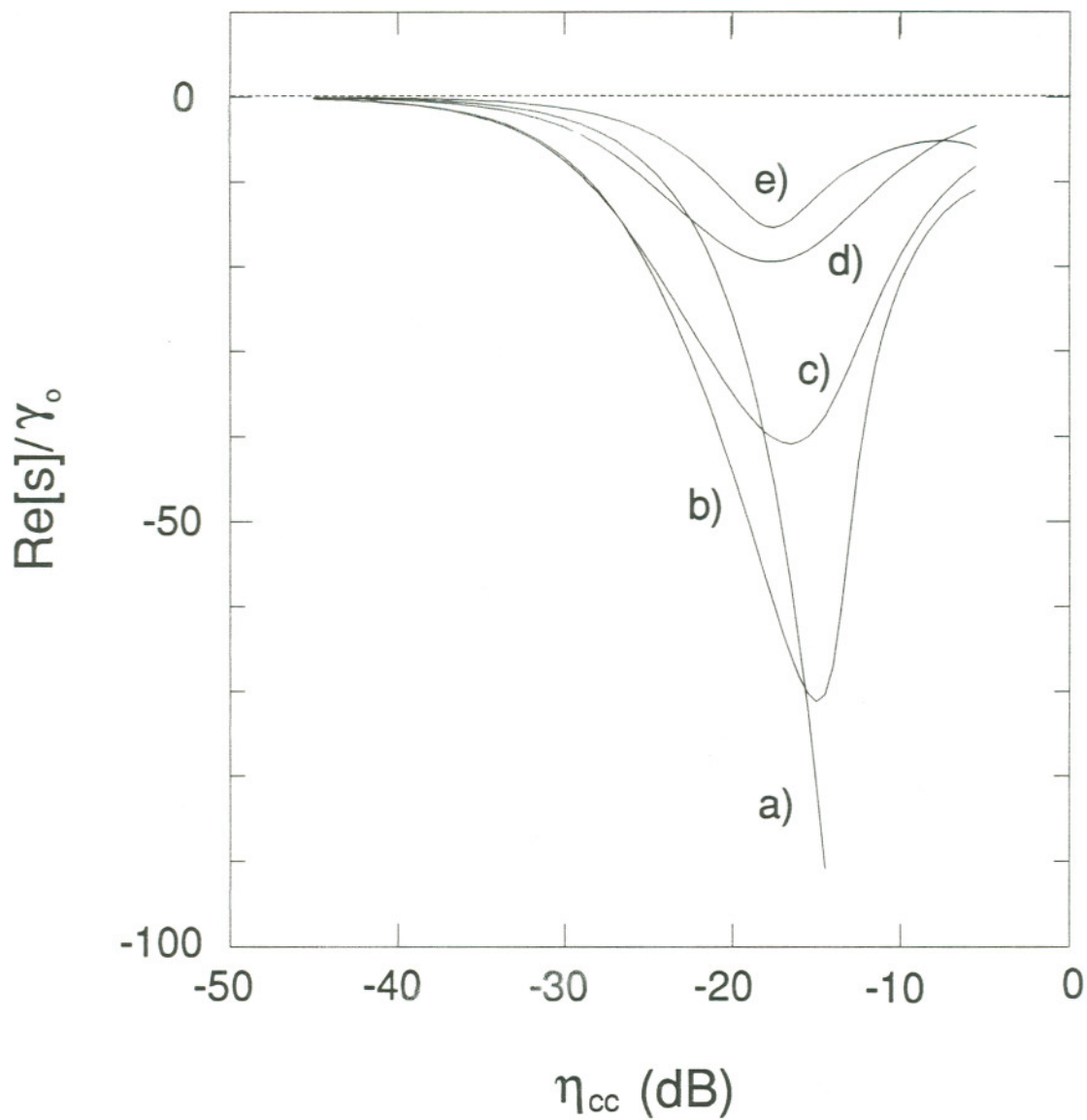


Figure 2.6 Roots of $D(s)$ with $\text{Im}[s]=0$ at selected coupling phases. a) $\psi_{cc}=0$, b) $\psi_{cc}=\pi/4$, c) $\psi_{cc}=\pi/2$, d) $\psi_{cc}=3\pi/4$, e) $\psi_{cc}=-\pi/20$. Symmetric mode, $\alpha=3$, $\sigma=1500$, $\Delta\rho=0.67$.

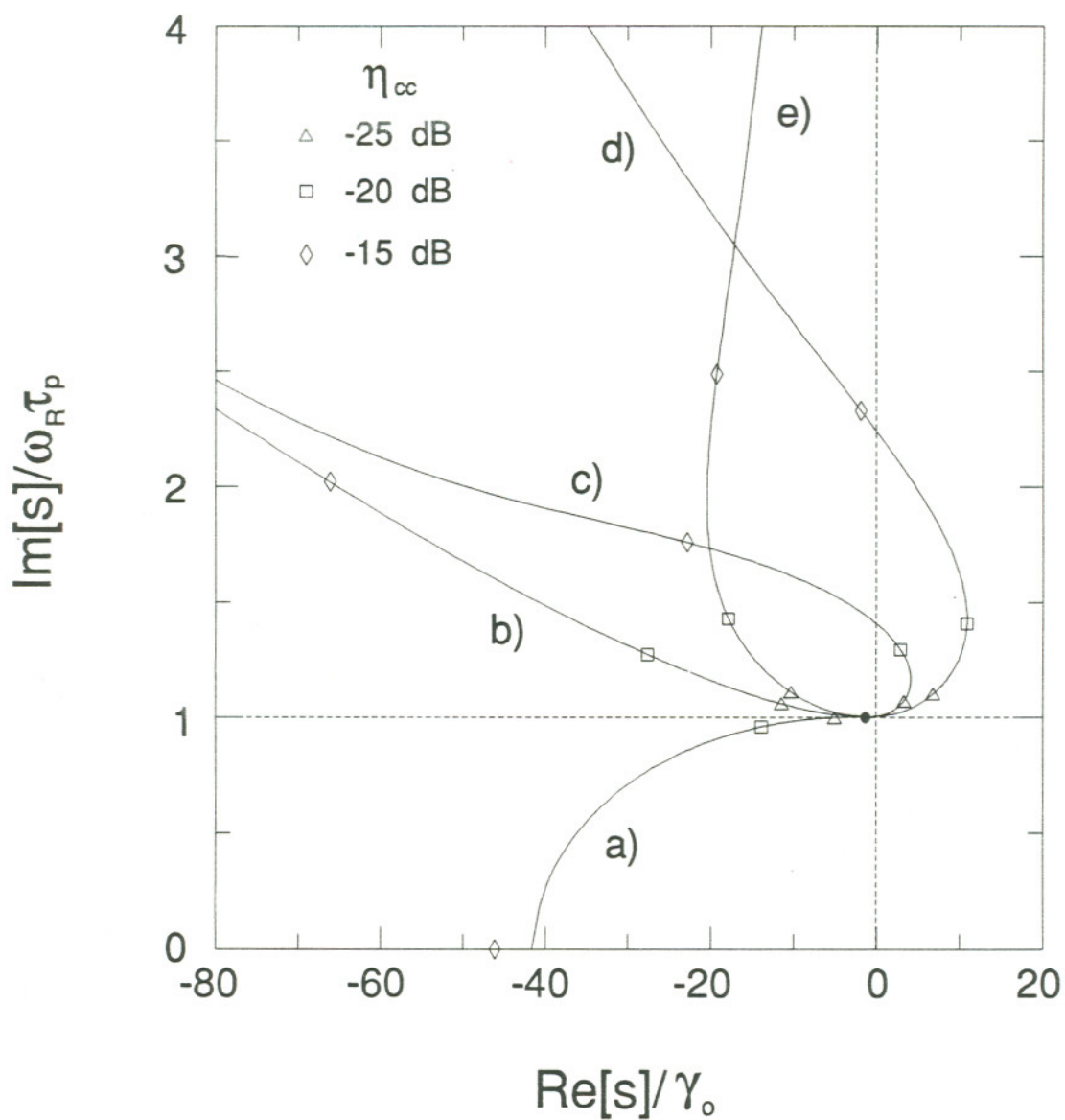


Figure 2.7 Roots of $D(s)$ with $\text{Im}[s] \neq 0$ at selected coupling phases. a) $\psi_{cc} = 0$, b) $\psi_{cc} = -\pi/4$, c) $\psi_{cc} = \pi/4$, d) $\psi_{cc} = \tan^{-1}\alpha$. e) $\psi_{cc} = -\pi/2$. Symmetric mode, $\alpha = 3$, $\sigma = 1500$, $\Delta\rho = 0.67$.

be explained as follows: In a solitary laser, relaxation oscillations are well-damped as a result of gain saturation; i.e., an increase in intensity is accompanied by a reduction in inversion, below the lasing threshold, due to the excess simulated emission. This, in turn, reduces the rate of increase in the intensity, and the laser undergoes a series of relaxation oscillations in returning to steady-state. The larger the intensity spike, the greater the deviation in gain from threshold and therefore damping. In a coupled system, however, the threshold gain is not a constant, as evidenced by equation (2.3.13). Therefore, a transient will induce a shift in threshold gain from the steady-state condition, as well as a change in carrier number. If the threshold shift is in a direction which increases the deviation in unsaturated carrier number from threshold, gain saturation is enhanced and relaxation oscillations are better damped. Otherwise, intensity self-pulsations at ω_R may result.

Depending on the value of ψ_{cc} , the laser can be "biased" to operate in stable or unstable regions. When $\alpha=0$, for example, maximum damping occurs at the coupling phase promoting the lowest equilibrium carrier number, or threshold gain, in the laser. This is at $\psi_{cc}=0$ for the even mode and π for the odd. When α is non-zero, however, an additional mechanism contributes to relaxation oscillation damping. Here, the refractive index change associated with a transient carrier fluctuation can also influence the instantaneous threshold gain. The coupling phase promoting maximum relaxation oscillation damping in this case shifts from the $\alpha=0$ location by $-\tan^{-1}\alpha$. This effect is known to cause self-pulsation over much of the locking range of an injection-locked semiconductor laser⁷¹. The α contribution to damping is dominant at weak coupling levels, $\eta_{cc} \lesssim 10^{-3}$, as evidenced in Figure 2.5. At larger coupling

magnitudes, the two effects compete with each other, with the former determining the stability properties above $\eta_{cc} = 10^{-2}$.

To summarize, the stability of two mutually coupled semiconductor lasers is characterized by three distinct regimes. At very weak η_{cc} , the optical coupling has little effect on the damping properties of lasers afforded by gain saturation, and stable operation in the even or odd mode is predicted, regardless of the coupling phase. This may be a preferred region of operation when the coupling phase is not easily controlled. Except near $\psi_{cc} = 0, \pi$, stable operation is interrupted at moderate coupling levels. Instability will result in intensity self-pulsations near the relaxation resonance frequency of the isolated lasers. For large coupling magnitudes, damping in the coupled system becomes independent of α . Relaxation oscillations are best damped at ψ_{cc} which minimize the equilibrium carrier number. Hence, the symmetric mode is most stable for $\psi_{cc} = 0$, while the asymmetric mode prefers $\psi_{cc} = \pi$. As discussed in the last section, these states also offer balanced output powers and the best mode suppression of the non-lasing mode. A trade-off must be made, however, as the lockband may be very small, especially for large α . While large regions have been identified in the complex η_{cc} plane which are unstable for both modes, the opposite is not true; bistability is not expected. Finally, self-coupling was found to have a minor influence on the stability of the mutually coupled system.

Large signal response of the coupled rate equations is considered separately in Chapters 3 and 4, and compared to experiment.

2.5 Coupling Coefficients

To this point, generalized rate equations have been presented which include complex coupling coefficients to account for optical interaction of the lasers. The magnitude and phase of these coefficients were shown to have a significant impact on the steady-state phase-locking and stability properties of mutually coupled lasers. To determine the value of a coupling coefficient, however, one must generally solve for the individual and compound cavity eigenmodes and their frequencies, performing a number of overlap integrals which are subsequently summed. This is often difficult; numerical techniques may prove necessary.

As will be discussed in the introduction to Chapter 4, there are several advantages in a study of phase-locking such as this to consider longitudinally coupled lasers. Here, the fields from the individual lasers overlap in localized regions of space, allowing the coupling coefficients to be more readily determined. A simple, yet general derivation of self and cross-coupling coefficients for two longitudinally coupled semiconductor lasers immediately follows this introduction. In Section 2.5.1 these coupling coefficients are evaluated for the specific case in which the coupling region consists of a passive gap of variable length with a fixed optical loss. Coupling delays are also taken into account. This situation is chosen for future comparison to the experimental portion of this dissertation presented in Chapters 3 and 4.

Consider a system of two axially coupled lasers which each support a single, dominant mode. The eigenmode of each individual laser will overlap in a

region hereafter referred to as the *coupling junction*. The transfer of energy between the field in each laser can be described, without specifying precisely what the coupling mechanism is, by treating the junction as a two-port scattering network. This approach has been used extensively^{4,6,124} to model the mode suppression and modulation properties of cleaved-coupled-cavity (C^3) lasers. Since one cavity in a C^3 laser is often operated below threshold, the effect of optical coupling has usually been treated as a perturbation to the dominant laser and included in a frequency dependent loss term⁸. In what follows, however, scattering terms are written in a form suggestive of a coupling coefficient.

The relationship between the incident E_j, E_k and exited E_j', E_k' traveling waves at the coupling junction is given by the linear system,

$$\begin{bmatrix} E_j' \\ E_k' \end{bmatrix} = \begin{bmatrix} \tilde{S}_{jj} & \tilde{S}_{jk} \\ \tilde{S}_{kj} & \tilde{S}_{kk} \end{bmatrix} \begin{bmatrix} E_j \\ E_k \end{bmatrix}. \quad (2.5.1)$$

The self-coupling scattering elements $\tilde{S}_{jj,kk}$ and cross-coupling elements $\tilde{S}_{jk,kj}$ describe the proper linear combination of the input amplitudes $E_{j,k}$ comprising an output $E_{j,k}'$ from the coupling junction. In this sense, there is a definite connection to the role of the self and cross-coupling coefficients from the coupled mode theory of Section 2.2. Physically, $\tilde{S}_{jj,kk}$ is the effective reflection coefficient of the junction with respect to laser j,k , while $\tilde{S}_{jk,kj}$ is the effective transmission coefficient from cavity k to j and vice versa.

The outgoing field in laser j is expressed, from equation (2.5.1), as

$$E_j' = \tilde{S}_{jj}E_j + \tilde{S}_{jk}E_k \quad (2.5.2)$$

Therefore, in a round-trip of laser j , the steady-state (threshold) condition requires that

$$\tilde{S}_{jj}^o(\tilde{S}_{jj}E_j + \tilde{S}_{jk}E_k) \exp [(g_{m,j} - \alpha_{int,j} + 2i\beta_{m,j})L_{Dj}] = E_j. \quad (2.5.3)$$

Here, \tilde{S}_{jj}^o is the self-coupling coefficient of laser j operating in isolation. $g_{m,j}$ is the modal gain per unit length, $\alpha_{int,j}$ is the internal loss per unit length, $\beta_{m,j}$ is the modal propagation constant and L_{Dj} denotes the physical length of the resonator for laser j . From equation (E.4), the internal loss can be written in terms of the photon lifetime as

$$v_{gj}\alpha_{int,j} = \frac{1}{\tau_{pj}} - \frac{1}{\tau_{mir,j}}, \quad (2.5.4)$$

where $\tau_{mir,j}$ is the rate of optical loss from laser j due to outcoupling. Taking the natural log of both sides of (2.5.3) then results in

$$\frac{v_{gj}}{L_{Dj}} \ln \left[\tilde{S}_{jj}^o \left(\tilde{S}_{jj} + \tilde{S}_{jk} \frac{E_k}{E_j} \right) \right] + G_j - \frac{1}{\tau_{pj}} + \frac{1}{\tau_{mir,j}} - i\alpha_j \frac{\partial G_j}{\partial N} \Delta N = 0. \quad (2.5.5)$$

The mode index, which is hidden in the propagation constant $\beta_m = \beta_o \mu$, was assumed to be a linear function of carrier density about threshold, as in equation (A.9). Therefore, the α parameter could be introduced using (A.11). The remaining constant round trip phase accrual $2i\beta_{oj}\mu_{th,j}$ was absorbed into the phase of complex field amplitude E_j .

The outcoupling can be identified in terms of the isolated self-coupling

coefficient \tilde{S}_{jj}^o through⁸⁷

$$\frac{1}{\tau_{mir,j}} = -\frac{1}{\tau_{Dj}} \ln \left((\tilde{S}_{jj}^o)^2 \right). \quad (2.5.6)$$

τ_{Dj} is the round trip time in laser j . Hence, with a little manipulation, (2.5.5) can finally be written,

$$\frac{1}{\tau_{Dj}} \left(\frac{\tilde{S}_{jj}}{\tilde{S}_{jj}^o} - 1 \right) \tilde{E}_j + \frac{1}{\tau_{Dj}} \left(\frac{\tilde{S}_{jk}}{\tilde{S}_{jj}^o} \right) \tilde{E}_k e^{-i\Delta\omega_{oj}t} + \frac{1}{2} \left(G_j - \frac{1}{\tau_{pj}} - i\alpha_j \frac{\partial G_j}{\partial N} \Delta N \right) \tilde{E}_j = 0. \quad (2.5.7)$$

It was assumed that the coupling terms were small enough in magnitude to make the approximation $\ln(1+x) \approx x$ valid. This imposes the following restrictions on the scattering elements

$$\left| \frac{\tilde{S}_{jj}}{\tilde{S}_{jj}^o} - 1 \right| \ll 1, \quad \text{and} \quad |\tilde{S}_{jk}| \ll |\tilde{S}_{jj}^o|. \quad (2.5.8)$$

These conditions generally place an upper limit to the level of optical coupling, as will become more clear later in this section. (2.5.7) can be directly compared to the stationary solution of the coupled rate equations (2.2.15) to define the coupling coefficients

$$\bar{\kappa}_{jj} \equiv \frac{1}{\tau_{Dj}} \left(\frac{\tilde{S}_{jj}}{\tilde{S}_{jj}^o} - 1 \right) \quad (2.5.9)$$

$$\bar{\kappa}_{jk} \equiv \frac{1}{\tau_{Dj}} \frac{\tilde{S}_{jk}}{\tilde{S}_{jj}^o}. \quad (2.5.10)$$

This formulation allows a wide range of coupling scenarios to be adequately modeled simply by determining the appropriate scattering matrix that describes the coupling junction. The coupling junction may be active or passive. It might consist of a gap, as in the case of C^3 lasers, a grating, waveguide, etc., or even include intervening optics, as in the following description.

In the remainder of this section, scattering elements and coupling coefficients are derived to model the experiments of Chapters 3 and 4. Since the lasers are physically separated by many centimeters, the electric field amplitudes and phases cannot be assumed constant during time delays accrued in the coupling junction. Although not explicitly shown in the derivation leading up to (2.5.9) and (2.5.10), coupling delays may be incorporated into time-dependent coupling coefficients, for a passive coupling junction. This avoids the necessity to solve an additional coupled rate equation for the field in the coupling junction. Delay-differential equations result which are analyzed in later chapters.

2.5.1 Self-Coupling

The experimental study of Chapter 3 employs a self-coupling configuration, as shown in Figure 2.8 a). Here, the coupling junction consists of a gap of width L_{ext} between the output facet of a laser and an external reflector with power reflectance, R_{2k} . This scenario is useful for studying external cavity lasers, or the effects of inadvertent optical feedback from an external reflector. The complex field $E_r(t)$ returned to laser j from its inner facet (with power reflectance R_{2j}) and the coupling junction at time t is given by

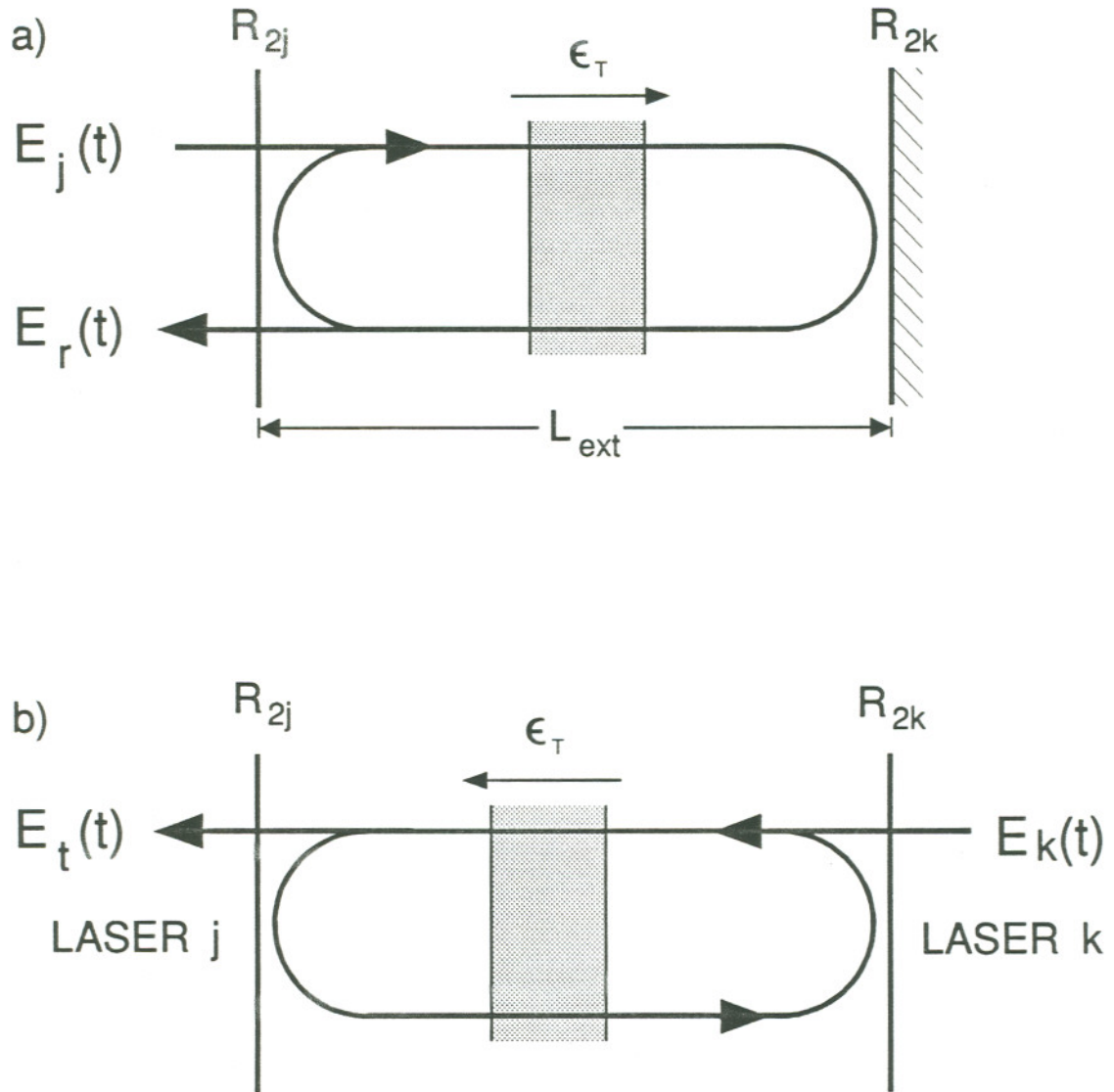


Figure 2.8 Schematic representations of a) self, and b) cross coupling for a passive, lossy gap.

$$\begin{aligned}
E_r(t) = & \sqrt{R_{2j}}E_j(t) + (1-R_{2j})\sqrt{R_{2k}}\epsilon_T^2\xi E_j(t-\tau) \\
& + (1-R_{2j})R_{2k}\sqrt{R_{2j}}\epsilon_T^4\xi E_j(t-2\tau) + \dots
\end{aligned} \tag{2.5.11}$$

τ is the round trip delay time of the passive cavity. Any losses accrued in the gap are included in a power transmission coefficient ϵ_T^2 , while amplitude coupling losses to the guided mode of laser j are described by a separate parameter ξ . Ignoring cross-coupling, (2.5.1) gives

$$E_j'(t) = E_j(t) \cdot \tilde{S}_{jj}(t) \tag{2.5.12}$$

in the time dependent case. Then in comparison to (2.5.11),

$$\begin{aligned}
\tilde{S}_{jj}(t) \equiv & \sqrt{R_{2j}} + (1-R_{2j})\sqrt{R_{2k}}\epsilon_T^2\xi \frac{E_j(t-\tau)}{E_j(t)} e^{i(\omega_{oj}\tau + \Delta\phi_j(t,\tau))} \\
& + (1-R_{2j})R_{2k}\sqrt{R_{2j}}\epsilon_T^4\xi \frac{E_j(t-2\tau)}{E_j(t)} e^{i(2\omega_{oj}\tau + \Delta\phi_j(t,2\tau))} \\
& + \dots
\end{aligned} \tag{2.5.13}$$

The definition $\Delta\phi_j(t, n\tau) = \phi_j(t) - \phi_j(t - n\tau)$ has been incorporated above. $\tilde{S}_{jj}(t)$ represents the ratio of returned amplitude to that incident on facet R_{2j} inside laser j , and describes the total self-coupling behavior of the facet and coupling junction combined. Substituting equation (2.5.13) into expression (2.5.9) for the coupling coefficient gives

$$\begin{aligned}
\tau_{Dj} \bar{\kappa}_{jj}(t) = & \frac{(1-R_{2j})\sqrt{R_{2k}}}{\sqrt{R_{2j}}} \epsilon_T^2 \xi \frac{E_j(t-\tau)}{E_j(t)} e^{i(\omega_{oj}\tau + \Delta\phi_j(t,\tau))} \\
& + (1-R_{2j})R_{2k} \epsilon_T^4 \xi \frac{E_j(t-2\tau)}{E_j(t)} e^{i(2\omega_{oj}\tau + \Delta\phi_j(t,2\tau))} + \dots
\end{aligned} \tag{2.5.14}$$

For weak coupling (ie. small ϵ_T^2), all but the first order terms in ϵ_T^2 can be neglected. One finds that the rate of coupling simplifies to the form

$$\tilde{\kappa}_{jj}(t) = \frac{1}{\tau_{Dj}} \frac{(1-R_{2j})\sqrt{R_{2k}}}{\sqrt{R_{2j}}} \epsilon_T^2 \xi \frac{E_j(t-\tau)}{E_j(t)} e^{i(\omega_{oj}\tau + \Delta\phi_j(t,\tau))}. \quad (2.5.15)$$

This is essentially the form of the feedback coefficient used in previous work to describe optical feedback¹¹⁹. It is clear that if the time delay τ goes to zero, the coupling coefficient becomes time-independent.

2.5.2 Cross-Coupling

A similar approach can be taken to determine the form of the cross-coupling coefficient $\tilde{\kappa}_{jk}(t)$, for the situation depicted in Figure 2.8 b). Consider the total transmitted field $E_t(t)$ at time t coupled to laser j from laser k

$$\begin{aligned} E_t(t) = & \sqrt{1-R_{2k}}\sqrt{1-R_{2j}}\epsilon_T\xi E_k(t-\tau) \\ & + \sqrt{1-R_{2k}}\sqrt{1-R_{2j}}\sqrt{R_{2j}}\sqrt{R_{2k}}\epsilon_T^3\xi E_k(t-3\tau) \\ & + \sqrt{1-R_{2k}}\sqrt{1-R_{2j}}R_{2j}R_{2k}\epsilon_T^5\xi E_k(t-5\tau) + \dots \end{aligned} \quad (2.5.16)$$

Note that here the coupling time delay τ is for a single pass of the coupling gap, while in Section 2.5.1 it was measured in a round trip. From (2.5.1), the above expression can once again be written in the form

$$E_t(t) = \tilde{S}_{jk}(t) \cdot E_k(t). \quad (2.5.17)$$

With $\tilde{S}_{jk}(t)$ given by (2.5.16) and (2.5.17), substitution into (2.5.10) defines the cross-coupling coefficient as

$$\begin{aligned} \tau_{Dj} \tilde{\kappa}_{jk}(t) = & \sqrt{1-R_{2k}} \frac{\sqrt{1-R_{2j}}}{\sqrt{R_{2j}}} \epsilon_T \xi \frac{E_k(t-\tau)}{E_k(t)} e^{i[\omega_{ok}\tau + \Delta\phi_k(t,\tau)]} \\ & + \sqrt{1-R_{2k}} \sqrt{1-R_{2j}} \sqrt{R_{2k}} \epsilon_T^3 \xi \frac{E_k(t-3\tau)}{E_k(t)} e^{i[3\omega_{ok}\tau + \Delta\phi_k(t,3\tau)]} \\ & + \dots \end{aligned} \quad (2.5.18)$$

For $\epsilon_T \ll 1$, (2.5.18) becomes

$$\tilde{\kappa}_{jk}(t) = \frac{1}{\tau_{Dj}} \sqrt{1-R_{2k}} \frac{\sqrt{1-R_{2j}}}{\sqrt{R_{2j}}} \epsilon_T \xi \frac{E_k(t-\tau)}{E_k(t)} e^{i[\omega_{ok}\tau + \Delta\phi_k(t,\tau)]}. \quad (2.5.19)$$

2.5.3 Power Coupling Ratio

Coupling coefficients describing self and mutual coupling for the experimental arrangements indicated in Figure 2.8 have now been derived. Their magnitudes squared are a measure of the power transmitted or returned to laser j relative to the circulating power, and depend on a number of parameters involving both the laser and the coupling junction. In practice, however, it is much more convenient to define the coupling level in terms of only those parameters dependent on the coupling junction. These include the one-way power transmission of the junction ϵ_T^2 , the fraction of power coupling into the guided mode of the laser ξ^2 and, in the case of self-coupling, the external reflector power reflectivity. ξ^2 is included with the junction, since the modal

overlap between the lasing mode and the returned mode depends upon optical elements and/or diffraction in the junction.

The product of these parameters defines the *power coupling ratio*, which measures the power transmission or reflection of the coupling junction. For self-coupling,

$$PCR_{sc} \equiv \epsilon_T^4 R_{2k} \xi^2, \quad (2.5.20)$$

while for cross-coupling,

$$PCR_{cc} \equiv \epsilon_T^2 \xi^2. \quad (2.5.21)$$

These numbers are referred to in Chapters 3 and 4 to quantify the level of optical coupling, rather than citing values for the coupling coefficients. Techniques to measure the power coupling ratios are discussed in Appendix B.

The coupling coefficients can be further simplified by introducing the cold-cavity half bandwidth¹⁰⁸

$$\Delta\nu_{cc} \equiv \frac{1}{\tau_D} \frac{(1-R)}{2\pi\sqrt{R}} \quad (2.5.22)$$

of a Fabry-Perot etalon with power reflectivities R at each interface. With (2.3.11), the steady-state, self-coupling coefficient (2.5.15) is then

$$\tilde{\kappa}_{jj} = 2\pi\Delta\nu_{cc} \sqrt{PCR_{sc}} e^{i\omega_L\tau}, \quad (2.5.23)$$

while the cross-coupling coefficient (2.5.19) becomes

$$\tilde{\kappa}_{jk} = 2\pi\Delta\nu_{cc} \sqrt{PCR_{cc}} e^{i\omega_L\tau}, \quad (2.5.24)$$

assuming that the lasers have identical front facet reflectivities. Hence, the magnitude and phase of the coupling coefficients, referred to throughout Sections 2.3 and 2.4, relate to very simple and intuitive physical mechanisms in the present case. Clearly, the coupled power determines the magnitude, while the phase is that accrued in traversing the coupling junction.

Before proceeding, it is necessary to clarify what is meant by "weak" and "strong" coupling. Recall the approximations (2.5.8) which were made in writing the rate equation in the "weak" coupling form of (2.2.15). $|\tilde{S}_{jj}^0|^2$ represents the fraction of power returned to laser j operating in isolation. Therefore, the conditions (2.5.8) are equivalent to stating that the coupled power must be much smaller than the power fed back with the laser operating in isolation. In other words, the coupled field can be treated as a perturbation to the isolated steady-state.

Equations (2.5.8) can be rewritten in terms of the coupling coefficients as

$$\tilde{\kappa}_{jj,jk} \tau_{Dj} \ll 1, \quad \text{or} \quad \eta_{jj,jk} \ll \frac{\tau_{pj}}{\tau_{Dj}}. \quad (2.5.25)$$

As an example, the cross-coupling coefficient (2.5.18) can be summed in the steady-state, leaving

$$\tilde{\kappa}_{jk} = \frac{1}{\tau_{Dj}} \sqrt{1-R_{2k}} \frac{\sqrt{1-R_{2j}}}{\sqrt{R_{2j}}} \frac{\epsilon_T \xi e^{i\omega_L \tau}}{1 - \sqrt{R_{2j} R_{2k}} \epsilon_T^2 e^{2i\omega_L \tau}}. \quad (2.5.26)$$

Maximum coupling occurs when $\omega_L \tau = m\pi$. Condition (2.5.25) is then

$$\sqrt{1-R_{2k}} \frac{\sqrt{1-R_{2j}}}{\sqrt{R_{2j}}} \frac{\epsilon_T \xi}{1 - \sqrt{R_{2j} R_{2k}} \epsilon_T^2} \ll 1. \quad (2.5.27)$$

For a typical diode laser, facet reflectivities and ξ are on the order of .1. Hence, (2.5.27) requires $\epsilon_T \ll 1$. Intuitively, it is also clear that "strong" coupling is characterized by a power coupling ratio approaching one. It is easily shown that significant deviation of (2.5.24) from (2.5.26) occurs only for $\epsilon_T \gtrsim 0.2$, justifying the neglect of higher order terms in (2.5.14) and (2.5.18) in the present theoretical framework.

3. SELF-COUPLING (FEEDBACK)

This chapter investigates the operation of a semiconductor laser with a portion of its optical output fed back after a delay time τ . Recall that in Chapter 2, the self-coupling phase ψ_{sc} was treated as a constant. Its influence on the stationary operation, phase-locking properties and stability of two mutually coupled lasers was theoretically found to be minor, manifesting mainly in an additional contribution to the system's threshold gain. In general, however, the self-coupling phase is a function of both the time delay and the oscillating frequency of the coupled system. Multiple longitudinal modes may then result, associated with the cavity formed by the laser and external retro-reflector. Long coupling delays are shown to profoundly impact the spectral and stability properties of a semiconductor laser. For this reason, it is an important problem in the field of optical communications, and has recently become a favored topic of research.

This chapter is mainly experimental. Detailed spectral measurements are presented which include power coupling ratios from -80 dB to as high as -10 dB, while encompassing the full 2π range of coupling phase. The data can be considered an extension of the work of Tkach and Chraplyvy¹²⁵ who defined various "regimes" of effects with respect to coupling strength. Section 3.1 introduces useful formulae describing delayed self-coupling. Numerical simulations

based on these results, including spontaneous emission noise, are used extensively in the remainder of the chapter. The experimental arrangement employed for this work is detailed in Section 3.2. Sections 3.3 and 3.4 examine the stationary operation of a self-coupled laser in single and multimode regions. Stability issues associated with mode selection¹²⁶ are then discussed. Finally, Section 3.7 provides an investigation of the dynamic instability known as "coherence collapse."

3.1 Delayed Self-Coupling

Rate equations describing the operation of a self-coupled semiconductor laser can be obtained from (2.3.6) and (2.3.7). Substitution of the coupling coefficient (2.5.15), dropping cross-coupling terms, results in

$$\begin{aligned} \dot{e}(\hat{t}) = & \frac{1}{2} \left((2\Delta n(\hat{t}) + 1)G_P - 1 \right) e(\hat{t}) \\ & + \eta e(\hat{t} - \hat{\tau}) \cos[\tau_p \omega_o \hat{\tau} + \Delta\phi(\hat{t}, \hat{\tau})] + \frac{r_{sp}}{2e(\hat{t})} + F_e(\hat{t}) \end{aligned} \quad (3.1.1)$$

$$\dot{\phi}(\hat{t}) = \alpha\Delta n(\hat{t}) - \eta \frac{e(\hat{t} - \hat{\tau})}{e(\hat{t})} \sin(\tau_p \omega_o \hat{\tau} + \Delta\phi(\hat{t}, \hat{\tau})) + F_\phi(\hat{t}) \quad (3.1.2)$$

for the electric field amplitude and its phase. Equations (3.1.1) and (3.1.2) are of the form originally introduced by Lang and Kobayashi¹²⁷. The use of the self-coupling coefficient (2.5.15) is valid in the following analysis, since the lasers used were not AR-coated, and the maximum power coupling ratio expected was on the order of 10%. The accompanying carrier number rate equation appears

unchanged, as written in equation (2.3.8). Subscripts denoting the laser have been dropped for clarity. $\hat{\tau} \equiv \tau/\tau_p$ denotes the normalized round trip coupling delay time, while η is to be interpreted as the steady-state self-coupling magnitude throughout this chapter. Langevin noise sources $F_{\mathbf{x}}(\hat{t})$ associated with the dynamic variable \mathbf{x} have been introduced for future numerical simulations (see Appendix D). Noise is an essential factor in describing processes such as mode hopping, linewidth and mode selection.

3.1.1 Steady-State Operation

The stationary behavior of a self-coupled laser easily follows from (3.1.1) and (3.1.2). Steady-state solution of the field rate equation gives

$$\overline{\Delta n} = -\text{Re}[\tilde{\eta}]. \quad (3.1.3)$$

Since the carrier number is directly related to the threshold gain by (B.1), equation (3.1.3) shows again that the real part of the coupling coefficient imposes a threshold gain variation in the laser. Stationary solution of the phase rate equation (3.1.2) results in¹²⁷

$$\tau_p \Delta\omega_L = -\eta \sin\omega_L \tau - \alpha \eta \cos\omega_L \tau. \quad (3.1.4)$$

Recalling that $\tilde{\eta} \equiv \tau_p \tilde{\kappa}$, and $\omega_L = \omega_o + \Delta\omega_L$, expression (3.1.4) can also be written as

$$\Delta\omega_L \tau = -\kappa \tau \sqrt{1 + \alpha^2} \sin(\omega_o \tau + \Delta\omega_L \tau + \tan^{-1} \alpha), \quad (3.1.5)$$

a transcendental equation for the shift in oscillation frequency from the free-running condition.

Although the stationary solutions describing a self-coupled laser fall quite easily out of the rate equation approach, the physical reasoning for the threshold gain and frequency variations due to the coupling can be best understood pictorially, using a phasor representation. Let $E_c(t)$, in Figure 3.1 a), be the circulating electric field in the laser cavity measured at a plane just inside the output facet, traveling inward. After a round trip in the laser, this phasor becomes $E_i(t)$, just inside the facet. Further, let $E_r(t)$ denote the time-delayed reinjected field, which is dependent on $E_i(t)$ through the steady-state self-coupling coefficient (2.5.23). The three fields are related by

$$E_c(t) = \sqrt{R_{2j}} E_i(t) + E_r(t). \quad (3.1.6)$$

It is required that E_c replicate itself every round trip of the compound cavity. In other words, an oscillating mode must satisfy gain=loss and round-trip 2π phase conditions. This might be accomplished as shown in Figure 3.1 b). The difference between phasors E_c and E_i is made up by the reinjected field, E_r , whose length and phase are determined by the magnitude and phase of the self-coupling coefficient. If $\omega_L \tau$ is in the range $-(2m+1)\pi/2 < \omega_L \tau < (2m+1)\pi/2$, constructive interference lowers the threshold gain of the laser. Elsewhere, as evident in equation (3.1.3), the opposite is true.

Interference, which is necessary to satisfy the phase condition, manifests in a shift in oscillation frequency, given by the first term on the right-hand side of (3.1.4). The subsequent gain change, however, additionally contributes a fre-

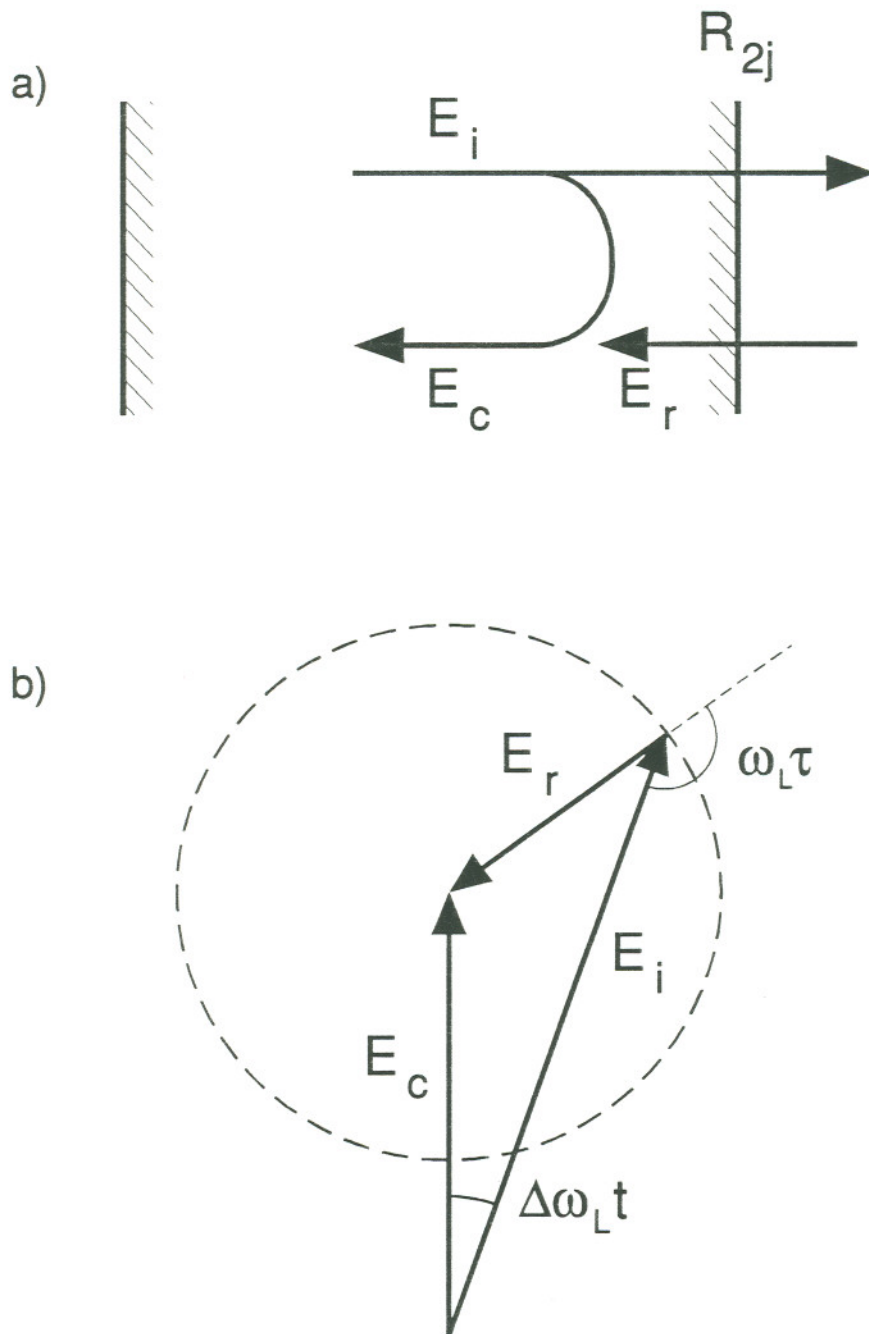


Figure 3.1 Phasor interpretation of self-coupling. a) Relationship between field amplitudes at output facet of the laser. b) Phasor diagram for stationary operation.

quency shift due to the carrier-dependent refractive index, described by α . As the coupling phase is rotated through a 2π range, (in practice this is accomplished by *pistoning* the position of the external retro-reflector on the order of a wavelength), the system of phasors trace out the dashed circle indicated in Figure 3.1 b). The maximum shift in oscillation frequency depends on the size of this circle, or in other words, on the magnitude of the coupling coefficient. From (3.1.5), this shift is found to be proportional to the square root of the power coupling ratio,

$$|\Delta\nu_L| \leq \Delta\nu_{cc} \sqrt{PCR_{sc}} \sqrt{1+\alpha^2}, \quad (3.1.7)$$

and occurs at a coupling-dependent external cavity length where

$$\omega_o\tau = (-1)^m \kappa\tau \sqrt{1+\alpha^2} - \tan^{-1}\alpha + (2m+1)\frac{\pi}{2}. \quad (3.1.8)$$

This "piston" location is equivalent to maintaining a relative phase difference between the lasing and reinjected fields of $(2m+1)\frac{\pi}{2} - \tan^{-1}\alpha$. Hence, for large values of α the tuning extremes nearly correspond to extremes in carrier number as well. Lower frequency modes are expected to possess a lower threshold gain.

Upon closer examination of (3.1.5), one finds that multiple solutions may exist whenever¹²⁸

$$\kappa\tau \sqrt{1+\alpha^2} > 1. \quad (3.1.9)$$

Most importantly, the allowed longitudinal modes associated with the external cavity have the same mode number. Multiple frequencies can therefore

oscillate, at a given $\omega_o\tau$, corresponding to the same number of wavelengths in the diode cavity. There is still, however, only one mode possible at a unique coupling *phase* $\omega_L\tau$. Note that multimode operation can easily be achieved at extremely low coupling levels for long coupling delays, a fact which makes inadvertent feedback from external optics so detrimental to stable, single mode operation. The coupling level necessary to attain multimode operation goes up linearly with a decrease in the coupling delay, making it less of a problem for short time delays. Numerical solutions to equations (3.1.3) and (3.1.5) are presented and compared to experiment in Sections 3.3 and 3.4, in connection with mode selection and stability.

3.1.2 Linewidth

The results of the previous section demonstrate that self-coupling is a powerful technique for spectral mode control in lasers. The frequency and threshold gain of longitudinal modes can be varied, through interference, by adjusting the coupling magnitude and phase. In doing so, however, the linewidth of the system is also affected. Simply put, interference between the circulating and reinjected fields effectively changes the rate of optical loss $1/\tau_p$, or equivalently the cavity Q, in the laser. By considering the laser oscillator as a regenerative noise amplifier, the gain-bandwidth product relationship therefore requires a variation in linewidth according to the modified Schawlow-Townes formula^{129,130}.

The linewidth of a semiconductor diode laser operating in an external cavity has been theoretically determined from the power spectrum of small signal linearized rate equations¹³¹. It is worthwhile, however, to consider an alternate approach based on the approximate phase rate equation derived in Appendix F. In the present case, with coupling coefficient (2.5.15), equation (F.2) reduces to

$$\dot{\phi}(t) = -\kappa\sqrt{1+\alpha^2}\sin[\omega_o\tau + \phi(t) - \phi(t-\tau) + \tan^{-1}\alpha] + F(t). \quad (3.1.10)$$

The Langevin source $F(t)$ is the same form as the reduced version (F.3). Consider small fluctuations $\delta\phi(t)$ in the phase about the steady-state operating condition,

$$\phi(t) = \Delta\omega_L t + \phi_o + \delta\phi(t). \quad (3.1.11)$$

The derivation relies on the assumption that phase deviations $\delta\phi$ remain small during a coupling delay time, τ . The phase fluctuation difference after one round trip can therefore be expanded to first order such that

$$\delta\phi(t) - \delta\phi(t-\tau) \approx \delta\dot{\phi}(t)\tau. \quad (3.1.12)$$

Note that this difference will be zero without Langevin noise sources driving the phase away from steady-state. Substituting (3.1.11) and (3.1.12) into (3.1.10) gives

$$\begin{aligned} \Delta\omega_L + \delta\dot{\phi}(t) &= -\kappa\sqrt{1+\alpha^2}\sin[\omega_o\tau + \Delta\omega_L\tau + \tan^{-1}\alpha + \delta\dot{\phi}(t)\tau] + F(t) \\ &= -\kappa\sqrt{1+\alpha^2}[\sin(\omega_o\tau + \Delta\omega_L\tau + \tan^{-1}\alpha) \\ &\quad - \delta\dot{\phi}(t)\tau\cos(\omega_o\tau + \Delta\omega_L\tau + \tan^{-1}\alpha)] + F(t). \end{aligned} \quad (3.1.13)$$

The Langevin source $F(t)$ is the same form as the reduced version of (F.3). Identifying the steady-state solution (3.1.5) above and rearranging leaves

$$\delta\dot{\phi}(t) = \frac{F(t)}{1 + \kappa\tau\sqrt{1+\alpha^2}\cos(\omega_o\tau + \Delta\omega_L\tau + \tan^{-1}\alpha)}. \quad (3.1.14)$$

A comparison can now be made to equation (D.16), describing the phase of an isolated laser. It is clear that the Langevin noise source driving the phase fluctuations in a self-coupled laser is modified from the free-running case by the denominator of (3.1.14). This is the linewidth reduction factor, or F factor referred to in several other works^{131,132}. It was shown in Appendix D that the linewidth goes as the mean square of the fluctuations in phase. This same argument could be followed through in the present case, resulting in^{131,133-135}

$$\Delta\nu = \frac{\Delta\nu^o}{[1 + \kappa\tau\sqrt{1+\alpha^2}\cos(\omega_L\tau + \tan^{-1}\alpha)]^2}. \quad (3.1.15)$$

The linewidth is seen to periodically reduce and broaden with external cavity length piston $\omega_o\tau$. The maximum linewidth reduction at a given feedback level is for $\omega_L\tau = -\tan^{-1}\alpha$. From equation (3.1.5), this condition is found to occur at the oscillation frequency of the isolated laser, $\Delta\omega_L\tau=0$. The broadest linewidth also occurs at $\omega_L=\omega_o$, where $\omega_o\tau=\pi-\tan^{-1}\alpha$. Note that the low linewidth and low threshold gain conditions are not at the same external cavity length, but are shifted from each other by $\tan^{-1}\alpha$. This is due to the non-zero value of α , and will become important when investigating mode selection and stability in later sections.

The use of external cavities for linewidth reduction of semiconductor lasers

has been attempted extensively in the past several years¹³⁶⁻¹⁴⁵ toward development of narrow band sources for optical communications. Extremely narrow linewidths on the order of 10 kHz have been achieved by AR-coating one facet of the semiconductor laser, thereby allowing strong coupling to an external mirror¹⁴⁶, fiber¹⁴⁷⁻¹⁴⁹ or grating¹⁵⁰⁻¹⁵⁴. Similar linewidths can be obtained by coupling the laser to an external, high-finesse resonator¹⁵⁵⁻¹⁵⁹ which is more akin, however, to injection-locking than self-coupling.

3.2 Experiment

Two types of commercially available semiconductor laser diodes were used as sources in the experiments investigating time-delayed self-coupling: The Hitachi HLP1400 channeled-substrate-planar¹⁶⁰⁻¹⁶² (CSP) and the Mitsubishi ML5101a transverse-junction-stripe¹⁶³⁻¹⁶⁶ (TJS) lasers. Both lasers incorporate index guided structures and sufficiently short cavities to allow single longitudinal diode mode operation, thereby satisfying the single mode assumption of the theory developed in Chapter 2. They are of AlGaAs/GaAs composition, resulting in an operating wavelength of about 0.8 μm . Operating parameters of these common lasers relevant to the theoretical modeling in this dissertation are measured in Appendix E, while other characteristics can easily be located in manufacturer documentation.

The optical portion of the experiment was arranged as shown in Figure 3.2. The output of the semiconductor diode laser (DL) was collimated by an AR-coated lens (μS1) and retro-reflected from a high-reflectivity mirror (HR1),

thereby forming an external cavity. Lens $\mu\text{S}2$, together with HR1, form a *cat-eye* retro-reflector, which is very insensitive to a tilt in HR1. This made optical alignment more forgiving. The position of HR1 at the focal plane of $\mu\text{S}2$ was insured by checking the collimation of the returning light using a shear-plate interferometer. This also allowed accurate collimation of the diode's output. Due to the mechanical mounting of the commercial lasers, light could only be collected from one end of the devices. Therefore, the portion of the output used for diagnostics had to be taken from the external cavity. This was accomplished at beam splitter BS1.

Spectral analysis was performed using a variable free spectral range (FSR) planar Fabry-Perot interferometer (PFP) and a 300 MHz FSR confocal Fabry-Perot (CFP). This combination allowed observation of spectral detail from about 1 MHz to hundreds of GHz in extent. A 0.75 m spectrometer was also used to determine if the laser was operating in a single longitudinal diode mode. The interferometer outputs were measured with photodiodes (PD1,2).

Since non-resonant light incident on a high-finesse etalon is nearly all reflected, it is clear that the scanning Fabry-Perots used in these experiments fed back considerable power during the majority of their scan range. In fact, the magnitude of this reflection could be larger than that returned from the external cavity. Furthermore, scattering and Fresnel reflections from the other optics also contributed unacceptable levels of spurious feedback. It was therefore important to optically isolate the diagnostic arm of the experiment, and to eliminate unwanted reflections from optics in the external cavity. Two Faraday isolators (ISO1,2), with about 30 dB of isolation each, were located preceding the diagnostic optics, as shown in Figure 3.2. A half-wave plate (HWP) was

used to maximize transmission through the isolators. Fabry-Perot reflections were avoided by tilting the interferometer slightly such that the reflection was clipped at the pin hole (PH) of the spatial filter. In doing so, a small amount of finesse was sacrificed. All other optics were tilted sufficiently so that Fresnel reflections were clipped. With these precautions, levels of undesired feedback were reduced below about -80 dB relative to the laser's output power (estimated as described in Appendix B).

The self-coupling level was controlled by inserting crossed Glan-Taylor type calcite crystal polarizers (XTAL POLS) in the external cavity. The polarizer nearest the diode was oriented with its pass axis in the plane of Figure 3.2 to match the predominantly TE output polarization of the laser. The second was mounted in a motorized rotation stage so that the polarizer's angle could be repositioned very accurately. A neutral density filter (NDF) was occasionally used to provide an additional fixed level of attenuation. Coupling to the guided mode of the laser was maximized by maintaining a *collapsed* spectrum (see Section 3.7) while adjusting the the position and angle of the retro mirror (HR1) as the transmission of the polarizers was steadily reduced. In this way, a given angle of the polarizers could be reliably associated with a specific coupling level to within a dB. Absolute determination of the power coupling ratio was obtained from spectral detail, as discussed in Appendix B.

Although the optics in the external cavity were mounted in the most compact method possible,[‡] external cavity lengths could not be made shorter than

[‡] In order to achieve shorter lengths, the laser should be pedestal mounted, with the external cavity on one side of the laser and diagnostics on the other. This configuration was not attempted in this work, since pedestal mounted lasers were not available.

about 20 cm. The cavity length, however, could be extended to over a meter. Since the phase of the reinjected light is critical in determining the behavior of the system, mirror HR1 was mounted on a piezo electric transducer (PZT), shown in Figure 3.2. This allowed the length of the external cavity to be varied in small steps, or *pistonned*, over a range of several wavelengths. Further, the entire cat eye retro-reflector assembly was movable in order to change the gross length of the cavity.

The diode laser was pumped with an ultrastable battery power supply. It was found that even extremely small 60-cycle or higher frequency ripple present on a good quality AC power supply was unacceptable, as linewidth broadening was easily observed with the confocal Fabry-Perot. Temperature drift of the lasing frequency was also a problem. Semiconductor lasers can be temperature stabilized with thermoelectric coolers quite nicely, as was done in the mutual coupling experiment (Chapter 4). However, in this experiment the laser was stabilized at room temperature by continuously flowing water through the laser mounting block from a large thermal reservoir (a bucket of water). This proved more than adequate.

Data acquisition consisted of digitizing the output of each Fabry-Perot as it was ramped. The LeCroy transient digitizer used had a maximum digitization rate of 5 Msamples/sec and was interfaced to a microcomputer through a CAMAC GPIB bus. It was desired to digitize one Fabry-Perot scan, covering one FSR, for each external cavity length step over a range of a wavelength or two. This was accomplished as depicted in Figure 3.3. The acquisition electronics were timed to the Fabry-Perot ramp through the Burleigh RC-42 controller's trigger output. Preceding every ramp, the voltage applied to the

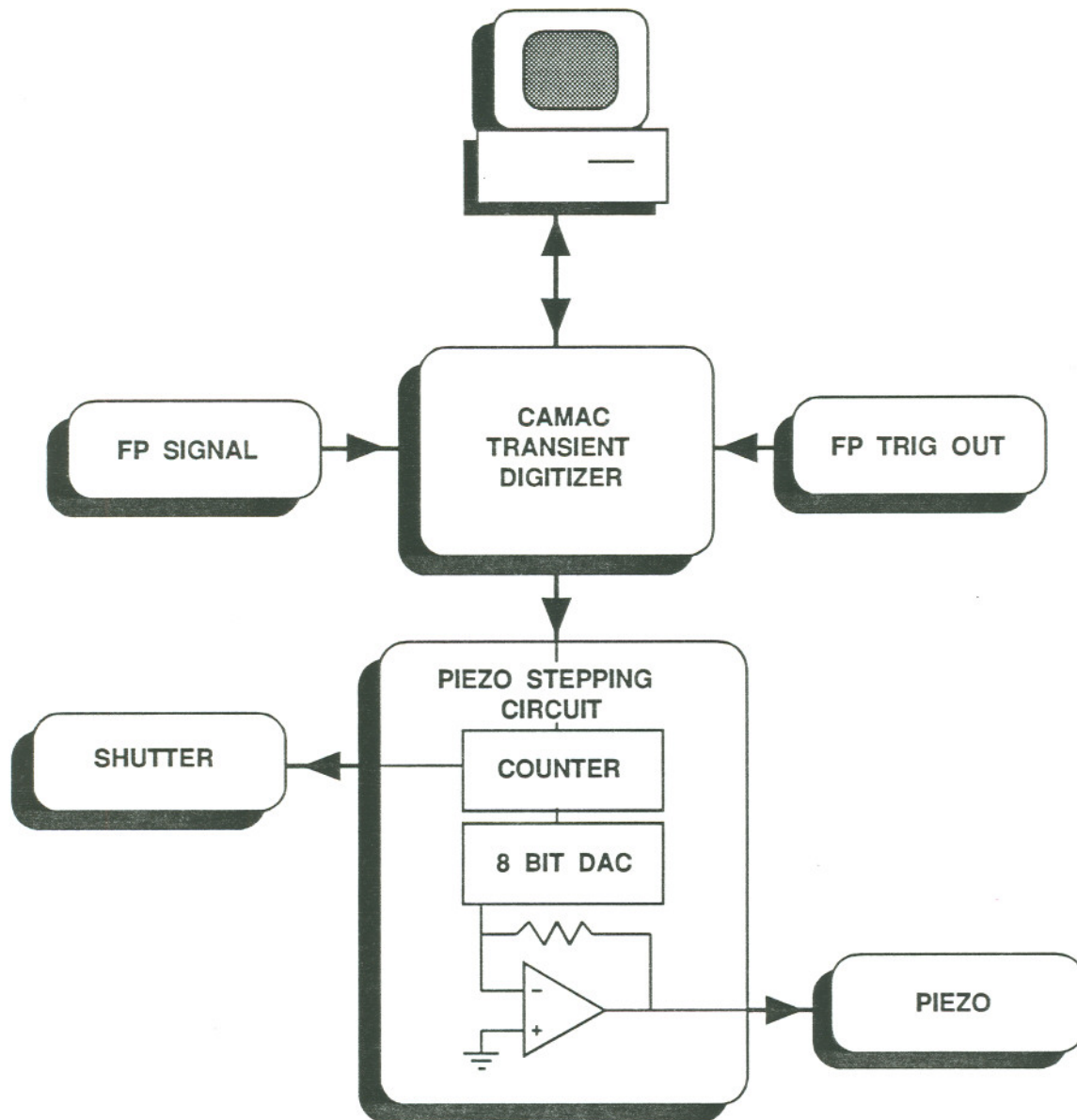


Figure 3.3 The setup used for data acquisition and control of the self-coupling experiment.

piezoelectric translator was staircased to a new level, using a counter and 8-bit DAC combination. The photodiode output was continuously digitized, including the ramp retrace. Appropriate portions of the signal were then extracted from the digitized stream after the fact, by computer. In order to determine the amount of frequency pulling due to the self-coupling, it was important to know the oscillation frequency of the isolated laser. The electronic shutter (ESH) in Figure 3.2 was therefore added in the external cavity. It was closed just before the last Fabry-Perot scan was digitized. In this way, the uncoupled spectrum could be stored without encountering drift problems. Experimental spectral data recorded with the above optical and electrical setup is presented in the next section in conjunction with theoretical comparisons and simulations.

3.3 Single Mode Operation

The experimental arrangement used to investigate the spectral behavior of a self-coupled semiconductor laser has been detailed; experimental results are now presented and compared to the theory developed in Section 3.1. To be methodical in approach, operation of the laser at weak coupling levels is first examined, proceeding in turn to successively higher levels. The bulk of the data described in this section was collected using a single, arbitrarily chosen HLP1400 CSP laser as source. However, similar behavior was observed in TJS lasers, and was reproduced with other CSP devices. Distributed feedback¹²⁵ and Bragg-reflecting¹⁶⁷ lasers have also been shown to demonstrate some of the following behaviors. The modeling approach should be valid for any weakly

self-coupled semiconductor laser as long as the variation in operating parameters¹³² is accounted for and an appropriate coupling coefficient determined.

Figure 3.4 depicts the optical spectrum of the CSP laser operating in a 40 cm external cavity with a 10 mW output power, well above (1.7 times) threshold, at a power coupling ratio of -67 dB. The 40 cm cavity length is shown consistently throughout this section, as it is an intermediate length in the range available with this experimental arrangement, and turns out to be representative of cavities longer than a few centimeters. Vertically, each trace represents a specific piston position of the external cavity mirror that is separated from its predecessor by about 1/25 of a wavelength. The full 300 MHz FSR of the confocal Fabry-Perot, used to record the spectrum, is displayed on the x-axis. The final scan in each case is taken with the external cavity blocked by the shutter, shown in Figure 3.2. The lasing mode is observed to tune periodically about the uncoupled frequency and to vary in linewidth, with a monotonically decreasing cavity length. With every half-wavelength of piston (a full wavelength round trip) a cycle is completed, and an additional wave is removed from the external cavity. Note that both the narrowest and broadest linewidths occur near the free-running frequency and are separated from each other by a half cycle. The -67 dB power coupling ratio, as defined in Section 2.5, includes coupling losses to the guided mode of the laser. Its magnitude was determined as outlined in Appendix B. This coupling level corresponds to

$$\kappa\tau\sqrt{1+\alpha^2}\approx 0.56, \quad (3.3.1)$$

indicating, based on equation (3.1.9), that the self-coupled laser is operating in the single longitudinal mode region.

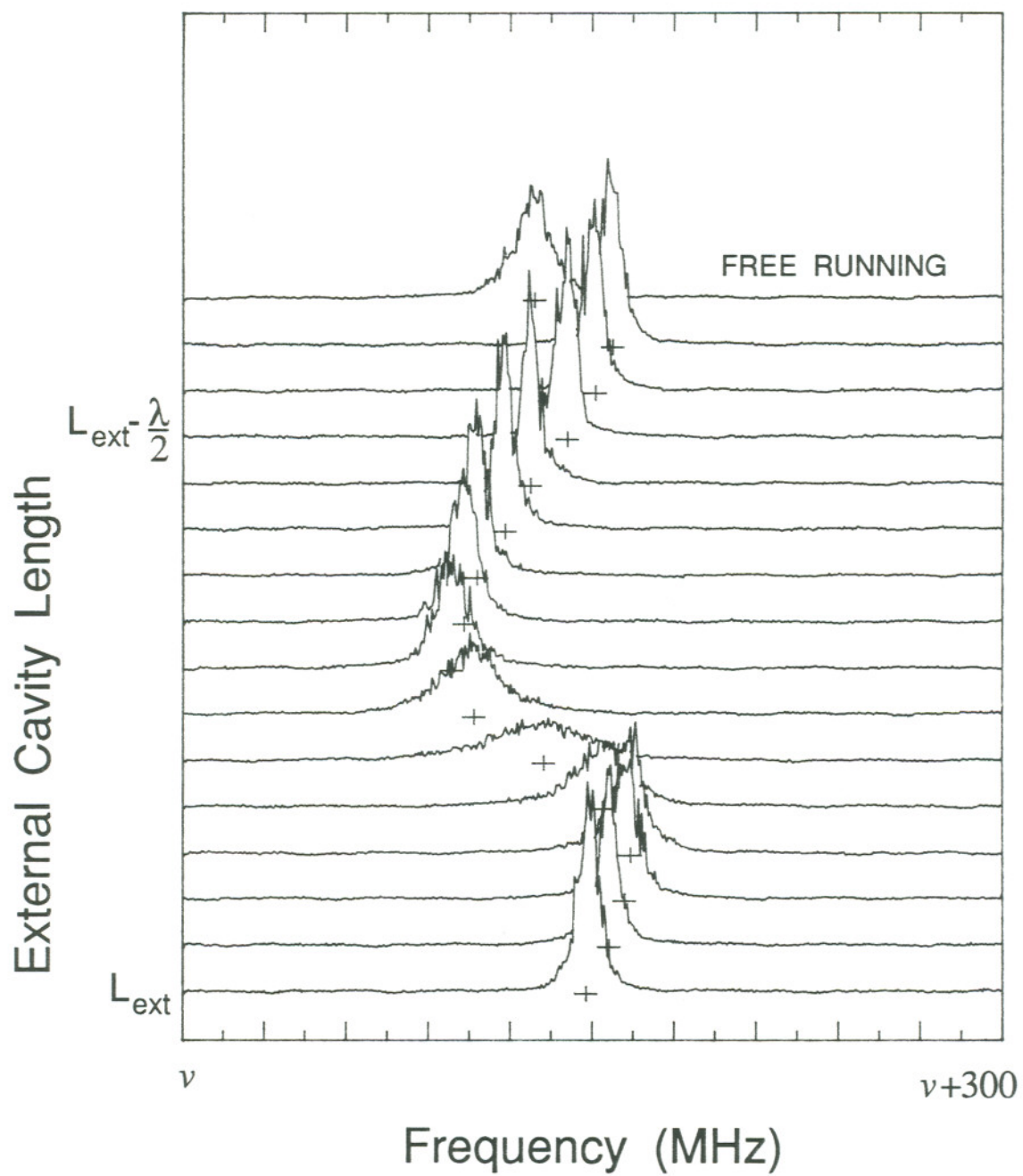


Figure 3.4 Experimental optical spectra versus external cavity length piston for a -67 dB power coupling ratio and a 40 cm cavity length.

Figures 3.5 a),b) and c) show numerical solutions to the transcendental equation (3.1.5) for the oscillation frequencies, equation (3.1.3) denoting the threshold gain change, and equation (3.1.15) giving the lasing mode's linewidth, respectively. Parameters used in the calculation were those measured for the HLP1400 CSP laser listed in Table E.1. There is clear agreement between the predicted mode frequencies and the experimental data. The lasing mode follows a qualitatively similar tuning trajectory in Figure 3.5 a) as the experiment, while the maximum tuning excursion of 33 MHz, given by equation (3.1.7), occurs at the expected relative piston location.

The threshold gain of the laser is predicted to vary with piston as well. Figure 3.5 b) shows $\overline{\Delta n}$ normalized to the reduced coupling magnitude. Power variations due to the maximum change in threshold gain are small at this coupling level and therefore go unnoticed in Figure 3.4. Lower threshold gain modes are seen to exist exclusively at oscillating frequencies smaller than that of the isolated laser. This is consistent with the expected increase in refractive index in the active region of the laser diode resulting from a decrease in the carrier density. Figure 3.5 c) predicts that the lasing linewidth narrows to 0.41 times its free-running value, while broadening to a maximum of about 5.4 times natural. This is approximately the case in Figure 3.4. Interestingly, both extremes occur at the isolated lasing frequency. Note that the linewidth minimum and the low threshold gain locations are shifted from each other in phase, as discussed in Section 3.1.2.

Figure 3.6 shows the numerical solution of the stochastic phase equation (3.1.10) for the same parameters used in Figures 3.5 a), b) and c). The result is to be compared to Figure 3.4. Each trace again corresponds to a small decrease

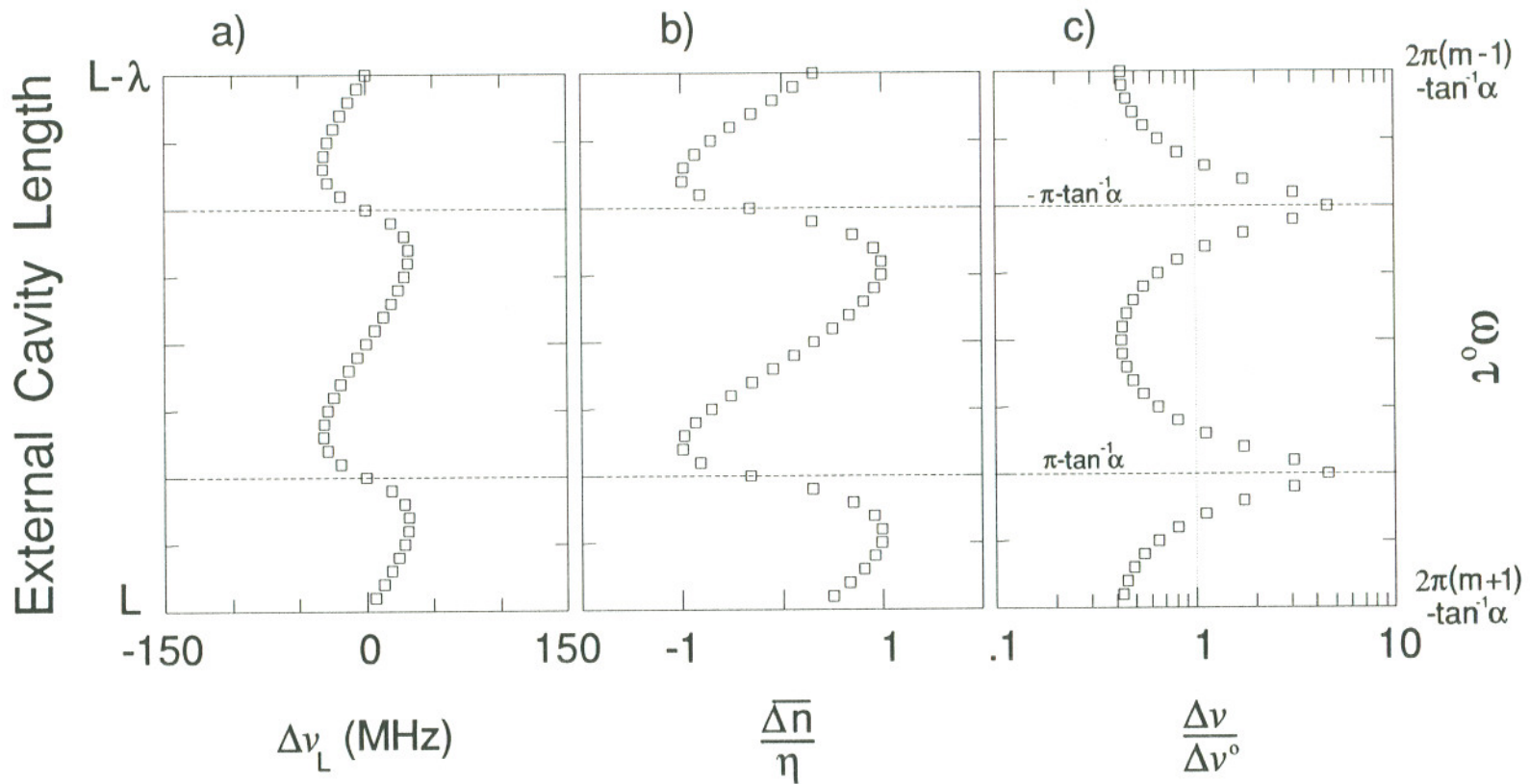


Figure 3.5 Stationary solutions depicting the change in a) oscillation frequency, b) threshold gain and c) linewidth for a self-coupled HLP1400 CSP diode laser at a power coupling ratio of -67 dB. 40 cm external cavity.

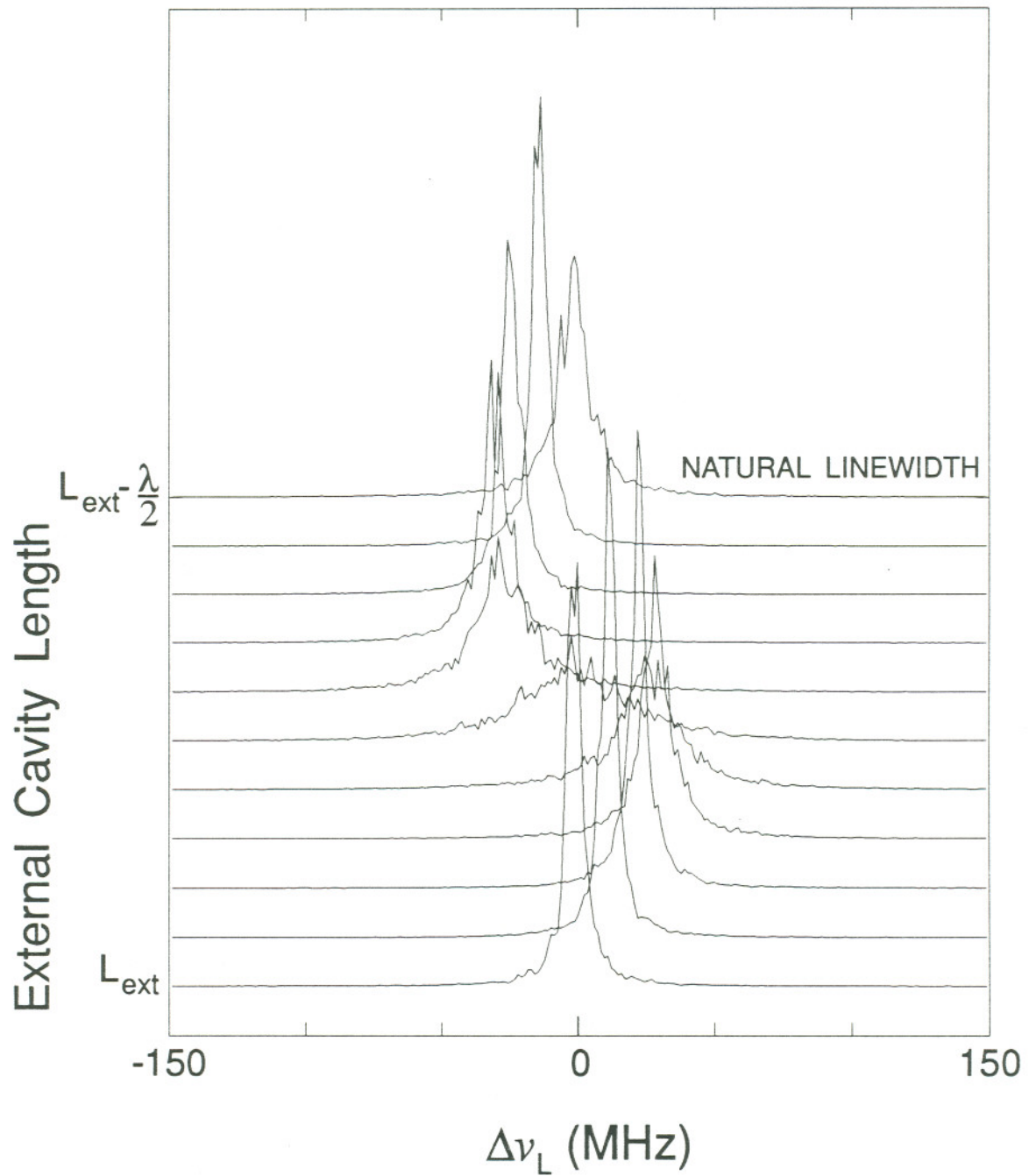


Figure 3.6 Numerical simulation of mode tuning for a self-coupled HLP1400 CSP laser at a power coupling ratio of -67 dB. 40 cm external cavity, 12 MHz natural linewidth.

in the external cavity length over a total of one-half wavelength. As discussed in Appendix D, the noise source included in the numerical integration was chosen to result in the correct natural linewidth, which is displayed in the last trace with no coupling. The time series of the phase was calculated using Heun's method¹⁶⁸ (a simple predictor-corrector integrater; note that the phase equation (3.1.10) is no longer stiff, as it was when coupled to the field equation). An FFT routine then transformed the complex field amplitude to the frequency domain, whose time-averaged magnitude squared is plotted in Figure 3.6. This figure, along with similar plots presented later, simulates the output of the confocal Fabry-Perot used in the experiments by accounting for the interferometer's finite resolution in the FFT routine. The good agreement with experiment justifies the use of (3.1.10) to describe very weak coupling. Recall that relaxation oscillations were approximated as well-damped, which is indeed the case, judging from their absence in Figure 3.4.

3.4 Multimode Operation

As the coupling level is increased from the -67 dB level employed in Figure 3.3, the system makes a transition to a regime where multiple external cavity modes are available. Figures 3.7 and 3.8 display this behavior experimentally at power coupling ratios of -58 dB and -53 dB, respectively. Again, the lasing mode tunes symmetrically about the free-running frequency, increasing in frequency as the cavity length decreases. Mode hopping is most obvious in Figures 3.7 and 3.8, in contrast to the continuous tuning behavior in Figure 3.3. Mode

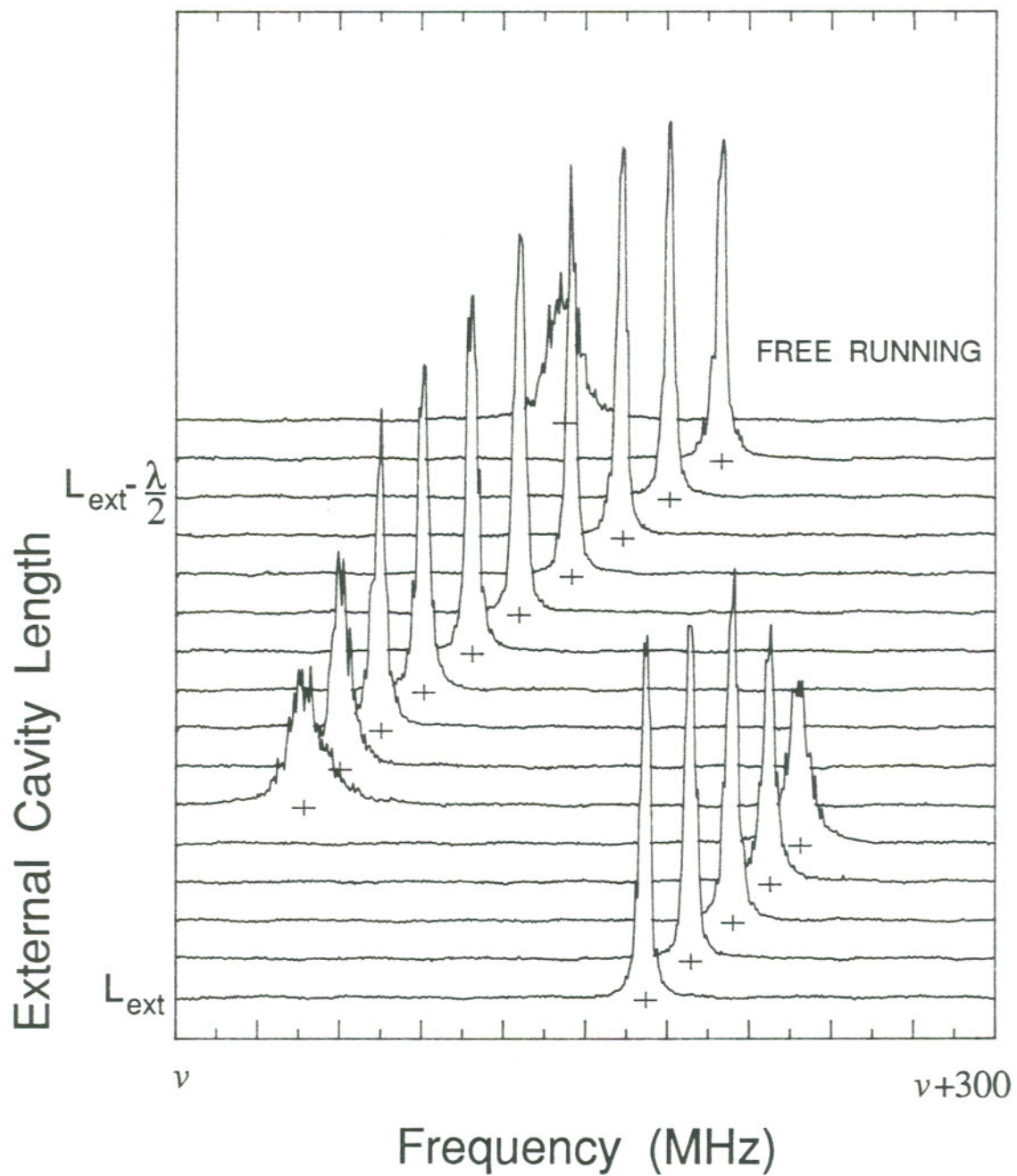


Figure 3.7 Experimental optical spectra versus external cavity length piston for a -58 dB power coupling ratio and a 40 cm cavity length.

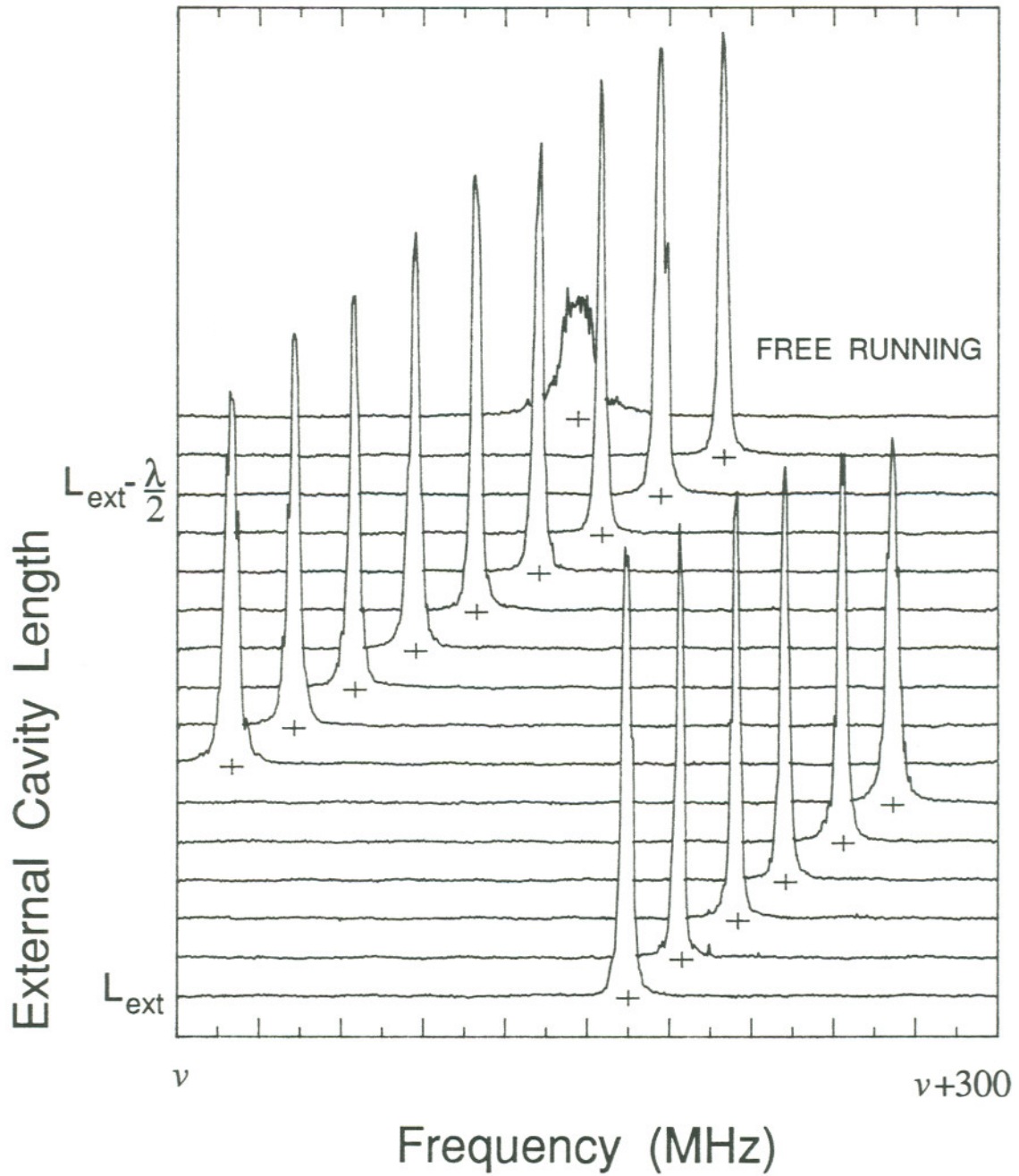


Figure 3.8 Experimental optical spectra versus external cavity length piston for a -53 dB power coupling ratio and a 40 cm cavity length.

hops occur every half wavelength of cavity piston, while the hop frequency separation steadily increases with coupling. Note that the linewidth of the lasing emission in these figures has narrowed considerably. Furthermore, in Figure 3.8, the linewidth is narrowed for all cavity lengths.

Although the self-coupled laser in Figures 3.7 and 3.8 is theoretically operating in the region of multiple solutions to equation (3.1.5), multimode behavior is not apparent in examining the figures. Two distinct peaks in the Fabry-Perot spectra were observed experimentally, however, when the cavity length was pistoned precisely to the mode hop boundary. Numerical solutions to equation (3.1.10) are offered in Figure 3.9 to demonstrate this behavior. These results were obtained in an identical manner as that illustrated in Figure 3.6, with $\omega_0\tau = \pi - \tan^{-1}\alpha$. The broadened mode at -67 dB, similar to the sixth trace in Figure 3.3, transitions to two peaks as the power coupling ratio is increased. This transition from single to multiple mode operation has been described as "mode splitting" by Tkach and Chraplyvy¹⁶⁹, probably after previous work regarding Doppler-broadened lasers¹⁷⁰. In the latter work, multiple frequencies associated with the same mode number were shown to stem from index dispersion in the wings of a high gain resonance, whereas in the present situation they are due strictly to the influence of the external cavity. Unfortunately, the term "mode splitting" implies that a single resonance is being somehow split in two. In actuality, two separate modes appear as a single, double peaked mode due to their large linewidths. The frequency separation of these modes is observed to approach that of the external cavity with large coupling, but are pulled from this value at low coupling levels. The dependence of the frequency separation of the two external cavity modes on coupling level can

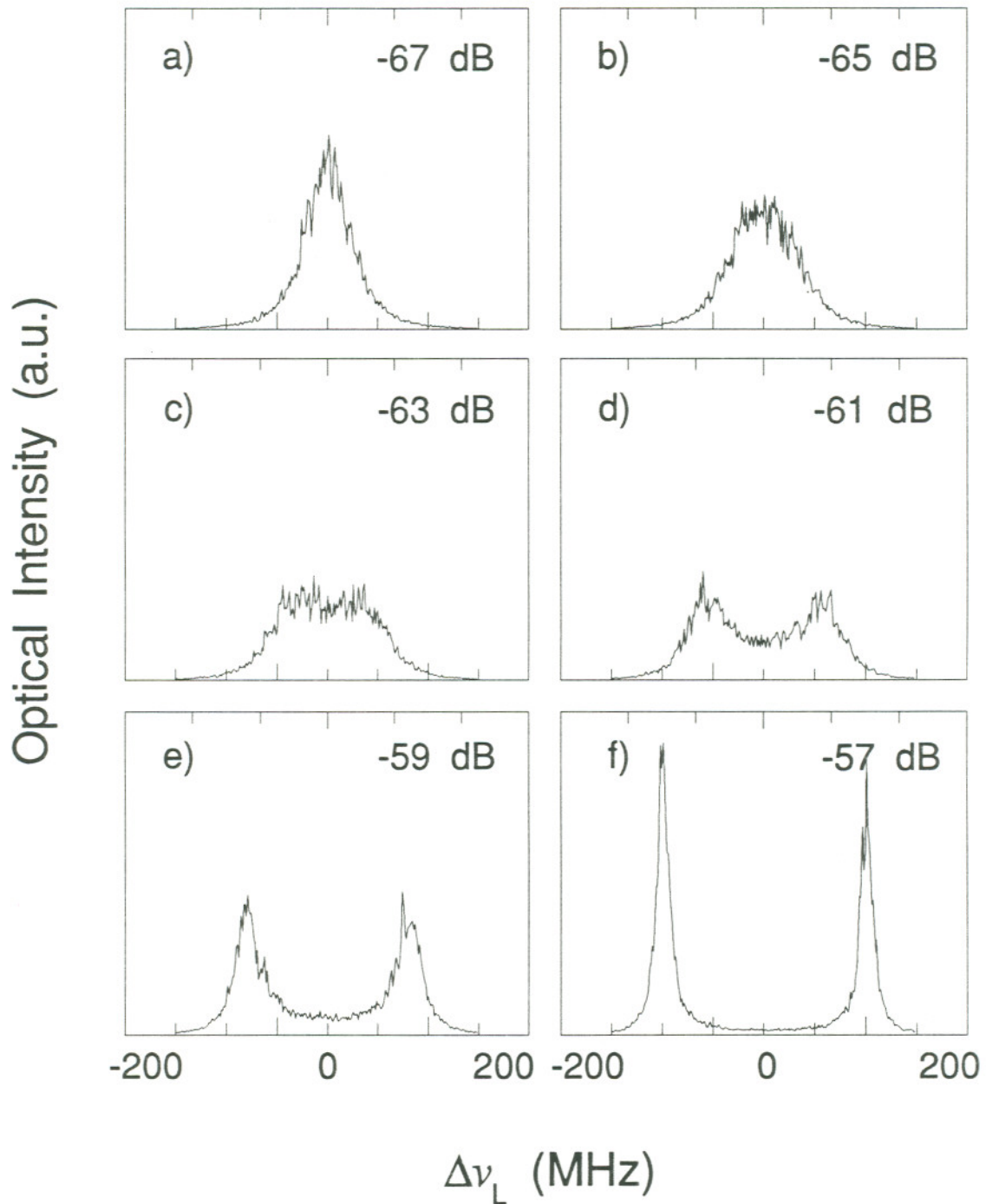


Figure 3.9 The transition from single to multimode operation for a self-coupled HLP1400 CSP laser. Numerical simulations assume a 40 cm external cavity, 12 MHz natural linewidth, and $\omega_0\tau = \pi - \tan^{-1}\alpha$.

be very useful in calibrating the power coupling ratio, as described in Appendix B.

Numerical solutions for the modes, their threshold gains and linewidths in the multimode region are given in Figure 3.10 as a function of external cavity length. The power coupling ratio is -53 dB, corresponding to the experimental case in Figure 3.8, while other parameters used in the calculation are those of the HLP1400 CSP laser listed in Table E.1. For cavity lengths within the shaded regions of the figure, three longitudinal modes are available to the system. However, the central roots in Figure 3.10 a), denoted by solid dots, are later shown to be dynamically unstable. The system is therefore bistable in the multimode regions, and the double peaks which develop in Figure 3.9 at the larger coupling levels must then correspond to the outer two modes in Figure 3.10 a). Since the mode hop in Figure 3.8 is symmetric about the free-running oscillation frequency, a direct comparison to Figure 3.10 a) shows that the mode hops occur about $\omega_o \tau = (2m + 1)\pi - \tan^{-1}\alpha$. It is apparent that a large number of the available roots do not show up experimentally.

As shown in Figure 3.10 b), the threshold gain varies about the uncoupled threshold value with external cavity piston due to interference, as described previously. A study of the experimental spectra in Figures 3.7 and 3.8 reveals that the mode with the lowest threshold gain in the multimode region does not necessarily lase, as has been assumed in the past¹⁷¹⁻¹⁷⁴. In fact, there are cases in which the *highest* threshold mode runs. This is most counterintuitive and contradicts the commonly assumed criterion that low threshold gain determines the lasing mode. Mode selection is considered in more detail in Section 3.6.

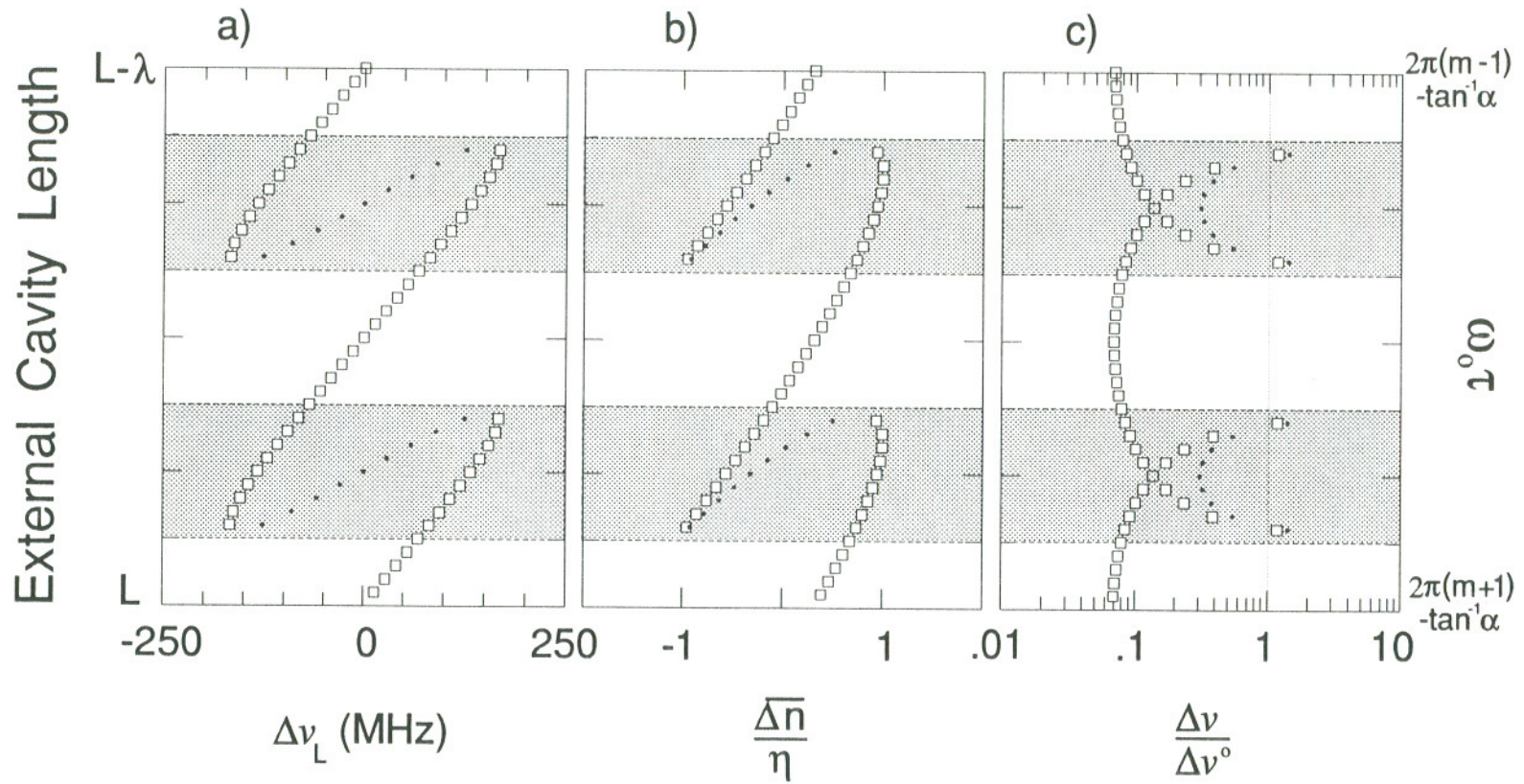


Figure 3.10 Stationary solutions depicting the change in a) oscillation frequency, b) threshold gain and c) linewidth for a self-coupled HLP1400 CSP diode laser at a power coupling ratio of -53 dB. 40 cm external cavity.

The minimum linewidth ($0.07 \cdot \Delta\nu^0$), predicted in Figure 3.10 c), still occurs at the free-running frequency of the laser. This is consistent with the experimental data of Figure 3.8, recalling that the theoretical linewidth is approaching the resolution limit of the confocal Fabry-Perot used to take the measurements. The maximum linewidth, as measured from Figure 3.8, has a FWHM of a few MHz and is located at a cavity piston just at the mode hop boundary. Again, it is clear that several of the predicted modes are not seen experimentally, even though they are dynamically stable.

Figure 3.11 displays the numerical integration of the phase equation (3.1.10) for a power coupling ratio of -58 dB, comparable to the experimental results of Figure 3.7. A natural linewidth of 12 MHz was assumed, while other parameters were identical to those in Figures 3.10. The mode frequencies, tuning extremes and linewidths are in striking agreement with the experimental results, and the laser's behavior at the mode hop boundary is clearly duplicated.

3.5 Modal Stability

It was mentioned previously that many of the possible modes of the self-coupled system do not represent dynamically stable states. This is in sharp contrast to the stability analysis performed in Section 2.4, where coupling delays were neglected. It is not necessary, at this point, to return to the full set of rate equations (3.1.1) and (3.1.2) to determine which modes are stable, however. Dynamic stability can also be analyzed, when relaxation oscillations play a minor role, from the phase equation (3.1.10). Consider the phase with respect

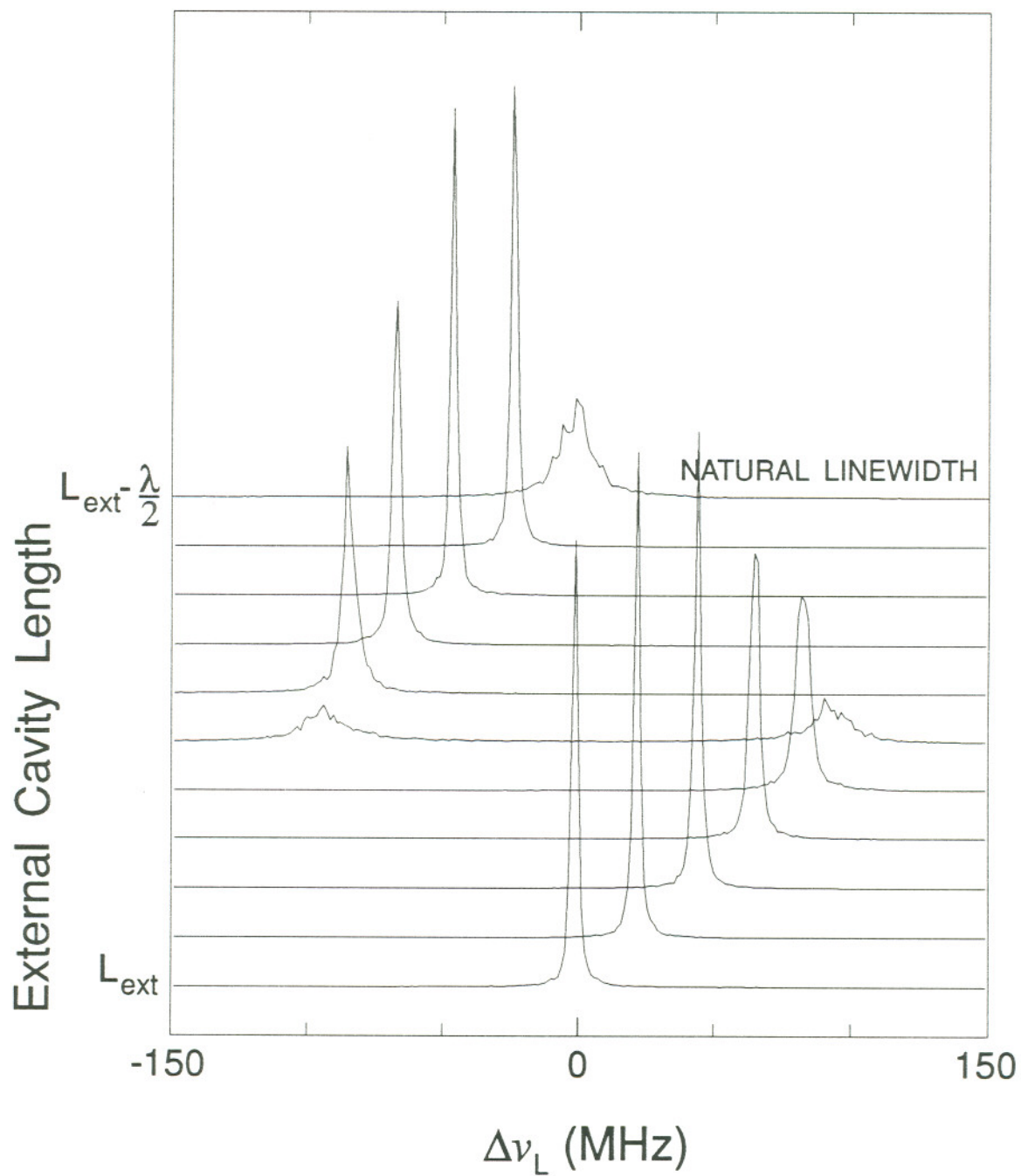


Figure 3.11 Numerical simulation of mode tuning for a self-coupled HLP1400 CSP laser at a power coupling ratio of -58 dB. 40 cm external cavity, 12 MHz natural linewidth.

to the steady-state given by (3.1.11), where $\delta\phi(t)$ again denotes the small fluctuations in phase about the steady-state due to perturbations from noise sources such as spontaneous emission. Direct substitution of (3.1.11) into equation (3.1.10), invoking that $\delta\phi(t)$ is small, leaves

$$\delta\dot{\phi}(t) = -\kappa\sqrt{1+\alpha^2}\cos(\omega_o\tau + \Delta\omega_L\tau + \tan^{-1}\alpha)\cdot[\delta\phi(t)-\delta\phi(t-\tau)]. \quad (3.5.1)$$

To test the dynamic stability of a mode, a solution of the form $\delta\phi(t) \sim \exp(st)$ is assumed. Substitution gives

$$x = C(1 - e^{-x}), \quad (3.5.2)$$

where $x \equiv s\tau$ and

$$C \equiv -\kappa\tau\sqrt{1+\alpha^2}\cos(\omega_o\tau + \Delta\omega_L\tau + \tan^{-1}\alpha). \quad (3.5.3)$$

Graphically, the roots x of equation (3.5.2) lie at the intersection of a line of slope unity and the exponential factor on the right-hand side of the equation, as shown in Figure 3.12 a). The piston location of the external cavity, $\omega_o\tau$, is used as a free parameter, allowing the value of the coefficient C to vary over the range

$$-\kappa\tau\sqrt{1+\alpha^2} \leq C \leq \kappa\tau\sqrt{1+\alpha^2}. \quad (3.5.4)$$

The requirement for a stable solution is that $s < 0$, or $x < 0$, so that the solution damps exponentially under a perturbation from steady-state. Therefore, stable solutions lie in the left half-plane of Figure 3.12 a). It is clear that if no roots are to fall in the right half-plane, the slope of the exponential function

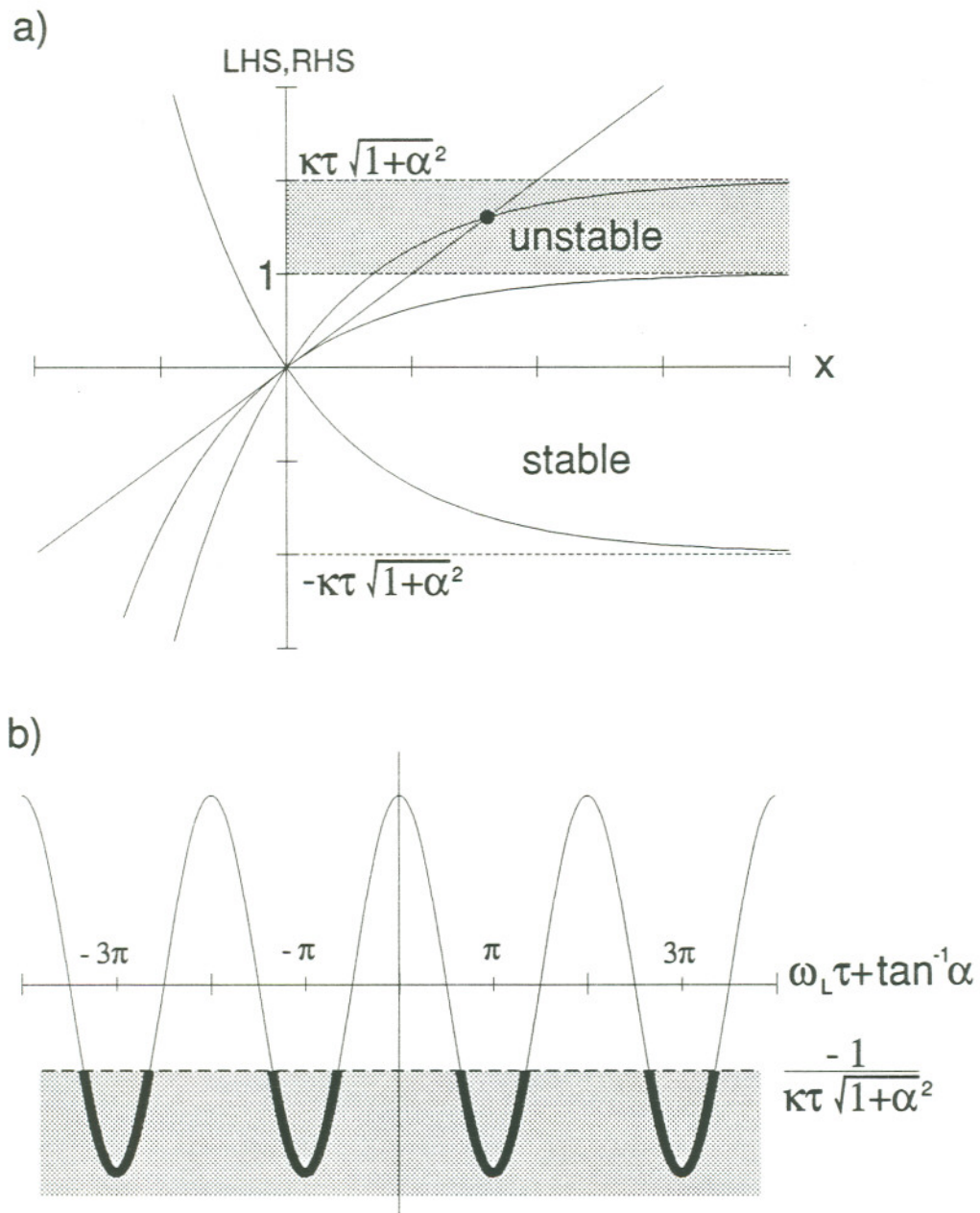


Figure 3.12 Graphical representations of the stability criterion (3.5.6) for a self-coupled semiconductor laser.

evaluated at the origin must be less than one. Mathematically,

$$\frac{d}{dx} \left(C(1 - e^{-x}) \right)_{x=0} < 1. \quad (3.5.5)$$

Performing the differentiation and substituting for C , the following stability criterion^{127, 128, 175} is derived:

$$1 + \kappa\tau\sqrt{1+\alpha^2}\cos(\omega_o\tau + \Delta\omega_L\tau + \tan^{-1}\alpha) > 0. \quad (3.5.6)$$

When written in the form

$$\cos(\omega_L\tau + \tan^{-1}\alpha) > -\frac{1}{\kappa\tau\sqrt{1+\alpha^2}}, \quad (3.5.7)$$

the consequences of (3.5.6) are easily interpreted from Figure 3.12 b). In the single mode regime, where $\kappa\tau\sqrt{1+\alpha^2} < 1$, solutions are stable for all cavity lengths. However, as the coupling level is increased into the multimode region, solutions near piston values of $\omega_o\tau = m\pi - \tan^{-1}\alpha$ become unstable, as shown in the figure. These short-lived modes, indicated by solid dots in Figures 3.10, are not seen experimentally. In the phasor representation of Figure 3.1, the unstable regions correspond to coupling phases which force destructive interference between the circulating and reinjected fields. The size of the unstable region grows with increasing coupling, cavity length and α parameter, asymptotically encompassing half of the possible coupling phases. (3.5.6) is therefore the self-coupling equivalent of stability criterion (2.4.19) for mutually coupled lasers.

Notice that the left-hand side of the stability criterion in equation (3.5.6) is the same factor determining the linewidth given by (3.1.15). This is perhaps

not surprising, recalling that the linewidth merely represents fluctuations due to phase noise. By introducing the external cavity, the stability of the laser against phase perturbations can be changed, resulting in a change in linewidth. A closer examination of (3.1.15) shows that the predicted linewidth diverges at the boundaries of the unstable region. The approximations behind (3.1.15) are, of course, invalid when the solution is dynamically unstable. By eliminating unstable modes, line-narrowing almost exclusively occurs in the multimode region, as was evident in the experimental spectra.

Differentiating equation (3.1.5) with respect to the free-running oscillation frequency ω_o , results in the expression

$$\frac{d\nu_L}{d\nu_o} = \left(1 + \kappa\tau\sqrt{1+\alpha^2}\cos(\omega_L\tau + \tan^{-1}\alpha)\right)^{-1}. \quad (3.5.8)$$

Therefore, the stability criterion (3.5.6) can also be written as

$$\frac{d\nu_o}{d\nu_L} > 0. \quad (3.5.9)$$

In words, an increase in the isolated oscillation frequency of the laser must be associated with a corresponding increase in the coupled lasing frequency, and vice versa. At the stability limit¹⁷³, $\frac{d\nu_o}{d\nu_L} = 0$. Therefore, the stability boundaries are located where the slope of the tuning trajectory, as in Figure 3.10 a), goes to zero.

The transition to multimode operation illustrated by Figure 3.9 represents a pitchfork bifurcation¹⁷⁶ of a single, stable solution into three new states, one

of which is unstable. Such a transition is by no means unique to a self-coupled laser. Interesting analogies, for example, can be made to the first-order phase transition of an ideal van der Waals gas¹⁷⁷. Isotherms in the PV plane are similar in appearance to the piston versus frequency plots of Figures 3.5 a) and 3.10 a). With a reduction in temperature, multiple states are allowed for a given pressure. However, the central portion of the isotherm violates the stability criterion

$$\left(\frac{\delta P}{\delta V} \right)_T < 0. \quad (3.5.10)$$

As the pressure is monotonically varied through the multi-stable region, the system "hops" (undergoes a phase transition) between the two extreme states in volume, governed by the lever rule.

3.6 Mode Selection

To this point it has been demonstrated how dynamic stability reduces the number of allowed modes in a self-coupled system. Although numerical simulations have been shown to predict the observed spectral behavior, it is still unclear why the system chooses to lase in the modes it does. As mentioned earlier, it is evident in Figure 3.10 b) that the lowest threshold gain mode of the system is not always the one that runs. The lasing mode hops from lower to higher threshold gain or vice-versa, depending upon the direction in which the external cavity is pistoned.

To determine the reason for this behavior, the time evolution of the system was investigated for piston locations near the mode hop boundary. Experimental data was collected using the planar Fabry-Perot interferometer shown in Figure 3.2 as a tuned filter. The spectral resolution of the instrument was increased to about 40 MHz by shortening the mirror separation. This bandwidth was chosen as a compromise, so that the entire linewidth of one mode could be collected over a range of power coupling ratios, while insuring rejection of the other. The Fabry-Perot was arbitrarily tuned to the mode with the higher frequency, and the external cavity simultaneously pistoned to the center of a multimode region. The center, located at $\omega_0\tau = \pi - \tan^{-1}\alpha$, could be found accurately by balancing the spectral brightness of the two competing modes. Holding the system at that point, however, was non-trivial. Electrical noise, mechanical vibrations, thermal variations, etc., all made this measurement difficult. The precautions discussed in Section 3.2 were instituted to help stabilize the measurement. Throughput of the Fabry-Perot filter was digitized, collecting various length records of power versus time located in the higher frequency mode. Each time series, in essence, gives a time-resolved spectrum, since there are only two possible states in which the system may operate. Fine positioning of the cavity length from the center of the multiple mode region was attained by electronically stepping the voltage to the piezo translator of Figure 3.2 just before data was digitized. In this way, long term drifts could be avoided.

Time series for a small region of cavity length about $\omega_0\tau = \pi - \tan^{-1}\alpha$ are shown in Figure 3.13 at a power coupling ratio of -52 dB. The modes at this coupling level are essentially the same as in Figure 3.10 a), with slightly larger

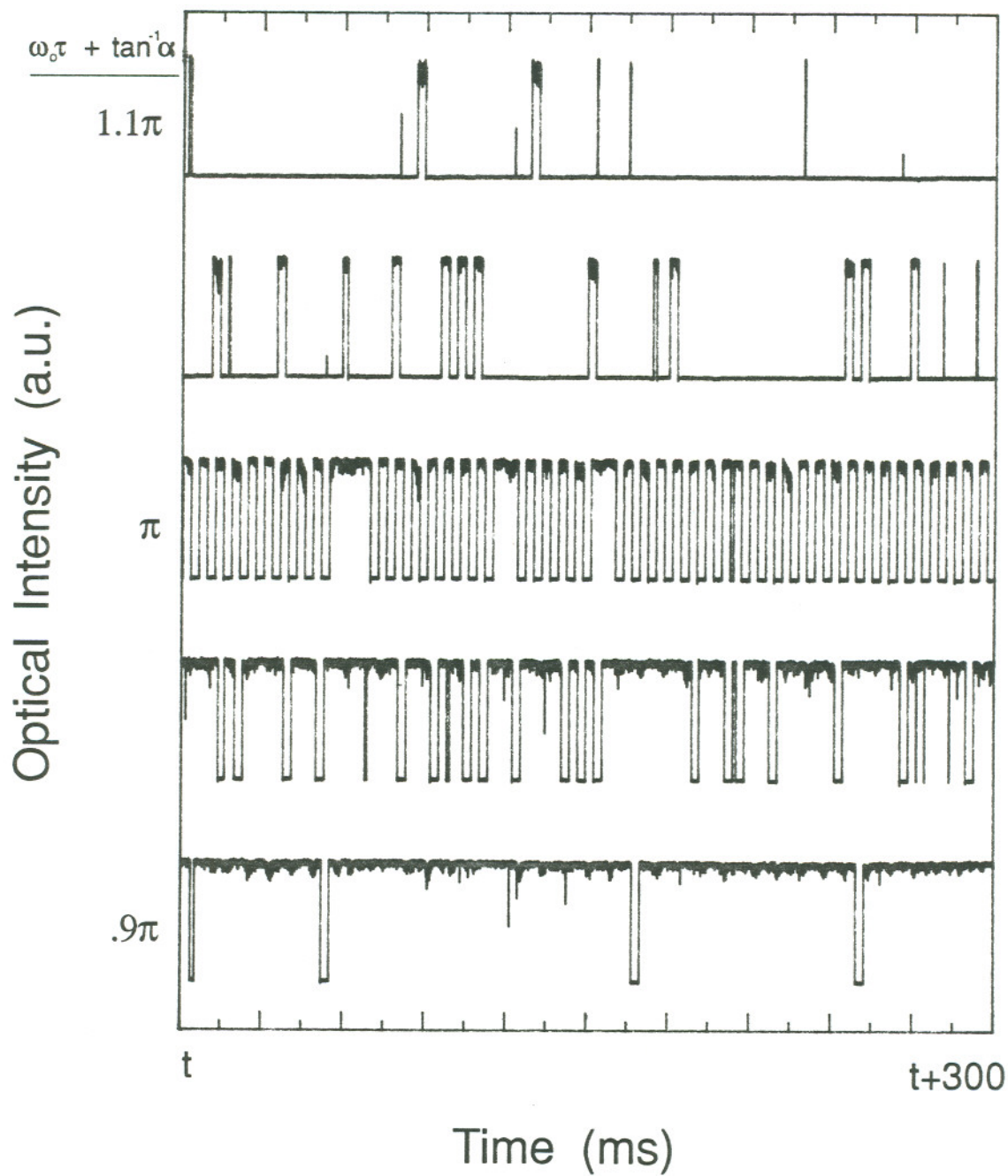


Figure 3.13 Experimental measurements of mode hopping in the vicinity of the hop boundary $\omega_0\tau = \pi - \tan^{-1}\alpha$. HLP1400 CSP laser diode in a 40 cm external cavity, -52 dB power coupling ratio.

multimode regions with respect to $\omega_0\tau$. Although not obvious in the experimental data of Figures 3.7 and 3.8, no definite hop boundary between the two stable branches of Figure 3.10 a) exists. These branches are in a highly dynamic mode competition where competing modes alternately run. The dwell time in each mode is a sensitive function of τ . As the external cavity is pistoned in a direction favorable to one branch, the dwell time of that mode increases at the expense of the unfavored mode. The longer dwell time shows up as a larger average intensity^{178,179}. Note also that the piston range covered in Figure 3.13 is a fraction of the complete multimode range.

Assuming that mode hops in this figure are initiated by amplified spontaneous emission (ASE) noise in the laser, the stability of the allowed modes against phase perturbations induced by this noise must then be changing as a function of τ . Near $\omega_0\tau = \pi - \tan^{-1}\alpha$, the dwell times in each mode are about equal. Yet when pistoned off slightly, a mode is either more or less likely to be perturbed from that state. Mode selection is therefore determined by phase stability, not threshold gain. This conclusion is further substantiated by a close examination of Figure 3.10 c), which reveals that the lowest linewidth mode predominates in bistable regions¹²⁵.

As the coupling level is further increased, the character of the emission spectrum changes dramatically. Figures 3.14 and 3.15 show typical spectra versus external cavity length for power coupling ratios of -46 dB and -44 dB, respectively. Operating conditions in these figures are identical, other than the coupling level, to those in Figures 3.3, 3.7 and 3.8. The spectra were taken with the planar Fabry-Perot in Figure 3.2, at a FSR of 2 GHz. Therefore, narrowed linewidths are not resolvable. The external cavity length was first

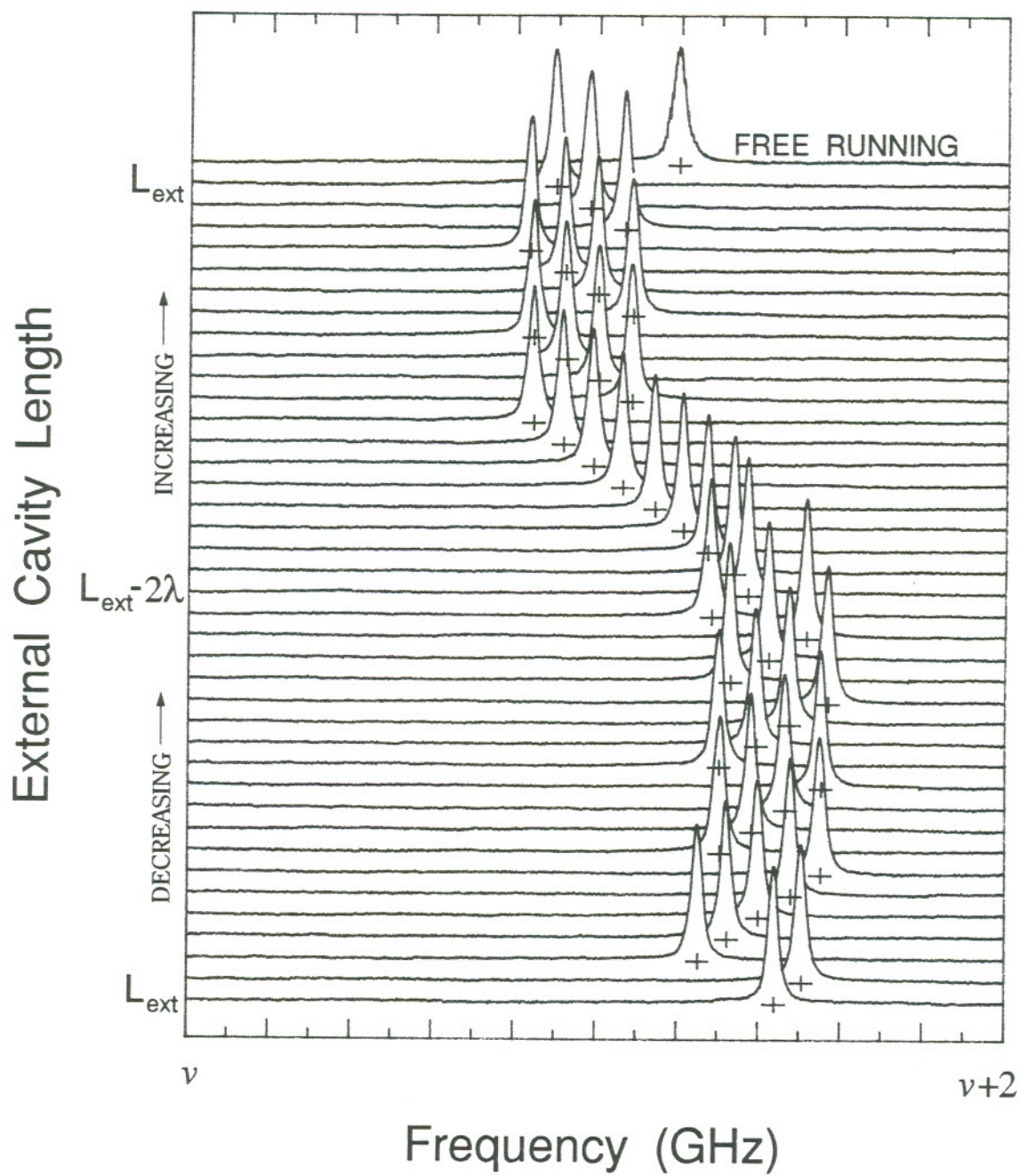


Figure 3.14 Experimental optical spectra showing hysteretic mode tuning for a self-coupled HLP1400 CSP laser at a power coupling ratio of -46 dB, in an external cavity of length 40 cm.

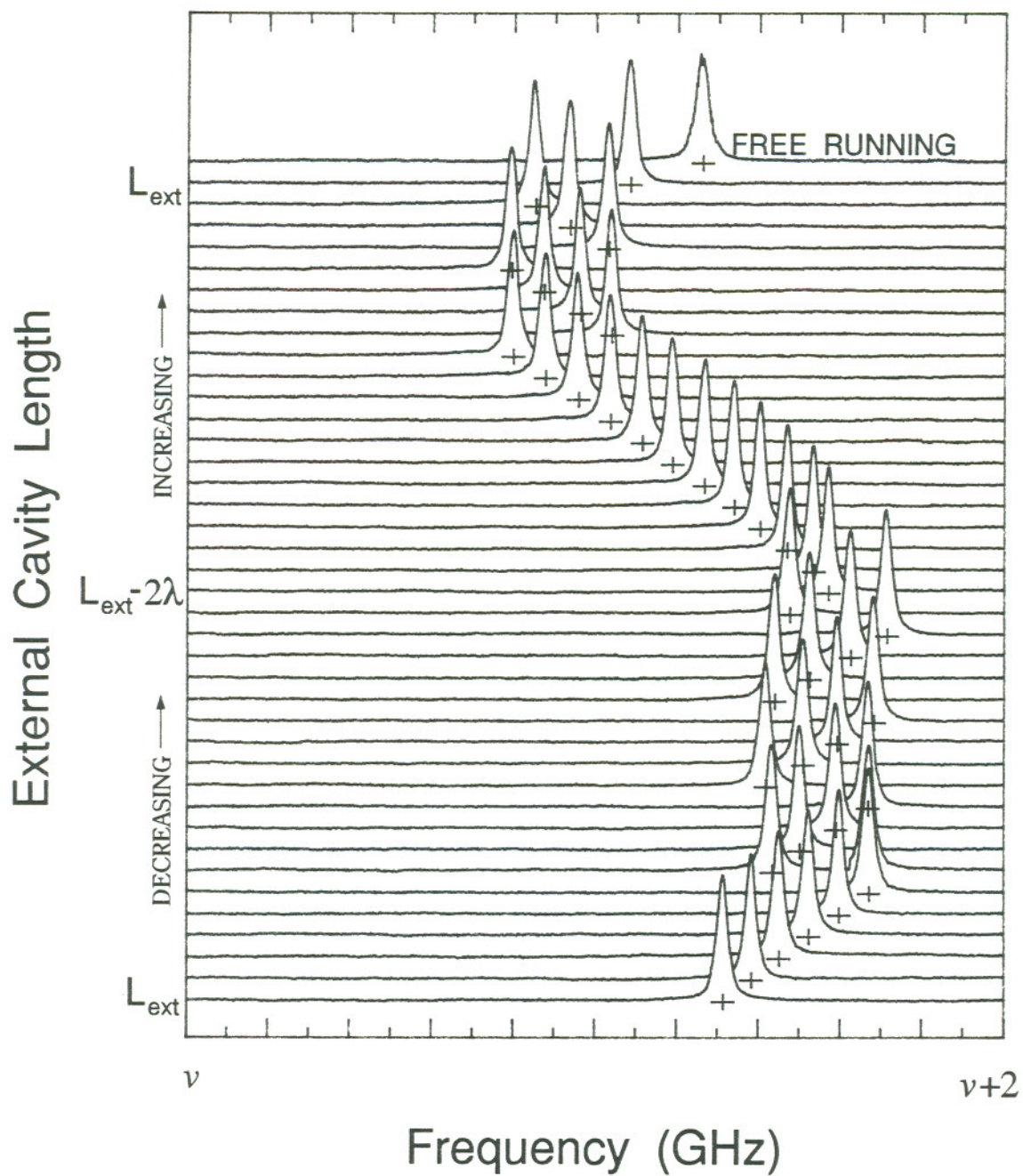


Figure 3.15 Experimental optical spectra showing hysteretic mode tuning for a self-coupled HLP1400 CSP laser at a power coupling ratio of -44 dB, in an external cavity of length 40 cm.

decreased by about two wavelengths in (twenty) small steps, whereupon its direction of motion was immediately reversed, returning the cavity to its original length. The first and last traces in the figures are of the uncoupled lasing line. Mode hops have ceased to be symmetric about the free-running oscillation frequency. Further, the tuning trajectory is hysteretic. When the external cavity length is decreased, hops occur entirely on the high frequency side of the isolated frequency, while the opposite is true when the cavity length is increased. It is interesting that when the piston direction is reversed, the laser is able to tune *more* than 2π of piston without hopping.

Equation (3.1.5) is once again solved numerically, in Figure 3.16, to determine the available modes of the system at a coupling level of -46 dB. Modes which violate the stability criterion (3.5.6) have been eliminated for clarity. By comparing the experimental data with the allowed states of the system, the tuning trajectory can easily be superimposed on Figure 3.16. Thin lines indicate the path taken as the cavity length is decreased, while thicker lines depict the subsequent return of the cavity to its initial length. Note that there are multiple modes available for all cavity lengths at this coupling level. Mode hops are observed to occur only when the system reaches the tuning extremes given by (3.1.7). It is evident from the figure that any stable mode of the system can be accessed by using the proper trajectory.

Mode hopping behavior was further examined with respect to the power coupling ratio, as shown in Figure 3.17. Each trace was taken at the hop boundary $\omega_0\tau = \pi - \tan^{-1}\alpha$. Hence, dwell times in each mode are approximately equal. Hop rates clearly slow with an increase in power coupling. This implies that the system is becoming more stable against phase perturbations at larger

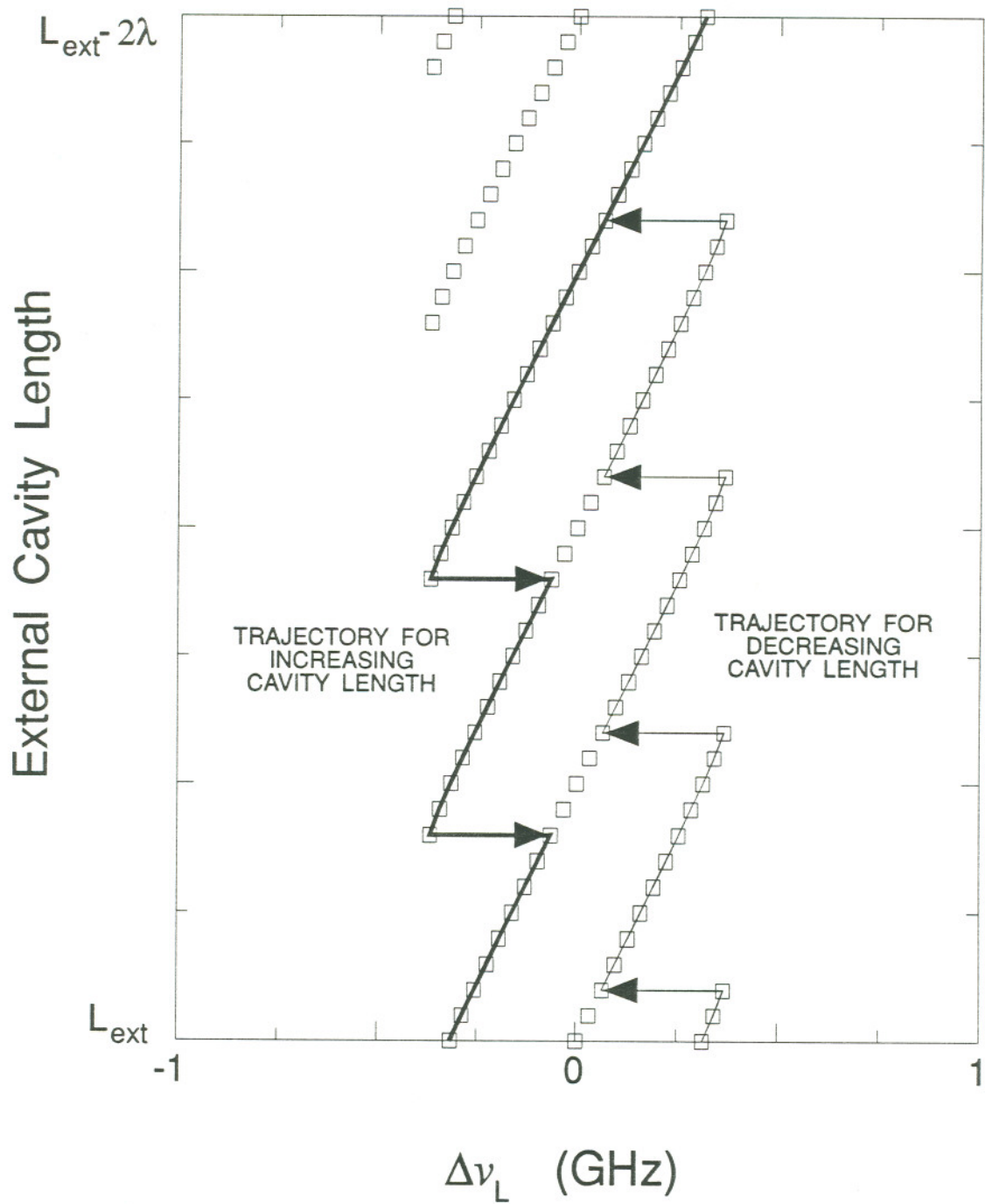


Figure 3.16 Mode tuning trajectory of a self-coupled HLP1400 CSP laser at a power coupling ratio of -46 dB and an external cavity length of 40 cm.

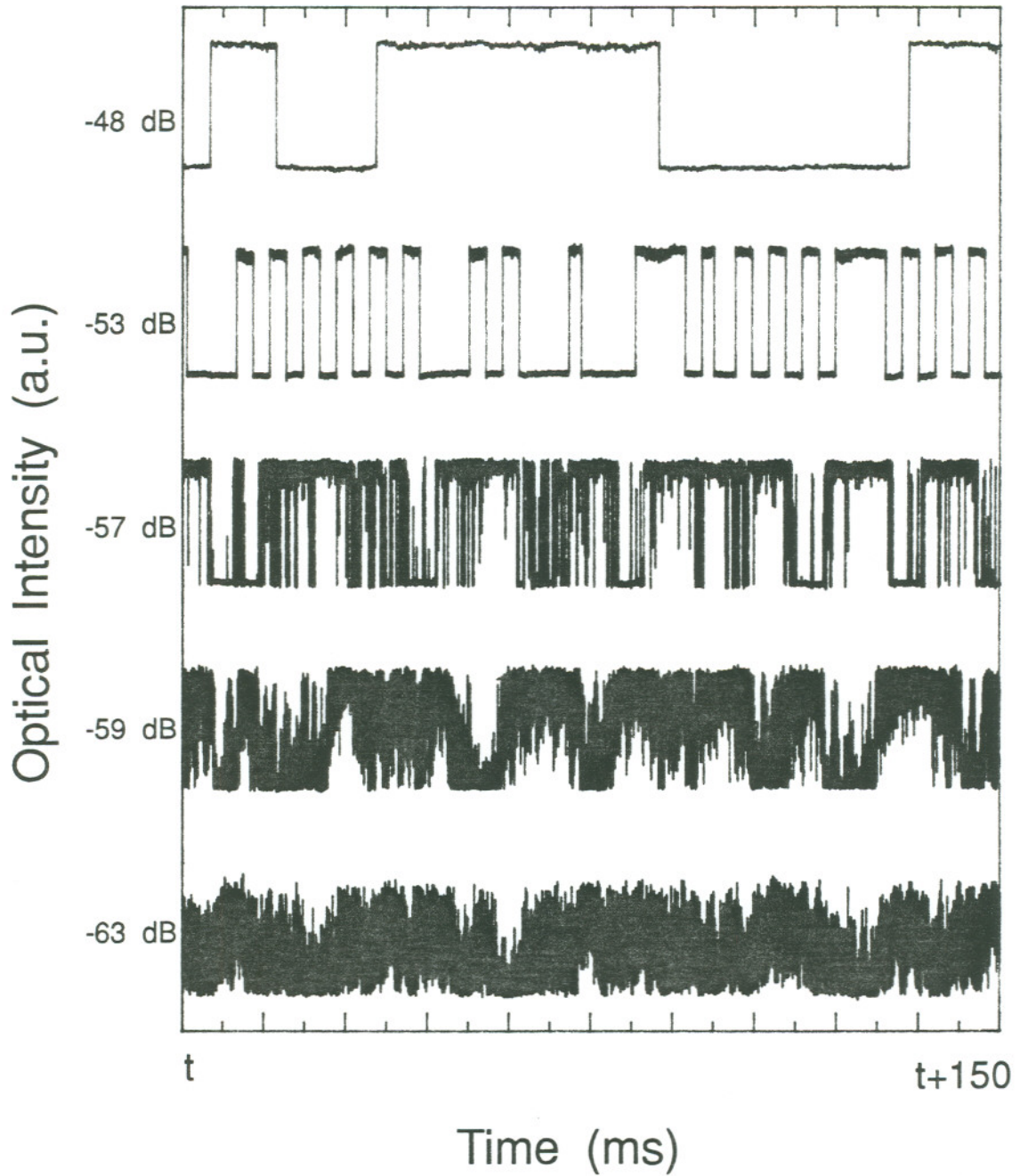


Figure 3.17 Experimental measurements of mode hopping versus power coupling ratio for an HLP1400 CSP laser diode in a 40 cm external cavity.

coupling levels. Hence, spontaneous emission noise becomes insufficient to perturb the system from its current state, explaining the hysteretic tuning characteristics in Figures 3.14 and 3.15. Similar hysteretic behavior has been observed in the output power of the self-coupled laser¹⁸⁰ due to variations in threshold gain throughout the tuning trajectory. In this early work, however, the effect was incorrectly attributed to spectrally asymmetric gain suppression.

For shorter external cavities, multimode operation occurs at much larger coupling levels, where quantum noise cannot induce mode hops. In this case, hysteresis is to be expected throughout the multimode regime, and has indeed been observed with changes in injection current in a 4.5 mm cavity¹²⁷. Only when gain differences between neighboring modes become sufficiently large, such as in the case of frequency selective feedback¹⁸¹, is the low threshold gain mode expected to dominate.

Figure 3.17 illustrates the stabilizing effect of the reinjected signal on the phase noise in the laser, which manifests as a reduced linewidth and reduced mode hopping at larger coupling levels. This induced stability can be likened to injection-locking¹⁸². The Adler equation¹⁸³ describing the phase of the slave laser can be written as

$$\dot{\phi}_S(t) = \omega_S - \omega_M - \frac{1}{\tau_D} \frac{E_M}{E_S} \sin[\phi_S(t) - \phi_M] + F(t). \quad (3.6.1)$$

The sinusoidal term on the right hand side of (3.6.1) acts as a restoring force, keeping the phase of the slave ϕ_S confined. If the slave is well-locked, the phase tracks that of the master oscillator ϕ_M , which is assumed to be highly stabilized. In the case of self-coupling, the Adler-like phase equation (3.1.10),

written with respect to the steady-state, becomes

$$\delta\dot{\phi}(t) = -\kappa\sqrt{1+\alpha^2}\cos(\omega_L\tau+\tan^{-1}\alpha)\sin[\delta\phi(t)-\delta\phi(t-\tau)] + F(t). \quad (3.6.2)$$

Here, a similar restoring force is present. When $\delta\phi(t)-\delta\phi(t-\tau)$ becomes non-zero, the sinusoid acts to minimize this difference. The strength of the restoring force depends on the magnitude of the coupling coefficient; hence, the reduced hop rates at larger coupling levels. An analogy can be made to a potential well problem. The depth of the well is determined by the coupling level, and its width gives the linewidth of the mode. A mode hop, then, is analogous to the particle obtaining a large enough kick from spontaneous emission events to escape the well, landing in the potential well of the next mode. The deeper the potential well, the harder it is to get out of the well. This approach has been recently used to theoretically predict the reduction in hopping frequency with increasing coupling^{179,184}. It is important to realize that the effect of self-coupling is not to reduce the noise amplitude, for the noise is independent of the coupling level, but to reduce the diffusion in phase resulting from the noise.

3.7 Coherence Collapse

Thus far, the stability of a self-coupled laser at weak coupling levels, where the power coupling ratio is below about -40 dB has been examined. The system was in general multimode, and mode selection was determined by phase stability. The stability of the self-coupled laser was shown to improve with increasing coupling level. This trend, however, does not continue indefinitely. At

higher feedback levels, the lasing line has been observed to broaden to a width of tens of GHz^{125,185,186}. This enormous broadening results in a corresponding decrease in the temporal coherence length of the laser, and thus was originally termed "coherence collapse" by Lenstra *et al.*¹⁸⁷ in 1985. The loss of coherence was verified through visibility measurements; however, its origin was not explained. Since that time, a great deal of effort has been devoted to its understanding, primarily to determine the usefulness of diode lasers for sources in coherent optical communications applications. This section investigates the behavior of delayed self-coupling, for a semiconductor laser operating in the coherence collapse regime. Experimental optical and intensity noise spectra are presented and compared to numerical simulations of the full nonlinear rate equations.

Before proceeding, it is necessary to distinguish two domains of instability encountered at moderate self-coupling levels, resulting in decidedly different behaviors, which are sometimes both referred to as coherence collapse¹³². It was first observed by Fujiwara *et al.*¹⁸⁸ that the light versus current characteristic of a strongly self-coupled laser displays a kink just above threshold. This occurs typically at about 1.1 - 1.2 times the lasing threshold with feedback, which, for strong enough coupling, can be below the free-running laser threshold¹⁸⁹. This kink was linked to previous observations^{190,191} of low frequency fluctuations (LFF) in the 1-100 MHz range. Further studies^{192,193} revealed that the optical power displayed abrupt drops followed by a periodic buildup of power in steps¹⁹⁴ corresponding to the inverse of the external cavity mode spacing. The total recovery time of about 10-15 steps is responsible for the LFF frequency. The power dropouts were explained¹⁷⁴ as a second-order

instability due to the carrier-dependent refractive index and initiated by spontaneous emission which dislodges the laser from its stable operating state. Other studies¹⁹⁵⁻¹⁹⁷ have proposed that noise is not necessary to explain the persistence of the LFFs once initiated, while experimental evidence also exists^{189,198-200} demonstrating a possible route to optical chaos. Above the kink in the light versus current characteristic, the LFF disappear²⁰¹, and the low frequency noise level returns to that of the free-running laser. This study is concerned with the stability of the self-coupled laser above the kink, where it operates well above threshold at reasonable output power levels. The character of the progressive instability with respect to coupling level and phase, rather than current, is investigated. This is the situation which was originally referred to as coherence collapse by Lenstra, *et al.*.

Figures 3.18 - 3.20 experimentally show the transition from the extremely stable operation achieved in Section 3.6 to the coherence collapsed state. Figures 3.18 and 3.19 are a continuation of the survey of Sections 3.3 through 3.6, incorporating the same CSP laser operating at $1.7 I_{th}$ in an external cavity of 40 cm. At -43 dB (a power coupling ratio slightly higher than in Figure 3.16) secondary peaks are observed in the Fabry-Perot spectrum separated from the carrier by the relaxation oscillation frequency and its second harmonic. Their presence indicates intensity self-pulsations in the time domain. The FSR is 2 GHz in the figure; hence, the sidebands have been wrapped around from another order of the Fabry-Perot. A hysteretic tuning trajectory still persists, while tuning extremes have increased, as predicted by equation (3.1.7). The damping of the oscillations is seen to be dependent upon the coupling phase, where lower frequency modes appear to be better damped. This observation is

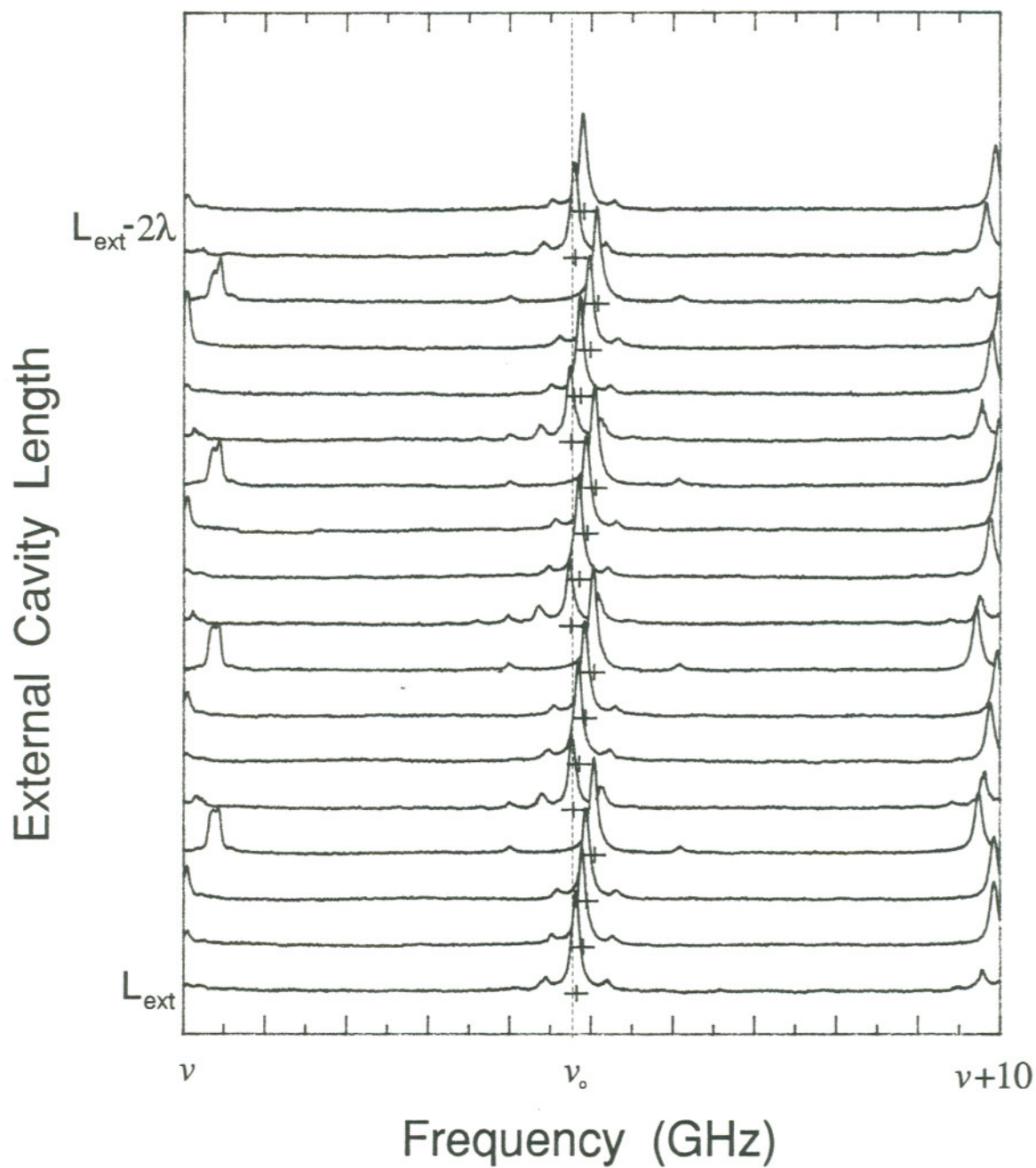


Figure 3.19 Experimental optical spectra demonstrating the transition to multiple external cavity mode operation during coherence collapse. HLP1400 CSP laser, -38 dB power coupling ratio, 40 cm external cavity.

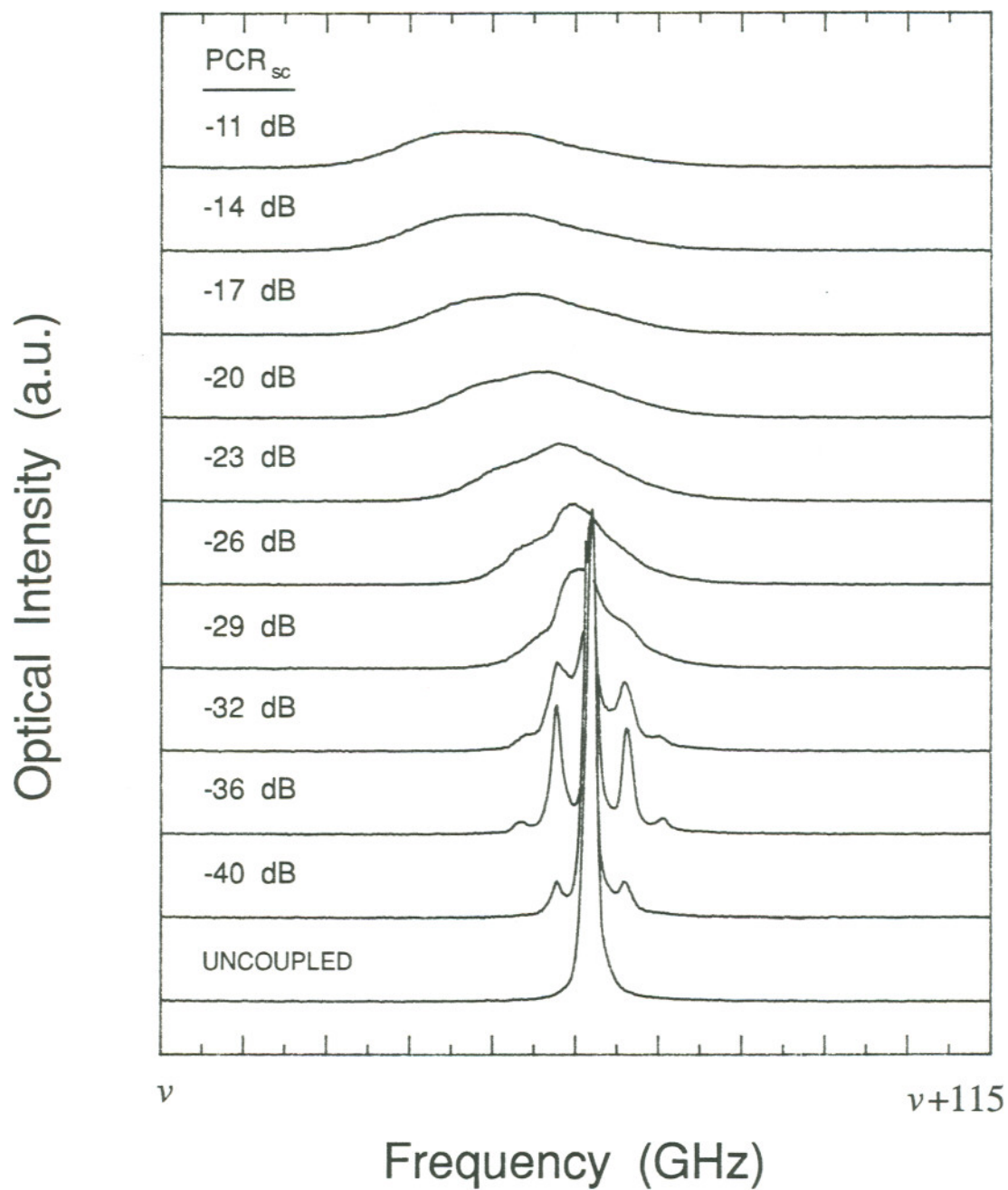


Figure 3.20 Experimental optical spectra during coherence collapse for an HLP1400 CSP laser diode in a 40 cm external cavity.

consistent with the discussion of damping in Section 2.4, noting that the low frequency and low threshold gain modes nearly coincide for large α .

Figure 3.19 shows the spectrum of the same laser at a power coupling ratio of about -38 dB, with the FSR increased to 10 GHz in order to avoid confusion due to wrap-around. The relaxation sidebands barely fit inside this FSR, and are slightly distorted due to a nonlinearity of the Fabry-Perot voltage ramp. Nevertheless, it is clear that the very stable single longitudinal mode behavior just prior to the appearance of relaxation oscillations has degraded. Several external cavity modes are found to run depending upon the cavity length piston, while the magnitude of the relaxation sidebands have now become relatively insensitive to $\omega_0\tau$ at this coupling level.

At larger coupling levels, the spectra become more and more complicated, with external cavity modes and relaxation sidebands filling in the entire FSR. It is therefore necessary to go to a larger FSR. Figure 3.20 shows the spectral collapse of the CSP laser with a FSR of 115 GHz. The relaxation sidebands and their harmonics are more clearly seen in this case. As the power coupling is increased, the self-pulsation of the system becomes more violent, as indicated by larger sidebands. The subsequent operation of many external cavity modes begins to fill in the spectrum and broaden it to over 20 GHz. This broadening corresponds to over 1000 times the natural linewidth of the laser. The center of the spectral envelope is observed to shift to lower frequencies well into the coherence collapse regime. The spectral collapse shown in Figure 3.20 was typical of all the lasers looked at, and further, was virtually unchanged for cavity lengths L_{ext} ranging from 10-100 cm.

Figure 3.21 displays a numerical simulation of the optical spectrum during coherence collapse corresponding to the experimental data of Figure 3.20. Numerical integration of the rate equations was performed using a variable-order, variable-step Gear method designed to handle systems of nonlinear, stiff, first order differential equations. The step size was chosen to be 10 ps, much smaller than the inverse of the highest expected frequency. Langevin noise sources were modeled as outlined in Appendix D. The dynamic variables were initially set to their stationary values. Integration then proceeded for several round trips of the external cavity (~ 10 ns) to insure all transients had died out before ~ 200 ns time series were collected of the electric field amplitude and phase. The spectral density function of the complex electric field amplitude was then obtained by a fast Fourier transformation (FFT). So that a direct comparison to the Fabry-Perot data of Figure 3.20 could be made, the spectral density was then convolved with a Lorentzian instrument function with FWHM corresponding to the first trace in Figure 3.20. The excellent agreement is clear. All important features observed in the experiment are recreated. Relaxation oscillations become undamped at approximately the expected power coupling ratio. Further, their relative peak heights match the experiment well.

The spectral asymmetry to the low frequency side, evident in the experimental data near -30 dB, is also duplicated. This asymmetry has also been seen in free-running semiconductor lasers²⁰² and was explained as correlated amplitude and phase noise fluctuations from spontaneous emission noise due to the carrier dependence of the refractive index. This implies that the reinjected light is becoming less coherent with the circulating field as dynamic instability worsens. The coherence collapsed state can therefore be likened to a laser

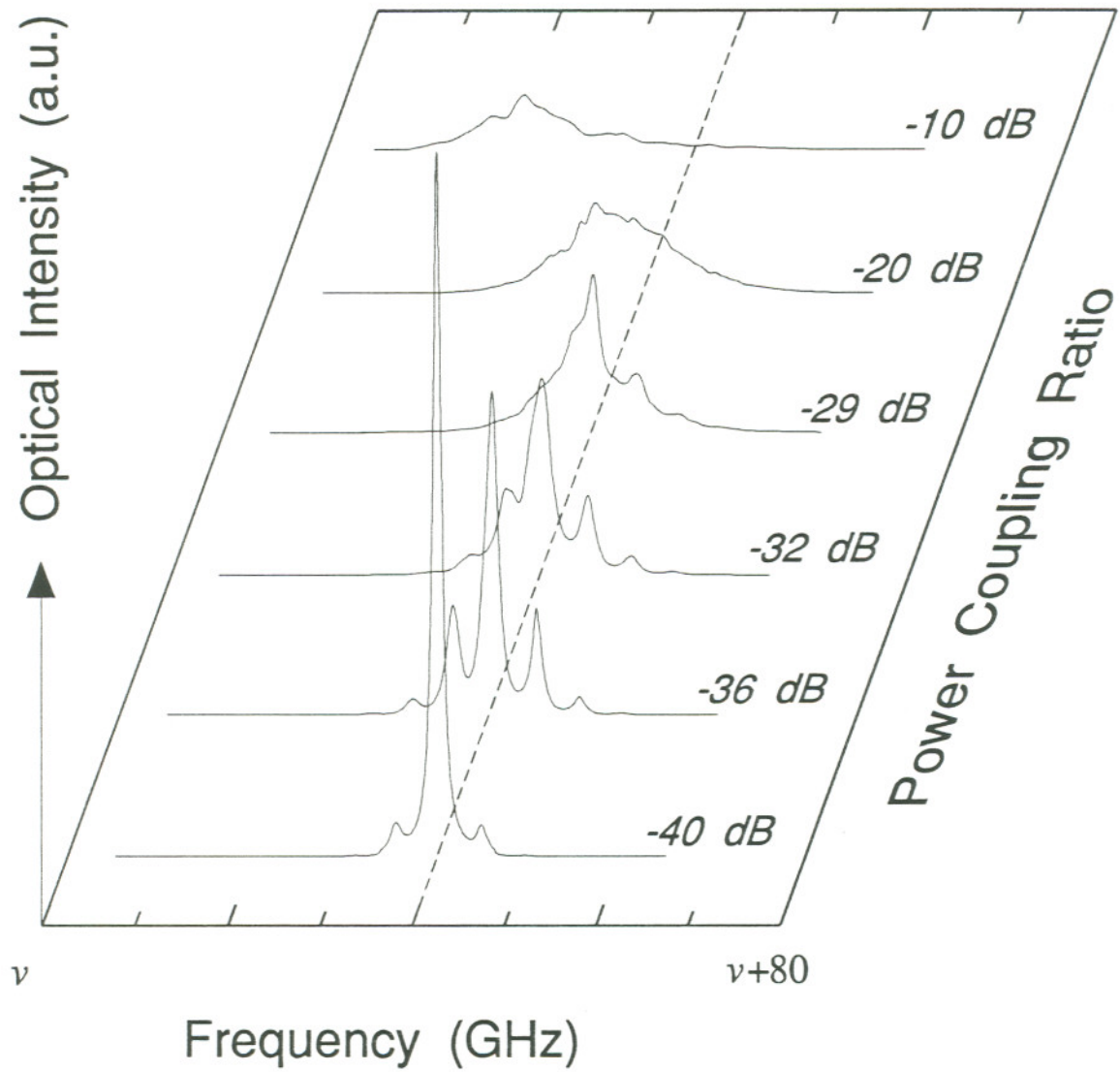


Figure 3.21 Numerically simulated optical spectra during coherence collapse, 40 cm cavity.

operating under the influence of an extremely large noise source. The partially coherent feedback viewpoint has been advocated by Olesen, *et al.*¹⁷³ to explain differences between their numerical simulations based on small signal versus full nonlinear forms of the self-coupled rate equations. A similar, though more extreme, approach has been used^{187,203,204} to describe coherence collapse for the case in which the coherence time, corresponding to the overall spectral width $1/\Delta\nu$, is much shorter than the round trip delay τ . The optical feedback is considered completely incoherent, and the delayed reinjected field is replaced by an external noise source with Gaussian correlation properties. This description does not address the origin of the coherence collapse, but simply assumes that the state already exists. Numerical simulations based on this theory have also nicely modeled gross spectral features, similar to those shown in Figure 3.20, between about -40 and -20 dB power coupling ratio²⁰⁵. The strong pulling of the spectrum to lower frequencies above -20 dB, however, is not predicted in this model. It is later shown that the pulling behavior is related to a partial recovery of coherence as the system transitions to a decidedly different operating regime.

A closer examination of the numerical simulations in Figure 3.21, without convolving with the instrument function, reveals that the spectral envelopes actually consist of a large number of external cavity modes separated, for the 40 cm cavity, by 375 MHz. Figure 3.22 shows relative intensity noise (RIN) spectra, defined by¹³²

$$RIN(\omega) = \frac{2\Delta\nu S_{\delta P}(\omega)}{\langle P \rangle^2}, \quad (3.7.1)$$

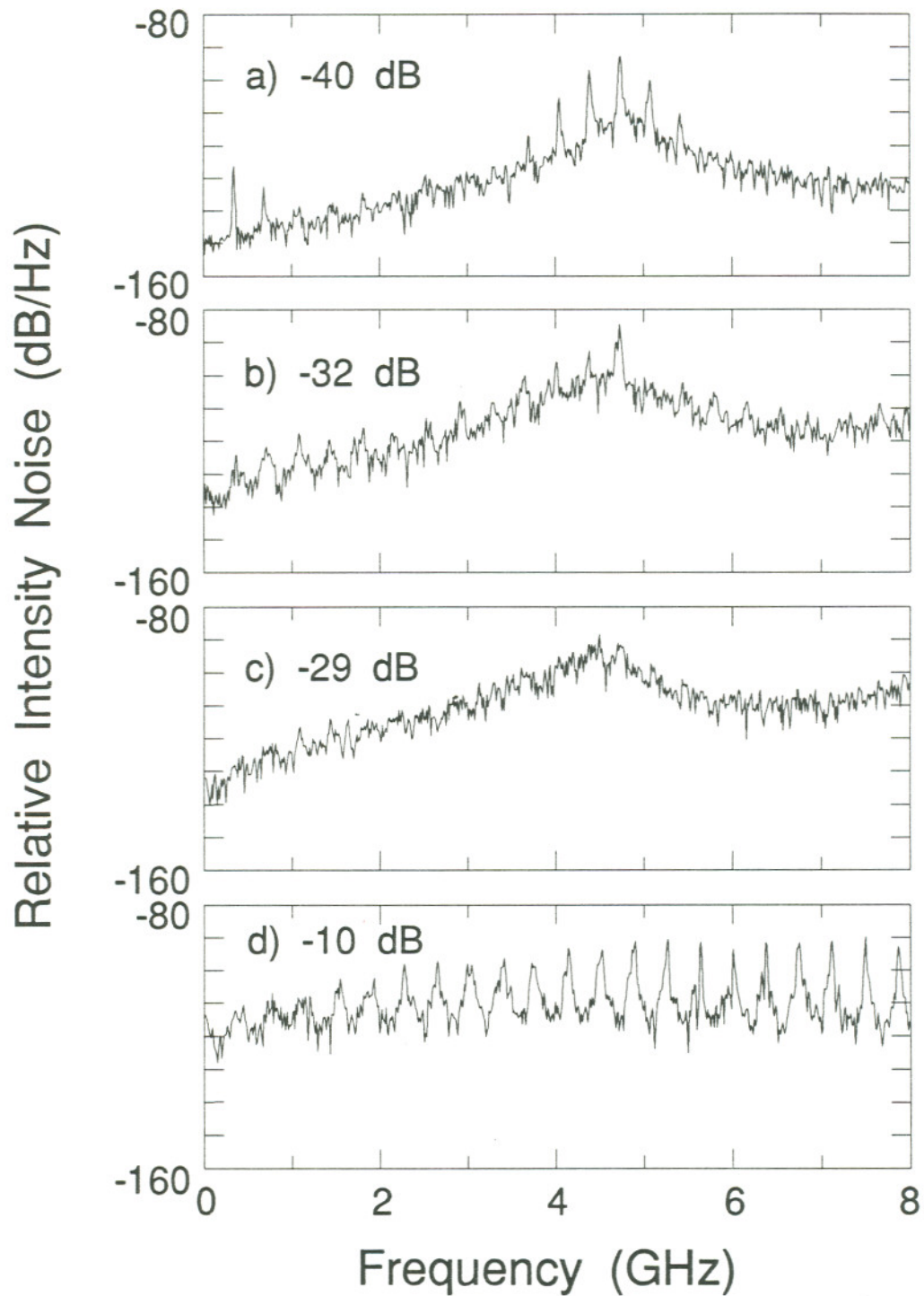


Figure 3.22 Numerical simulations of relative intensity noise during coherence collapse for a HLP1400 CSP laser in a 40 cm external cavity.

as a function of power coupling ratio during collapse. Here, $P(t) = \langle P \rangle + \delta P(t)$ is the time-varying optical power output of the laser, $\langle P \rangle$ is its average value, and $S_{\delta P}(\omega)$ is the spectral density function of the power fluctuations $\delta P(t)$. External cavity modes are readily apparent in Figure 3.22 a) and b). As the coupling level is increased, however, the noise baseline rises, eventually engulfing all substructure at a power coupling ratio of about -30 dB. At this point, an incoherent injection model of the self-coupled laser is truly valid. Surprisingly, the noise level reduces above this point, revealing a broad spectrum of peaks separated by $c/2L_{ext}$, as shown in Figure 3.22 d). The coherence time corresponding to each external cavity mode is in fact longer than the coupling delay, indicating that the feedback is indeed *coherent*, even well into collapse. Similar external cavity mode substructure in the optical spectrum was reported in an early work²⁰⁶ for what appears to be a coherence collapsed state with an external fiber cavity of 7.5 km in length, clearly outside of the coherence length of the isolated laser, even with no feedback. It is evident that the coherent rate equation approach is valid well into the coherence collapse regime.

While it is difficult to experimentally resolve the external cavity modes in the optical spectra well into coherence collapse, their behavior is readily observed in the intensity power spectrum. Figure 3.23 displays experimental measurements of the intensity power spectrum at various power coupling ratios in the collapsed state. The external cavity is 25 cm in this case. Clearly, the signal level is too weak to see the entire noise spectrum shown in Figures 3.22. A sufficiently wide-band preamplifier was not available for the experiment. The noise baseline of the photodiode/spectrum analyzer combination therefore

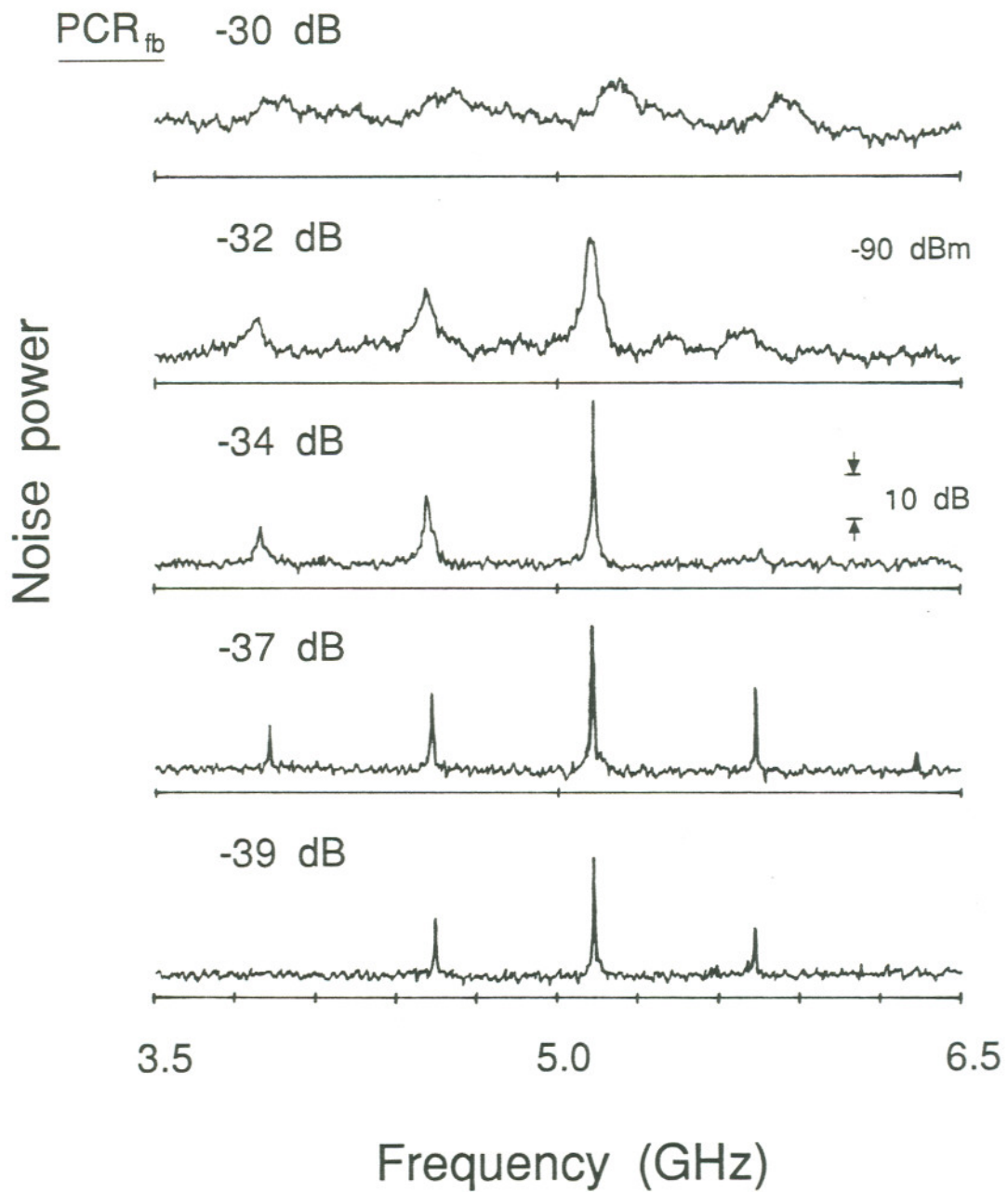


Figure 3.23 Experimental power spectra of the optical intensity during coherence collapse for a HLP1400 CSP laser diode in a 25 cm external cavity.

corresponds to a RIN of approximately -110 dB/Hz in Figure 3.22. Nevertheless, progressive spectral broadening and noise baseline increase is evident in the 3 GHz range shown about the relaxation resonance frequency.

Quite similar spectra were observed at a number of other cavity lengths, ranging from 20 to 100 cm. In contrast to the numerical simulations, the spectral filling continued past -30 dB, eventually resulting in a flat, noisy spectrum. This behavior was found to occur at nearly the same power coupling ratio for all cavity lengths investigated. Further examination proved the spectral broadening to be due to a rapid decrease in the mode suppression of the longitudinal *diode* modes. The longitudinal diode mode spectrum in the coherence collapse regime as a function of power coupling ratio is later shown in Figure 3.25 b) for a 40 cm cavity. The possibility of multiple diode mode operation was not accounted for in the single mode rate equation simulations.

An effort was made to study the intensity spectrum of the self-coupled laser during coherence collapse with a streak camera, which affords a much larger bandwidth than a typical spectrum analyzer. The signal-to-noise ratio at the experimentally available light levels, however, was insufficient to follow the laser's temporal dynamics. The dynamic operation of the undamped diode longitudinal modes, on the other hand, was found to occur on a much longer time scale, and was able to be studied in the time domain using the streak camera and spectrometer combination shown in Figure 3.24. The exit slit of the spectrometer was imaged onto the entrance slit of the streak camera by lens (L2). A cylindrical lens (CL) was used to increase the light throughput to the streak camera by compressing the image perpendicular to the slit. The external cavity setup remained unchanged. Modes were found to hop on a relatively

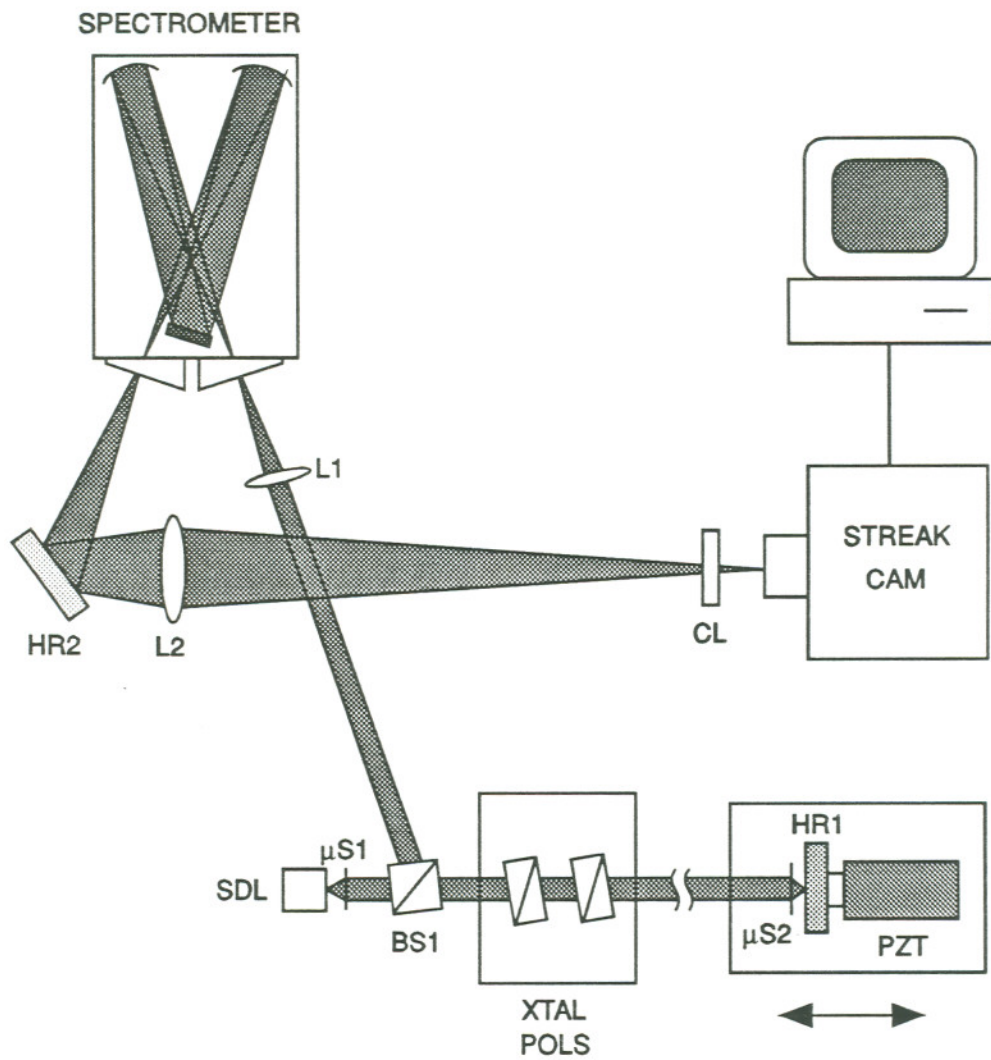


Figure 3.24 Experimental setup to observe longitudinal diode mode hopping.

long ($\sim \mu\text{s}$) time scale. A typical hopping pattern is displayed in Figure 3.25 for a -26 dB power coupling ratio and 40 cm cavity length. It is likely that the external cavity modes within each diode mode are also hopping during collapse. This would also account for the lack of a strong beat note at the fundamental cavity mode spacing frequency.

In Section 2.4, it was shown that the small signal stability properties of a self-coupled laser with little or no coupling delay are nearly identical to an isolated laser. The coupling merely shifts the frequency and damping rate of relaxation oscillations. Based on the preceding experimental data and numerical simulations, however, a coupling delay appears to radically change this previously stable operation. Small signal stability can be extended to include time delays by proceeding, in the same fashion as Section 2.4, from equations (3.1.1), (3.1.2) and (2.3.8)^{172,207}. The secular equation (2.4.8), in this case, is given by

$$\begin{aligned}
 & s^3 + s^2 \left(2\eta\cos\omega_L\tau(1 - e^{-\hat{\tau}s}) + 2\gamma \right) \\
 & + s \left(\Omega_R^2 + \eta^2(1 - e^{-\hat{\tau}s})^2 + 4\gamma\eta\cos\omega_L\tau(1 - e^{-\hat{\tau}s}) \right) \\
 & + \Omega_R^2\eta\sqrt{1+\alpha^2}(1 - e^{-\hat{\tau}s})\cos(\omega_L\tau + \tan^{-1}\alpha) + 2\gamma\eta^2(1 - e^{-\hat{\tau}s})^2 = 0, \quad (3.7.2)
 \end{aligned}$$

where Ω_R and γ are defined by (2.4.14). Coupling delays are plainly incorporated in the exponential terms of (3.7.2). When $\hat{\tau}$ goes to zero, the characteristic equation simplifies to (2.4.12), indicating unconditionally stable operation.

Unfortunately, stability boundaries cannot be determined from the Hurwitz criterion, since equation (3.7.2) is not a polynomial in s as a result of the cou-

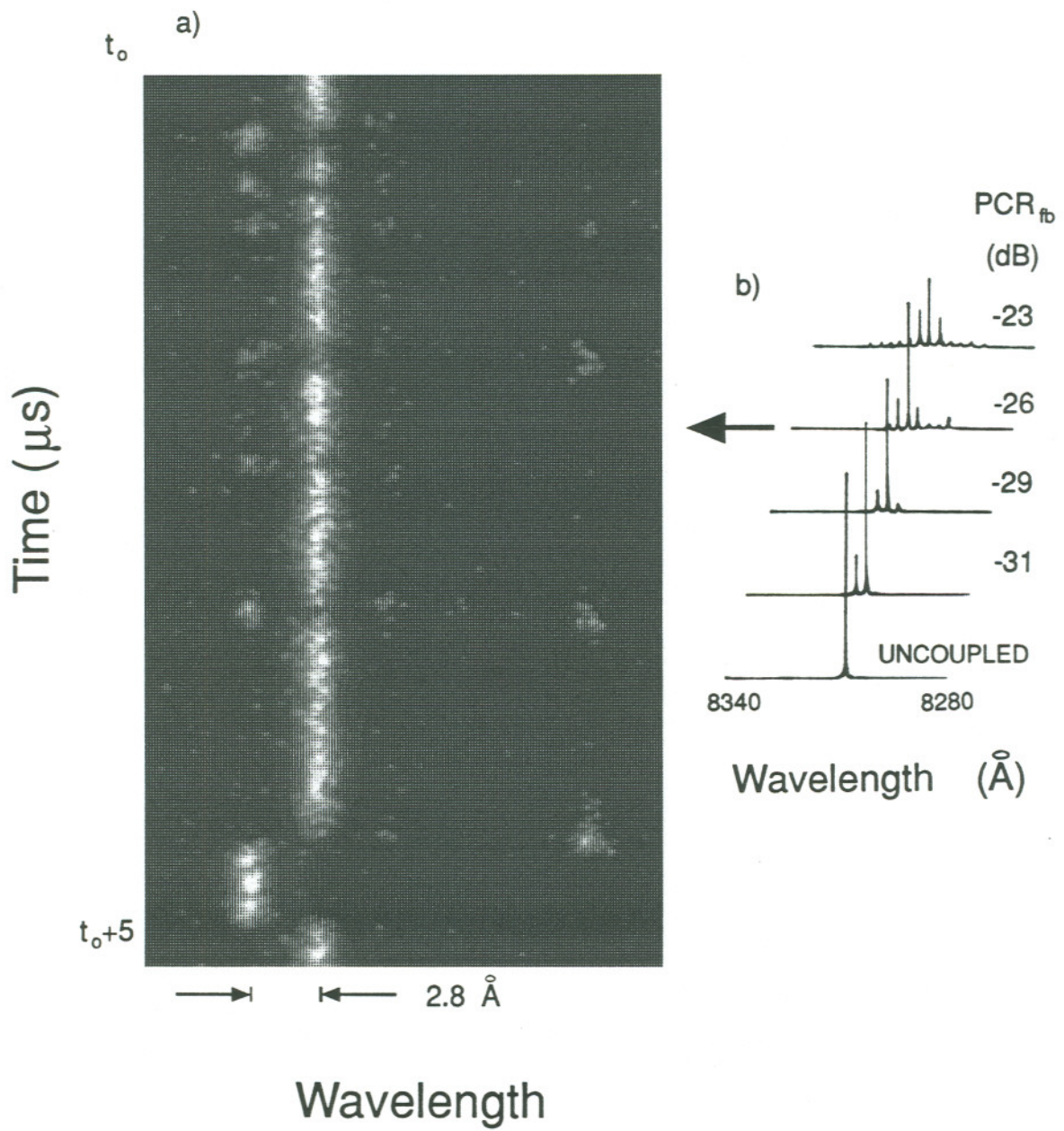


Figure 3.25 Longitudinal diode modes during coherence collapse. a) Mode spectrum, b) Typical mode hopping behavior at a -26 dB power coupling ratio.

pling delay. Furthermore, the delay terms make numerical evaluation of the eigenvalues s impossible using standard QL or QR algorithms¹⁶⁸. Some understanding of the stability properties, however, can be acquired for small η . By definition, the stability limit is reached when s crosses into the right half of the complex plane. Therefore, at a given coupling delay $\hat{\tau}$, the stability boundaries can be located by substituting $s = i\Omega$ into (3.7.2). Neglecting terms second order in η and γ , the imaginary part of (3.7.2) leads to

$$\Omega^2 - \Omega_R^2 = 2\Omega\gamma\cot\left(\frac{\Omega\hat{\tau}}{2}\right), \quad (3.7.3)$$

which is valid for $\eta \lesssim 10^{-2}$. (3.7.3) is an expression for the resonant frequency Ω of an unstable root, given a coupling delay τ . This frequency is near the relaxation resonance $\Omega_R \approx \omega_R\tau_p$, and is independent of the coupling phase, as was the case in Figure 2.7.

Ω is plotted as a function of L_{ext} in Figure 3.26 using parameters measured for the experimental CSP laser diode, listed in Table E.1. Note that an infinite number of solutions exist at a given τ . Dark solid lines indicate the resonances closest to the relaxation oscillation frequency, which are the first to become undamped with increasing power coupling. Physically, for a given coupling delay, this undamping will appear as an intensity self-pulsation in the output of the laser at the indicated frequency. Dashed lines indicate the resonance frequencies of the external cavity, $Nc/2L_{ext}$. Although advocated in the past²⁰⁸, it is clear that the resonant frequency of the system does not lock to a multiple of the external cavity, but attempts to maintain a value of Ω_R . In fact, for long external cavities, Ω is approximately equal to Ω_R at all τ .

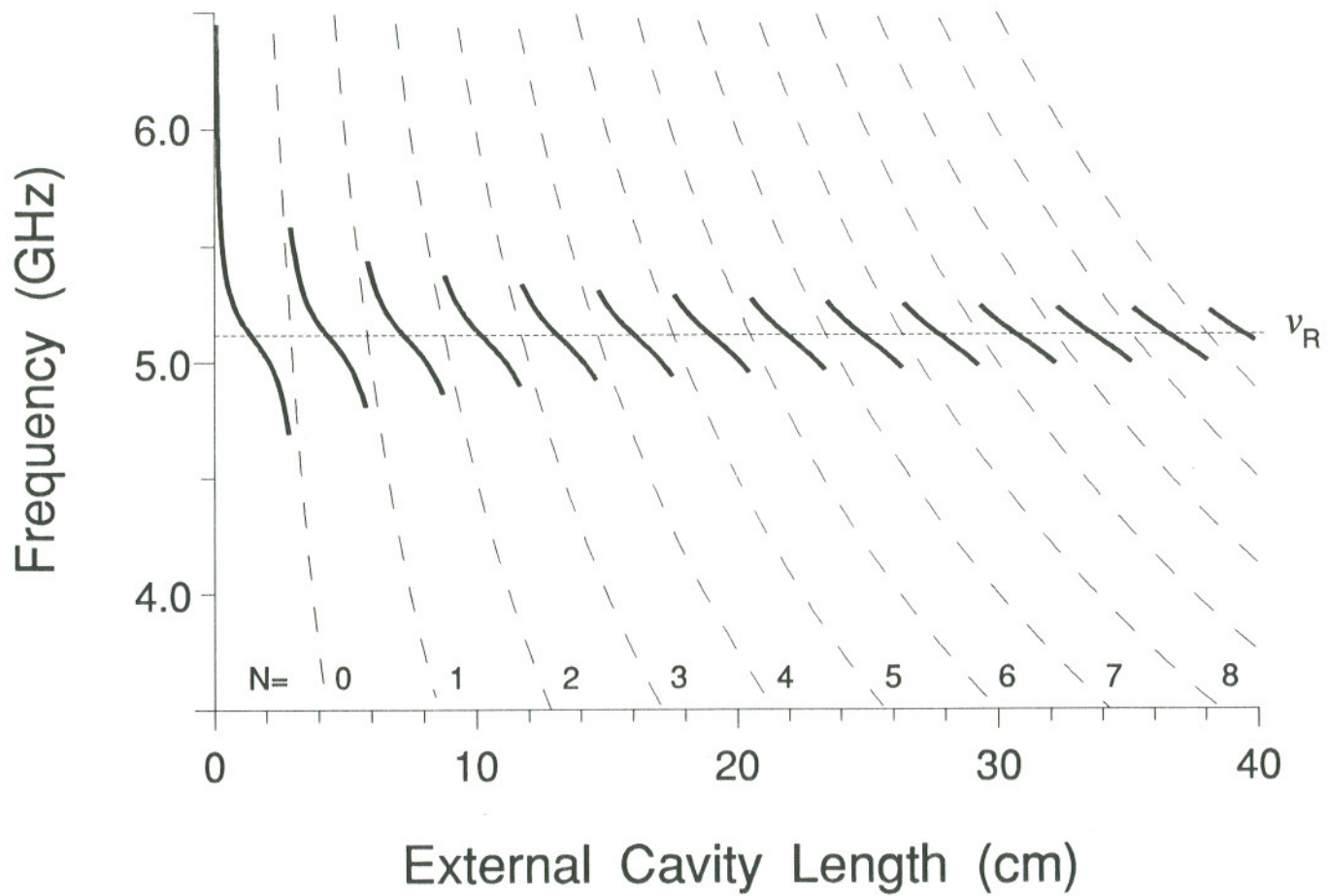


Figure 3.26 Resonances of a self-coupled HLP1400 CSP laser diode as a function of external cavity length (solid lines). Dotted lines denote external cavity modes.

The critical coupling level where a mode of the system becomes unstable can be determined from the real part of the secular equation (3.7.2), knowing Ω from (3.7.3). Figure 3.27 displays stability boundaries in the $\tilde{\eta}$ plane at four distinct coupling delay times, τ . Also depicted (dashed) is the $\Omega \neq 0$ stability boundary for the even mode of a mutually coupled CSP laser, similar to that shown in Figure 2.5. The boundary b), where $\tau\nu_R = 1$, is observed to follow the former quite closely, within the approximation on η . An examination of (3.7.2) reveals that these boundaries are identical whenever the inverse coupling delay $1/\tau$ is an odd multiple of the relaxation resonance frequency ν_R , and are approximately the same for $\tau\nu_R$ products larger than one. To the contrary, as τ approaches zero, (cases c) and d) in Figure 3.27) the region of stable operation is observed to grow rapidly, eventually encompassing the entire $\tilde{\eta}$ plane. Based on the results of Section 2.4, stability is expected to improve in the right-half $\tilde{\eta}$ plane for $\eta > 10^{-2}$, due to an increase in damping rate encountered there.

The limiting case of stability criterion (3.7.6) is also plotted in Figure 3.27 e) for $\hat{\tau} = 2\pi/\Omega_R$. Unstable operation exists in the region below this boundary in the figure. Since this instability boundary corresponds to $\Omega=0$, modes located in this region do not represent oscillating states of the self-coupled laser. The boundary moves outward from the origin as τ approaches zero, while for large τ , it effectively cuts the $\tilde{\eta}$ plane into stable and unstable halves. A crossing of this boundary with increasing η indicates the onset of multiple mode operation at a given $\omega_0\tau$.

It is clear from Figure 3.27 that the self-coupled laser will operate stably, regardless of the coupling phase, for sufficiently small η . When η becomes too large, however, the system may develop self-sustained relaxation oscillations.

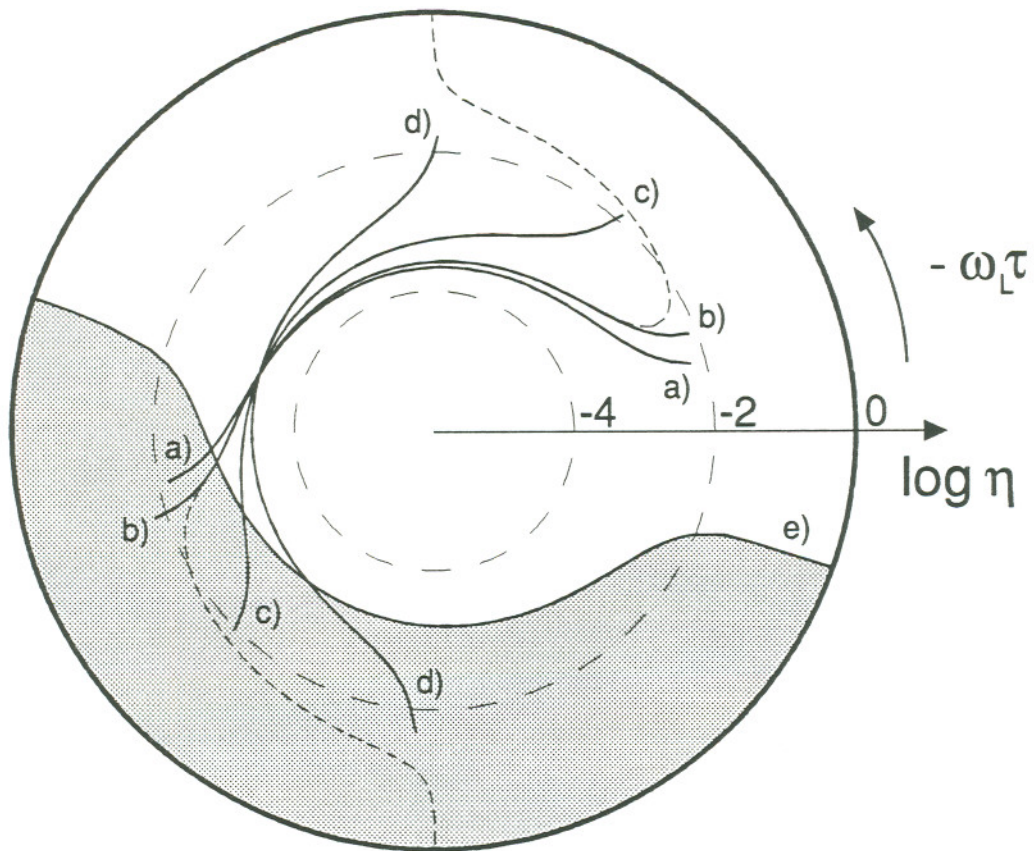


Figure 3.27 Stability boundaries for a self-coupled semiconductor laser diode. $\alpha = 3$, $\sigma = 1500$, $\Delta\rho = .67$.
 a) $\tau_R = 2.0$, b) $\tau_R = 1.0$, c) $\tau_R = .03$, d) $\tau_R = .001$,
 e) stability condition (3.5.6) for $\tau_R = 2.0$, shaded area is unstable.

The critical coupling level where this occurs depends not only on the values of τ and $\omega_0\tau$, but on the mode in which the system is currently operating. Note that any one (or more) of the available modes may penetrate the instability boundary at a given $\omega_0\tau$. The location of these modes in the $\tilde{\eta}$ plane will be discussed in Section 4.5. Figure 3.28 plots the lowest possible η where self-pulsation may occur versus the distance between the laser and retroreflector. It is notable that for long coupling delays the critical power coupling ratio is nearly independent of τ and is given approximately by (2.4.22). This result also approximately predicts the onset of coherence collapse²⁰⁹ measured in the preceding experiments. The coherence collapse instability is therefore initiated when a mode of the self-coupled system penetrates a stability boundary corresponding to undamped self-pulsation. Hence, relaxation oscillations observed experimentally at the start of coherence collapse appear to be the cause of, rather than a product of, the dynamic instability. Recall, for example, Figure 3.18, where relaxation oscillations were found to interrupt the extremely stable, narrow linewidth operation at a -45 dB power coupling ratio.

Expression (2.4.22) actually underestimates the coupling level for the onset of coherence collapse. In fact, a value of $\gamma = 6.6 \times 10^{-3}$ (about four times larger than that indicated by the parameters in Table E.1) was used to generate Figure 3.28, to match the -40 dB critical power coupling ratio observed experimentally. The discrepancy is attributable to gain compression, which was neglected in the small signal analysis. Gain compression significantly enhances the damping of relaxation oscillations, moving outward the stability boundaries a)-d) in Figure 3.27. Comparison between experiment and numerical integration of the full nonlinear rate equations (3.1.1) and (3.1.2) including gain

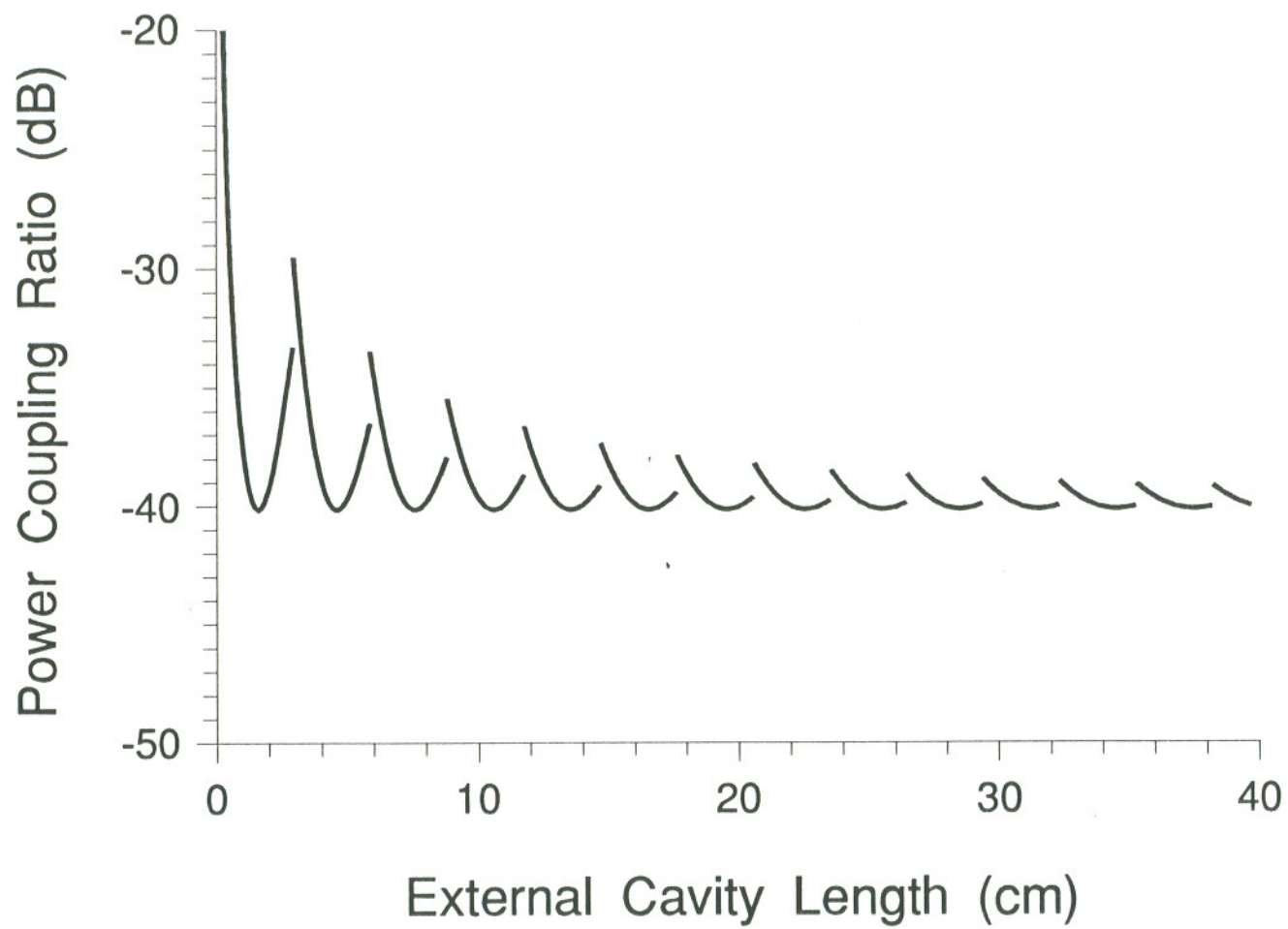


Figure 3.28 Critical power coupling ratio for the onset of self-pulsation at the relaxation resonance frequency of a self-coupled HLP1400 CSP laser diode.

compression was used to estimate the self-saturation coefficient. A value of $\beta_{oo} = 1.3 \times 10^{-8}$ was found to be appropriate. Given the measured parameters in Table E.1, this corresponds to a value of 0.6 W^{-1} with respect to the power output from the front facet, slightly lower than the 1 W^{-1} (or larger)¹⁷⁸ value typically used in numerical studies.

Figure 3.28 also shows that at small τ , where $\Omega_R \hat{\tau} \ll \pi$, extremely high coupling levels are required to undamp the relaxation resonance of the laser. It is not surprising, then, that numerical studies of short external cavity lasers have demonstrated that for cavity lengths below a few millimeters the system operates stably, without any coherence collapse^{210,211}. Indeed, semiconductor lasers are often coupled to very short external cavities to achieve dynamic single longitudinal mode stabilization²¹²⁻²¹⁵.

Physically, intensity self-pulsation is enabled by the proximity of the relaxation resonance frequency ω_R to a multiple of the fundamental external cavity mode frequency $1/\tau$. Its existence, however, is not sufficient to explain the severity of the instability. Coherence collapse is a large signal phenomenon, requiring the full nonlinear rate equations for its theoretical description. Schunk and Petermann¹⁷⁸ have performed a quite exhaustive numerical survey of the parameter dependencies of coherence collapse. Of particular interest is the absence of coherence collapse when $\alpha=0$, although equation (2.4.22) shows that the small signal instability boundary corresponding to sustained self-pulsation may still be exceeded, albeit at a higher coupling level. Other numerical simulations of the coherence collapse instability, with the isolated laser operating well above threshold, have indicated an extreme sensitivity of the rate equations to initial conditions²¹⁶ and abrupt transitions from stable to unstable

operation¹⁷³ in which noise was found to play no important role, prime indicators of chaos.

Judging from the routes to chaos identified in the previously referenced studies of LFFs, with the isolated laser operating very near or below its threshold, it is probable that the coherence collapse instability is also a form of optical chaos. However, while the optical and intensity spectra in Figures 3.18 - 3.23 indeed became complicated as the coupling level was increased, no route to chaos could be determined. This was true of all cavity lengths considered. Similar intensity noise spectra have been reported for DBR lasers²¹⁷. Recently, a quasiperiodic route was demonstrated^{218,219} in the specific case where the resonance frequency of the laser was an integer multiple of the external cavity fundamental frequency. Here, two system resonances, shown in Figure 3.26, are equidistant from ν_R and therefore have equal amplitudes. Competition between these modes was regarded as the mechanism leading to chaos. This is by no means generally true, however, since most often a single relaxation resonance peak is dominant.

4. MUTUAL COUPLING

This chapter experimentally analyzes the operation of a mutually coupled pair of semiconductor diode lasers. In Chapter 2, it was demonstrated that, given a set of material constants characterizing a specific gain medium, the primary parameter governing the stability properties of two coupled lasers is the cross-coupling coefficient. It is therefore desirable to exercise precise control over the magnitude and phase of the coupling coefficient experimentally, so that stable and unstable regions of operation predicted by theory can be verified. This can be a difficult, if not impossible, proposition employing the coupling techniques referred to in the introduction²²⁰. In the present case, however, mutual coupling is accomplished axially between two individual Fabry-Perot diode lasers, via conventional optics. Such a scheme has been considered previously^{221, 222}, and incorporates several advantages.

The magnitude of the optical interaction, in this configuration, is controlled simply by introducing attenuation between the lasers, while the coupling phase is controlled by varying the separation of the lasers in fractions of the emitting wavelength. Both parameters are therefore continuously variable, but more importantly, can be adjusted independently. As discussed in Appendix B, this allows for quite accurate quantification of the coupling coefficient for comparison to theory.

By coupling at a distance, however, additional longitudinal modes are introduced into the system, associated with the cavity formed between the lasers. Oscillators coupled at a distance have been treated theoretically by Dente *et. al.*²²², based on a steady-state spectral domain model. Multiple longitudinal mode operation was identified as the mechanism responsible for a degradation of phase-locking observed experimentally above a limiting coupling strength in semiconductor lasers. Coupling delays have also been cited in a microwave system of mutually coupled relativistic magnetrons²²³ as a source of instability. Since coupling paths many wavelengths long are often unavoidable, the associated delay could represent a potential limitation of phase-locking. This phenomenon certainly deserves further investigation.

This chapter is divided into four parts. Section 4.1 develops the theoretical framework necessary to model the experiment. These results follow directly from Chapter 2. The experimental arrangement is discussed in Section 4.2. Spectral and coherence measurements are then presented for resonant and non-resonant lasers and compared to theory in Sections 4.3 and 4.4, respectively. Finally, dynamic instability is shown to develop at moderate coupling levels. Its origins and parameter dependencies are studied via numerical simulations from the coupled rate equations.

4.1 Delayed Mutual Coupling

In modeling the experimental results which follow, rate equations (2.3.6)-(2.3.7) describing mutual coupling, with cross-coupling coefficient (2.5.19),

become

$$\begin{aligned} \dot{e}_j(\hat{t}) = & \frac{1}{2} \left((2\Delta n_j(\hat{t}) + 1)G_{Pj} - 1 \right) e_j(\hat{t}) + \frac{r_{sp}}{2e_j(\hat{t})} + F_{e_j}(\hat{t}) \\ & + \eta e_k(\hat{t} - \hat{\tau}) \cos(\tau_p \omega_{ok} \hat{\tau} + \tau_p \Delta \omega_{ok} \hat{t} + \phi_j(\hat{t}) - \phi_k(\hat{t} - \hat{\tau})) \end{aligned} \quad (4.1.1)$$

$$\begin{aligned} \dot{\phi}_j(\hat{t}) = & \alpha \Delta n_j(\hat{t}) + F_{\phi_j}(\hat{t}) \\ & - \eta \frac{e_k(\hat{t} - \hat{\tau})}{e_j(\hat{t})} \sin(\tau_p \omega_{ok} \hat{\tau} + \tau_p \Delta \omega_{ok} \hat{t} + \phi_j(\hat{t}) - \phi_k(\hat{t} - \hat{\tau})) \end{aligned} \quad (4.1.2)$$

$$j \neq k = 1, 2.$$

Rate equations (2.3.8), for $\overline{\Delta n}$ in each laser, remain appropriate as written. Single-pass cross-coupling, assumed in the derivation of (2.5.19), is also suitable here since experimentally the maximum power transmission through the coupling junction was $\epsilon_T^2 \sim 0.1$, much less than one. Self-coupling is therefore at least one order of magnitude smaller than cross-coupling, as it requires two passes of the junction, and has been neglected above. η is to be interpreted as the cross-coupling coefficient throughout this chapter, while the normalized coupling delay $\hat{\tau} = \tau/\tau_p$ now reflects the time accrued in a single pass between the lasers. Coupling is taken to be symmetric, $\tilde{\eta}_{jk} = \tilde{\eta}_{kj} = \tilde{\eta}$, as nearly identical lasers were used in the experiments. Reduced Langevin sources $F_{x_j}(\hat{t})$, associated with the dynamic variable x , were added in (4.1.1) and (4.1.2) to model the effect of spontaneous emission noise.

4.1.1 Steady-State Operation

With (2.5.24), the stationary equations (2.3.20), (2.3.16) and (2.3.19) respectively become

$$\frac{\Delta\bar{\rho}_j - \bar{e}_j^2}{1 + 2\bar{e}_j^2} = -\eta \frac{\bar{e}_k}{\bar{e}_j} \cos(\Delta\phi_{Lj} - \omega_L \tau) \quad (4.1.3)$$

$$j \neq k = 1, 2.$$

$$\begin{aligned} \tau_p \Delta\omega_o &= \eta \sqrt{1+\alpha^2} \left(\frac{\bar{e}_k}{\bar{e}_j} + \frac{\bar{e}_j}{\bar{e}_k} \right) \sin\Delta\phi_L \cos(\omega_L \tau + \tan^{-1}\alpha) \\ &\quad - \eta \sqrt{1+\alpha^2} \left(\frac{\bar{e}_k}{\bar{e}_j} - \frac{\bar{e}_j}{\bar{e}_k} \right) \cos\Delta\phi_L \sin(\omega_L \tau + \tan^{-1}\alpha) \end{aligned} \quad (4.1.4)$$

$$\begin{aligned} 2\tau_p \Delta\omega_L &= \eta \sqrt{1+\alpha^2} \left(\frac{\bar{e}_k}{\bar{e}_j} - \frac{\bar{e}_j}{\bar{e}_k} \right) \sin\Delta\phi_L \cos(\omega_L \tau + \tan^{-1}\alpha) \\ &\quad - \eta \sqrt{1+\alpha^2} \left(\frac{\bar{e}_k}{\bar{e}_j} + \frac{\bar{e}_j}{\bar{e}_k} \right) \cos\Delta\phi_L \sin(\omega_L \tau + \tan^{-1}\alpha) \end{aligned} \quad (4.1.5)$$

Recall that $\Delta\phi_{Lj} = -\Delta\phi_{Lk} \equiv \Delta\phi_L$, and that the locked frequency shift $\Delta\omega_L$ is referenced to the average uncoupled frequency through (2.3.17). As shown in Section 2.3, the preceding equations generally require numerical solution to obtain $\bar{e}_{j,k}$, $\Delta\omega_L$ and $\Delta\phi_L$ given the parameters η , $\Delta\omega_o$, α , τ_p and τ . In the present case, however, their solution has become more complicated due to the frequency dependence of the coupling phase. This results in a possibility for

additional longitudinal modes associated with both the symmetric and asymmetric solutions.

(4.1.3)-(4.1.5) can be simplified, for $\eta \leq 0.1$, by approximating that $\bar{e}_j \approx \bar{e}_k$. This implicitly assumes that the lasers are equally pumped. All information about phase-locking is therefore contained in the two equations

$$\Delta\omega_o = 2\kappa\sqrt{1+\alpha^2}\sin\Delta\phi_L\cos(\omega_L\tau + \tan^{-1}\alpha) \quad (4.1.6)$$

$$\Delta\omega_L = -\kappa\sqrt{1+\alpha^2}\cos\Delta\phi_L\sin(\omega_L\tau + \tan^{-1}\alpha), \quad (4.1.7)$$

where $\bar{\kappa} = \bar{\eta}/\tau_p$. These equations can be simultaneously solved for the unknowns $\Delta\omega_L$ and $\Delta\phi_L$. Numerical solutions are pursued later in comparison to experiment.

When the lasers are resonantly tuned, (i.e. their free-running oscillation frequencies are identical so that $\Delta\omega_o = 0$), the locked phase difference between the lasers $\Delta\phi_L$ must assume a value of 0 or π so that (4.1.6) is satisfied at all τ . These values correspond to the even and odd modes discussed in Section 2.3. Modes are then found from

$$\Delta\omega_L\tau = \pm \kappa\tau\sqrt{1+\alpha^2}\sin(\bar{\omega}_o\tau + \Delta\omega_L\tau + \tan^{-1}\alpha), \quad (4.1.8)$$

which is nearly identical in form to the frequency determining equation (3.1.5) for self-coupling. The (-) sign denotes symmetric solutions, while (+) is for asymmetric. As in the self-coupled case, multiple modes associated with both the even and odd solutions may occur, at a given $\bar{\omega}_o\tau$, for κ satisfying (3.1.9). It is important to note the distinction between the cross-coupling phase

$\psi_{cc} = -\omega_L \tau$ and the phase "piston" term $\bar{\omega}_o \tau$, which is determined by the coupling delay. Although multiple roots can exist at a given $\bar{\omega}_o \tau$, each root is associated with a unique coupling phase ψ_{cc} . This is later shown to have a significant impact on the stability properties and mode selection of the mutually coupled system.

As the lasers are detuned, the locked phase difference compensates up to a point which defines the lockband, as described in Section 2.3. The locking range in the delayed coupling case, however, is a complicated function of the coupling delay, τ . Further, it depends on which mode the system occupies. The maximum allowable detuning, on the other hand, is clearly

$$|\Delta\omega_{o,max}| \leq 2\kappa \sqrt{1+\alpha^2} \quad (4.1.9)$$

from (4.1.6), in agreement with (2.3.22).

4.1.2 Stability

There are at least two solutions to equations (4.1.6) and (4.1.7) at a given coupling delay time τ , with the possibility for several more when the $\kappa\tau$ product becomes much larger than one. Many of these modes, however, can be ignored since they do not represent dynamically stable states. It is therefore desirable to obtain a stability criterion, similar to (3.5.6), for two mutually coupled lasers. Stability can be addressed, where relaxation oscillations are well damped, from the Adler-like phase equation (F.2). In the present case, using (2.5.19) and neglecting self-coupling, (F.2) becomes

$$\dot{\phi}_j(t) = \kappa \sqrt{1+\alpha^2} \sin[\Delta\omega_o t - \omega_{ok}\tau + \phi_k(t-\tau) - \phi_j(t) - \tan^{-1}\alpha], \quad (4.1.10)$$

where again $\bar{e}_j = \bar{e}_k$ is assumed. Writing the phase of laser j with respect to the phase-locked steady-state given by (2.3.11)

$$\phi_j(t) = (\omega_L - \omega_{oj})t + \phi_{Lj} + \delta\phi_j(t), \quad (4.1.11)$$

equation (4.1.10) can be rewritten as

$$\delta\dot{\phi}_j(t) = \kappa \sqrt{1+\alpha^2} \cos(\omega_L\tau - \Delta\phi_{Lj} + \tan^{-1}\alpha) \cdot [\delta\phi_k(t-\tau) - \delta\phi_j(t)]. \quad (4.1.12)$$

It has been assumed that the phase fluctuations $\delta\phi_{j,k}(t)$, due to spontaneous emission noise, are much smaller than π . Note that there are two equations above, one for each laser j, k . Defining the coefficients

$$C_j \equiv \kappa\tau \sqrt{1+\alpha^2} \cos[\omega_L\tau - \Delta\phi_{Lj} + \tan^{-1}\alpha], \quad (4.1.13)$$

the equations (4.1.12) are

$$\delta\dot{\phi}_j(t) = C_j [\delta\phi_k(t-\tau) - \delta\phi_j(t)]/\tau \quad (4.1.14)$$

$$\delta\dot{\phi}_k(t) = C_k [\delta\phi_j(t-\tau) - \delta\phi_k(t)]/\tau. \quad (4.1.15)$$

To test stability, solutions of the form

$$\delta\phi_j(t) = \delta\phi_{j0} e^{st}, \quad \delta\phi_k(t) = \delta\phi_{k0} e^{st} \quad (4.1.16)$$

are assumed. Substituting into equations (4.1.14) and (4.1.15) leaves

$$s\tau\delta\phi_{j0} = C_j [\delta\phi_{k0} e^{-s\tau} - \delta\phi_{j0}] \quad (4.1.17)$$

$$s\tau\delta\phi_{k0} = C_k [\delta\phi_{j0} e^{-s\tau} - \delta\phi_{k0}]. \quad (4.1.18)$$

This system of linear simultaneous equations can be solved for non-trivial values of s by requiring that the determinant of the coefficients of $\delta\phi_{j_0, k_0}$ is zero. This results in the characteristic equation

$$C_j C_k e^{-2z} = (C_j + x)(C_k + x), \quad (4.1.19)$$

where $x \equiv s\tau$. Stability requires that $x < 0$, so that perturbations damp exponentially. $x=0$ is always a root. In general, a mode can be evaluated for stability by first solving equations (4.1.6) and (4.1.7) for the locked frequency and phase difference at a given $\bar{\omega}_o\tau$, coupling level κ and detuning $\Delta\omega_o$. This fixes the values of $C_{j,k}$. Equation (4.1.19) can then be solved numerically for the eigenvalue s , and stability checked. This procedure was used in the simulations which follow.

An important case is where the lasers are resonant, $\Delta\omega_o=0$. Here, equation (4.1.19) can be rewritten as

$$-C^2(1 - e^{-2z}) = x^2 + 2xC, \quad (4.1.20)$$

where $C_{j,k} \equiv C$. The left (solid line) and right-hand (dashed) sides of (4.1.20) are plotted in Figure 4.1. The coefficient C can be positive or negative; both cases are displayed in the figure. It is clear that no root can exist in the right half plane for $C > 0$, while the opposite is true for $C < 0$. The stability criterion is therefore

$$\cos\Delta\phi_L \cos(\omega_L\tau + \tan^{-1}\alpha) > 0, \quad (4.1.21)$$

where $\Delta\phi_L$ can assume the values 0 or π , for the even and odd modes, respectively. (4.1.21) is an approximate formulation of the stability criterion (2.4.19),

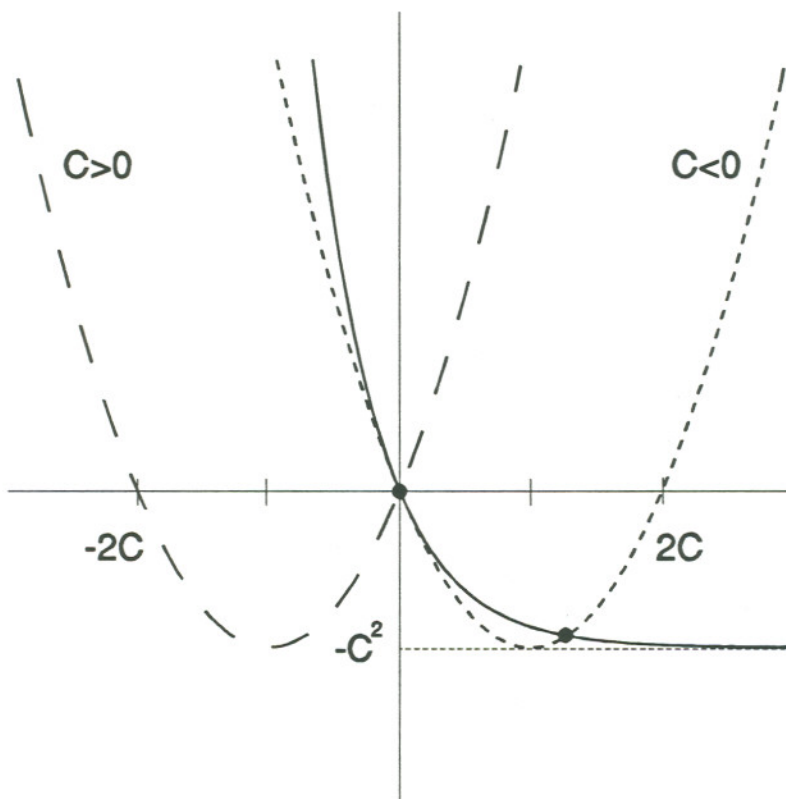


Figure 4.1 Graphical solution of stability criterion (4.1.20).

developed for no coupling delay. It divides the $\bar{\eta}$ plane into complimentary stable and unstable halves for the even and odd modes, as did (2.4.19), but doesn't predict the narrow, stable areas at very large η shown in Figure 2.5. Note that $\text{Im}[s]=0$ here, so that trajectories in phase space in the vicinity of an unstable equilibrium are directed outward radially. Therefore, these modes will never appear experimentally. As in self-coupling, modes which do not meet the stability criterion (4.1.21) have coupling phases which force destructive interference between the two lasing fields in order to meet the round trip 2π phase condition in the compound cavity.

4.2 Experiment

The semiconductor lasers used to investigate mutual coupling at a distance were the same types described in the self-coupling experiments of Section 3.2. Again, the reader is referred to Appendix E for information regarding the operating characteristics of the devices. In order for phase-locking to occur, it is required that the free-running oscillation frequencies of the lasers match to within the locking range given by (2.3.22). Furthermore, it was desired to arbitrarily adjust the initial detuning while maintaining approximately constant output powers. Therefore, some mechanism for individually tuning the lasers was necessary.

Fortunately, the operating frequency of a semiconductor laser above threshold can be tuned through the temperature dependence of the refractive index^{224, 225}. This is accomplished in two ways. First, the temperature in the

active layer of the diode laser could be changed several degrees by heating or cooling the entire laser, heatsink and submount. Since typical tuning rates of $\sim 0.5 \text{ \AA}^\circ\text{C}$ were observed in these lasers, initial wavelength differences of no more than about one longitudinal mode spacing ($\sim 3 \text{ \AA}$) could be tolerated. At a given output power, however, the variation in operating frequency of a batch of CSP and TJS lasers was found to extend over a range several times larger. Acquiring two suitable semiconductor lasers proved difficult for this reason.

Fine adjustment of the lasing frequency could also be induced through small variations of the injection current, changing the local temperature near the active region, primarily due to ohmic heating. Another contributing mechanism might be changes in temperature associated with optical absorption and scattering, since the circulating power is linearly dependent on the injection current. A typical -6.5 GHz/mA tuning rate was experimentally measured for the $300 \text{ }\mu\text{m}$ long ML5101a TJS lasers. Tuning with injection current proved to be advantageous for varying the relative detuning between the lasers within the lockband. For changes in current of $\sim 1 \text{ mA}$, the output power variations were small.

Temperature tuning and frequency stability were accomplished using thermoelectric coolers sandwiched between brass heat sinks, on one of which the laser was mounted. This mechanical arrangement is shown in Figure 4.2. A thermistor was attached very near the laser to sense temperature variations. Its resistance was compared to a standard in a bridge configuration, where op-amp circuitry and power drivers controlled the current directed to the thermoelectric elements. The experimental setup was heavily insulated to reduce thermal variations, especially in the heat sinks upon which the lasers were attached. Time

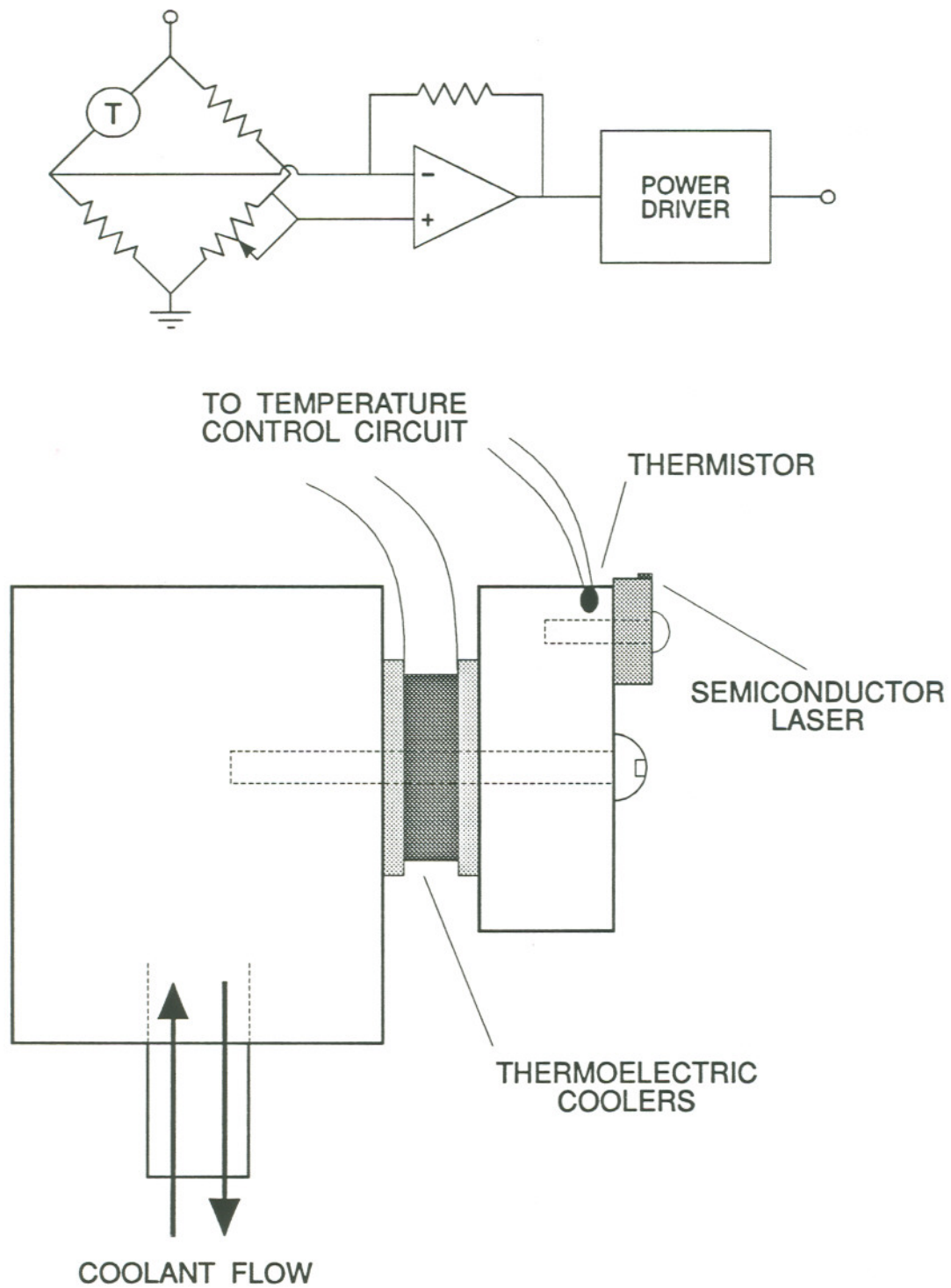


Figure 4.2 Experimental arrangement employed to control the temperature of the semiconductor laser diodes.

constants associated with "cycling" of the temperature control circuitry were thereby reduced in amplitude and lengthened in period to approximately one minute. This allowed an adequate window over which data could be taken without large frequency drift. Maximum frequency drift over long periods of time was measured at about ± 25 MHz. The heatsink temperature, using this scheme, was variable by approximately $\pm 10^\circ$ C about room temperature. A fairly large temperature difference between the lasers could then be maintained if one was heated above room temperature and the other was cooled. However, room temperature variations then affected each laser in the opposite sense, enhancing drifts. Cooling or heating both lasers by different amounts was the preferred method of temperature tuning.

The optical experimental arrangement for mutual coupling is shown in Figure 4.3. After a lengthy search, a few usable pairs of diode lasers (DL1,2) were found. The lasers were pumped via battery power supplies for the same reasons discussed in Section 3.2. AR-coated collimation lenses (μ S1,2) formed the coupling junction between the lasers. Since the lasers were not pedestal mounted, diagnostic light had to be collected from within the coupling junction, limiting the minimum cavity length to about 20 cm. The beam splitters (BS1,2) sampled light directed from a single laser. Secondary radiation from the opposite laser which traversed the attenuators, a beam splitter, reflected from a laser facet and was finally partially reflected to the diagnostics, was orders of magnitude smaller in power than the primary laser output. A similar argument could be given to justify the theoretical neglect of self-coupling.

The magnitude of coupling was determined by a set of three crossed Glan-Taylor type calcite polarizers (XTAL POLS). The outer two were oriented such

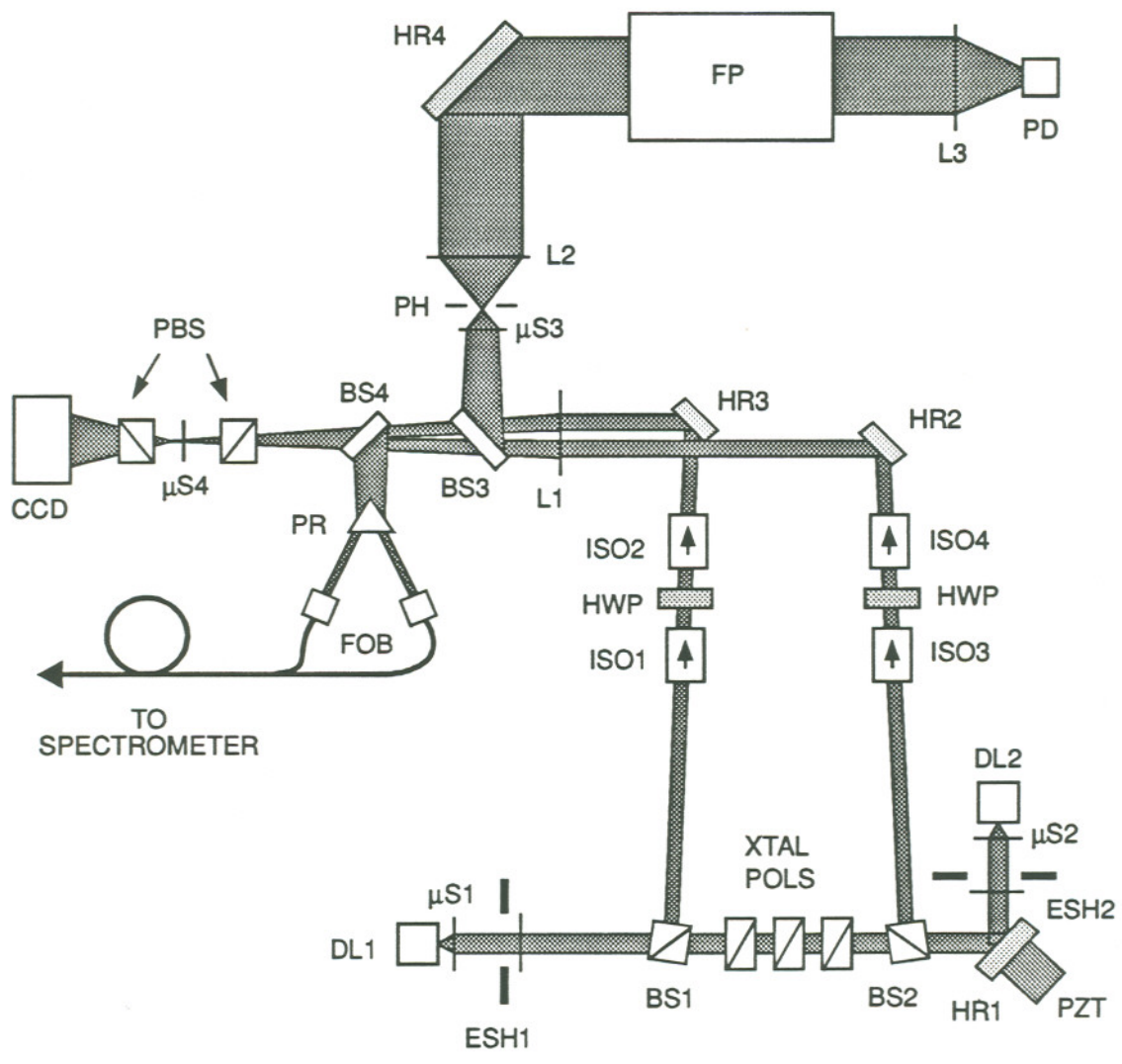


Figure 4.3 Experimental optical setup for mutual coupling. Abbreviations explained in text.

that the pass axes matched the TE polarization of the diode emission. The center polarizer was mounted in a motorized rotation stage, and its angle determined the amount of power transmission. One-way power transmissions from zero to -12 dB could be addressed from one end of the coupling junction to the other, as measured with a power meter. To enable the phase of coupling to be adjusted, the cavity was folded by 90° where the folding mirror (HR1) was mounted on a piezo electric transducer (PZT). Movement of the mirror also induced small movements of the collimated beams. However, the cat-eye assembly of the collimation optics focused the spot to the same point on the laser facet regardless of a slight displacement of the incoming beam, maintaining a constant coupling level.

Mutual coupling between the lasers in this experiment was insured by using the experimental setup indicated in Figure 4.4. Lens L1 imaged the near field of laser A, with a large magnification, onto the CCD array. Laser A was operated below threshold for this alignment so as not to saturate the camera. The attenuator was set so that an adequate amount of power from laser B was transmitted and imaged onto the facet of laser A. Its reflection was in turn imaged onto the CCD array by lens L1. The two spots were then overlapped by moving laser A perpendicular to the optic axis. Assuming that the laser mounts were built with the optic axis normal to the plane of the laser output facet, this alignment alone guaranteed mutual coupling. As a check, the same procedure was repeated from the other beam splitter (BS1,2) in Figure 4.3, indicating the mounts were indeed square. The procedure was conducted before each data set was taken.

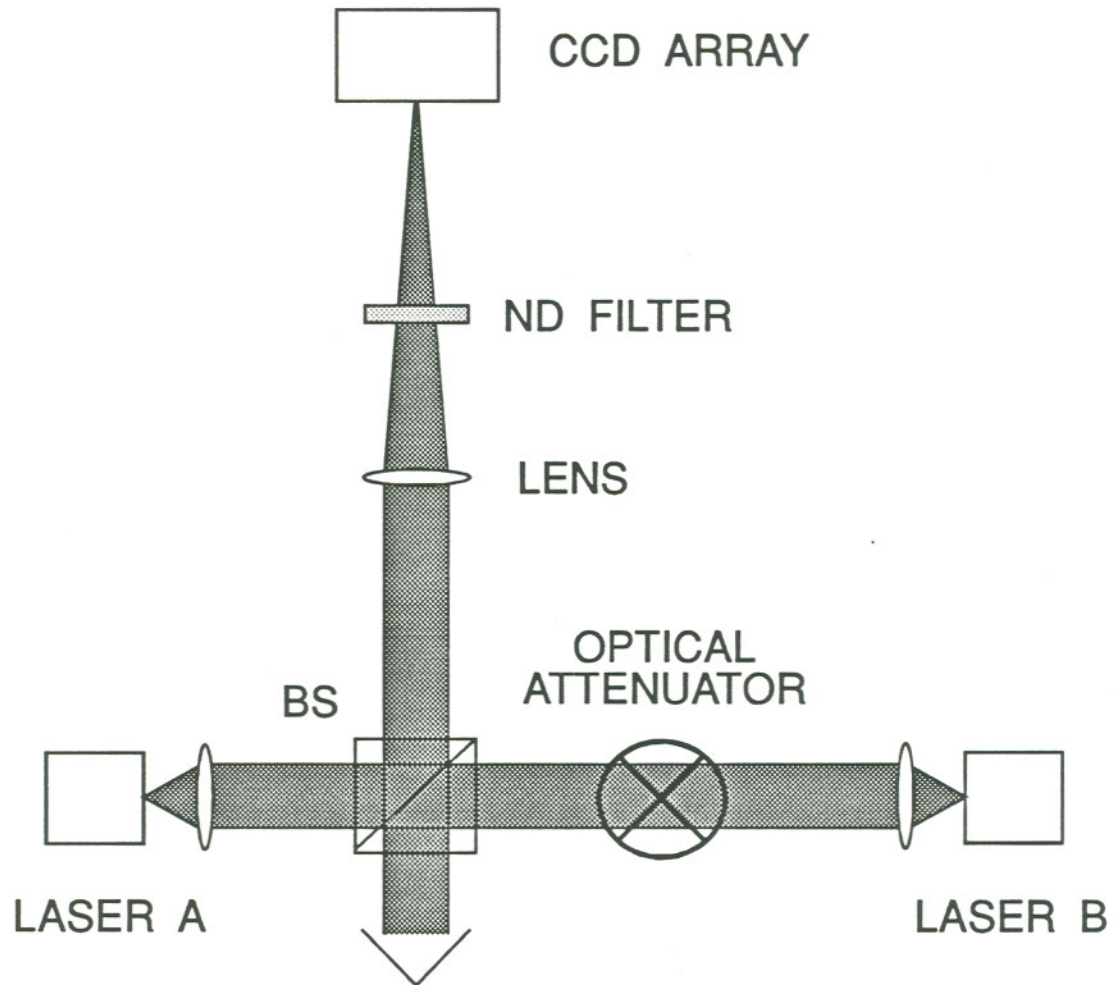


Figure 4.4 Experimental method to insure mutual coupling between the lasers.

The collimated laser outputs to be analyzed were sent through two optical Faraday isolators (ISO) per path. This eliminated the feedback problems from diagnostic optics discussed in Chapter 3. The half wave plates (HWP) were included to insure maximum transmission through the isolators. The HR folding mirrors (HR1,2) shown in Figure 4.3 were aligned to direct the beams parallel to each other a few mm apart. A weak lens (L1) was then used to slowly converge the beams, overlapping them to produce interference fringes. These fringes were used to assess the quality of phase-locking, as described in Appendix C. The power of the lens and the distance between the beams determined the angle at which they converged and consequently the number of fringes. Too fast a convergence resulted in great difficulty getting light through the pinhole (PH) without large reflections. A compromise was made that produced several fringes yet still coupled ample power to the Fabry-Perot (FP). A later version of the optical setup put the Fabry-Perot's beam splitter (BS3) before lens L1 and worked much better. The microscope objective ($\mu S4$) imaged the interference plane onto a CCD array with a large magnification, for observation and digitization. Crossed polarizing beam splitters (PBS) were employed to avoid saturation of the CCD camera.

Gross tuning of the individual lasers, to put them within the lockband, was performed with a .75 m grating spectrometer. This instrument further allowed multiple longitudinal mode operation to be observed. The beam splitter (BS4), in Figure 4.3, picked off a portion of the two converging beams, which were then separated to a reasonable distance by a prism (PR) and sent to the spectrometer via fiber optic bundles (FOB). It was found that roughly collimated light coupled best to the bundles. Two linear CCD arrays were used at the exit

slit of the spectrometer to observe the spectra. Their output was displayed on an oscilloscope and recorded with a scope camera.

Much finer detail was needed to tune the lasers within the lockband. The Fabry-Perot interferometer (FP) was used for this purpose. The mutually coupled mode spectrum versus laser separation was recorded with this instrument. As in the self-coupling experiment, a spatial filter was used to clean up the beam. It consisted of a microscope objective ($\mu S3$), 25 μm pinhole (PH) and collimation lens (L2). Two parallel beams entered the Fabry-Perot aperture separated by about 3 cm. Therefore, the interferometer had to be aligned extremely well so that parallelism of its mirrors was maintained throughout the entire scan range. If not, the identical frequency of the two laser beams, when phase-locked, would be passed at different points in the voltage ramp to the Fabry-Perot. This would appear as two frequencies in the spectral output. Proper alignment of the Fabry-Perot could therefore be attained only when the lasers were phase-locked.

Simultaneous measurement of the optical spectrum and interference fringes was desired as a function of coupling level and cavity length piston. A program was written to control all data acquisition through a GPIB. Figure 4.5 schematically illustrates the manner in which this was done. At the request of the operator, the laser separation was pistoned by staircasing the voltage delivered to the piezoelectric translator, using a DAC and a high-voltage amplifier. A transient digitizer subsequently recorded and transferred to computer the next available Fabry-Perot scan from the photodiode (PD) in Figure 4.3, initiated by a trigger output supplied by the Fabry-Perot controller. The interference image on the CCD array was then frame-grabbed, whereupon a few

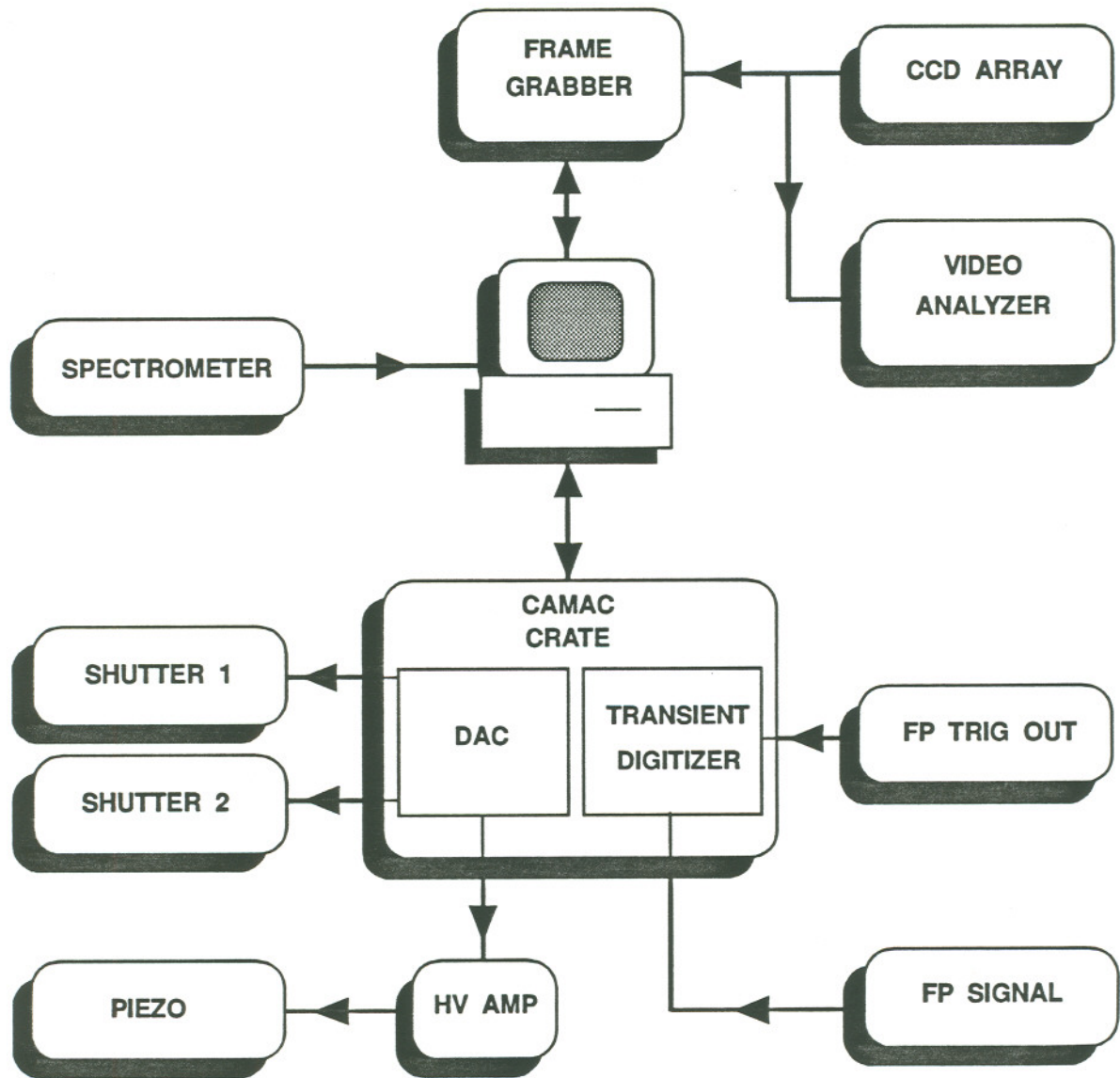


Figure 4.5 An overall view of the automated data acquisition and control setup used in the mutual coupling experiment.

lines through the fringe data were saved in computer memory. This process was repeated any number of times without stopping to process the data. In this way, the entirety of data could be recorded in the minimum time so thermally induced drift was not a problem. Approximately one piston position per second could be recorded with this arrangement. After the desired number of piston levels had been recorded, the computer sorted out the data and saved it to disk. The electronic shutters (ESH1,2) indicated in Figure 4.3 were used to block the appropriate beams to collect background data, uncoupled spectral and interference data, and to check for drift. Shutters were actuated by computer at the start and end of each data set. Another electronic shutter, not shown in Figure 4.3, was placed between the beam splitters BS1 and BS2 to turn off the coupling. It was manually closed before a data set was taken to set the desired amount of detuning. It should be pointed out that all the diagnostic equipment which needed to be altered during the course of an experimental session could be accessed from *outside* of the enclosed optical table. Power supplies and the Fabry-Perot controller were also located outside the table's hood. A stable lock could then be maintained for tens of minutes by minimizing outside influences such as air currents and vibrations.

4.3 Resonant Locking

The experimental data reported in this section describes the operation of two diode lasers whose isolated oscillation frequencies are nearly resonant. The length of the coupling junction in each case was 45 cm, including the extra opt-

ical pathlength associated with transmission through glass. The following behavior, however, is representative of all laser separations investigated, ranging from 20 to 80 cm. Two ML5101a TJS laser diodes were used as optical sources, operating CW at $1.7I_{th}$, with power outputs of about 7 mW. Results are presented in the order of ascending power coupling ratio.

The spectral and coherence measurements displayed in Figure 4.6 were taken at a power coupling ratio of -70 dB. Part a) shows the coupled optical spectrum obtained with the 2 GHz FSR Fabry-Perot interferometer shown in Figure 4.3, while part b) displays slices through the simultaneously recorded interference fringe patterns (taken perpendicular to the fringes). Each trace vertically represents a different laser separation increased in steps of about $1/20$ th of a wavelength, thereby representing a specific value of $\bar{\omega}_o\tau$. The average uncoupled oscillation frequency is indicated by a dashed line in the figure. The spectra of the lasers, when coupled, lock to a single frequency which is narrower than the isolated linewidths and tunes to lower frequencies with an increase in the laser separation. Further, mode hops are observed to occur with every $\frac{\lambda}{2}$ added to the cavity, as in the case of self-coupling, with two modes operating for a range of laser separations near the hop. The frequency separation (~ 90 MHz) of the modes at the hop boundary was used to determine the coupling level by the method outlined in Appendix B.

Although the spectral data indicates that the coupled lasers appear to operate at the same frequency, whether or not they are phase-locked can only be ascertained from the interference data in Figure 4.6 b). Visibilities for each fringe profile were determined as described in Appendix C and are labeled just

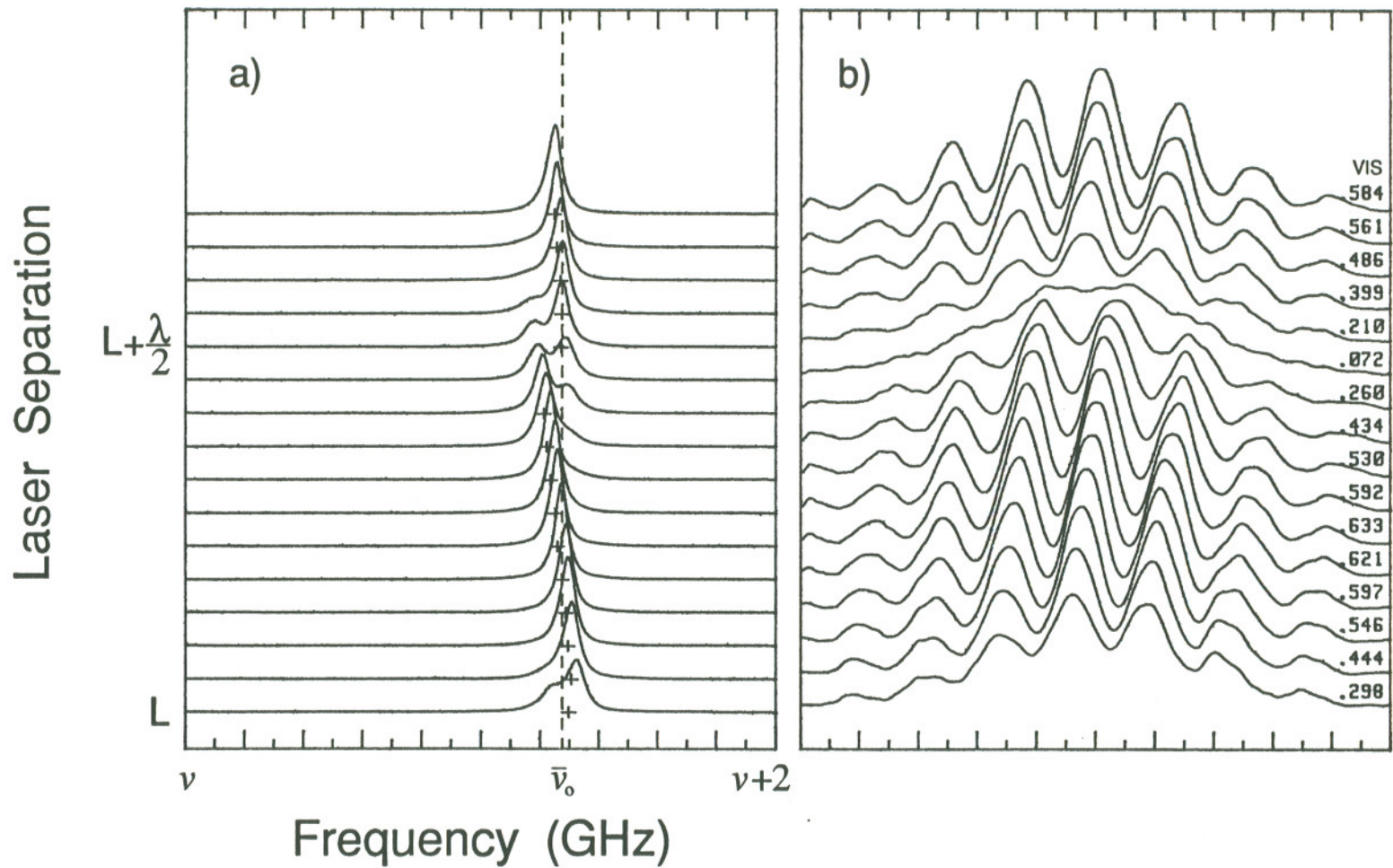


Figure 4.6 Experimental spectral and coherence measurements for two mutually coupled TJS lasers. a) optical spectrum, b) cross-section through interference fringe pattern. -70 dB power coupling ratio, 45 cm laser separation.

above each trace. The appreciable visibilities obtained for most diode separations indicate that a substantial degree of coherence has been established between the lasers even at such a weak coupling level. Visibility falls off dramatically in the vicinity of a mode hop. Fringe peaks move with respect to a piston in diode separation due to the location of the piezoelectric translator in the optical path of one laser (see Figure 4.3). As a result, every additional wavelength added to the cavity shifted the fringes by 2π . This coupling configuration was chosen to allow the shortest possible coupling delay by minimizing the number of required optical elements between the lasers.

It is apparent in Figure 4.6 b) that the mode hop initiates a π phase shift in the fringes, or equivalently, in the locked phase difference between the lasers. This is not attributable to the 90 MHz change in the coupled frequency due to the mode hop. Pathlengths to the interference plane were matched sufficiently so that changes in the coupled oscillation frequency (≤ 10 GHz) produced a negligible contribution to fringe movement.

Stationary solutions predicted by equation (4.1.8) are displayed in Figure 4.7 a) at a power coupling ratio of -70 dB, using parameters measured for the ML5101a TJS laser listed in Table E.1. Note that there are two modes available to the system at any cavity length, a symmetric (square) and asymmetric (circle) mode, where $\Delta\phi_L = 0, \pi$ respectively. Not all the allowed modes are stable, however. Modes which do not meet the stability criterion (4.1.21) have been indicated by solid dots. A direct comparison to Figure 4.6 a) shows that the symmetric and asymmetric modes alternately run over half wavelength ranges of laser separation. The unstable roots, as expected, do not show up experimentally.

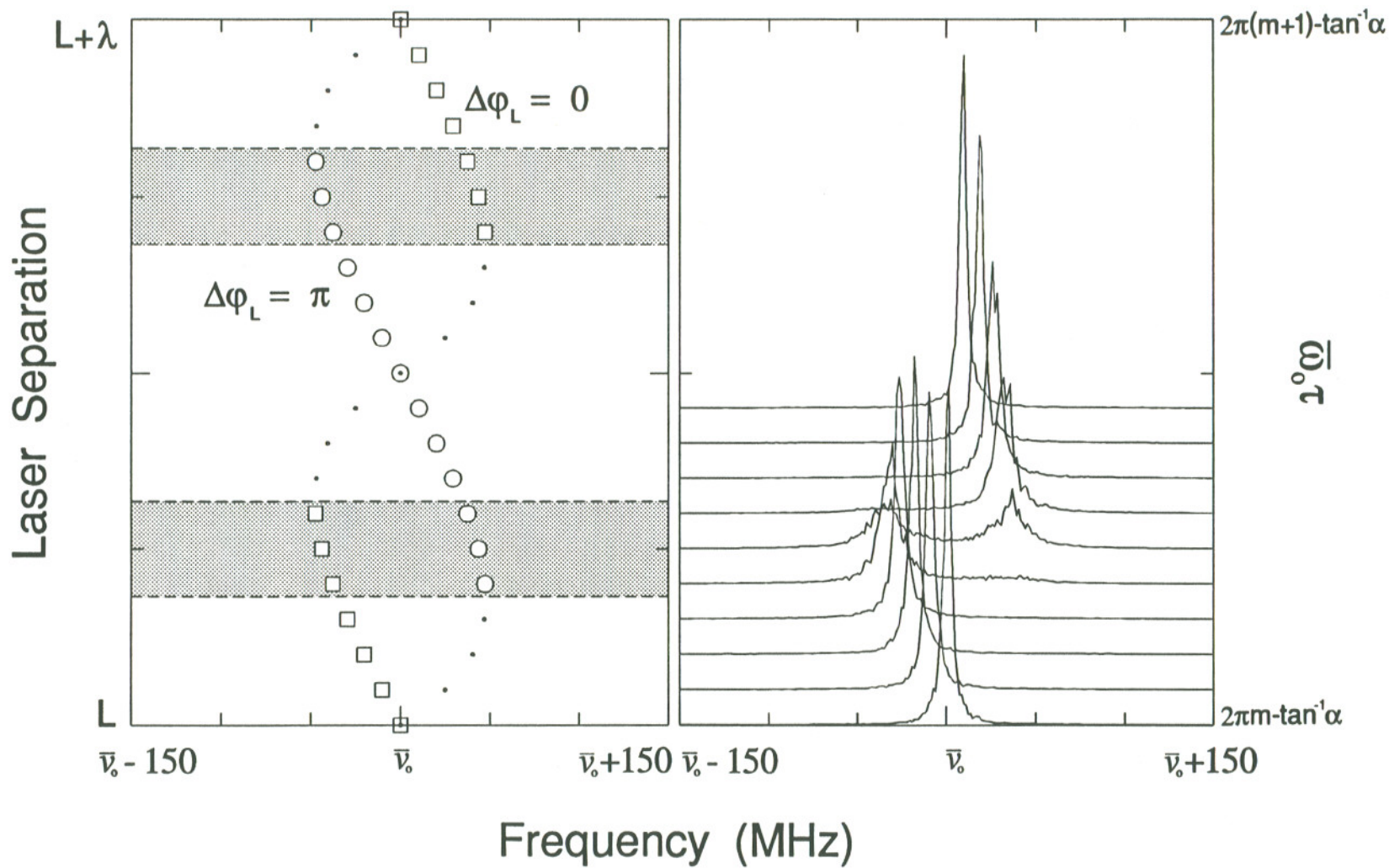


Figure 4.7 Modes of two mutually coupled TJS lasers at a -70 dB power coupling ratio. a) Stationary solutions, b) numerically simulated tuning trajectory. 45 cm laser separation.

In contrast to the stability analysis of Section 2.4, bistable regions exist about $\bar{\omega}_o \tau = (2m + 1)\pi/2 - \tan^{-1}\alpha$ due to the coupling delay. The width of these multimode regions increases with increasing coupling level. It is clear that a mode hop must be initiated as the laser separation is monotonically pistoned through one of these regions, since the operating mode ceases to be stable. The mode hop occurs from the symmetric to asymmetric mode or vice-versa, in agreement with the experimental observation that the fringes shift by π upon hopping. A further discussion of behavior at the mode hop boundary is presented later.

Figure 4.7 b) displays a simulation of mode tuning at the -70 dB power coupling ratio, obtained by integrating the noise-driven phase equation (4.1.10). The separation of 90 MHz at the hop point agrees with the stationary solutions of Figure 4.7 a) and experimental data of Figure 4.6 a), while the tuning trajectory discussed above is duplicated. The linewidth has narrowed from the experimentally measured value of 18 MHz, which was also used in the simulation to determine the level of spontaneous emission noise. The maximum line narrowing cannot be resolved in the data of Figure 4.6 a), however.

Figures 4.8 and 4.9 display the behavior of the mutually coupled lasers with increasing power coupling. Better locks are found to occur at higher coupling levels, as evidenced by the fringe data. Visibilities approaching 80% are obtained at the moderate power coupling ratio of -51 dB. The interference fringes are once again observed to shift by π about the mode hop boundary, indicating a shift from symmetric to asymmetric mode operation or vice-versa. Note that the frequency separation of the two involved modes has increased. As outlined in Appendix B, this dependence on κ was exploited to determine

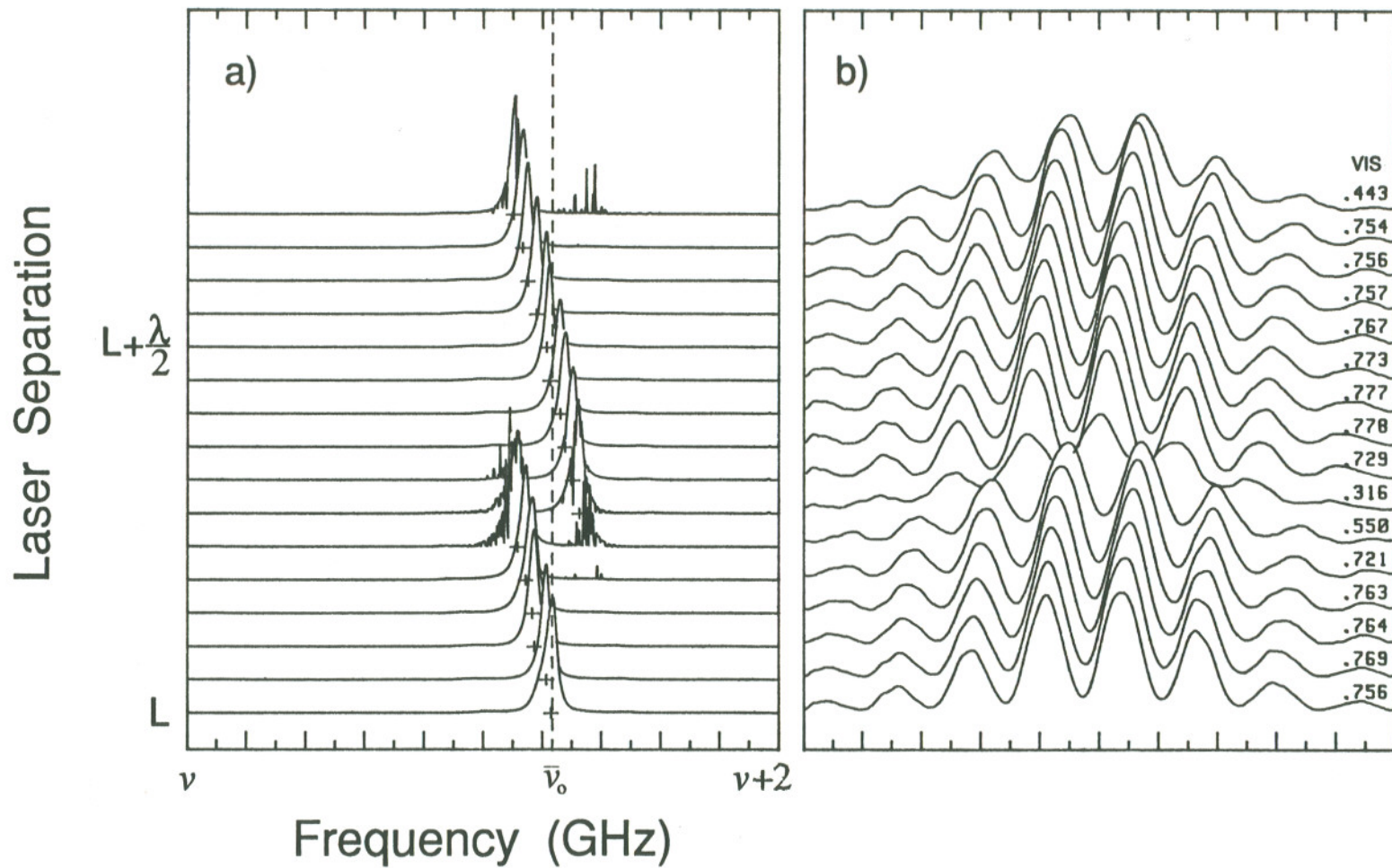


Figure 4.8 Experimental spectral and coherence measurements for two mutually coupled TJS lasers. a) optical spectrum, b) cross-section through interference fringe pattern. -55 dB power coupling ratio, 45 cm laser separation.

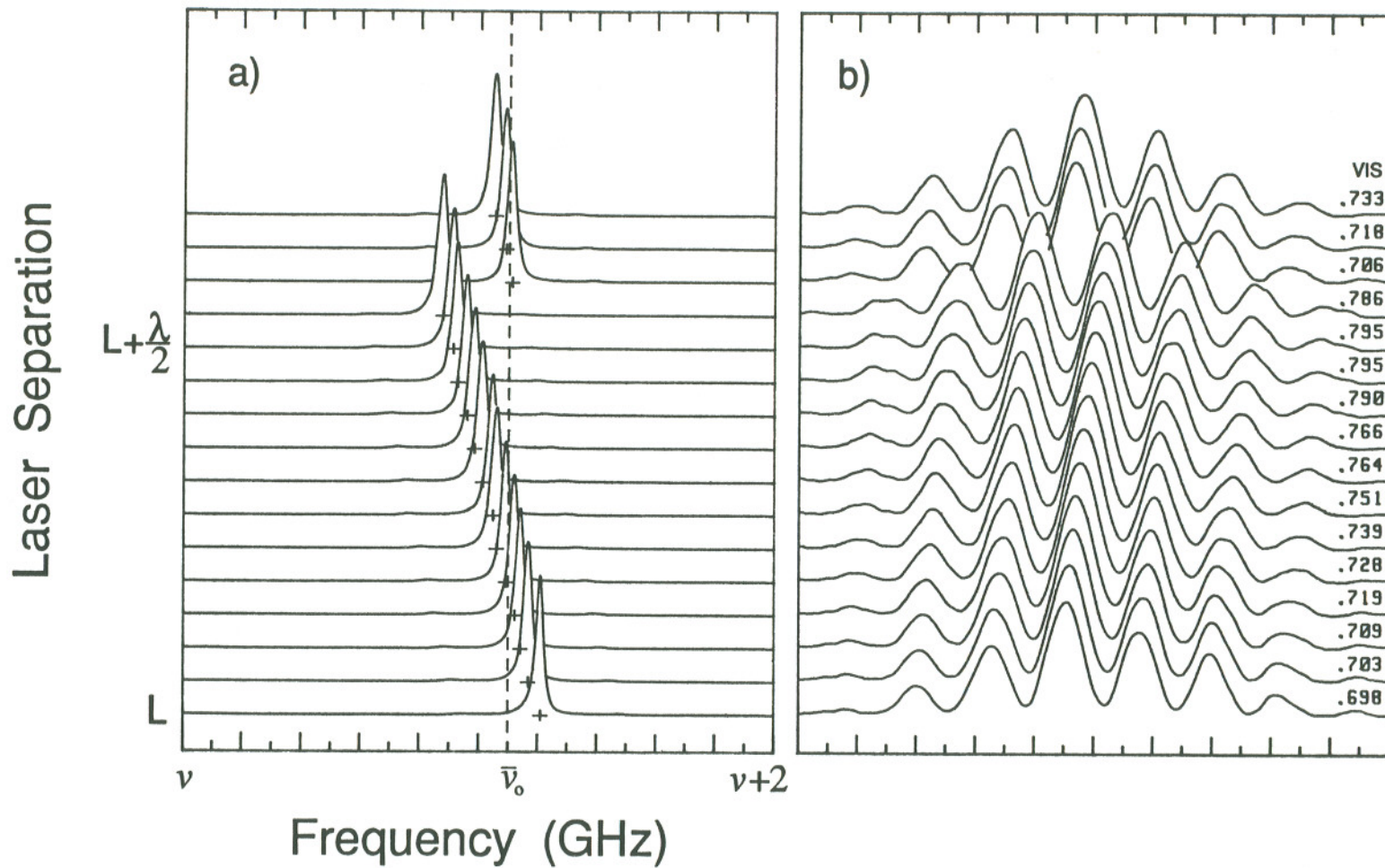


Figure 4.9 Experimental spectral and coherence measurements for two mutually coupled TJS lasers. a) optical spectrum, b) cross-section through interference fringe pattern. -51 dB power coupling ratio, 45 cm laser separation.

the power coupling magnitudes listed throughout this section.

The noisy "drop outs" in the spectrum of Figure 4.8 a) at -55 dB are a clear indication of mode hopping. The reduction in visibility about the hop point, however, is becoming less severe at higher coupling levels, resulting in good locks at nearly all coupling phases. Hop rates were generally observed to slow with increasing power coupling ratio, as in the case of self-coupling. Hence, the lack of obvious mode hopping in Figure 4.6 a), where hop rates are too rapid to be resolved. Conversely, mode hops have become less likely at -51 dB, allowing the spectrum to maintain a single mode over more than $\lambda/2$ of added laser separation. The mode hop here is obviously not centered about the isolated lasing frequencies. Hysteretic tuning trajectories, similar to those shown in Figure 3.14, were indeed observed experimentally for power coupling ratios above about -53 dB.

Many more roots are allowed by equation (4.1.8) at higher coupling levels. Figure 4.10 a) shows the static solutions at a power coupling ratio of -55 dB. Once again, symmetric roots are indicated as squares and asymmetric modes as circles. The maximum deviation from the uncoupled frequency has increased, while as many as four roots are found to exist at a given laser separation. Solutions denoted by solid dots were determined to be dynamically unstable, from (4.1.12). Note that all of these roots correspond to the same longitudinal mode number, or in other words, to the same number of waves in the composite laser cavity. Through direct comparison to the data of Figure 4.8 a), the mode tuning trajectory of the mutually coupled system has been indicated by a dark line in Figure 4.10 a). Although a mode hop has been indicated precisely at $\bar{\omega}_o \tau = (2m+1)\pi/2 - \tan^{-1}\alpha$, hopping is evident for a range of laser separations

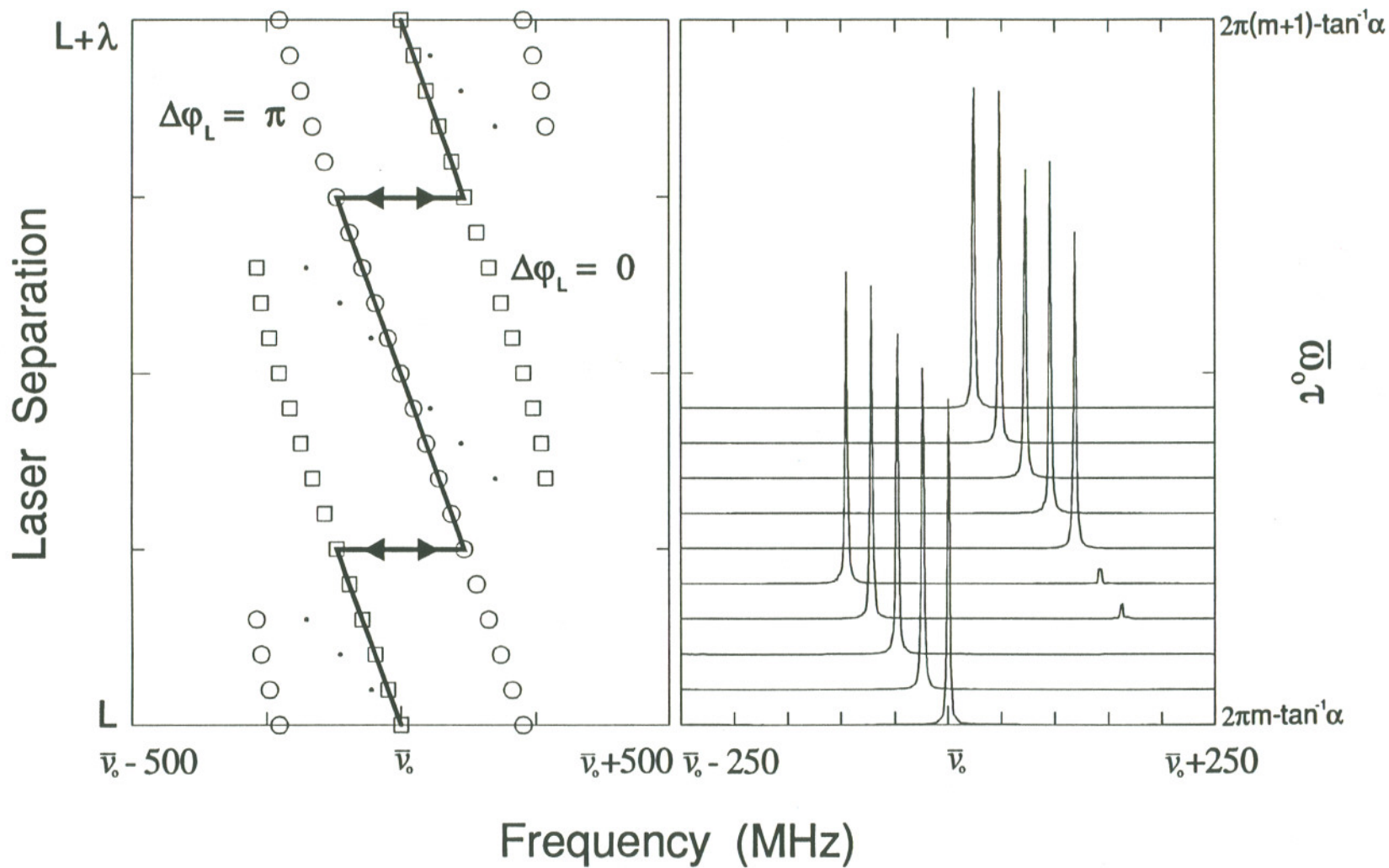


Figure 4.10 Modes of two mutually coupled TJS lasers at a -55 dB power coupling ratio. a) Stationary solutions, b) numerically simulated tuning trajectory. 45 cm laser separation.

about this location in the experiment. Further evidence of the indicated trajectory is provided by numerical integration of the phase equation (4.1.10) for a -55 dB power coupling ratio, as displayed in Figure 4.10 b). A mode hop occurs at the expected piston location with a mode spacing of ~ 250 MHz, which agrees with both the stationary solutions and experiment. Note the considerable line narrowing of the locked mode.

Based on the discussion of mode selection in Section 3.6 for a self-coupled laser, it is likely that the mutually coupled system also oscillates in the mode possessing the greatest phase stability, rather than with the lowest threshold gain. This inference can be proved by considering equation (4.1.12) describing small phase fluctuations in laser j about the steady-state condition. Note that there is a similar expression for the phase in laser k , found by interchanging the indexes. One can define the instantaneous difference in the phases as

$$\delta\Phi(t) \equiv \delta\phi_k(t) - \delta\phi_j(t). \quad (4.3.1)$$

Assuming the phase fluctuations $\delta\phi_{j,k}$ are small, the difference terms in equation (4.1.12) can be approximated to first order as

$$\delta\phi_k(t-\tau) - \delta\phi_j(t) = \delta\dot{\Phi}(t)\tau, \quad (4.3.2)$$

$$\delta\phi_j(t-\tau) - \delta\phi_k(t) = -\delta\dot{\Phi}(t)\tau. \quad (4.3.3)$$

Substitution of equations (4.3.2) and (4.3.3) into equation (4.1.12), recalling that $\Delta\phi_{Lj} = -\Delta\phi_{Lk} \equiv \Delta\phi_L$, results in

$$\delta\dot{\Phi}(t) = \frac{F(t)}{1 + 2\kappa\tau\sqrt{1 + \alpha^2\cos\Delta\phi_L}\cos(\omega_L\tau + \tan^{-1}\alpha)}, \quad (4.3.4)$$

where $F(t) \equiv F_k(t) - F_j(t)$. This gives an expression governing fluctuations from steady-state in the phase difference between the lasers, due to quantum noise associated with spontaneous emission. Note that with no coupling $\delta\Phi(t) = F(t)$; the phase difference then executes Brownian motion, driven by the *difference* of the noise sources. The denominator of (4.3.4) therefore describes a reduction (or increase, depending on the coupling phase) in fluctuations of the locked phase difference due to the influence of mutual coupling. As discussed in Appendix D, the frequency excursion goes as the square of the phase fluctuations such that

$$\Delta\nu = \frac{\Delta\nu^o}{\left(1 + 2\kappa\tau\sqrt{1+\alpha^2}\cos\Delta\phi_L\cos(\omega_L\tau + \tan^{-1}\alpha)\right)^2}. \quad (4.3.5)$$

Note that (4.3.5) does *not* give the linewidth of the coupled system, as it did in self-coupling. It is actually the Fourier transform of the mutual-coherence function²²⁶ between the lasers. As such, it is a measure of the stability of the phase-lock in the spectral domain, analogous to the role of visibility in the spatial domain.

Figure 4.11 shows the numerical evaluation of equation (4.3.5) for the power coupling ratio of -55 dB. The experimentally observed tuning trajectory is superimposed on the solutions as a solid black line, and can be directly compared to that given in Figure 4.10 a). It is clear that the lasing mode alternately hops from symmetric to asymmetric solutions every π change in $\bar{\omega}_o\tau$, maintaining the solution with the smallest $\Delta\nu$, or the most stable locked phase difference. Therefore, mode selection is again determined by phase stability, not threshold gain, at the present coupling level. $\Delta\nu$ is generally found to decrease

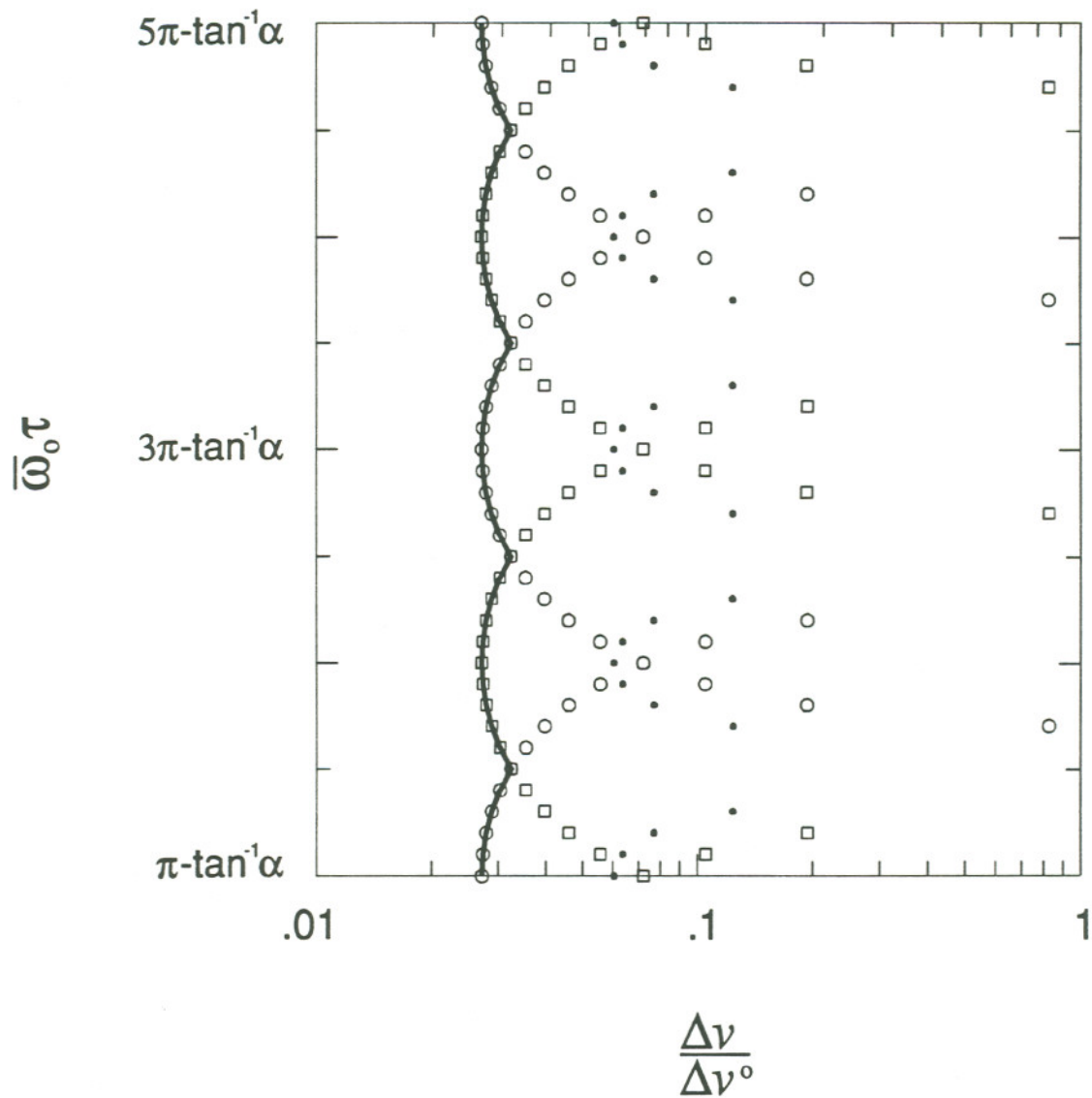


Figure 4.11 Width of the spectral density function describing fluctuations in the phase difference between two mutually coupled TJS lasers at a -55 dB power coupling ratio, 45 cm laser separation. The experimentally observed tuning trajectory is indicated by a solid line.

with increasing coupling, in agreement with the increase in visibility with coupling level observed experimentally, while it becomes nearly independent of $\bar{\omega}_o\tau$ at moderate coupling levels. Therefore good quality locks are expected at nearly all coupling phases for power coupling ratios above about -50 dB, as found in Figure 4.9 b). The best phase-locks are predicted to exist at $\bar{\omega}_o\tau$ products half way between mode hops. This is generally the case observed experimentally (see Figures 4.6 b) and 4.8 b)) below the onset of hysteresis.

The slight decrease in stability of the mutually coupled system near a mode hop boundary, however, is insufficient to explain the significant reduction in visibility depicted in Figure 4.8 b). It becomes necessary to examine the dynamic operation of the phase difference. Where the relaxation resonance is well damped, numerical integration of the approximate phase equation (4.1.10) for mutually coupled lasers gives quite satisfactory results. Figures 4.12 a) and b) display the temporal evolution of the individual phases and phase difference between the lasers at a -64 dB power coupling ratio, with $\bar{\omega}_o\tau = \frac{\pi}{2} - \tan^{-1}\alpha$. Parameters used in the calculation were those measured for a ML5101 TJS laser. The phases in each laser were initially set to zero and then computed versus time under the influence of stochastic noise sources, with magnitudes corresponding to the measured linewidth of 18 MHz.

Mode hops are indicated by a sign change in the slope of the phase versus time plots in Figure 4.12 a), where the slope gives the angular frequency deviation of the phase-locked mode from the average uncoupled frequency. When a perturbation induces a mode hop, the phase difference shifts by some odd multiple of π in making a transition from the even to odd mode or vice-versa. Note

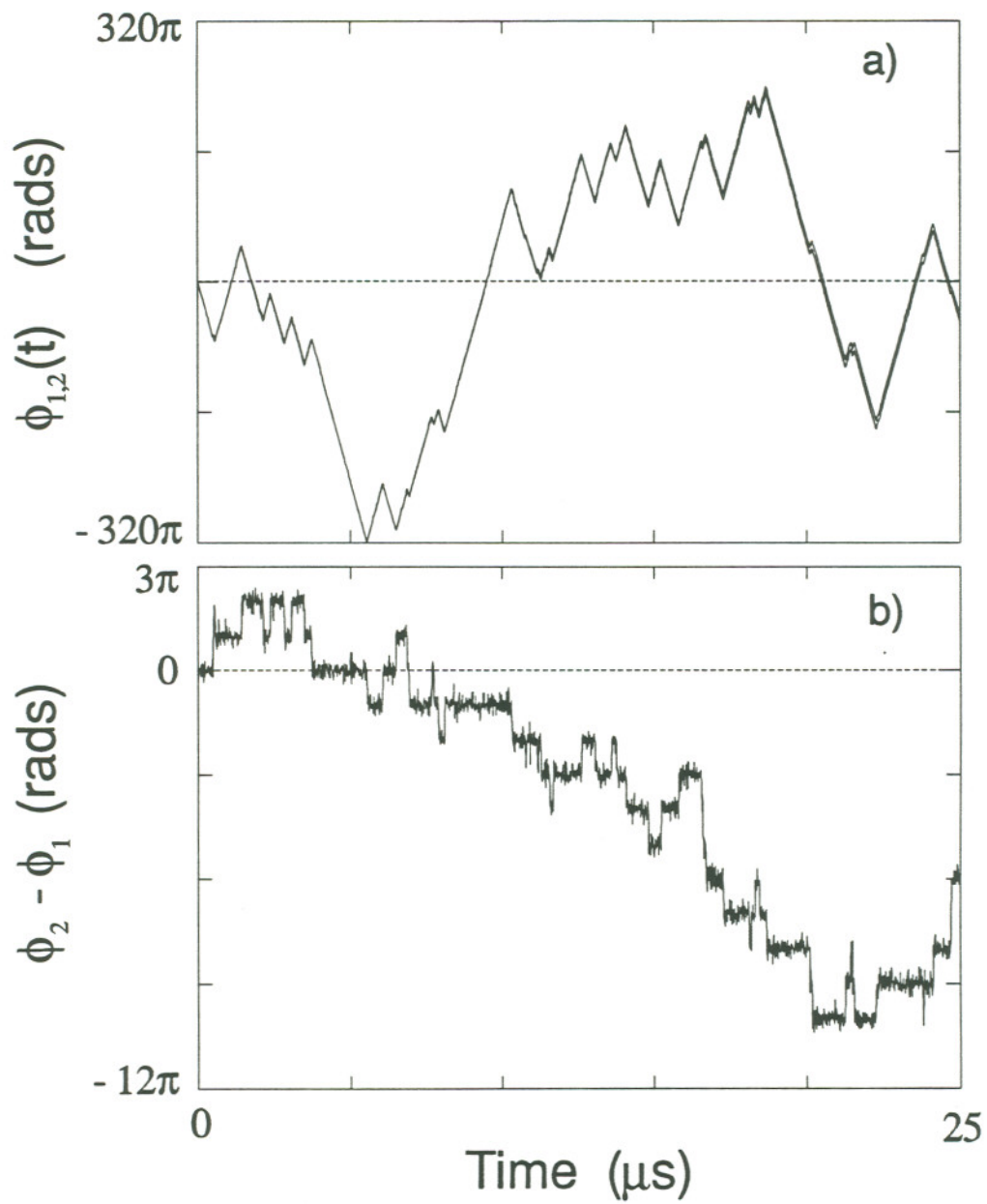


Figure 4.12 Numerical simulation of mode hopping for two mutually coupled TJS lasers at a -64 dB power coupling ratio.

that due to the time delay in coupling, the phase difference slips until a new lock can be acquired after several round trip times of the coupling junction. Although the lasers are well locked most of the time, poor visibilities are still expected, since the system spends about equal time with $\Delta\phi_L(t)$ equal to $2m\pi$ and $(2m+1)\pi$. A visibility of only 0.078 was calculated for Figure 4.12 b) by the method described in Appendix C. Only when mode hops become extremely unlikely in the hysteretic regime of coupling are substantial visibilities obtained at the hop boundary.

Figure 4.13 displays the visibility of the two mutually coupled TJS lasers as a function of the power coupling ratio. Crosses locate theoretical visibilities, which were calculated from time series similar to those shown in Figure 4.13. Here, however, the laser separation was assumed to be such that $\bar{\omega}_o\tau = -\tan^{-1}\alpha$, where the best phase locks were obtained in Figure 4.11. Experimentally measured values, denoted by squares in Figure 4.13, were recorded at laser separations half way between mode hops. The theory has been adjusted for spontaneous emission background using (C.12), while the experimental data was compensated, in a similar fashion, for the effectively incoherent contribution of secondary longitudinal diode modes (see Appendix C).

Visibility is observed to fall off rapidly below approximately -70 dB. This is attributable to the small power exchange between the lasers. At -80 dB, for example, a fractional number of photons

$$P_{out} \frac{\tau_D}{h\nu} PCR_{cc}(1-R) \cong 10^{-3} \quad (4.3.6)$$

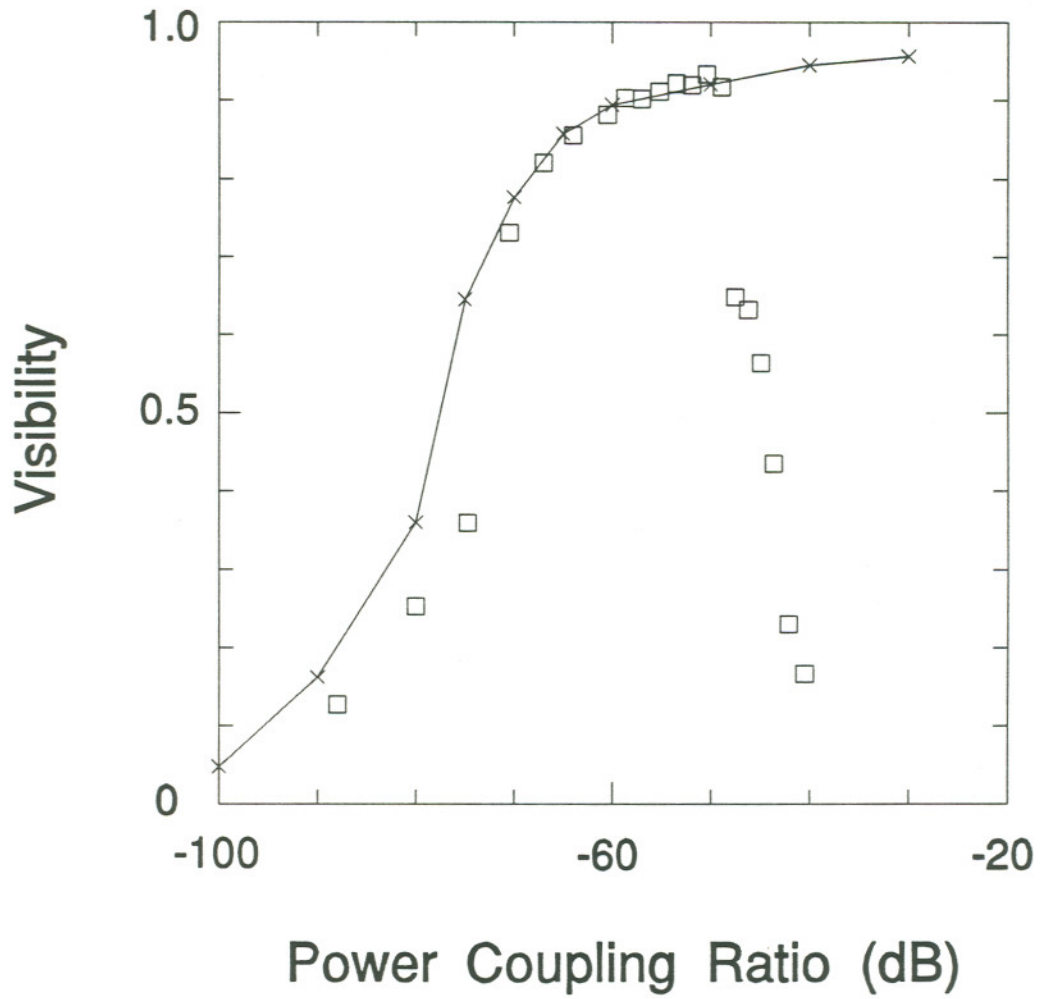


Figure 4.13 Visibility of two mutually coupled TJS lasers versus power coupling ratio. Squares denote experimental measurements, crosses are numerically generated.

are coupled in a single round trip of a laser. In contrast, it was shown in Appendix D that on average ~ 10 spontaneously emitted photons are added to the lasing mode in the same time interval. The phase noise associated with the dominant spontaneous emission makes it difficult for one laser to acquire the phase of the other. Phase locks are consequently poor.

Visibility climbs with increasing power coupling, asymptotically approaching one. Experimentally, however, the coherence drops sharply at -45 dB, due to the onset of dynamic instability, which will be discussed in Section 4.5. This leaves a small ~ 10 dB "window," centered at a -50 dB power coupling ratio, where quality phase-locking can be achieved. Degradation of the phase-lock due to quantum noise in general becomes less of a factor at large coupling levels.

4.4 Non-Resonant Locking

This section expands the experimental analysis of stationary mutual coupling to the case where the semiconductor lasers have different free-running oscillation frequencies. Experimental data presented here was taken under identical operating conditions as in resonant locking, except for the detuning and coupling level.

The series of Figures 4.14 - 4.17 depicts the operation of the coupled TJS lasers as a function of the detuning between their isolated oscillation frequencies, at a power coupling ratio of -53 dB. In each case, part a) displays the optical spectrum measured with a Fabry-Perot interferometer at a 2 GHz FSR,

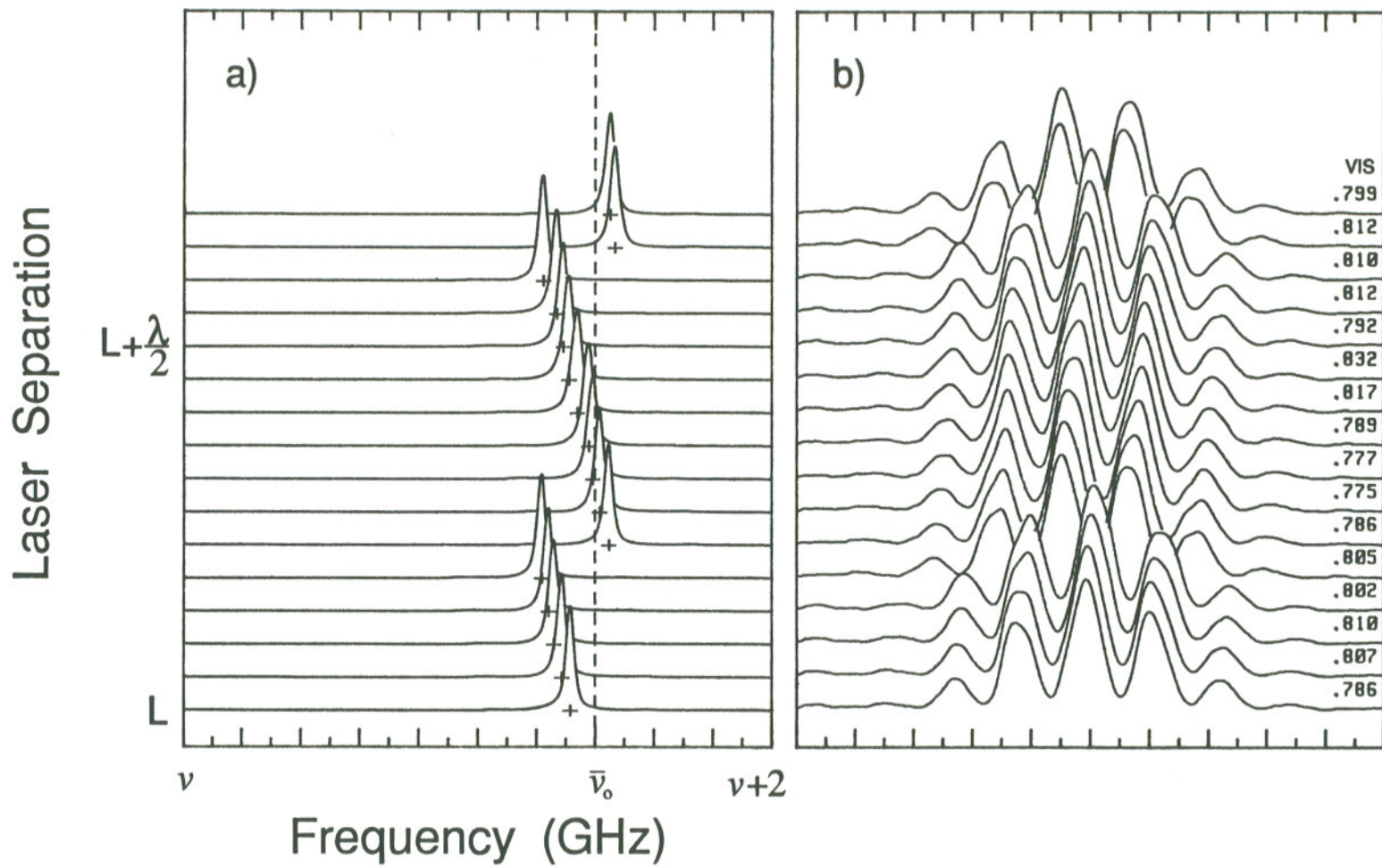


Figure 4.14 Experimental spectral and coherence measurements for two mutually coupled, resonantly tuned TJS lasers. a) optical spectrum, b) fringe pattern. -53 dB power coupling ratio.

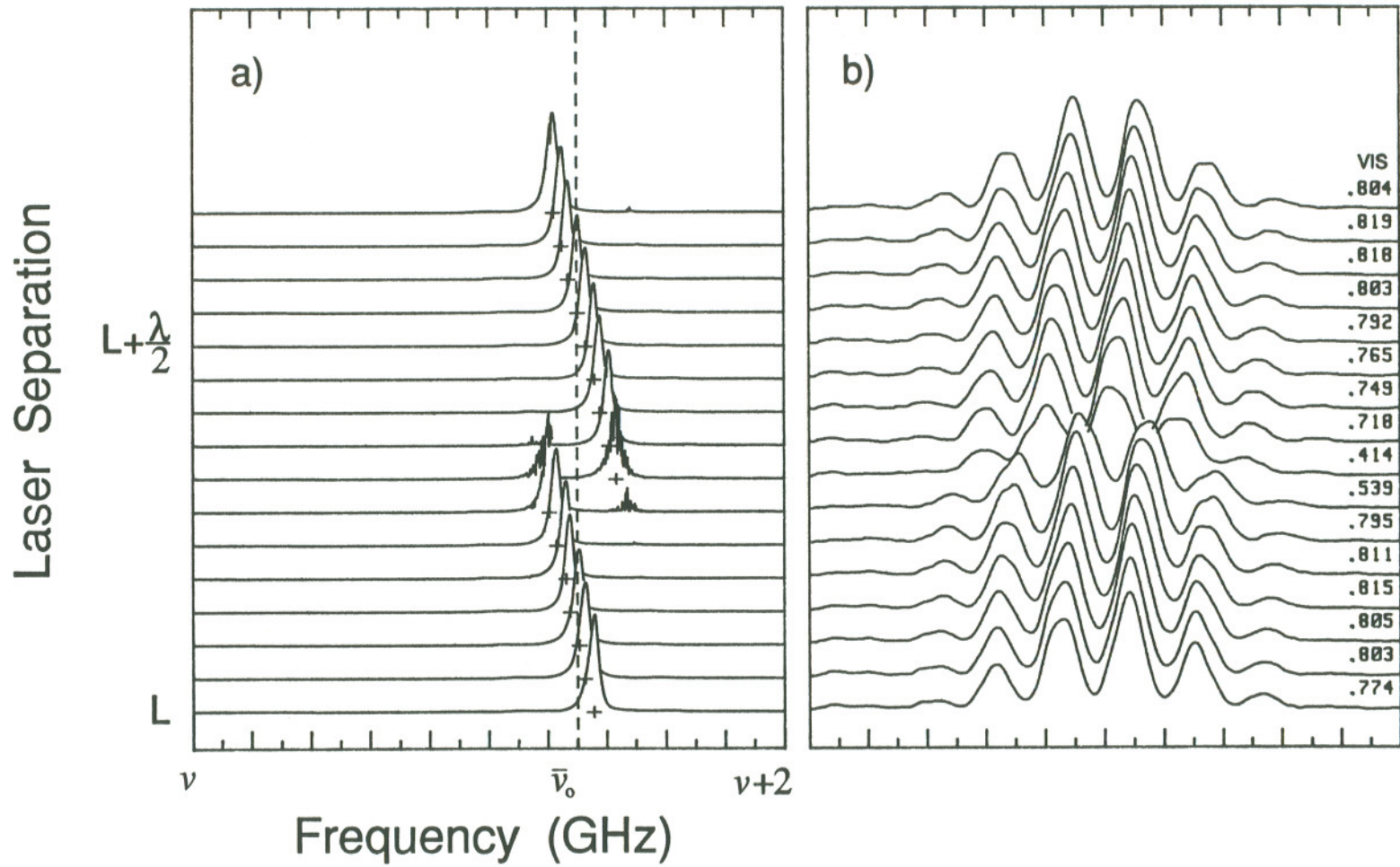


Figure 4.15 Experimental spectral and coherence measurements for two mutually coupled TJS lasers detuned by 255 MHz. a) optical spectrum, b) fringe pattern. -53 dB power coupling ratio, 45 cm laser separation.

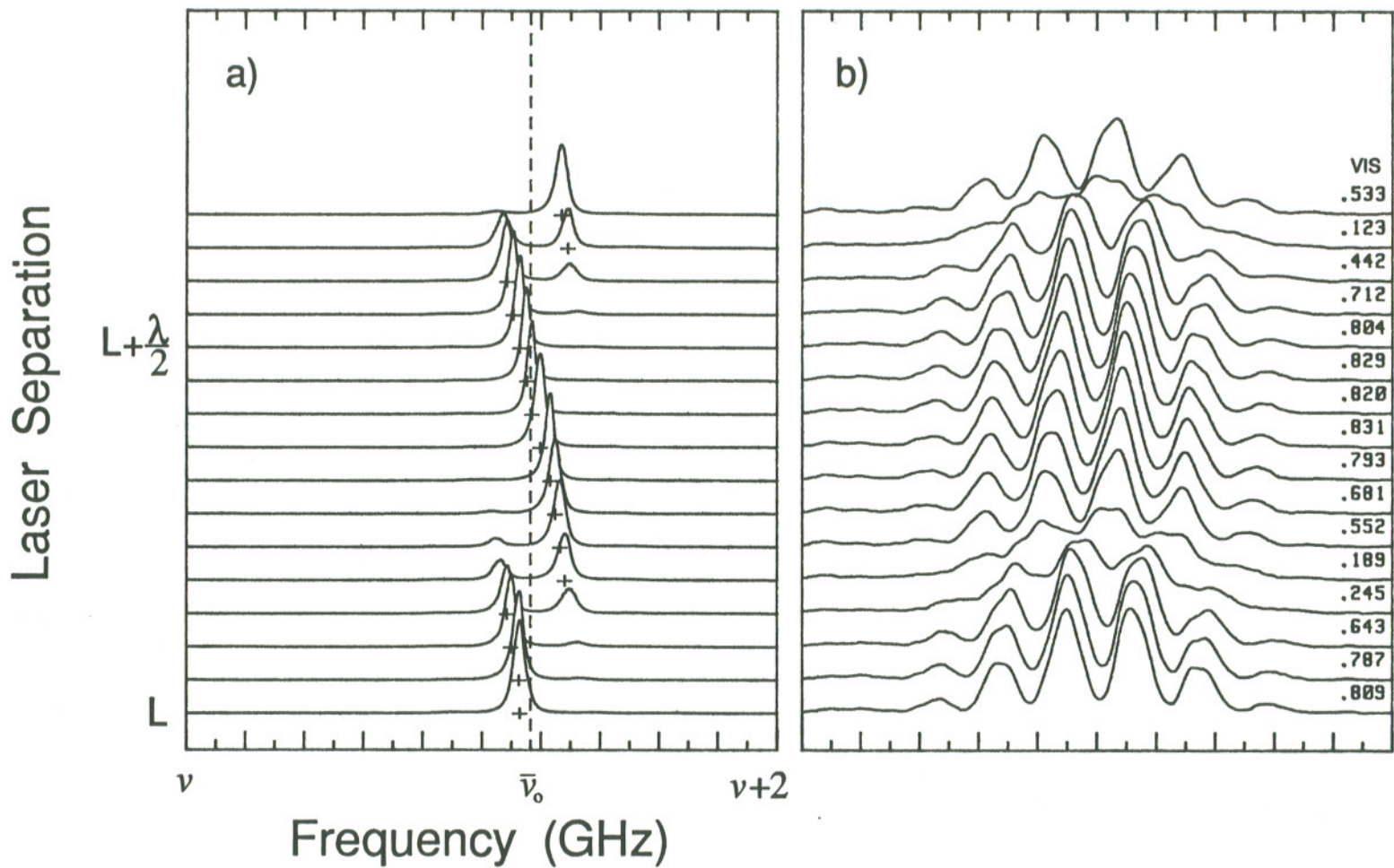


Figure 4.16 Experimental spectral and coherence measurements for two mutually coupled TJS lasers detuned by 470 MHz. a) optical spectrum, b) fringe pattern. -53 dB power coupling ratio, 45 cm laser separation.

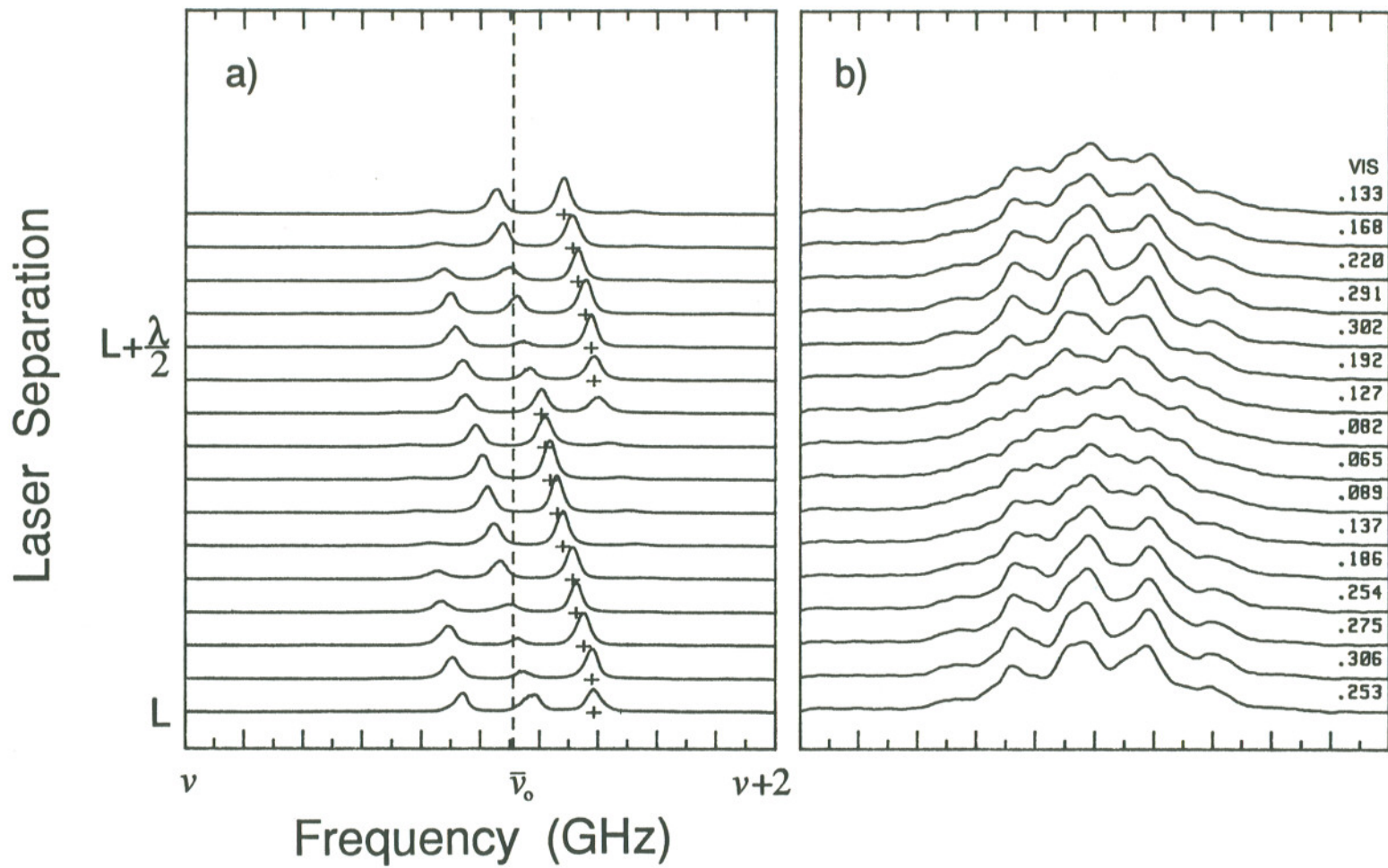


Figure 4.17 Experimental spectral and coherence measurements for two mutually coupled TJS lasers detuned by 623 MHz. a) optical spectrum, b) fringe pattern. -53 dB power coupling ratio, 45 cm laser separation.

while part b) shows the simultaneously recorded interference fringe pattern of the two laser outputs. As before, each trace vertically represents a steadily increasing separation of the lasers in about $1/20$ th wavelength steps.

In Figures 4.14 a) and b) the lasers are nearly resonant. The spectral tuning trajectory at the present coupling level borders on the hysteretic regime of operation, as evidenced by the asymmetric appearance of mode hops with respect to the average uncoupled oscillation frequency. Figure 4.14 b) shows that good quality phase locks are obtained, independent of the coupling phase, at -53 dB power coupling. When detuned, according to Figures 4.15 and 4.16, the lasers continue to display phase-locked operation. Peak visibilities are observed to remain roughly unchanged from the resonant case to detunings of over 450 MHz, after which visibilities gradually reduced to zero. Any power imbalance, which was found to accompany detuning in Section 2.3, should contribute negligibly to the measured visibility. The lasers appear to be almost completely unlocked in Figure 4.17 at a detuning of 623 MHz, with appreciable visibilities confined to laser separations farthest from hop boundaries. The optical spectrum in this case has become very complicated.

Interestingly, the hysteretic tuning behavior encountered in the resonant case ceases as the lasers are detuned. Spontaneous emission noise is then able to initiate hops between the even and odd modes (note the π phase shift in fringes) with every half wavelength of added laser separation, as it did at lower coupling levels among resonantly tuned lasers. Mode hopping is obvious in the spectral data of Figure 4.15 a), and undoubtedly contributes to the reduction in visibility encountered there. The increase in hop rates with detuning indicates that modes near the hop boundary are becoming less stable.

Stationary solutions to equations (4.1.6) and (4.1.7) are displayed in Figure 4.18 for a power coupling ratio and values of detuning corresponding to the four experimental cases. Parameters used in the numerical calculations were those listed in Table E.1 for the ML5101a TJS diode laser. Only dynamically stable roots have been plotted for clarity, as a number of unstable equilibria, in addition to those shown in Figure 4.10 a), are possible for non-zero detuning. Stability was determined by numerical solution of the transcendental equation (4.1.19). Open squares in the figure denote symmetric roots with $(2m - 1/2)\pi < \Delta\phi_L < (2m + 1/2)\pi$, while dark squares are for asymmetric solutions having $(2m + 1/2)\pi < \Delta\phi_L < (2m + 3/2)\pi$.

A comparison of Figure 4.18 a) with the experimental spectra of Figure 4.14 a) reveals that the maximum excursion of the locked frequency predicted theoretically is much larger than that observed experimentally. This is again a consequence of phase stability. Modes with relatively large values of $\Delta\omega_L$ are less stable than those near $\Delta\omega_L = 0$, allowing spontaneous emission noise to initiate mode hops to more stable states. The tuning trajectory therefore never "sees" the outermost modes at this coupling level. These modes correspond to a principal value of the cross-coupling phase near $\psi_{cc} = \pm\pi/2 + \tan^{-1}\alpha$.

It is also evident in Figure 4.18 that stationary solutions with the largest $\Delta\omega_L$ are lost as the detuning is increased. Note, however, that the solutions are not lost due to a failure to meet the stability criterion, as implied by the observed increase in hopping rates. Stable as well as unstable modes have simply ceased to be solutions of equations (4.1.6) and (4.1.7), since the lockband has been exceeded at that ψ_{cc} . Recall the discussion of Section 2.3 where the

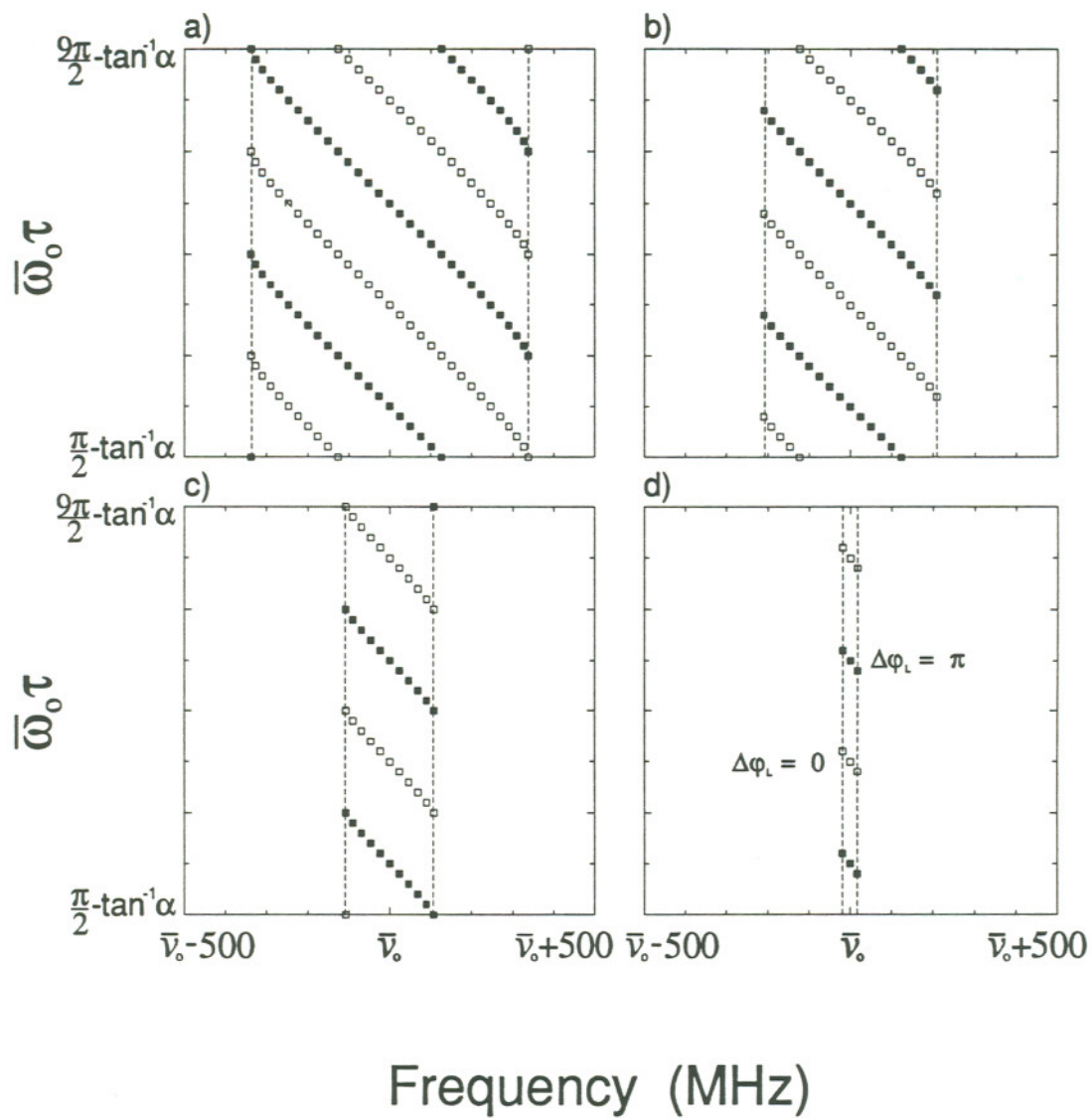


Figure 4.18 Stationary solutions versus detuning for two mutually coupled TJS lasers. a) resonantly tuned, b) 255 MHz detuning, c) 460 MHz, d) 623 MHz. 45 cm laser separation, -53 dB power coupling ratio.

lockband was shown to be a function of the coupling phase through equation (2.3.21). Because several modes with different ψ_{cc} are available at a given laser separation, phase-locking is not limited in the experiment until the detuning reaches approximately 500 MHz. As shown in Figure 4.18 d), regions of laser separation near $\bar{\omega}_o\tau = (2m+1)\pi/2 - \tan^{-1}\alpha$ have no phase-locked equilibria, since the lockband has been exceeded at those particular coupling phases. Alternately, phase-locked operation is confined to laser separations near $\bar{\omega}_o\tau = m\pi - \tan^{-1}\alpha$. At the maximum locking range of 677 MHz, given by (2.3.22), locked modes exist only at $\bar{\omega}_o$.

The experimental spectra in Figures 4.14 - 4.17 a) can be well simulated by integrating equations (4.1.10) for the phases in each laser versus time. Figures 4.19 a)-d) display the results of numerical calculations carried out at a power coupling ratio of -55 dB and a laser separation of 45 cm. This coupling level was chosen since an impractical amount of computer time was required at -53 dB to model the less frequent mode hopping. Still, agreement with experiment is evident. Figure 4.19 a), representing the resonant case, is identical to Figure 4.10 b). As the lasers are detuned, the experimentally observed tuning trajectories are duplicated. Recognize that without noise in the model, the trajectory would look much different (hysteretic). Modes near the hop boundary in Figures 4.19 b) and c) display broadened linewidths indicating reduced phase stability and resulting in a greater probability of mode hops. Figure 4.19 d) was calculated for a detuning of 600 MHz and is thus well outside the 540 MHz lockband given by equation (2.3.22). Yet some influence of coupling still exists. The individual laser resonances are pulled from their isolated locations to within 500 MHz, depending on the coupling phase. Frequency pulling was found to

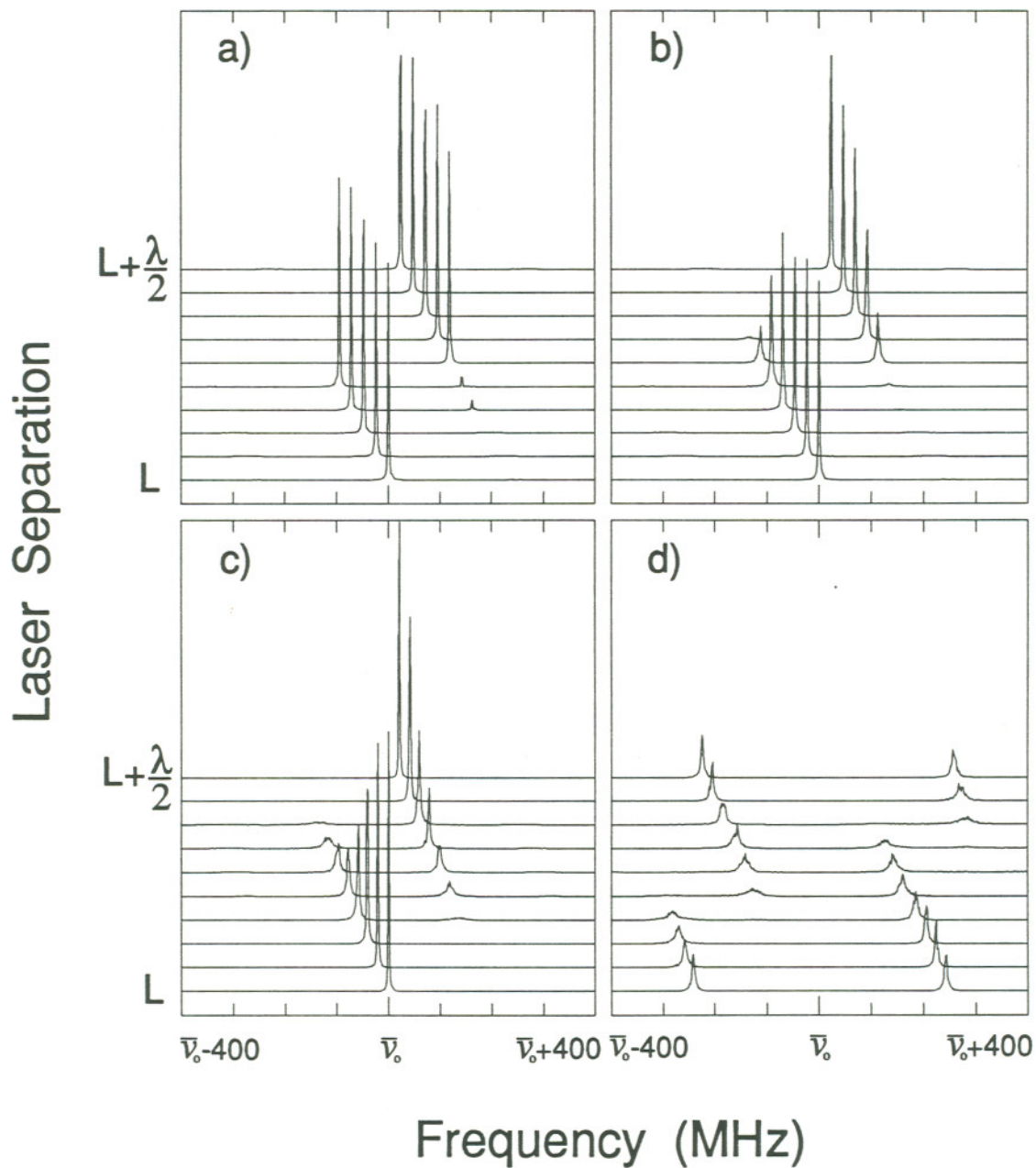


Figure 4.19 Numerical simulations of optical spectra versus detuning for two mutually coupled TJS lasers. -55 dB power coupling ratio, 45 cm laser separation. a) resonantly tuned, b) 200 MHz detuning, c) 400 MHz, d) 600 MHz.

reduce at larger detunings. Similar pulling behavior outside the lockband is well known in master-slave injection-locking configurations^{129,183}. The tuning and hopping behavior simulates well the experimental spectra shown in Figure 4.17 a), although in that case the lasers are still partially locked at some laser separations.

It is apparent from the data presented in Figures 4.14 - 4.17, as well as other experimental observations not shown here, that there is no distinct transition from locked to unlocked behavior. Furthermore, phase-locked operation always is limited to detunings much smaller than the theoretical locking range given by (2.3.22). The expected lockband corresponding to the experimental data in Figures 4.14 - 4.17 at -53 dB, for example, is 677 MHz. Yet a comparison to Figure 4.17 b) shows that at a detuning of 623 MHz, still well within the lockband, peak visibilities are just over 0.3. For laser separations near $\bar{\omega}_o\tau = (2m+1)\pi/2 - \tan^{-1}\alpha$, this can be attributed to either mode hopping or to the absence of a stationary locked solution, as described earlier. However, when $\bar{\omega}_o\tau = m\pi - \tan^{-1}\alpha$, these arguments do not hold.

Figure 4.20 displays time series of the phase difference between the lasers and their optical spectra for three values of detuning near the lockband edge, at a power coupling ratio of -53 dB. The simulations were obtained from numerical integration of (4.1.10). Flat portions of the time series indicate phase-locked operation, while the slope of other regions corresponds to the pulled beat frequency of the (unlocked) lasers. In Figure 4.20 a), for $\Delta\nu^o = 500$ MHz, the phase lock begins to break randomly in response to noise perturbations. The system then slips multiple 2π before reattaining a locked state. This random slipping of the locked phase, due to the presence of spontaneous emission noise,

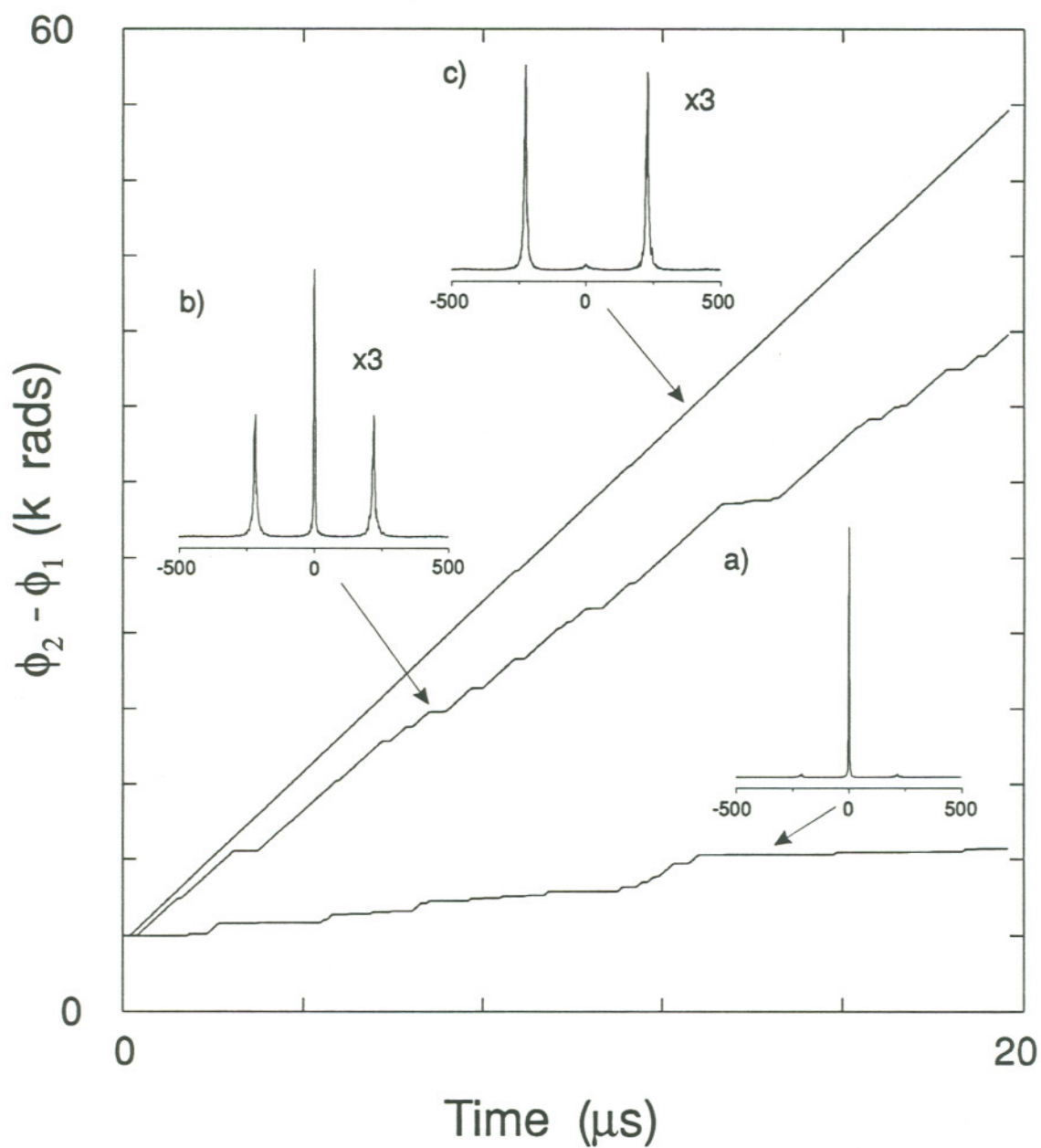


Figure 4.20 Numerical simulation of phase-locking near the lockband edge for two mutually coupled TJS lasers. a) 500 MHz detuning, b) 600 MHz, c) 650 MHz. -53 dB power coupling ratio, 45 cm laser separation. $\bar{\omega}_\tau = -\tan^{-1}\alpha$.

manifests in reduced visibility. Further detuning results in a greater fraction of time spent in an unlocked state. The optical spectrum then consists of three peaks: a locked mode and the two individual frequency-pulled laser resonances, as shown in Figure 4.20 b). This spectrum is similar to the experimental illustrated in Figure 4.17 a) for laser separations where $\bar{\omega}_o \tau = m\pi - \tan^{-1}\alpha$. At a detuning of 650 MHz, displayed in Figure 4.20 c), the lasers are running almost exclusively in an unlocked condition. It is important to note that this happens *inside* the 677 MHz lockband given by equation (2.3.22).

The range of detuning permitting high visibility phase-locks is therefore smaller than that predicted in a noiseless environment. The phase transition from locked to unlocked operation is not sharp. Rather, the system is able to spend less time in a locked state near the lockband edge, resulting in a softer transition. Figure 4.21 displays visibility data for power coupling ratios of -63 dB and -53 dB. Crosses represent the average of three visibilities calculated from 20 μ s time series, similar to those in Figure 4.20, by the method described in Appendix C. These numbers were corrected for spontaneous emission background via equation C.12. Lines are drawn from point to point as a visual aide, and are not curve fit. A value of $\bar{\omega}_o \tau = -\tan^{-1}\alpha$ was employed, since the best visibilities were found experimentally at this laser separation. The "softened" lockband edge is easily seen. The visibility falls off well inside the theoretical lockband, indicated in the figure by vertical lines. When noise is turned off, however, near perfect locks are obtained for detuning values all the way to the lockband edge. Phase-locks near $\Delta\omega_{LB}$ are therefore less stable and much more easily perturbed than those close to $\Delta\omega_o = 0$.

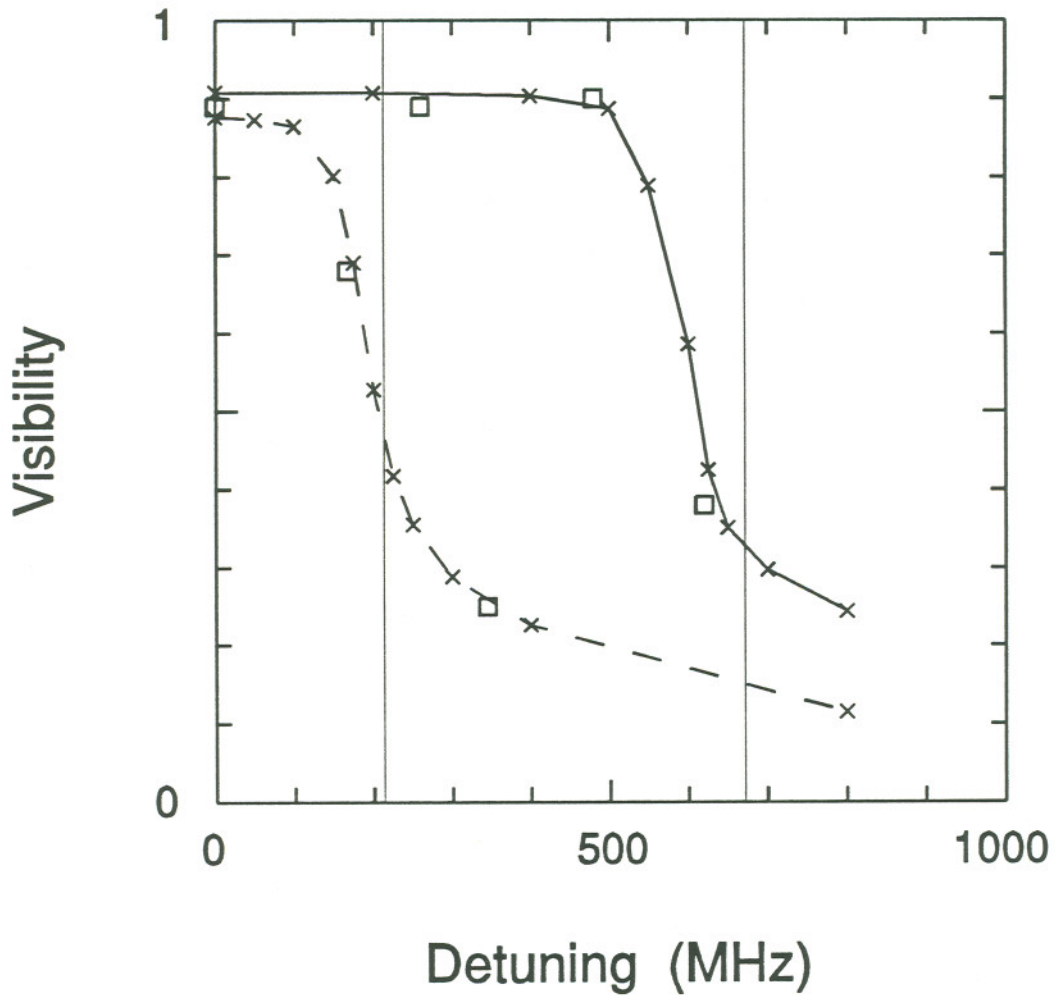


Figure 4.21 Reduction of visibility near the lockband edge. Squares denote experimental measurements, crosses are numerically generated.
 — -53 dB, - - - -63 dB power coupling ratio.
 Vertical lines locate the lockband edge.

Squares in Figure 4.21 represent experimentally measured visibilities, also taken at $\bar{\omega}_0\tau = -\tan^{-1}\alpha$. These values have all been compensated for the presence of secondary longitudinal diode modes, as discussed in Appendix C. Nevertheless, there is a reasonable agreement with experiment. When the lasers are unlocked, visibilities still appear relatively large in both experiment and numerical simulations. Further, they do not abruptly drop to zero outside the lockband. This is a result of "slipping"^{129,183,227}, a well known quasi-periodic increase in the phase difference of *unlocked* coupled oscillators just outside and very near to the lockband edge. The usage here is not to be confused with slips in the locked phase due to spontaneous emission noise discussed previously.

The maximum locking range was experimentally determined to increase approximately as the square root of the power coupling ratio, as predicted by equation (2.3.22), for coupling levels $\lesssim -50$ dB. Maintaining the same longitudinal diode mode with a detuning larger than a few GHz, however, was sometimes difficult. The lasers would often seek out an alternate diode mode possessing a lower threshold gain, due to a coincidence of secondary modes in the lasers, as is well known for C^3 lasers.

4.5 Overcoupling

The very stable operation encountered in Section 4.3 degrades as the coupling level is further increased. The rapid fall-off in visibility with power coupling ratio, shown in Figure 4.13, was first observed experimentally by Dente *et al.*²²² and referred to as *overcoupling*. In their steady-state model, the

phenomenon was attributed to a second longitudinal mode of the compound laser cavity which was able to come above threshold at a critical coupling level, beating with the lasing mode and inciting dynamic instability. Spectral broadening with increasing optical coupling was also referred to by Salathe²²¹ in a much earlier study, without explanation. Since the multiple longitudinal modes are associated with the coupling delay, a critical delay time may be calculated under which overcoupling does not pose a problem. This section investigates this problem more fully, offering an alternative explanation of the instability based on the preceding time-dependent theoretical framework.

Figure 4.22 displays optical spectra along with simultaneously recorded interference fringe measurements for two mutually coupled diode lasers at a power coupling ratio of -42 dB. The lasers and their operating conditions are identical to those given in Section 4.3. The figure demonstrates a rapid spectral broadening and reduction in visibility as the lasers are "overcoupled". In Figure 4.22 a), taken at a FSR of 10 GHz, several modes associated with the resonant cavity formed between the two output facets are observed to oscillate at a given laser separation. The time-average power distribution among these modes is a sensitive function of the phase $\bar{\omega}_0\tau$. Sidebands, separated from the dominant mode by the relaxation resonance frequency of the isolated lasers, are apparent as well. Their existence implies modulation of intensity and phase in the time domain, and hence, dynamic instability. Relaxation resonance sidebands and compound cavity modes were found to first appear at nearly the same power coupling ratio. The visibility corresponding to each operating state is listed above its interference fringe pattern in Figure 4.22 b). Coherence is quite poor at this stage of overcoupling as a result of the dynamic instability, and depends

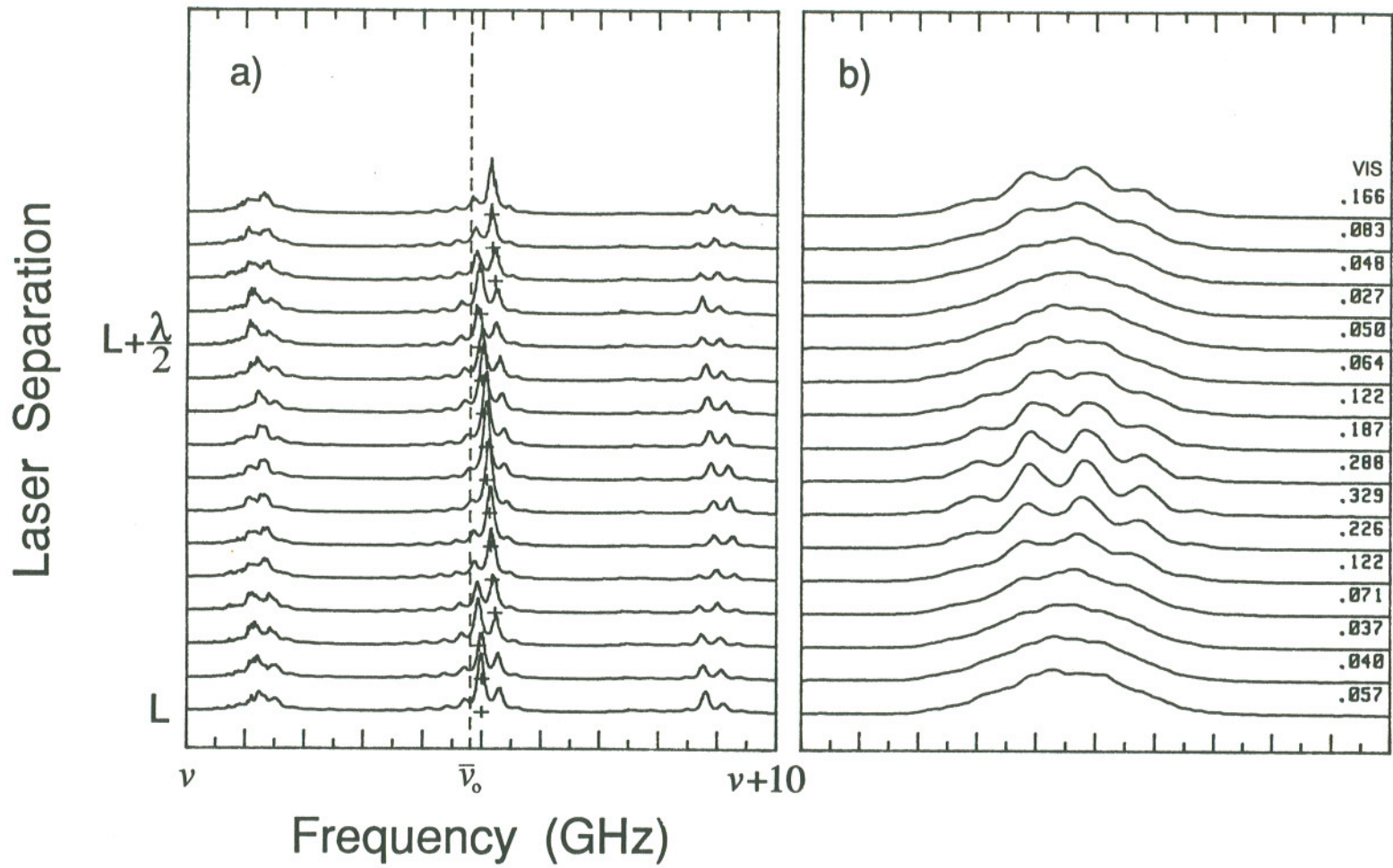


Figure 4.22 Experimental spectral and coherence measurements for two mutually coupled TJS lasers. -42 dB power coupling ratio, 45 cm laser separation.

on the phase $\bar{\omega}_o\tau$.

The optical spectrum broadens further at larger coupling levels. Figure 4.23 shows the numerically generated spectral density function of the lasers' optical field as the overcoupling regime is entered. The traces were calculated through Fourier transformation of time series obtained from numerical integration of the rate equations (4.1.1), (4.1.2) and (2.3.8). The result was also convolved with a 1 GHz FWHM Lorentzian, which smoothed out the spectra, to mimic the output of a Fabry-Perot interferometer. In doing so, however, the large number of composite cavity modes which comprised each spectrum was hidden. Similarity to coherence-collapsed spectra of the self-coupled laser in Figures 3.20 and 3.21 is clear, and the discussion in Section 3.7 can also be used to elucidate the present behavior. Not surprisingly, the intensity spectra of the mutually coupled lasers were also found to be comparable to the self-coupled case in Figures 3.22 and 3.23, here with a compound cavity mode spacing of 333 MHz. It was found experimentally that the spectral progression shown in Figure 4.23 was virtually independent of $\bar{\omega}_o\tau$, as well as the gross coupling delay τ , for laser separations longer than 20 cm.

Figure 4.24 shows the visibility between the mutually coupled lasers as the power coupling ratio is increased, continuing the results of Figure 4.13. Symbols denote numerically calculated visibilities at several selected coupling phases in the interval $(0, 2\pi)$. Each point represents a value calculated from 165 ns time series for the field and phase of each laser, using the method described in Appendix C. Other parameters used in integrating the rate equations were those measured for the ML5101a TJS laser. Error bars are utilized in the figure to display the maximum and minimum visibilities measured experimentally at a

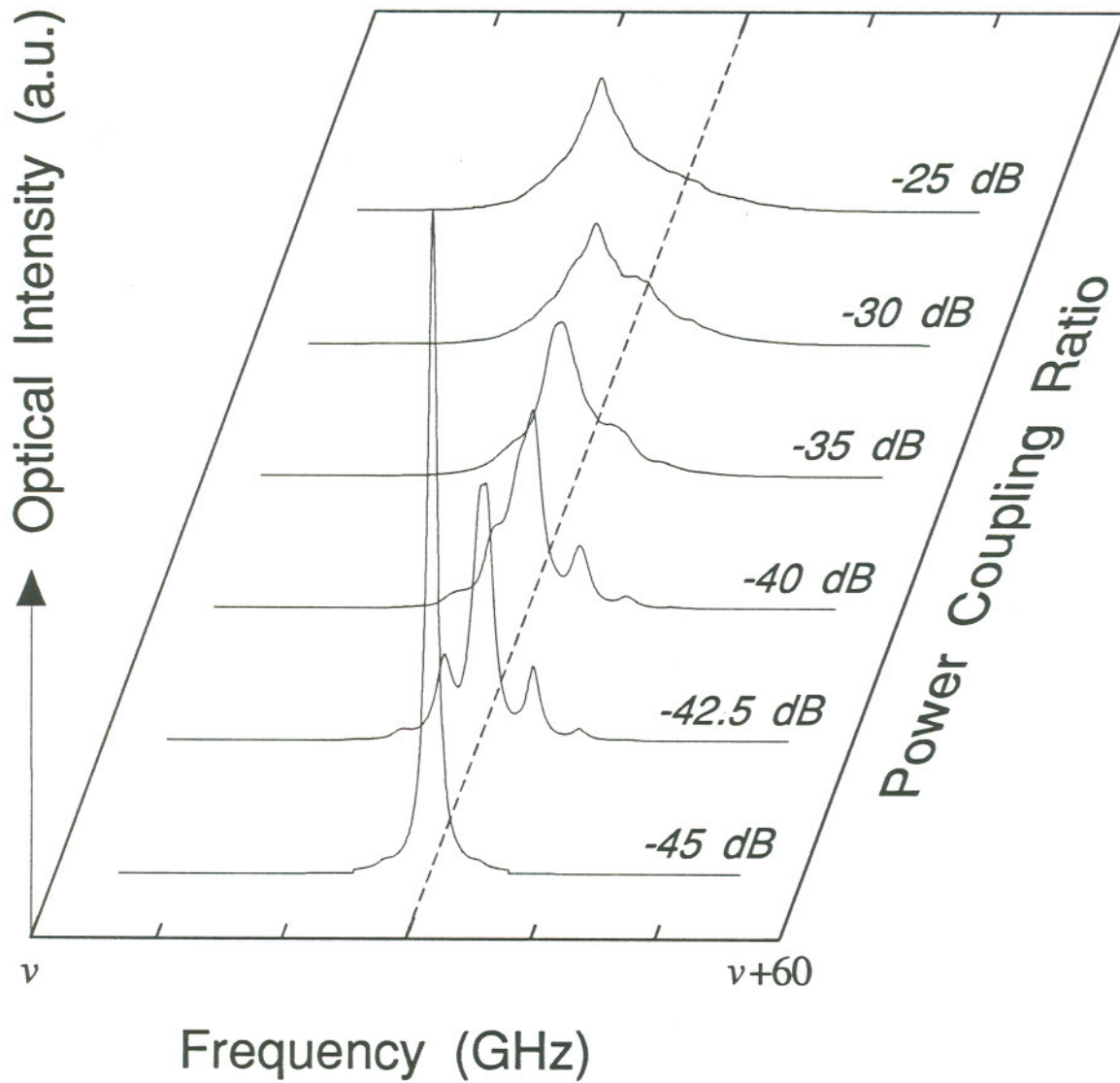


Figure 4.23 Numerically simulated optical spectra of two mutually coupled semiconductor lasers during overcoupling. 45 cm laser separation.

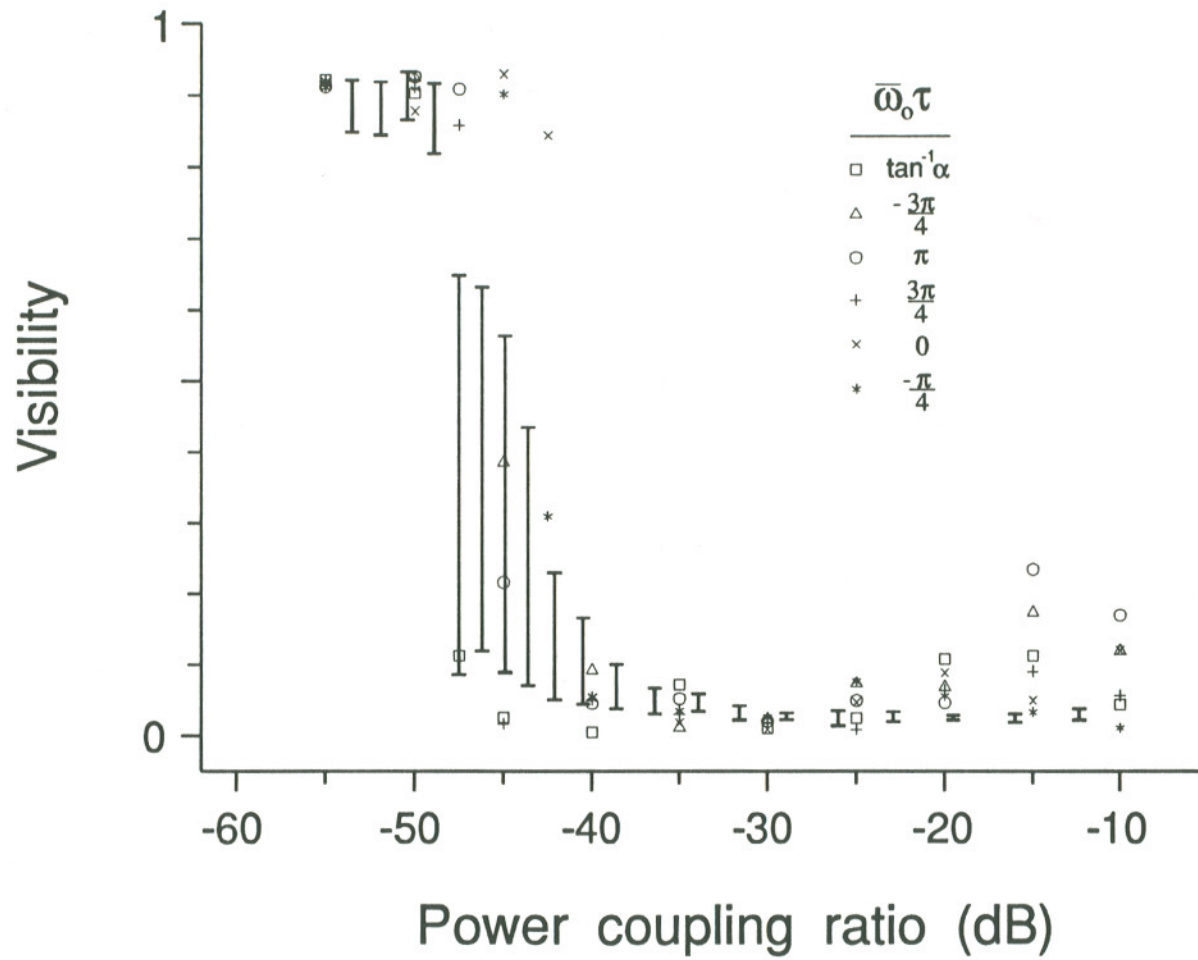


Figure 4.24 Visibility versus power coupling ratio for two mutually coupled TJS lasers. Numerically generated values at selected laser separations are represented by the given symbols. Vertical bars denote the maximum and minimum experimentally measured visibilities.

given coupling level, as it became difficult, if not impossible, to relate the laser separation to a specific value of $\bar{\omega}_o\tau$ well into the instability. Ideally, theoretical visibilities should fall within these bounds. So that a direct comparison could be made, the numerical visibilities were compensated for the spontaneous emission background of the TJS lasers using equation (C.12). Further, experimental values were adjusted, as described in Appendix C, for the incoherent contribution of secondary longitudinal diode modes due to pathlength differences.

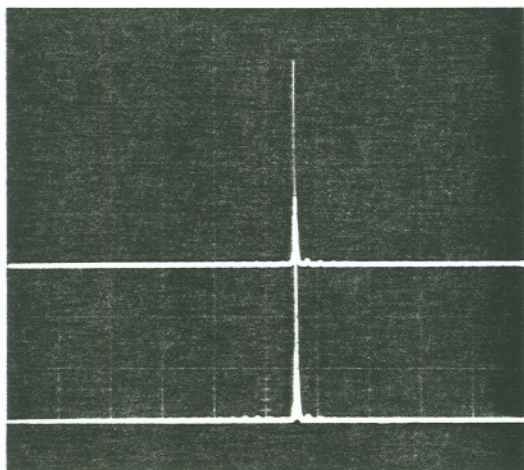
Figure 4.24 shows that high-visibility, quality phase locks can be obtained at power coupling ratios ranging from -60 to -50 dB. As detailed in Section 4.3, the system oscillates in a single, narrowed longitudinal mode here, with very little dependence on the value of $\bar{\omega}_o\tau$. At approximately -48 dB, however, a dramatic drop-off in coherence is observed, accompanying the undamped relaxation oscillation sidebands and spectral filling, as shown in Figures 4.22 and 4.23. This critical coupling level approximately corresponds to that given by equation (2.4.22), after accounting for nonlinear gain. A self-saturation coefficient of $\beta_{oo} = 6.8 \times 10^{-8}$ was used in the numerical simulations throughout this section for the TJS lasers. In contrast to the operation below -48 dB, during the transition from a state of high to low coherence, the visibility depends sensitivity on $\bar{\omega}_o\tau$. Numerical values range from a few percent to over 90 percent at a given power coupling ratio. This behavior is later shown to result from differing stability properties of the available modes at a specific coupling phase. Experimentally measured visibilities do not exhibit quite as large a variation during the transition, probably because the discrete laser separations addressed with the piezoelectric translator in Figure 4.3 "stepped over" these very coherent

states.

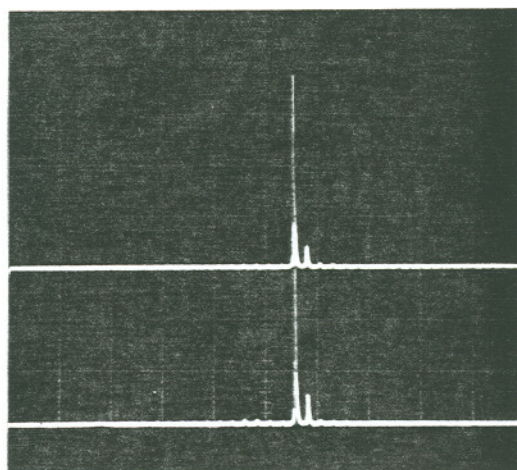
As the power coupling ratio was further increased, the visibility continued to reduce, and became relatively independent of $\bar{\omega}_o\tau$. At -30 dB, Figure 4.24 shows an almost total loss of coherence between the lasers. To this point the figure demonstrates a reasonable agreement between the calculated and experimentally measured values. Numerical simulations, however, show a partial recovery in the visibility above -30 dB which is not observed experimentally. The discrepancy can be explained as a result of the emergence of additional longitudinal diode modes, as shown in Figure 4.25. Part a) displays the isolated optical spectra of each laser, one above the other, taken with a 0.75 m grating spectrometer. The dominant single mode of each laser has been temperature tuned to spectral coincidence. At a -42 dB power coupling ratio, shown in part b), a second mode emerges. Evidently, the difference in gain between the modes due to spectral gain roll-off is not sufficient to maintain mode suppression during the highly dynamic instability. The converse is not true; instability is already well-developed at this point and cannot be attributed to the emergence of this mode.

The mode suppression further reduces at larger coupling levels, with several modes oscillating at -32 dB, as shown in Figure 4.25 d). The diode mode spectrum remained essentially unchanged with larger power coupling. The width of the spectral envelope above -32 dB requires a pathlength difference $\ll 100\mu\text{m}$, in order to avoid degradation of the interference fringes due to the temporal coherence limitation. Experimentally, however, the optical pathlengths to the interference plane were not matched to this tolerance. Therefore, any rise in visibility beyond a -30 dB power coupling ratio that may

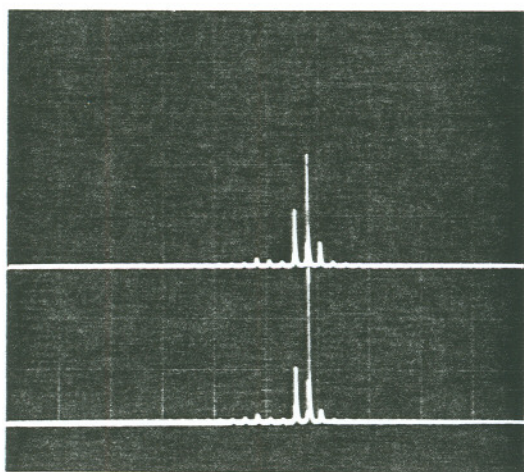
a) UNCOUPLED



b) -42 dB



c) -38 dB



d) -32 dB

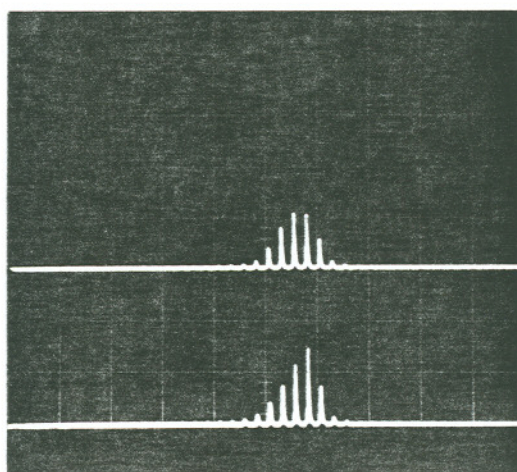


Figure 4.25 Longitudinal diode mode spectra during overcoupling.

have occurred would not appear in experimental measurements of Figure 4.24. The numerical visibilities were calculated by assuming a zero pathlength difference to the interference plane, and are furthermore based on single longitudinal mode rate equations. It is not clear whether a partial recovery in coherence would be observed experimentally at large coupling levels. One thing is certain: the lasers do not return to stable, phase-locked operation.

It was also found that, although the coherence was poor during overcoupling, the lasers remained spectrally locked. By blocking the emission of one laser before the Fabry-Perot interferometer, for example, the spectrum in Figure 4.22 was reduced uniformly in intensity while retaining the same overall structure. This implies that the overcoupled lasers operated with identical spectra, and is clearly the case in the diode mode spectra of Figure 4.25. Furthermore, when the current in one laser was adjusted slightly, thereby tuning its spectrum, the other laser followed precisely. Spectral locking, however, does not necessarily imply phase-locking, as the visibility measurements confirm.

The largely unstable behavior shown in Figure 4.24 for the two mutually coupled semiconductor lasers differs from the small signal analysis investigated in Section 2.4 for no coupling delays. In that case, large areas of $\bar{\eta}$ space were found to be dynamically stable, especially at strong coupling levels. Here, to the contrary, stability is limited to weak coupling exclusively, and becomes virtually independent of coupling phase. This difference is attributable to multistability introduced by the coupling delay. Figure 4.26 displays the modes of the mutually coupled TJS lasers during overcoupling, corresponding to the case of Figure 4.24. Part b) shows them in terms of the phase $\bar{\omega}_0\tau$, while part a) fixes their locations in the $\bar{\eta}$ plane at an arbitrarily chosen piston location. Squares

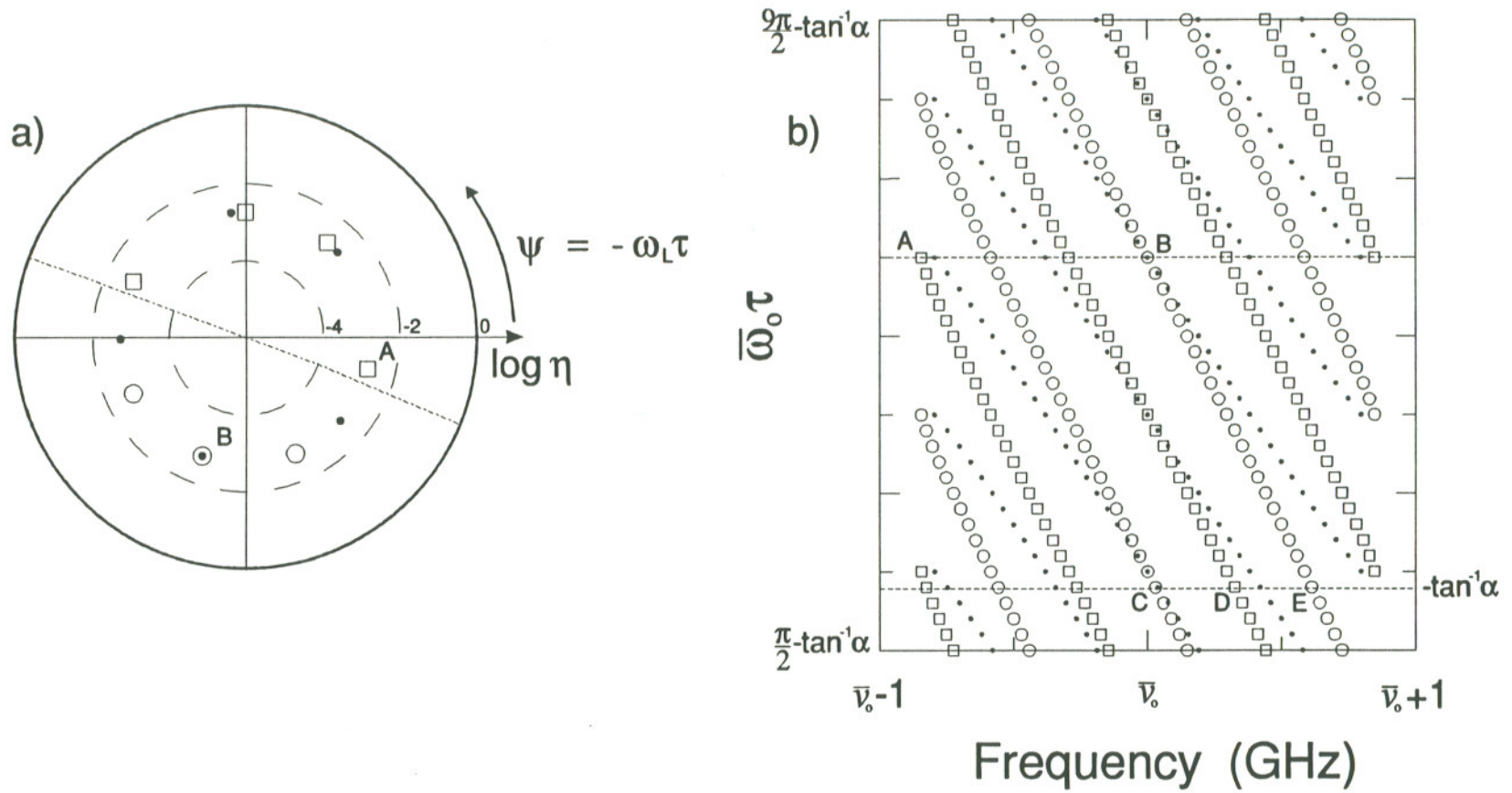


Figure 4.26 Modes of two mutually coupled TJS lasers in the overcoupling regime. 45 cm laser separation, -45 dB power coupling ratio. \square $\Delta\phi_L = 0$, \circ $\Delta\phi_L = \pi$, \bullet unstable.

denote even modes, circles are odd and solid dots are modes which do not meet the stability criterion (4.1.21). This criterion divides the $\bar{\eta}$ plane into two halves separated by the dashed line in Figure 4.26 a), above which the odd mode is unstable, and below which the even mode is unstable.

It is clear that several stable modes are available at a given $\bar{\omega}_o\tau$, and are spread throughout the $\bar{\eta}$ plane. Each mode therefore possesses a different coupling phase and different stability properties. The mode labeled "A" in the figures, for example, has the lowest threshold gain, while mode "B" is the most stable, as discussed earlier. This is in contrast to the results of Section 2.4, where the two modes of the coupled system were never bistable. Since the modes rotate on a constant η contour in Figure 4.26 a) as $\bar{\omega}_o\tau$ is changed, their stability properties are also a function of $\bar{\omega}_o\tau$.

The rate equations (4.1.1) and (4.1.2), describing mutually delay-coupled lasers, can be linearized in the same way as the self-coupled laser in Section 3.7. Determining stability boundaries, on the other hand, becomes analytically untractable, due to the necessity to retain all six equations. A number of inferences regarding the effect of the time delay, however, can be made from the results of Section 3.7. Recall that the modes of a self-coupled system are identical to those of the even mode shown in Figure 4.26. Based on the stability boundaries displayed in Figure 3.27, it should then be possible to piston the cavity to a point where a single mode is stable (mode "A" in Figure 4.26, for example). This was not the case experimentally, or in the numerical simulations, as dynamic instability was found to exist independent of $\bar{\omega}_o\tau$. Hence, although the small-signal linearized rate equations nicely predict the critical coupling level for relaxation oscillation undamping, it appears that the full

nonlinear rate equations are necessary to adequately describe the large signal operation of the delay-coupled system in regimes of dynamic instability. Numerical analysis of the full nonlinear rate equations is therefore relied on in the remainder of this section. While more time-consuming, it does present a complete description of the problem from which to infer parameter dependencies and analyze dynamics.

Figure 4.27 shows numerically integrated time series depicting the dynamic operation of the mutually coupled lasers during overcoupling. The laser separation is chosen as 45 cm to compare to Figure 4.24 and experiment, while the power coupling ratio is -45 dB, just after the lasers began exhibiting self-pulsations. The modes available to the system at the phase $\bar{\omega}_o \tau = \tan^{-1} \alpha$, used in this example, are indicated in Figure 4.26. These (C,D,E) were identified from the slope of their individual phase time series, which gives the oscillation frequency deviation from the average isolated value. Abrupt transitions are clearly evident in Figure 4.27. Hopping occurs between even and odd modes of the compound laser, explaining the poor visibility in Figure 4.24. In the several cases examined at this stage of overcoupling, it was found that the coupled lasers prefer to oscillate in modes close to $\bar{\omega}_o$, rather than those of low threshold gain. Note the short-lived mode "E" in Figure 4.27 b), for example. The system will therefore dwell in these states for a longer time, which in the time-average appears very much like the experimental case of Figure 4.22. The presence of several compound cavity modes in the spectra suggests that however briefly, the system eventually samples all the states. Although spontaneous emission noise is included in the simulation of Figure 4.27, the transitions cannot be attributed to noise alone. Recall from Figure 4.13 that the noise was

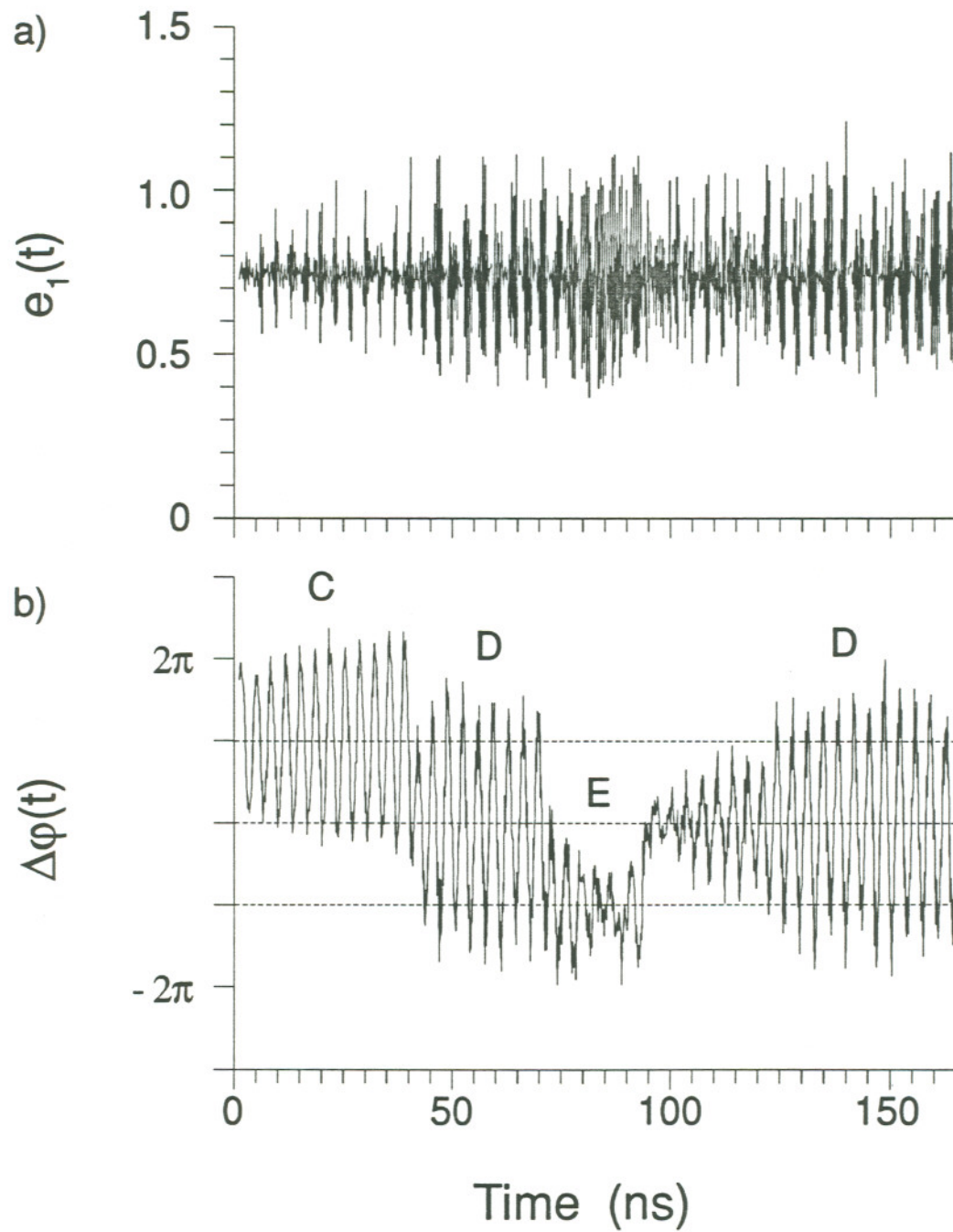


Figure 4.27 Dynamic operation of two mutually coupled TJS lasers in the overcoupling regime. -45 dB power coupling ratio, 45 cm laser separation.

insufficient to cause mode hops above a power coupling ratio of about -50 dB. Here, the system is continually sampling the different states of the system, while performing large relaxation oscillations in field, phase and carrier number. There are also strong oscillations at the mode spacing of the compound cavity.

The frequency of transitions increases as the power coupling ratio becomes larger, shortening the dwell time in each state. Figure 4.28 shows the dynamic operation of the coupled TJS lasers at -30 dB. The phase difference between the lasers appears to randomly fluctuate over many π , resulting in the near zero visibility of Figure 4.24. Although this behavior is reminiscent of phase-locking at very low, noise dominated coupling levels, noise again cannot be designated as the cause of the poor phase-locking. Amplitude variations no longer show well-developed relaxation oscillations, but rather, spike violently. The coherence between the lasers is naturally low at this stage of overcoupling, based on Figures 4.28. Coherence, however, improves beyond this point. Figure 4.29 shows typical operation at a power coupling ratio of -15 dB. Mode hopping is clearly indicated in part b). In contrast to Figure 4.27, transitions between states can now be accompanied by large phase slips (note the larger vertical scales). The states have distinctly different stability properties, with the amplitude displaying periods of low noise comparable to that of the isolated laser, followed by violent noise bursts.

The individual phases were found to have large negative slopes, indicating an oscillation frequency near the maximum negative excursion allowed by equation (3.1.7). This manifests in the pulled optical spectra described experimentally and theoretically in Figures 3.20, 3.21 and 4.23 at large coupling levels. The large slopes made it difficult to identify the exact operating states from the

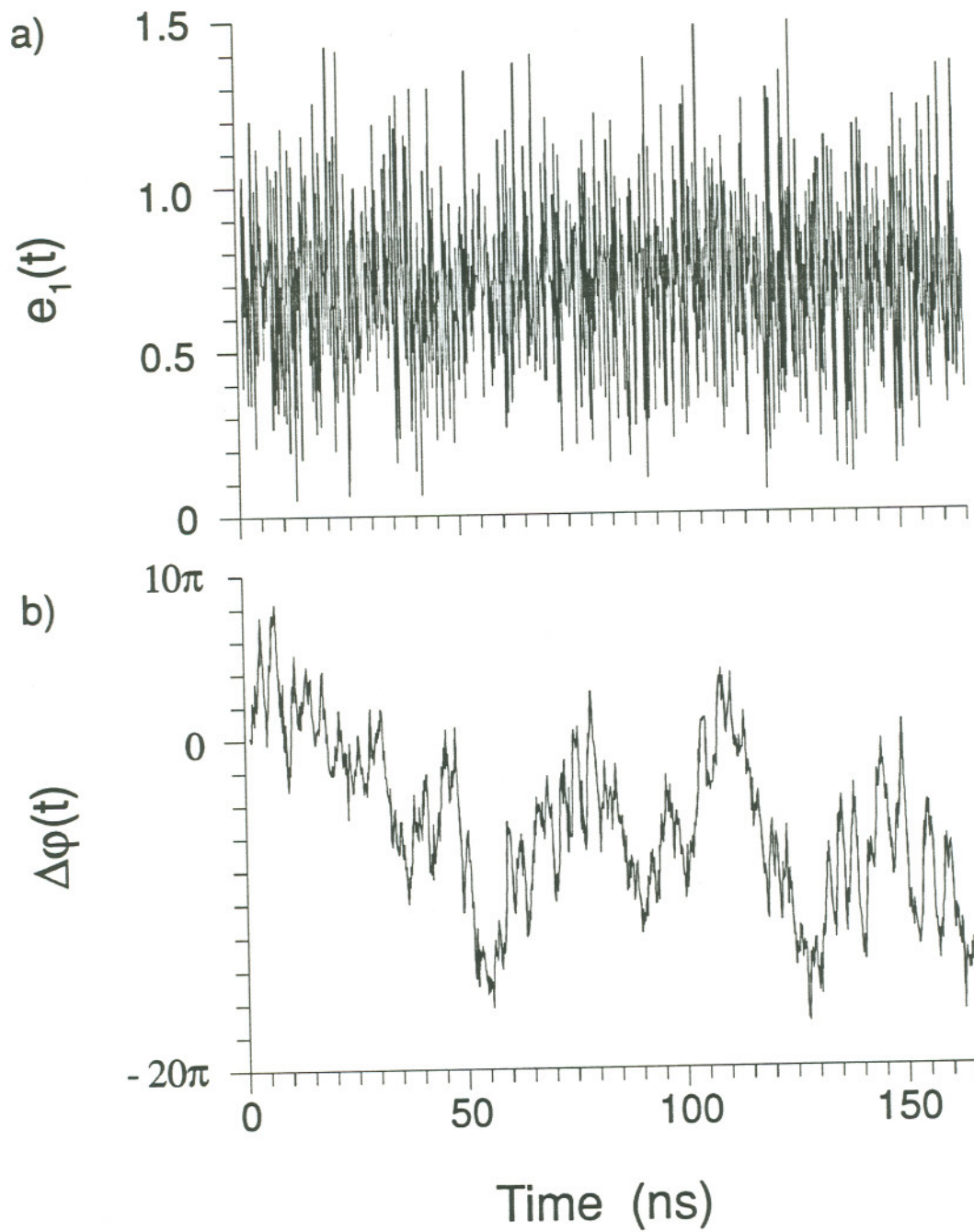


Figure 4.28 Dynamic operation of two mutually coupled TJS lasers in the overcoupling regime. -30 dB power coupling ratio, 45 cm laser separation.

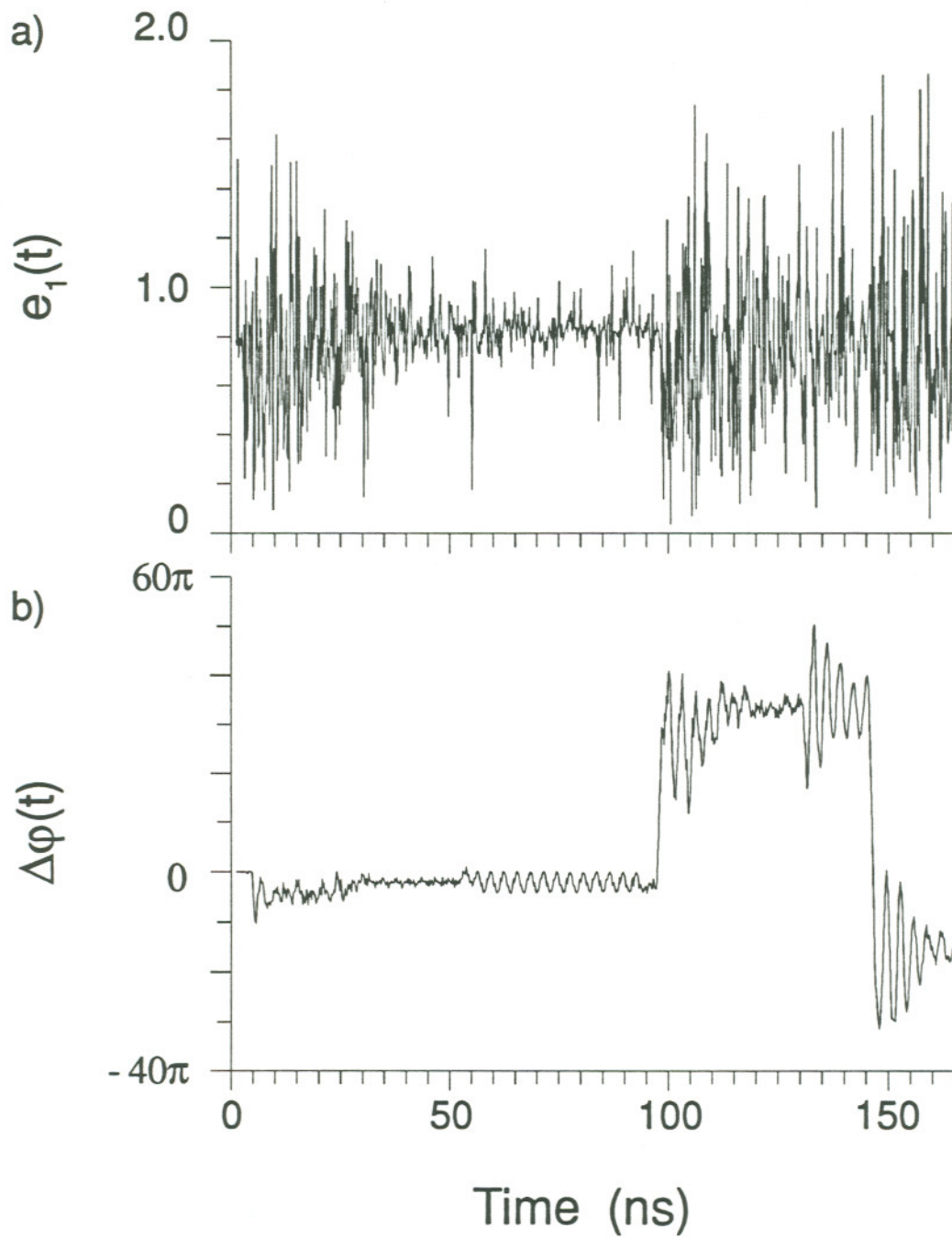


Figure 4.29 Dynamic operation of two mutually coupled TJS lasers in the overcoupling regime. -15 dB power coupling ratio, 45 cm laser separation.

large number available, as was done in Figure 4.27. Nevertheless, it is important that these lower frequency modes also possess the lowest threshold gains, and provide the largest damping against relaxation oscillations at this coupling level, according to the discussion in Section 2.4. The recovery in coherence is therefore attributable to a transition from a regime where gain differences are small and modes selected based on their phase stability, to one where stability and mode selection is dominated by threshold gain.

It has been demonstrated how the coupling delay τ is responsible for multiple modes and multistability in the present coupling configuration, which leads to very complicated dynamics above a critical coupling level. In the case of self-coupling, the coupling delay was further found to have a significant impact on the location of small signal stability boundaries. A resonance of the system was pulled toward the nearest external cavity mode. Stability improved the farther this frequency was from the relaxation oscillation frequency. This separation can be increased by shortening the coupling delay. Figure 4.30 shows the visibility for two mutually coupled diode lasers as a function of the coupling delay. Other than α , TJS parameters listed in Table E.1 were used in the calculations. The fine-scale laser separation was assumed to give $\bar{\omega}_o\tau = 0$, and η was set to 5×10^{-3} , where instability was the most severe. The value of α in the lasers is shown to be of the utmost importance to their stability.

With $\alpha=0$, for instance, the lasers show no sign of instability for any coupling delay. This is true even though, based on equation (4.1.8), multiple modes still are available. Furthermore, the critical η value given by (2.4.22) has been exceeded in Figure 4.30. The coupling of amplitude and phase fluctuations through the carrier number therefore appears to play the

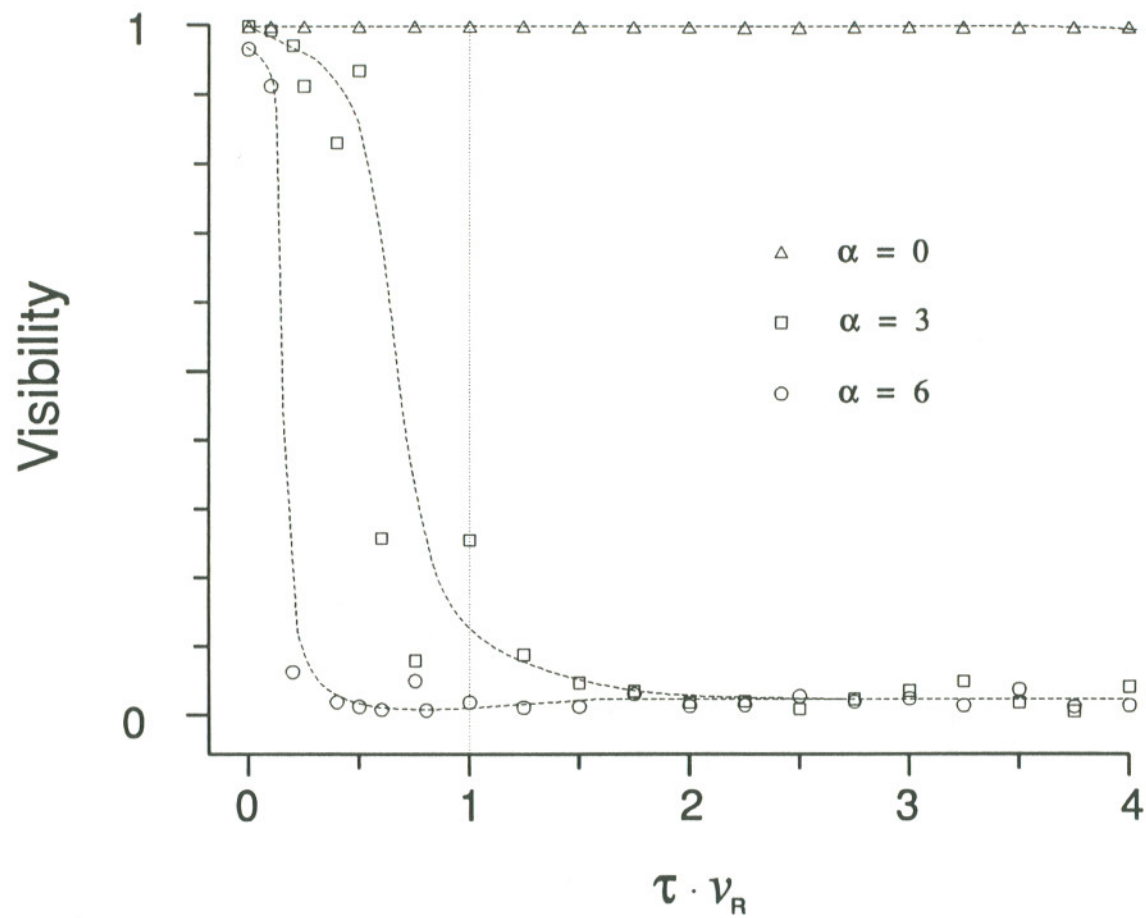


Figure 4.30 Numerically calculated visibility for two mutually coupled ML5101a TJS diode lasers versus coupling delay. -37 dB power coupling ratio, $\bar{\omega}_0\tau = 0$.

fundamental role in dynamic instability. This also implies that the overcoupling phenomenon is unique to semiconductor lasers, and does not explain instability in other types of coupled oscillators²²³. To the contrary, little or no coherence is obtained at this coupling level for large τ when α is non-zero. As expected, the visibility rises when the mode spacing is removed from the vicinity of the relaxation oscillation frequency, approaching one as the delay goes to zero. Stable operation, however, can also be limited by the onset of multiple modes, which is the case for $\alpha=6$ in the figure.

In the limit of zero coupling delay the number of allowed states in the system is reduced to two, the even and odd modes of the compound cavity. Figure 4.31 displays the visibility of two mutually coupled TJS lasers with $\tau=0$, at several different coupling phases. These were chosen to be representative of the even mode; the odd mode exhibits identical behavior. The graph confirms the stability boundaries shown in Figure 2.5. Note the reduction in visibility at low coupling levels due to spontaneous emission noise. Here, the most stable mode at $\tan^{-1}\alpha$ has the largest visibility, while the smallest belongs to the mode with lowest threshold gain. In contrast to the delay-coupled case, the system has no choice but to oscillate in the only stable mode available at a given coupling phase, regardless of its phase stability or threshold gain.

At intermediate coupling levels, except near $\psi_{cc}=0,\pi$, the visibility reduces to near zero, as was the case in Figure 4.24. Here, the optical spectrum was found to progressively broaden in a fashion similar to that demonstrated in Figures 3.21 and 4.23. Dynamics, however, are somewhat different than the mode hopping between stable states displayed in Figures 4.27 - 4.29. The system, instead of being multistable, has only two roots available, both unstable. Mode

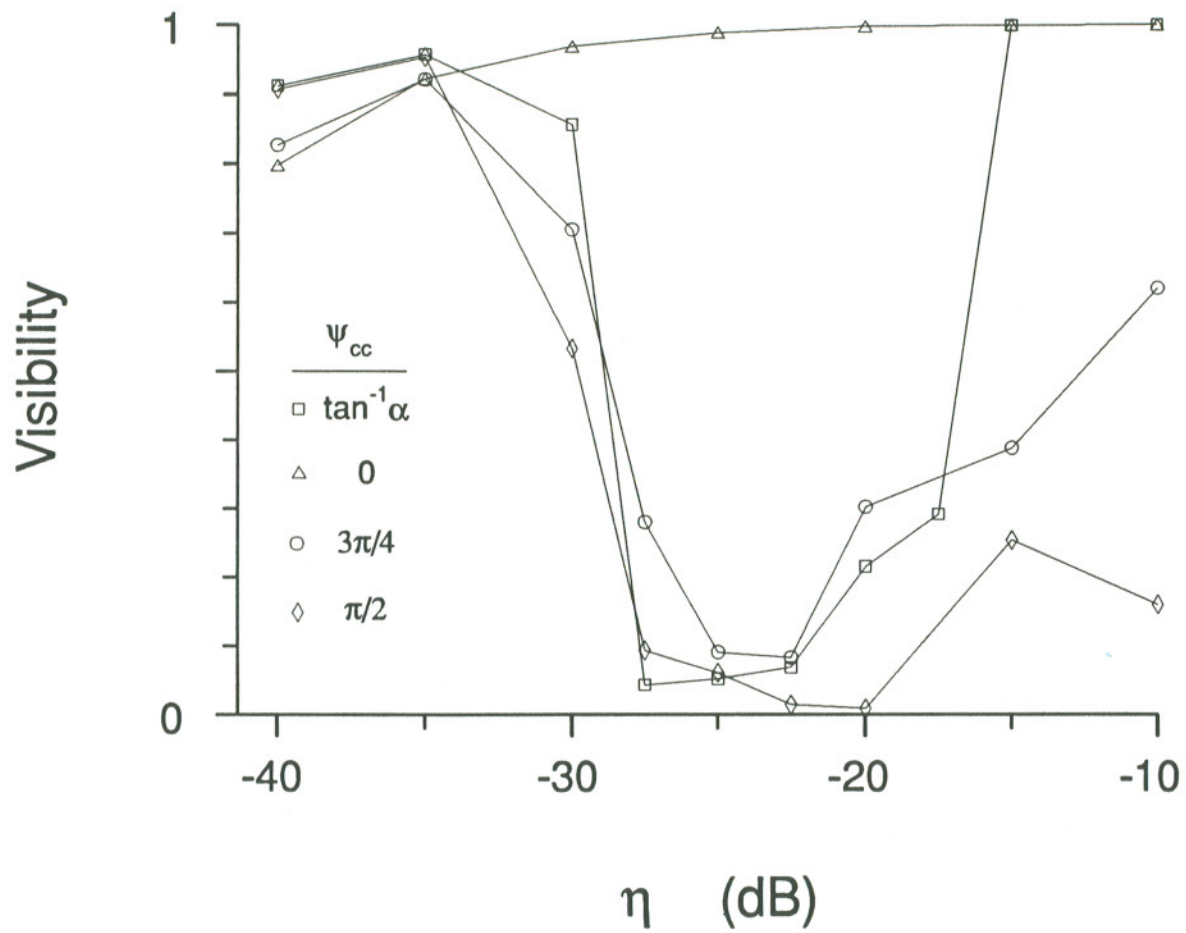


Figure 4.31 Numerically calculated visibility of two mutually coupled ML5101a TJS laser diodes with $\tau=0$.

hopping is therefore replaced by oscillations between these unstable states at the relaxation resonance frequency. Stability recovers above an η of 10^{-2} . Unlike the systems investigated in Chapters 3 and 4, however, recovery can be complete at coupling phases promoting a low threshold gain. "Overcoupling" is perhaps not a term appropriate to all mutually coupled systems of semiconductor lasers.

5. CONCLUSIONS

This research effort has investigated the stability of self and mutually coupled semiconductor diode lasers both theoretically and experimentally. The theoretical treatment was developed from time-dependent coupled mode theory, resulting in single-mode rate equations governing the time evolution of the optical field, phase and inversion in each laser. A carrier-dependent refractive index, nonlinear gain and spontaneous emission noise were included in the analysis, all of which were shown to have a significant impact on the stability properties of the coupled system. Throughout this dissertation, numerical simulations based on the coupled, noise-driven rate equations were demonstrated to give an adequate description of experimental results, justifying this approach. Stationary solution of the rate equations revealed the importance of the coupling phase and α parameter in determining phase-locking conditions for mutually coupled diode lasers. The locking bandwidth, for example, was shown to be a strong function of the coupling coefficient's phase. Previous analyses have been restricted to real coupling. Furthermore, due to α , the optimum lockband size was found to be incompatible with a large mode suppression ratio and power balance between the lasers.

Small signal stability properties of the coupled systems were also analyzed. Two distinct stability criteria were identified. The first confines stability to

coupling phases promoting constructive interference between the circulating and coupled fields in each laser. An unstable mode, in this case, corresponds to an eigenvalue of the system determinant on the positive real axis. Therefore, states not meeting this stability criterion do not represent oscillating modes of the compound laser cavity. Due to α , maximum stability is not obtained at the same phase which produces the lowest threshold gain. The second type of instability boundary is reached as a limit-cycle oscillation which, for $\eta \lesssim 10^{-2}$, is at or near the relaxation resonance frequency of the isolated laser diodes. Damping of relaxation oscillations, in coupled systems, was shown to be a function of coupling phase. The maximum damping rate for strong coupling occurs where the equilibrium carrier number is a minimum. Here, the location of stability boundaries was determined to be largely independent of α . For $\eta \lesssim 10^{-2}$, on the other hand, the location is shifted in phase by $-\tan^{-1}\alpha$, due to the carrier dependent refractive index.

These stability issues result in three distinctive operating regimes. First, for coupling levels satisfying $\eta < \gamma_0/\sqrt{1+\alpha^2}$, relaxation oscillations are well damped regardless of the coupling phase as a result of the lasers' intrinsic gain saturation. Therefore, stable operation is guaranteed in a mode of the coupled system regardless of the coupling phase. Based on comparison to experiment, however, it was concluded that this condition underestimates the critical value of η in real devices, due to the additional relaxation oscillation damping contribution of nonlinear gain compression. Spontaneous emission noise also affects the operation of the coupled system in this regime. Phase-locks and linewidths were shown to be quantum-limited below power coupling ratios of about 10^{-6} , with the most stable solutions existing at $\psi = m\pi + \tan^{-1}\alpha$ (which is also the

location of the maximum lockband). This left a ≈ 10 dB "window" of power coupling ratios for the experimental devices where quality locks and very narrow linewidths could be attained. Mode selection was experimentally shown to be determined by phase stability rather than the usual low threshold gain criterion in this regime, with mode hops initiated by spontaneous emission noise.

When the critical coupling level given above is exceeded, the coupled system may develop self-pulsations near the relaxation resonance frequency of the isolated laser. These oscillations drive very complicated dynamics, where the system exhibits frequent transitions between its different states. It was shown, however, that the coupled lasers still attempt to maintain the mode with the greatest phase stability. Dynamics quickly lead to a rapid decrease in correlation between the fields in each laser, reducing the coherence of the coupled system and broadening the lasing linewidth. The loss of coherence can become so severe that the lasers effectively look incoherent in the time average. At coupling levels $\eta \gtrsim 10^{-2}$, damping becomes large and dominant for coupling phases promoting the lowest carrier number. This effect was found to lead to a partial or even full recovery of stability at many coupling phases. Threshold gain, as opposed to phase stability, was shown to be the dominant mechanism for mode selection in this operating regime.

The dynamic instability described above does not occur when the α parameter is zero. In this case, the stability boundary relating to self-pulsation lies entirely inside the $\Omega=0$ instability region, and the system is stable in one of the compound cavity modes for any coupling phase. The overcoupling instability in semiconductor lasers is therefore of a different nature than instabilities encountered in other types of coupled oscillators²²². Another benefit of a zero α is

that the mode with the lowest threshold gain also possesses the greatest stability against phase perturbations and the maximum damping rate of relaxation oscillations at all η .

The coupled systems of diode lasers investigated experimentally incorporated non-negligible coupling delays, resulting in multiple compound cavity modes. These modes were shown to be multistable, affecting mode selection in the system. More importantly, a multiple of the mode spacing was near the relaxation resonance frequency of the individual lasers, which tended to drive self-pulsations in the coupled system. As a rule, stability was found to improve when $\Delta\nu_L \gg \nu_R$. This observation has severe consequences for the design of large, monolithic structures where mode spacings are typically on the order of the relaxation resonance frequency and threshold gain differences between the modes are small. However, even $\tau = 0$ does not guarantee stability for two mutually coupled semiconductor lasers. A collapse in coherence, equally as severe as in the delayed case, was shown to occur at moderate coupling levels.

This study has indicated mechanisms for instability in the two simplest systems of coupled semiconductor lasers. Since similar effects are expected to destabilize larger coupled arrays, the general problem of N coupled lasers begs to be theoretically analyzed. Recent stability analyses referenced in Chapter 1 are inadequate for modeling real devices due to the neglect of complex coupling, which has been shown to be of the utmost importance in this work. Another weakness of current dynamical models is that they are based in time-dependent coupled mode theory, limiting their applicability to weakly coupled systems. It may therefore be necessary to approach the problem from the composite resonator standpoint for some coupling schemes. Many real arrays also are

complicated by saturable absorption, nonuniform pumping, etc., which have yet to be addressed.

Future experimental research should focus on monolithic structures, where there is still a lack of correlation with theory. Here, the coupling coefficient is usually not controllable, at least not to the extent of the experiments in this work. The proper dimensions and growth parameters which enhance stable operation must be determined for *specific structures*, and verified experimentally. Resonant optical waveguide (ROW) arrays, for example, are promising candidates for exhibiting stable operation, and definitely deserve attention. On the other hand, it should be possible to demonstrate, in a monolithic array, the same spectral broadening and lack of coherence at moderate coupling levels encountered in this work. Such a device would enable an interesting experimental investigation of nonlinear dynamics and chaos in an optical system.

In closing, the author wishes to point out that while this dissertation has heavily emphasized the instabilities associated with the α parameter in coupled systems of semiconductor lasers, to say that these are "intrinsically unstable"²²⁸ is perhaps an overstatement. Large regions of η space exhibit stable operation, especially for strong, in-phase coupling. Here, visibilities near one and linewidths many times smaller than natural can, and have been, achieved. In the author's opinion, the factors affecting dynamic instability outlined in this thesis may all be overcome in a properly designed resonator. The ongoing development of low α gain media such as quantum-well and strained-layer material certainly is of benefit. The main obstacles to the realization of high power coupled arrays of semiconductor lasers may lie in much more practical matters, such as material uniformity and thermal variations across the wafer.

References

1. See references 136-159, for example.
2. C. Lin, C. A. Burrus, and L. A. Coldren, "Characteristics of single-longitudinal-mode selection in short-coupled-cavity (SCC) injection lasers," *J. Lightw. Techn.*, vol. LT-2, pp. 544-549, August 1984.
3. J. P. van der Ziel and R. M. Mikulyak, "Single-mode operation of 1.3 μ m InGaAsP/InP buried crescent lasers using a short external optical cavity," *IEEE J. Quantum Electron.*, vol. QE-20, pp. 223-229, March 1984.
4. C. H. Henry and R. F. Kazarinov, "Stabilization of single frequency operation of coupled-cavity lasers," *IEEE J. Quantum Electron.*, vol. QE-20, pp. 733-744, July 1984.
5. T.-P. Lee and C. A. Burrus, "An investigation of the frequency stability and temperature characteristics of 1.5 μ m coupled-cavity injection lasers," *IEEE J. Quantum Electron.*, vol. QE-20, pp. 374-384, April 1984.
6. L. A. Coldren and T. L. Koch, "Analysis and design of coupled-cavity lasers- Part I: Threshold gain analysis and design guidelines," *IEEE J. Quantum Electron.*, vol. QE-20, pp. 659-670, June 1984.
7. W. Streifer, D. Yevick, T. L. Paoli, and R. D. Burnham, "An analysis of cleaved coupled-cavity lasers," *IEEE J. Quantum Electron.*, vol. QE-20, pp. 754-764, July 1984.
8. L. A. Coldren and T. L. Koch, "Analysis and design of coupled-cavity lasers- part II: transient analysis," *IEEE J. Quantum Electron.*, vol. QE-20, pp. 671-682, June 1984.
9. W. Streifer, D. Yevick, T. L. Paoli, and R. D. Burnham, "Analysis of cleaved coupled-cavity (C^3) diode lasers- part II: frequency modulation, above threshold operation, and residual amplitude modulation," *IEEE J. Quantum Electron.*, vol. QE-21, pp. 539-550, June 1985.
10. G. P. Agrawal, "Coupled-cavity semiconductor lasers under current modulation: small-signal analysis," *IEEE J. Quantum Electron.*, vol. QE-21, pp. 255-263, March 1985.
11. See also papers referenced in 2-10. The explosion of papers regarding coupled-cavity lasers in and about 1984 is too lengthy to enumerate.
12. G. H. B. Thompson, *Physics of Semiconductor Laser Devices*, Wiley, Chichester, 1980.
13. D. R. Scifres, W. Streifer, R. D. Burnham, T. L. Paoli, and C. Lindstrom, "Near-field and far-field patterns of phase-locked semiconductor laser arrays," *Appl. Phys. Lett.*, vol. 42, pp. 495-497, 15 March 1983.
14. D. Botez and J. C. Connolly, "High-power phase-locked arrays of index-guided diode lasers," *Appl. Phys. Lett.*, vol. 43, pp. 1096-1098, 15 December 1983.
15. Y. Twu, A. Dienes, S. Wang, and J. R. Whinnery, "High power coupled ridge waveguide semiconductor laser arrays," *Appl. Phys. Lett.*, vol. 45, pp.

709-711, 1 October 1984.

16. E. Kapon, L. T. Lu, Z. Rav-Noy, M. Yi, S. Margalit, and A. Yariv, "Phased arrays of buried-ridge InP/InGaAsP diode lasers," *Appl. Phys. Lett.*, vol. 46, pp. 136-138, 15 January 1985.
17. L. J. Mawst, D. Botez, and T. J. Roth, "High-power, diffraction-limited-beam operation from diode-laser phase-locked arrays operating in coupled first-order modes," *Appl. Phys. Lett.*, vol. 53, pp. 1236-1238, 3 October 1988.
18. W. Streifer, D. F. Welch, P. S. Cross, and D. R. Scifres, "Y-junction semiconductor laser arrays: Part I - Theory," *IEEE J. Quantum Electron.*, vol. QE-23, pp. 744-751, June 1987.
19. D. F. Welch, W. Streifer, P. S. Cross, and D. R. Scifres, "Y-Junction semiconductor laser arrays: Part II - experiments," *IEEE J. Quantum Electron.*, vol. QE-23, pp. 752-756, June 1987.
20. D. Mehuys, K. Mitsunaga, L. Eng, W. K. Marshall, and A. Yariv, "Supermode control in diffraction-coupled semiconductor laser arrays," *Appl. Phys. Lett.*, vol. 53, pp. 1165-1167, 26 September 1988.
21. J. Z. Wilcox, W. W. Simmons, D. Botez, M. Jansen, L. J. Mawst, G. Peterson, T. J. Wilcox, and J. J. Yang, "Design considerations for diffraction coupled arrays with monolithically integrated self-imaging cavities," *Appl. Phys. Lett.*, vol. 54, pp. 1848-1850, 8 May 1989.
22. M. Orenstein, E. Kapon, J. P. Harbison, L. T. Florez, and N. G. Stoffel, "Phase locking of large two-dimensional arrays of vertical cavity surface-emitting lasers," *CLEO Technical Digest 1991*, vol. 10, pp. 342-343, Baltimore, MD, May 12-17 1991.
23. D. Botez, L. J. Mawst, G. Peterson, and T. J. Roth, "Resonant optical transmission and coupling in phase-locked diode laser arrays of antiguides: The resonant optical waveguide array," *Appl. Phys. Lett.*, vol. 54, pp. 2183-2185, 29 May 1989.
24. D. Botez, L. Mawst, G. L. Peterson, and T. J. Roth, "Phase-locked arrays of antiguides: Modal content and discrimination," *IEEE J. Quantum Electron.*, vol. 26, pp. 482-495, March 1990.
25. C. J. Chang-Hasnain, A. Dienes, J. F. Whinnery, W. Streifer, and D. R. Scifres, "Characteristics of the off-centered apertured mirror external cavity laser array," *Appl. Phys. Lett.*, vol. 54, pp. 484-486, 6 February 1989.
26. R. Waarts, D. Mehuys, D. Nam, D. Welch, W. Streifer, and D. Scifres, "900 mW, cw nearly diffraction-limited output from a GaAlAs semiconductor laser array in an external Talbot cavity," *CLEO 1991 Technical Digest*, vol. 10, p. 242, Baltimore, MD, May 12-17 1991. paper CWE7
27. G. A. Evans, N. W. Carlson, J. M. Hammer, M. Lurie, J. K. Butler, S. L. Palfrey, R. Amantea, L. A. Carr, F. Z. Hawrylo, E. A. James, C. J. Kaiser, J. B. Kirk, and W. F. Reichert, "Two dimensional coherent laser arrays using grating surface emission," *IEEE J. Quantum Electron.*, vol. 25, pp. 1525-1538, June 1989.

28. R. K. DeFreez, H. Ximen, D. J. Bossert, J. M. Hunt, G. A. Wilson, R. A. Elliott, J. Orloff, G. A. Evans, N. W. Carlson, M. Lurie, J. M. Hammer, D. P. Bour, S. L. Palfrey, and R. Amantea, "Spectral locking in an extended area two-dimensional coherent grating surface emitting laser array," *IEEE Photon. Techn. Lett.*, vol. 1, pp. 6-8, January 1990 .
29. D. J. Bossert, R. K. DeFreez, H. Ximen, R. A. Elliott, J. M. Hunt, G. A. Wilson, J. Orloff, G. A. Evans, N. W. Carlson, M. Lurie, J. M. Hammer, D. P. Bour, S. L. Palfrey, and R. Amantea, "Grating surface emitting lasers in a ring configuration," *Appl. Phys. Lett.*, vol. 56, pp. 2068-2070, 21 May 1990 .
30. D. Botez, L. Mawst, P. Hayashida, T. J. Roth, and E. Anderson, "Stable, single-(array)-mode operation from phase-locked, interferometric arrays of index-guided AlGaAs/GaAs diode lasers," *Appl. Phys. Lett.*, vol. 52, pp. 266-268, 25 January 1988.
31. L. J. Mawst, D. Botez, T. J. Roth, G. Peterson, and J. J. Yang, "Diffraction-coupled, phase-locked arrays of antiguided quantum-well lasers grown by metalorganic chemical vapor deposition," *Electron. Lett.*, vol. 24, pp. 958-959, 21 July 1988.
32. T.-S. Lay, S.-C. Lee, and H.-H. Lin, "Y-junction and misaligned-stripe diode laser arrays with nonuniform reflective diffraction coupler," *IEEE J. Quantum Electron.*, vol. 25, pp. 689-695, April 1989.
33. G. A. Evans, N. W. Carlson, J. M. Hammer, M. Lurie, J. K. Butler, J. Connolly, L. A. Carr, F. Z. Hawrylo, E. A. James, C. J. Kaiser, J. B. Kirk, and W. F. Reichert, "Two-dimensional, coherent Y-coupled grating surface-emitting laser arrays," *Electron. Lett.*, vol. 25, pp. 597-599, 27 April 1989.
34. G. A. Evans, D. P. Bour, N. W. Carlson, R. Amantea, J. M. Hammer, H. Lee, M. Lurie, R. C. Lai, P. F. Pelka, R. E. Farkas, J. B. Kirk, S. K. Liew, W. F. Reichert, C. A. Wang, H. K. Choi, J. N. Walpole, J. K. Butler, W. F. Ferguson, R. K. DeFreez, and M. Felisky, "Characteristics of coherent two-dimensional grating surface emitting diode laser arrays during CW operation," *IEEE J. Quantum Electron.*, vol. 27, pp. 1594-1608, June 1991.
35. See, for example, CLEO 1991 Technical Digest, volume 10, session CWE.
36. D. Botez, L. J. Mawst, M. Jansen, G. Peterson, and T. J. Roth, "High diffraction-limited powers from resonant arrays of antiguides," *Proceedings CLEO*, Baltimore, MD, 12-17 May 1991. paper CWE1
37. B. van der Pol, "The nonlinear theory of electric oscillations," *Proc. Inst. Radio Eng.*, vol. 22, pp. 1051-1086, September 1934.
38. R. Adler, "A study of locking phenomena in oscillators," *Proc. IRE*, vol. 34, pp. 351-357, June 1946.
39. R. Adler, "A study of locking phenomena in oscillators," *Proc. IEEE*, vol. 61, pp. 1380-1385, October 1973.
40. K. Kurokawa, "Injection locking of microwave solid-state oscillators," *Proc. IEEE*, vol. 61, pp. 1386-1410, October 1973. and references cited within.

41. N. Minorsky, *Introduction to non-linear mechanics*, J. W. Edwards, Ann Arbor, MI, 1947.
42. R. H. Pantell, "The laser oscillator with an external signal," *Proc. IEEE*, vol. 53, pp. 474-477, May 1965.
43. H. L. Stover and W. H. Steier, "Locking of laser oscillators by light injection," *Appl. Phys. Lett.*, vol. 8, pp. 91-93, February 1966.
44. C. L. Tang and H. Statz, "Phase-locking of laser oscillators by injected signal," *J. Appl. Phys.*, vol. 38, pp. 323-324, January 1967.
45. C. J. Buczek and R. J. Freiberg, "Hybrid injection locking of higher power CO₂ lasers," *IEEE J. Quantum Electron.*, vol. QE-8, pp. 641-650, July 1972.
46. C. J. Buczek, R. J. Freiberg, and M. L. Skolnick, "Laser injection locking," *Proc. IEEE*, vol. 61, pp. 1411-1431, October 1973.
47. S. Kobayashi and T. Kimura, "Injection locking characteristics of an AlGaAs semiconductor laser," *IEEE J. Quantum Electron.*, vol. QE-16, pp. 915-917, September 1980.
48. S. Kobayashi and Y. Kimura, "Injection locking in AlGaAs semiconductor laser," *IEEE J. Quantum Electron.*, vol. QE-17, pp. 681-689, May 1981.
49. R. Lang, "Injection locking properties of a semiconductor laser," *IEEE J. Quantum Electron.*, vol. QE-18, pp. 976-983, June 1982.
50. G. R. Hadley, "Injection locking of diode lasers," *IEEE J. Quantum Electron.*, vol. QE-22, pp. 419-426, March 1986.
51. S. Kobayashi, J. Yamada, S. Machida, and T. Kimura, "Single-mode operation of 500 Mbit/s modulated AlGaAs semiconductor laser by injection locking," *Electron. Lett.*, vol. 16, pp. 746-748, 11 September 1980.
52. H. Nishimoto, H. Kuwahara, and M. Motegi, "Injection-locked 1.5 μm InGaAsP/InP lasers capable of 450 Mbit/s transmission over 106 km," *Electron. Lett.*, vol. 19, July 1983.
53. H. Toba, Y. Kobayashi, K. Yanagimoto, H. Nagai, and M. Nakahara, "Injection-locking technique applied to a 170 km transmission experiment at 445.8 Mbit/s," *Electron. Lett.*, vol. 20, pp. 370-371, April 1984.
54. N. A. Olsson, H. Temkin, R. A. Logan, L. F. Johnson, G. J. Dolan, J. P. van der Ziel, and J. C. Campbell, "Chirp-free transmission over 82.5 km of single mode fiber at 2 Gbit/s with injection locked DFB semiconductor lasers," *J. Lightw. Techn.*, vol. LT-3, pp. 63-66, June 1985.
55. S. Kobayashi and T. Kimura, "Optical phase modulation in an injection locked AlGaAs semiconductor laser," *IEEE J. Quantum Electron.*, vol. QE-18, pp. 1662-1669, October 1982.
56. L. Goldberg, H. F. Taylor, J. F. Weller, and D. R. Scifres, "Injection locking of coupled-stripe diode laser arrays," *Appl. Phys. Lett.*, vol. 46, pp. 236-238, 1 February 1985.
57. M. K. Chun, L. Goldberg, and J. F. Weller, "Injection-beam parameter optimization of an injection-locked diode-laser array," *Optics Lett.*, vol. 14, pp. 272-274, 1 March 1989.

58. N. W. Carlson, J. H. Abeles, D. P. Bour, S. K. Liew, W. F. Reichert, P. S. D. Lin, and A. S. Gozdz, "Demonstration of a monolithic grating-surface-emitting master-oscillator-cascaded power amplifier array," *IEEE Photon. Techn. Lett.*, vol. 2, pp. 708-710, October 1990.
59. D. Mehuys, R. Parke, R. G. Waarts, D. F. Welch, A. Hardy, William Streifer, and D. R. Scifres, "Characteristics of multistage monolithically integrated master oscillator power amplifiers," *IEEE J. Quantum Electron.*, vol. 27, pp. 1574-1581, June 1991.
60. M. B. Spencer and W. E. Lamb, Jr., "Theory of two coupled lasers," *Phys. Rev. A*, vol. 5, pp. 893-898, February 1972.
61. W. J. Fader, "Theory of two coupled lasers," *IEEE J. Quantum Electron.*, vol. QE-21, pp. 1838-1844, November 1985.
62. G. E. Palma and W. J. Fader, "Coupled resonator beam combining," *Proc. SPIE*, vol. 440, pp. 153-160, 1983.
63. R. K. DeFreez, N. Yu, D. J. Bossert, M. Felisky, G. A. Wilson, R. A. Elliott, H. G. Winful, G. A. Evans, N. W. Carlson, and R. Amantea, "Experimental characterization of the picosecond spatiotemporal properties of coherent semiconductor laser arrays," *Proceedings of the OSA Conference on Nonlinear Dynamics in Optical Systems*, Afton, Oklahoma, 4-8 June 1990. paper ThA1
64. N. Yu, R. K. DeFreez, D. J. Bossert, R. A. Elliott, H. G. Winful, and D. F. Welch, "Observation of sustained self-pulsation in CW operated flared Y-coupled laser arrays," *Electron. Lett.*, vol. 24, pp. 1203-1204, 15 September 1988.
65. R. K. DeFreez, D. J. Bossert, N. Yu, K. Hartnett, R. A. Elliott, and H. G. Winful, "Spectral and picosecond temporal properties of flared guide Y-coupled phase-locked laser arrays," *Appl. Phys. Lett.*, 12 December 1988.
66. R. A. Elliott, R. K. DeFreez, T. L. Paoli, R.D. Burnham, and W. Streifer, "Dynamic characteristics of phase-locked multiple quantum well injection lasers," *IEEE J. Quantum Electron.*, vol. QE-21, pp. 598-602, June 1985.
67. R. K. DeFreez, D. J. Bossert, N. Yu, J. M. Hunt, H. Ximen, R. A. Elliott, N. W. Carlson, M. Lurie, G. A. Evans, J. M. Hammer, D. P. Bour, S. L. Palfrey, R. Amantea, H. G. Winful, and S. S. Wang, "Picosecond optical properties of a grating surface emitting two-dimensional coherent laser array," *IEEE Photon. Techn. Lett.*, vol. 1, pp. 209-211, August 1989.
68. N. Yu, R. K. DeFreez, D. J. Bossert, G. A. Wilson, R. A. Elliott, S. S. Wang, and H. G. Winful, "Spatiospectral and picosecond spatiotemporal properties of a broad area operating channeled-substrate-planar laser array," *Appl. Optics*, vol. 30, pp. 2503-2513, 20 June 1991.
69. M. Felisky, R. K. DeFreez, G. A. Wilson, G. A. Evans, N. W. Carlson, S. K. Liew, R. Amantea, J. H. Abeles, C. A. Wang, H. K. Choi, J. N. Walpole, and H. G. Winful, "Dynamics of cw grating-surface-emitting laser arrays," *Proceedings CLEO*, Baltimore, MD, 12-17 May 1991. paper CWE6
70. F. Mogensen, H. Olesen, and G. Jacobsen, "Locking conditions and stability properties for a semiconductor laser with external light injection,"

- IEEE J. Quantum Electron.*, vol. QE-21, pp. 784-793, July 1985.
71. C. H. Henry, N. A. Olsson, and N. K. Dutta, "Locking range and stability of injection locked 1.54 μm InGaAsP semiconductor lasers," *IEEE J. Quantum Electron.*, vol. QE-21, pp. 1152-1156, August 1985.
 72. I. Petitbon, P. Gallion, G. Debarge, and C. Chabran, "Locking bandwidth and relaxation oscillations of an injection-locked semiconductor laser," *IEEE J. Quantum Electron.*, vol. 24, pp. 148-154, February 1988.
 73. D. Lenstra, B. H. Verbeek, and A. J. Den Boef, "Coherence collapse in single-mode semiconductor lasers due to optical feedback," *IEEE J. Quantum Electron.*, vol. QE-21, pp. 674-679, June 1985.
 74. R. O. Miles, A. Dandridge, A. B. Tveten, H. F. Taylor, and T. G. Giallorenzi, "Feedback-induced line broadening in cw channel-substrate planar laser diodes," *Appl. Phys. Lett.*, vol. 37, pp. 990-992, 1 December 1980.
 75. R. W. Tkach and A. R. Chraplyvy, "Regimes of feedback effects in 1.5- μm distributed feedback lasers," *Jour. Lightw. Tech.*, vol. LT-4, pp. 1655-1661, November 1986.
 76. C. H. Henry, "Theory of the linewidth of semiconductor lasers," *IEEE J. Quantum Electron.*, vol. QE-18, pp. 259-264, February 1982.
 77. S. S. Wang and H. G. Winful, "Dynamics of phase-locked semiconductor laser arrays," *Appl. Phys. Lett.*, vol. 52, pp. 1774-1776, 23 May 1988.
 78. H. G. Winful and L. Rahman, "Synchronized chaos and spatiotemporal chaos in arrays of coupled lasers," *Phys. Rev. Lett.*, vol. 65, pp. 1575-1578, 24 September 1990.
 79. L. Rahman and H. G. Winful, "Synchronization of chaotic orbits in semiconductor laser arrays," *OSA Proceedings on Nonlinear Dynamics in Optical Systems*, vol. 7, p. 110, Afton, OK, 4-8 June 1990.
 80. H. G. Winful and S. S. Wang, "Stability of phase locking in coupled semiconductor laser arrays," *Appl. Phys. Lett.*, vol. 53, pp. 1894-1896, 14 November 1988.
 81. P. K. Jakobsen, R. A. Indik, J. V. Moloney, A. C. Newell, H. G. Winful, and L. Raman, "Diode-laser array modes: discrete and continuous models and their stability," *J. Opt. Soc. Am. B*, vol. 8, pp. 1674-1680, August 1991.
 82. H. Statz and G. de Mars, *Quantum Electronics*, p. 530, Columbia University Press, New York, 1960.
 83. K. Y. Lau and A. Yariv, "High-frequency current modulation of semiconductor injection/ lasers," *Semiconductors and Semimetals*, vol. 22, pp. 69-152, Academic Press, Orlando, 1985.
 84. W. E. Lamb, "Theory of an optical maser," *Phys. Rev.*, vol. 134, pp. A1429-A1450, 15 June 1964.
 85. M. Sargent, M. O. Scully, and W. E. Lamb, *Laser physics*, Addison-Wesley, Reading, Mass., 1974.
 86. R. F. Kazarinov, C. H. Henry, and R. A. Logan, "Longitudinal mode self-stabilization in semiconductor lasers," *J. Appl. Phys.*, vol. 53, pp. 4631-4644, July 1982.

87. G. P. Agrawal and N. K. Dutta, *Long-Wavelength Semiconductor Lasers*, Van Nostrand Reinhold Co., New York, 1986.
88. B. Zee, "Broadening mechanism in semiconductor (GaAs) lasers: limitations to single mode power emission," *IEEE J. Quantum Electron.*, vol. QE-14, pp. 727-736, October 1978.
89. D. Kasemset and C. G. Fonstad, "Gain saturation in semiconductor lasers: theory and experiment," *IEEE J. Quantum Electron.*, vol. QE-18, pp. 1078-1083, July 1982.
90. Y. Nishimura and Y. Nishimura, "Spectral hole burning and nonlinear-gain decrease in a band-to-band transition semiconductor laser," *IEEE J. Quantum Electron.*, vol. QE-9, pp. 1011-1019, October 1973.
91. M. Asada and Y. Suematsu, "Density-matrix theory of semiconductor lasers with relaxation broadening model - Gain and gain-suppression in semiconductor lasers," *IEEE J. Quantum Electron.*, vol. QE-21, pp. 434-442, May 1985.
92. M. Yamada, "Theoretical analysis of nonlinear optical phenomena taking into account the beating vibration of the electron density in semiconductor lasers," *J. Appl. Phys.*, vol. 66, pp. 81-89, 1 July 1989.
93. G. P. Agrawal, "Gain nonlinearities in semiconductor lasers: Theory and application to distributed feedback lasers," *IEEE J. Quantum Electron.*, vol. QE-23, pp. 860-868, June 1987.
94. G. P. Agrawal, "Spectral hole-burning and gain saturation in semiconductor lasers: Strong-signal theory," *J. Appl. Phys.*, vol. 63, pp. 1232-1235, 15 February 1988.
95. A. P. Bogotov, P. G. Eliseev, and B. N. Sverdlov, "Anomalous interaction of spectral modes in a semiconductor laser," *IEEE J. Quantum Electron.*, vol. QE-11, pp. 510-515, July 1975.
96. H. Ishikawa, M. Yano, and M. Takusagawa, "Mechanism of asymmetric longitudinal mode competition in InGaAsP/InP lasers," *Appl. Phys. Lett.*, vol. 40, pp. 553-555, April 1982.
97. J. Manning, R. Olshansky, D. M. Fye, and W. Powazinik, "Strong influence of nonlinear gain on spectral and dynamic characteristics of InGaAsP lasers," *Electron. Lett.*, vol. 21, pp. 496-497, 23 May 1985.
98. M. Nakamura, K. Aiki, N. Chinone, R. Ito, and J. Umeda, "Longitudinal mode behavior of mode stabilized AlGaAs injection lasers," *J. Appl. Phys.*, vol. 49, pp. 4644-4648, September 1978.
99. G. P. Agrawal, "Effect of nonlinear gain on single-frequency behavior of semiconductor lasers," *Electron. Lett.*, vol. 22, pp. 696-697, 19 June 1986.
100. C.-Z. Guo, J.-S. Xie, and F. Shen, "Effects of nonlinear-gain on single longitudinal mode behavior of semiconductor lasers," *IEEE J. Quantum Electron.*, vol. QE-21, pp. 794-803, July 1985.
101. D. J. Channin, "Effect of gain saturation on injection laser switching," *J. Appl. Phys.*, vol. 50, pp. 3858-3860, June 1979.
102. M. J. Adams and M. Osinski, "Influence of spectral hole burning on quaternary laser transients," *Electron. Lett.*, vol. 19, pp. 627-628, 4 August

- 1983.
103. R. Olshansky, D. M. Fye, J. Manning, and C. B. Su, "Effect of nonlinear gain on the bandwidth of semiconductor lasers," *Electron. Lett.*, vol. 21, pp. 721-722, 15 August 1985.
 104. R. S. Tucker, "High speed modulation of semiconductor lasers," *IEEE J. Lightw. Techn.*, vol. LT-3, pp. 1180-1192, December 1985.
 105. T. L. Koch and R. A. Linke, "Effect of nonlinear gain reduction on semiconductor laser wavelength chirping," *Appl. Phys. Lett.*, vol. 48, pp. 613-615, 10 March 1986.
 106. Y. Arakawa and T. Takahashi, "Effect of nonlinear gain on modulation dynamics in quantum-well lasers," *Electron. Lett.*, vol. 25, pp. 169-170, 19 January 1989.
 107. X. Pan, H. Olsen, and B. Tromborg, "Influence of nonlinear-gain on modulation dynamics in quantum-well lasers," *Electron. Lett.*, vol. 26, pp. 1074-1076, July 1990.
 108. A. Yariv, *Optical Electronics*, 3rd ed., CBS College Publishing, New York, 1985.
 109. B. C. Johnson and A. Mooradian, "Observation of gain compression in a GaAlAs diode laser through a picosecond transmission measurement," *Appl. Phys. Lett.*, vol. 49, pp. 1135-1137, 3 November 1986.
 110. K. Petermann, *Laser Diode Modulation and Noise*, Kluwer Academic Publishers, Dordrecht, 1988.
 111. M. B. Spencer and W. E. Lamb, "Laser with a transmitting window," *Phys. Rev. A*, vol. 5, pp. 884-892, February 1972.
 112. K. J. Ebeling and L. A. Coldren, "Analysis of multielement semiconductor lasers," *J. Appl. Phys.*, vol. 54, pp. 2962-2969, June 1983.
 113. D. Marcuse and T.-P. Lee, "Rate equation model of a coupled-cavity laser," *IEEE J. Quantum Electron.*, vol. QE-20, pp. 166-176, February 1984.
 114. S. A. Shakir and W. W. Chow, "Semiclassical theory of coupled lasers," *Optics Lett.*, vol. 9, pp. 202-204, June 1984.
 115. R. J. Lang and A. Yariv, "Analysis of the dynamic response of multielement semiconductor lasers," *IEEE J. Quantum Electron.*, vol. QE-21, pp. 1683-1688, October 1985.
 116. W. W. Chow, "A composite-resonator mode description of coupled lasers," *IEEE J. Quantum Electron.*, vol. QE-22, pp. 1174-1183, August 1986.
 117. D. Marcuse, "Coupled mode theory of optical resonant cavities," *IEEE J. Quantum Electron.*, vol. QE-21, pp. 1819-1826, November 1985.
 118. R. P. Salathe, "Diode lasers coupled to external resonators," *Appl. Phys.*, vol. 20, pp. 1-18, January 1979.
 119. R. Lang and K. Kobayashi, "External optical feedback effects on semiconductor injection laser properties," *IEEE J. Quantum Electron.*, vol. QE-16, pp. 347-355, March 1980.

120. R. L. Lang and A. Yariv, "Coupling coefficients for coupled-cavity lasers," *IEEE J. Quantum Electron.*, vol. QE-23, pp. 287-289, March 1987.
121. H. Kressel and J. K. Butler, *Semiconductor Lasers and Heterojunction LEDs*, Academic Press, New York, 1977.
122. W. W. Chow, "Frequency locking in weakly coupled lasers," *Optics Lett.*, vol. 10, pp. 442-444, September 1985.
123. L. A. Zadeh and C. A. Desoer, *Linear system theory*, McGraw-Hill, New York, 1979.
124. H. K. Choi, K.-L. Chen, and S. Wang, "Analysis of two-section coupled-cavity semiconductor lasers," *IEEE J. Quantum Electron.*, vol. QE-20, pp. 385-393, April 1984.
125. R. W. Tkach and A. R. Chraplyvy, "Regimes of feedback effects in 1.5- μm distributed feedback lasers," *Jour. Lightw. Tech.*, vol. LT-4, pp. 1655-1661, November 1986.
126. D. Bossert, D. Gallant, and C. Moeller, "Mode selection in lasers with feedback," *21st Winter Colloquium on Quantum Electronics*, Snowbird, UT, January 6-9, 1991.
127. R. Lang and K. Kobayashi, "External optical feedback effects on semiconductor injection laser properties," *IEEE J. Quantum Electron.*, vol. QE-16, pp. 347-355, March 1980.
128. G. A. Acket, D. Lenstra, A. J. Den Boef, and B. H. Verbeek, "The influence of feedback intensity on longitudinal mode properties and optical noise in index-guided semiconductor lasers," *IEEE J. Quantum Electron.*, vol. QE-20, pp. 1163-1169, October 1984.
129. A. E. Siegman, *Lasers*, University Science Books, Mill Valley, 1986.
130. A. Yariv, *Optical Electronics*, 3rd ed., CBS College Publishing, New York, 1985.
131. G. P. Agrawal, "Line narrowing in a single-mode injection laser due to external optical feedback," *IEEE J. Quantum Electron.*, vol. QE-20, pp. 468-471, May 1984.
132. K. Petermann, *Laser Diode Modulation and Noise*, Kluwer Academic Publishers, Dordrecht, 1988.
133. K. Kikuchi and T. Okoshi, "Simple formula giving spectrum-narrowing ratio of semiconductor-laser output obtained by optical feedback," *Electron. Lett.*, vol. 18, pp. 10-12, 7 January 1982.
134. E. Patzak, H. Olesen, A. Sugimura, S. Saito, and T. Mukai, "Spectral linewidth reduction in semiconductor lasers by an external cavity with weak optical feedback," *Electron. Lett.*, vol. 19, pp. 938-940, 27 October 1983.
135. E. Patzak, A. Sugimura, S. Saito, T. Mukai, and H. Olesen, "Semiconductor laser linewidth in optical feedback configurations," *Electron. Lett.*, vol. 19, pp. 1026-1027, 24 November 1983.
136. C. J. Nielsen and J. H. Osmundsen, "Linewidth stabilization of semiconductor lasers in an external cavity," *J. Opt. Comm.*, vol. 5, pp. 42-45, 1984.

137. N. Schunk and K. Petermann, "Minimum bitrate of DPSK transmission for semiconductor lasers with a strong linewidth reduction," *J. Lightw. Techn.*, vol. LT-5, pp. 1309-1314, September 1987.
138. K.-Y. Liou and C. A. Burrus, "Spectral linewidth of a GRECC laser with added external cavity," *Electron. Lett.*, vol. 21, pp. 353-354, 11 April 1985.
139. T. P. Lee, S. G. Menocal, and H. Matsumura, "Characteristics of linewidth narrowing of a 1.5 μm DFB laser with a short GRIN-rod external coupled cavity," *Electron. Lett.*, vol. 21, pp. 655-656, 18 July 1985.
140. T. P. Lee, S. G. Menocal, S. Sakano, V. Valster, and S. Tsuji, "Linewidth and FM characteristics of a distributed feedback laser monolithically integrated with a tunable external cavity," *Electron. Lett.*, vol. 23, pp. 153-154, 12 February 1987.
141. S. Murata, S. Yamazaki, I. Mito, and K. Kobayashi, "Spectral characteristics for 1.3 μm monolithic external cavity DFB lasers," *Electron. Lett.*, vol. 22, pp. 1197-1198, 23 October 1986.
142. T. Fujita, J. Ohya, K. Matsuda, M. Ishino, H. Sato, and H. Serizawa, "Narrow spectral linewidth characteristics of monolithic integrated-passive-cavity InGaAsP/InP semiconductor lasers," *Electron. Lett.*, vol. 21, pp. 374-376, 25 April 1985.
143. O. Nilsson, S. Saito, and Y. Yamamoto, "Oscillation frequency, linewidth reduction and frequency modulation characteristics for a diode laser with external grating feedback," *Electron. Lett.*, vol. 17, pp. 589-591, 20 August 1981.
144. J. Mark, E. Bodtker, and B. Tromborg, "Measurement of Rayleigh backscattered-induced linewidth reduction," *Electron. Lett.*, vol. 21, pp. 1008-1009, 24 October 1985.
145. R. Favre, D. LeGuen, and J. C. Simon, "Optical feedback effects upon laser diode oscillation field spectrum," *IEEE J. Quantum Electron.*, vol. QE-18, pp. 1712-1717, October 1982.
146. A. R. Chraplyvy, K. Y. Liou, R. W. Tkach, G. Eisenstein, Y. K. Jhee, T. L. Koch, P. J. Anthony, and U. K. Chakrabarti, "Simple narrow-linewidth 1.5 μm InGaAsP DFB external-cavity laser," *Electron. Lett.*, vol. 22, pp. 88-90, 16 January 1986.
147. K.-Y. Liou, Y. K. Jhee, G. Eisenstein, R. S. Tucker, R. T. Ku, T. M. Shen, U. K. Chakrabarti, and P. J. Anthony, "Linewidth characteristics of fiber-extended-cavity distributed-feedback lasers," *Appl. Phys. Lett.*, vol. 48, pp. 1039-1041, 21 April 1986.
148. E. Brinkmeyer, W. Brennecke, M. Zurn, and R. Ulrich, "Fibre Bragg reflector for mode selection and line-narrowing of injection lasers," *Electron. Lett.*, vol. 22, pp. 134-135, 30 January 1986.
149. F. Favre and D. LeGuen, "FM noise and linewidth reduction in semiconductor laser weakly coupled to a single-mode fibre resonator," *Electron. Lett.*, vol. 21, pp. 467-469, 23 May 1985.
150. N. A. Olsson and J. P. Van der Ziel, "Performance characteristics of 1.5- μm external cavity semiconductor lasers for coherent optical communication," *J. Lightw. Techn.*, vol. LT-5, pp. 510-515, April 1987.

151. R. Wyatt and W. J. Devlin, "10 kHz linewidth 1.5 μ m InGaAsP external cavity laser with 55 nm tuning range," *Electron. Lett.*, vol. 19, pp. 110-111, 3 February 1983.
152. R. Wyatt, "Spectral linewidth of external cavity semiconductor lasers with strong, frequency-selective feedback," *Electron. Lett.*, vol. 21, pp. 658-659, 18 July 1985.
153. S. Saito and Y. Yamamoto, "Direct observation of Lorentzian lineshape of semiconductor laser and linewidth reduction with external grating feedback," *Electron. Lett.*, vol. 17, pp. 325-327, 30 April 1981.
154. C.-Y. Kuo and J. P. van der Ziel, "Linewidth reduction of 1.5- μ m grating loaded external cavity semiconductor laser by geometric reconfiguration," *Appl. Phys. Lett.*, vol. 48, pp. 885-887, 7 April 1986.
155. B. Dahmani, L. Hollberg, and R. Drullinger, "Frequency stabilization of semiconductor lasers by resonant optical feedback," *Optics Lett.*, vol. 12, pp. 876-878, November 1987.
156. H. Li and H. R. Telle, "Efficient frequency noise reduction of GaAlAs semiconductor lasers by optical feedback from an external high-finesse resonator," *IEEE J. Quantum Electron.*, vol. 25, pp. 257-264, March 1989.
157. P. H. Laurent, A. Clairon, and C. H. Breant, "Frequency noise analysis of optically self-locked diode lasers," *IEEE J. Quantum Electron.*, vol. 25, pp. 1131-1142, June 1989.
158. C.-H. Shin, M. Teshima, M. Ohtsu, T. Imai, J. Yoshida, and K. Nishide, "FM characteristics and compact modules for coherent semiconductor lasers coupled to an external cavity," *IEEE Photon. Techn. Lett.*, vol. 2, pp. 167-169, March 1990.
159. A. Hemmerich, D. H. McIntyre, D. Schropp, D. Meschede, and T. W. Hansch, "Optically stabilized narrow linewidth semiconductor laser for high resolution spectroscopy," *Opt. Comm.*, vol. 75, pp. 118-122, 15 February 1990.
160. K. Aiki, M. Nakamura, T. Kuroda, J. Umeda, R. Ito, N. Chinone, and M. Maeda, "Transverse mode stabilized $Al_xGa_{1-x}As$ injection lasers with channeled-substrate-planar structure," *IEEE J. Quantum Electron.*, vol. QE-14, pp. 89-94, February 1978.
161. K. Aiki, M. Nakamura, T. Kuroda, and J. Umeda, "Channeled-substrate-planar structure (AlGa)As injection lasers," *Appl. Phys. Lett.*, vol. 48, pp. 649-651, June 1977.
162. J. K. Butler, G. A. Evans, and B. Goldstein, "Analysis and performance of channeled-substrate-planar double-heterostructure lasers with geometrical asymmetries," *IEEE J. Quantum Electron.*, vol. QE-23, pp. 27-28, 5 January 1989.
163. H. Namizaki, "Transverse-junction-stripe-geometry-heterostructure lasers with very low threshold current," *J. Appl. Phys.*, vol. 45, pp. 2785-2786, June 1974.
164. H. Namizaki, M. Ishii, H. Kan, E. Ohmura, R. Hirano, and A. Ito, "Long-life GaAs-GaAlAs TJS laser with low threshold current and fundamental

- transverse and single longitudinal mode," *Opt. Comm.*, vol. 18, pp. 39-40, July 1976.
165. K. Isshiki, K. Kaneno, H. Kumabe, K. Namizaki, K. Ikeda, and W. Susaki, "Ten-thousand-hour operation of crank transverse-junction-stripe lasers grown by metal-organic chemical vapor deposition," *J. Lightwave Technol.*, vol. LT-4, pp. 1475-1481, October 1986.
 166. S. Nita, H. Namizaki, S. Takamiya, and W. Susaki, "Single-mode junction-up TJS lasers with estimated lifetime of 10^6 hours," *IEEE J. Quantum Electron.*, vol. QE-15, pp. 1208-1209, November 1979.
 167. Y. C. Chung and Y. H. Lee, "Effects of optical feedback on vertical-cavity top-surface-emitting lasers," *CLEO Technical Digest Series*, vol. 10, pp. 340-341, Baltimore, MD, 12-17 May 1991.
 168. R. L. Burden, J. D. Faires, and A. C. Reynolds, *Numerical Analysis*, 2nd ed., PWS, Boston, 1981.
 169. R. W. Tkach and A. R. Chraplyvy, "Linewidth broadening and mode splitting due to weak feedback in single-frequency $1.5\mu\text{m}$ lasers," *Electron. Lett.*, vol. 21, pp. 1081-1083, 7 November 1985.
 170. L. Casperson and A. Yariv, "Longitudinal modes in a high-gain laser," *Appl. Phys. Lett.*, vol. 17, pp. 259-261, 15 September 1970.
 171. J. H. Osmundsen, B. Tromborg, and H. Olesen, "Experimental investigation of stability properties for a semiconductor laser with optical feedback," *Electron. Lett.*, vol. 19, pp. 1068-1070, 8 December 1983.
 172. B. Tromborg, J. H. Osmundsen, and H. Olesen, "Stability analysis for a semiconductor laser in an external cavity," *IEEE J. Quantum Electron.*, vol. QE-20, pp. 1023-1032, September 1984.
 173. H. Olesen, J. H. Osmundsen, and B. Tromborg, "Nonlinear dynamics and spectral behavior for an external cavity laser," *IEEE J. Quantum Electron.*, vol. QE-22, pp. 762-773, June 1986.
 174. C. H. Henry and R. F. Kazarinov, "Instability of semiconductor lasers due to optical feedback from distant reflectors," *IEEE J. Quantum Electron.*, vol. QE-22, pp. 294-301, February 1986.
 175. G. P. Agrawal and N. K. Dutta, *Long-Wavelength Semiconductor Lasers*, Van Nostrand Reinhold Co., New York, 1986.
 176. S. Wiggins, *Introduction to applied nonlinear dynamical systems and chaos*, Springer-Verlag, New York, 1990.
 177. H. B. Callen, *Thermodynamics and an Introduction to Thermostatistics*, 2nd Ed., Wiley, New York, 1985.
 178. N. Schunk and K. Petermann, "Numerical analysis of the feedback regimes for a single-mode semiconductor laser with external feedback," *IEEE J. Quantum Electron.*, vol. 24, pp. 1242-1247, July 1988.
 179. J. O. Binder and G. D. Cormack, "Mode selection and stability of a semiconductor laser with weak optical feedback," *IEEE J. Quantum Electron.*, vol. 25, pp. 2255-2259, November 1989.
 180. J. W. M. Biesterbos, A. J. Den Boef, W. Linders, and G. A. Acket, "Low-frequency mode-hopping optical noise in AlGaAs channeled substrate lasers

- induced by optical feedback," *IEEE J. Quantum Electron.*, vol. QE-19, pp. 986-990, June 1983.
181. P. Zorabedian, W. R. Trutna, and L. S. Cutler, "Bistability in grating-tuned external-cavity semiconductor lasers," *IEEE J. Quantum Electron.*, vol. QE-23, pp. 1855-1860, November 1987.
 182. H. A. Haus and Y. Yamamoto, "Quantum noise of an injection locked laser oscillator," *Phys. Rev. A*, vol. 29, pp. 1261-1274, 1984.
 183. R. Adler, "A study of locking phenomena in oscillators," *Proc. IEEE*, vol. 61, pp. 1380-1385, October 1973.
 184. J. Mork and B. Tromborg, "The mechanism of mode selection for an external cavity laser," *IEEE Photon. Techn. Lett.*, vol. 2, pp. 21-23, January 1990.
 185. R. O. Miles, A. Dandridge, A. B. Tveten, H. F. Taylor, and T. G. Giallorenzi, "Feedback-induced line broadening in cw channel-substrate planar laser diodes," *Appl. Phys. Lett.*, vol. 37, pp. 990-992, 1 December 1980.
 186. L. Goldberg, H. F. Taylor, A. Dandridge, J. F. Weller, and R. O. Miles, "Spectral characteristics of semiconductor lasers with optical feedback," *IEEE J. Quantum Electron.*, vol. QE-18, pp. 555-564, April 1982.
 187. D. Lenstra, B. H. Verbeek, and A. J. Den Boef, "Coherence collapse in single-mode semiconductor lasers due to optical feedback," *IEEE J. Quantum Electron.*, vol. QE-21, pp. 674-679, June 1985.
 188. M. Fujiwara, K. Kubota, and R. Lang, "Low-frequency fluctuation in laser diodes with external optical feedback," *Appl. Phys. Lett.*, vol. 38, pp. 217-220, 15 February 1981.
 189. T. Mukai and K. Otsuka, "New route to optical chaos: successive-subharmonic-oscillation cascade in a semiconductor laser coupled to an external cavity," *Phys. Rev. Lett.*, vol. 55, pp. 1711-1714, 21 October 1985.
 190. T. Morikawa, Y. Mitsuhashi, J. Shimada, and Y. Kojima, "Return-beam-induced oscillations in self-coupled semiconductor lasers," *Electron. Lett.*, vol. 12, pp. 435-436, 19 August 1976.
 191. C. Risch and C. Voumard, "Self-pulsation in the output intensity and spectrum of GaAs-AlGaAs cw diode lasers coupled to a frequency-selective external optical cavity," *J. Appl. Phys.*, vol. 48, pp. 2083-2085, May 1977.
 192. R. Ries and F. Sporleder, "Low frequency instabilities of laser diodes with optical feedback," *Proc. 8th Europ. Conf. on Opt. Comm.*, pp. 285-290, Sept 1982.
 193. H. Temkin, N. A. Olsson, J. H. Abeles, R. A. Logan, and M. B. Panish, "Reflection noise in index-guided InGaAsP lasers," *IEEE J. Quantum Electron.*, vol. QE-22, pp. 286-293, February 1986.
 194. R. P. Salathe, "Diode lasers coupled to external resonators," *Appl. Phys.*, vol. 20, pp. 1-18, January 1979.
 195. R. Muller and P. Glas, "Bistability, regular self-pulsing, and chaos in lasers with external feedback," *J. Opt. Soc. Am. B*, vol. 2, pp. 184-192, January 1985.

196. J. Mork, B. Tromborg, and P. L. Christiansen, "Bistability and low-frequency fluctuations in semiconductor lasers with optical feedback: a theoretical analysis," *IEEE J. Quantum Electron.*, vol. 24, pp. 123-133, February 1988.
197. B. Tromborg and J. Mork, "Nonlinear injection locking dynamics and the onset of coherence collapse in external cavity lasers," *IEEE J. Quantum Electron.*, vol. 26, pp. 642-654, April 1990.
198. Y. Cho and T. Umeda, "Observation of chaos in a semiconductor laser with delayed feedback," *Opt. Comm.*, vol. 59, pp. 131-136, 15 August 1986.
199. H. Kawaguchi and K. Otsuka, "A new class of instabilities in a diode laser with an external cavity," *Appl. Phys. Lett.*, vol. 45, pp. 934-936, 1 November 1984.
200. W. H. Loh, Y. Ozeki, and C. L. Tang, "High-frequency polarization self-modulation and chaotic phenomena in external cavity semiconductor lasers," *Appl. Phys. Lett.*, vol. 56, pp. 2613-2615, 25 June 1990.
201. R. O. Miles, A. Dandridge, A. B. Tveten, T. G. Giallorenzi, and H. F. Taylor, "Low-frequency noise characteristics of channel substrate planar GaAlAs laser diodes," *Appl. Phys. Lett.*, vol. 38, pp. 848-850, 1 June 1981.
202. K. Vahala, C. Harder, and A. Yariv, "Observation of relaxation resonance effects in the field spectrum of semiconductor lasers," *Appl. Phys. Lett.*, vol. 42, pp. 211-213, 1 February 1983.
203. J. S. Cohen and D. Lenstra, "Spectral properties of the coherence collapsed state of a semiconductor laser with delayed optical feedback," *IEEE J. Quantum Electron.*, vol. 25, pp. 1143-1151, June 1989.
204. J. Wang and K. Petermann, "Noise analysis of semiconductor lasers within the coherence collapse regime," *IEEE J. Quantum Electron.*, vol. 27, pp. 3-8, January 1991.
205. J. S. Cohen, F. Wittgreffe, M. D. Hoogerland, and J. P. Woerdman, "Optical spectra of a semiconductor laser with incoherent optical feedback," *IEEE J. Quantum Electron.*, vol. 26, pp. 982-990, June 1990.
206. G. P. Agrawal, N. A. Olsson, and N. K. Dutta, "Effect of fiber-far-end reflections on intensity and phase noise in InGaAsP semiconductor lasers," *Appl. Phys. Lett.*, vol. 45, pp. 597-599, 15 September 1984.
207. J. S. Cohen, R. R. Drenten, and B. H. Verbeek, "The effect of optical feedback on the relaxation oscillation in semiconductor lasers," *IEEE J. Quantum Electron.*, vol. 24, pp. 1989-1995, October 1988.
208. R. F. Broom, E. Mohn, C. Risch, and R. Salathe, "Microwave self-modulation of a diode laser coupled to an external cavity," *IEEE J. Quantum Electron.*, vol. QE-6, pp. 328-334, June 1970.
209. J. Helms and K. Petermann, "A simple analytic expression for the stable operation range of laser diodes with optical feedback," *IEEE J. Quantum Electron.*, vol. 26, pp. 833-836, May 1990.
210. N. Schunk and K. Petermann, "Stability analysis for laser diodes with short external cavities," *IEEE Photon. Techn. Lett.*, vol. 1, pp. 49-51, March 1989.

211. K. Kikuchi and T.-P. Lee, "Spectral stability analysis of weakly coupled external-cavity semiconductor lasers," *J. Lightw. Techn.*, vol. LT-5, pp. 1269-1272, September 1987.
212. N. Chinone, K. Aiki, and R. Ito, "Stabilization of semiconductor laser outputs by a mirror close to a laser facet," *Appl. Phys. Lett.*, vol. 33, pp. 990-992, 15 December 1978.
213. K. R. Preston, K. C. Woollard, and K. H. Cameron, "External cavity controlled single longitudinal mode laser transmitter module," *Electron. Lett.*, vol. 17, pp. 931-933, 26 November 1981.
214. L. A. Coldren, K. J. Ebeling, B. I. Miller, and J. A. Rentschler, "Single longitudinal mode operation of two-section GaInAsP/InP lasers under pulsed excitation," *IEEE J. Quantum Electron.*, vol. QE-19, pp. 1057-1062, June 1983.
215. J. P. van der Ziel and R. M. Mikulyak, "Single-mode operation of 1.3 μ m InGaAsP/InP buried crescent lasers using a short external optical cavity," *IEEE J. Quantum Electron.*, vol. QE-20, pp. 223-229, March 1984.
216. G. C. Dente, P. S. Durkin, K. A. Wilson, and C. E. Moeller, "Chaos in the coherence collapse of semiconductor lasers," *IEEE J. Quantum Electron.*, vol. 24, pp. 2441-2447, December 1988.
217. S. L. Woodward, T. L. Koch, and U. Koren, "Onset of coherence collapse in DBR lasers," *IEEE Photon. Techn. Lett.*, vol. 2, pp. 391-394, June 1990.
218. B. Tromborg and J. Mork, "Stability Analysis and the route to chaos for laser diodes with optical feedback," *IEEE Photon. Techn. Lett.*, vol. 2, pp. 549-552, August 1990.
219. J. Mork, J. Mark, and B. Tromborg, "Route to chaos and competition between relaxation oscillations for a semiconductor laser with optical feedback," *Phys. Rev. Lett.*, vol. 65, pp. 1999-2002, 15 October 1990.
220. S. Noda, K. Kojima, and K. Kyuma, "Mutual injection-locking properties of monolithically integrated surface-emitting multiple-quantum-well distributed feedback lasers," *IEEE J. Quantum Electron.*, vol. 26, pp. 1883-1894, November 1990.
221. R. Salathe, C. Voumard, and H. Weber, "Optical coupling of two diode lasers with variable coupling coefficient," *Phys. Stat. Sol.*, vol. 23, pp. 675-683, 1974.
222. G. C. Dente, C. E. Moeller, and P. S. Durkin, "Coupled oscillators at a distance: Applications to coupled semiconductor lasers," *IEEE J. Quantum Electron.*, vol. 26, pp. 1014-1022, June 1990.
223. J. Benford, H. Sze, W. Woo, R. R. Smith, and B. Harteneck, "Phase locking of relativistic magnetrons," *Phys. Rev. Lett.*, vol. 62, pp. 969-971, 20 February 1989.
224. H. C. Casey, Jr. and M. B. Panish, *Heterostructure Lasers, Part A: Fundamental Principles*, Academic Press, New York, 1978.
225. H. Kressel and J. K. Butler, *Semiconductor Lasers and Heterojunction LEDs*, Academic Press, New York, 1977.

226. E. Hecht, *Optics*, 2nd ed., Addison-Wesley, Reading Mass., 1987.
227. Lord Rayleigh, *Phil. Mag.*, vol. XIII, pp. 316-333, 1907.
228. S. S. Wang and H. G. Winful, "Dynamics of phase-locked semiconductor laser arrays," *Appl. Phys. Lett.*, vol. 52, pp. 1774-1776, 23 May 1988.
229. D. Marcuse, *Principles of Quantum Electronics*, Academic Press, New York, 1980.
230. R. H. Pantell and H. E. Puthoff, *Fundamentals of Quantum Electronics*, Wiley, New York, 1969.
231. A. Yariv, *Quantum Electronics*, Wiley, New York, 1989. 3rd ed.
232. A. E. Siegman, *Lasers*, University Science Books, Mill Valley, 1986.
233. J. D. Jackson, *Classical Electrodynamics*, 2nd Ed., Wiley, New York, 1975.
234. G. Arfken, *Mathematical Methods for Physicists*, 3rd Ed., Academic Press, Orlando, 1985.
235. A. Yariv, *Optical Electronics*, 3rd ed., CBS College Publishing, New York, 1985.
236. H. C. Casey, Jr. and M. B. Panish, *Heterostructure Lasers, Part A: Fundamental Principles*, Academic Press, New York, 1978.
237. C. H. Henry, R. A. Logan, and K. A. Bertness, "Spectral dependence of the change in refractive index due to carrier injection in GaAs lasers," *J. Appl. Phys.*, vol. 52, pp. 4457-4461, July 1981.
238. K. Vahala, L. C. Chiu, S. Margalit, and A. Yariv, "On the linewidth enhancement factor α in semiconductor injection lasers," *Appl. Phys. Lett.*, vol. 42, pp. 631-633, 15 April 1983.
239. J. S. Blakemore, *Solid State Physics*, 2nd ed., Cambridge University Press, Cambridge, 1985.
240. J. Manning, R. Olshansky, and C. B. Su, "The carrier-induced index change in AlGaAs and $1.3\mu\text{m}$ InGaAsP diode lasers," *IEEE J. Quantum Electron.*, vol. QE-19, pp. 1525-1530, October 1983.
241. G. H. B. Thompson, *Physics of Semiconductor Laser Devices*, Wiley, Chichester, 1980.
242. G. P. Agrawal and N. K. Dutta, *Long-Wavelength Semiconductor Lasers*, Van Nostrand Reinhold Co., New York, 1986.
243. J. G. Mendoza-Alvarez, F. D. Nunes, and N. B. Patel, "Refractive index dependence on free carriers for GaAs," *J. Appl. Phys.*, vol. 51, pp. 4365-4367, August 1980.
244. M. Osinski and J. Buus, "Linewidth broadening factor in semiconductor lasers - an overview," *IEEE J. Quantum Electron.*, vol. QE-23, pp. 9-29, January 1987.
245. G. H. B. Thompson, "A theory for filamentation in semiconductor lasers including the dependence of dielectric constant on injected carrier density," *Opto-Electron.*, vol. 4, pp. 257-310, August 1972.
246. P. A. Kirkby, A. R. Goodwin, G. H. B. Thompson, and P. R. Selway, "Observations of self-focusing in stripe geometry semiconductor lasers and

- the development of a comprehensive model of their operation," *IEEE J. Quantum Electron.*, vol. QE-13, pp. 705-719, August 1977.
247. R. Lang, "Lateral transverse mode instability and its stabilization in stripe geometry injection lasers," *IEEE J. Quantum Electron.*, vol. QE-15, pp. 718-726, August 1979.
 248. C. H. Henry, "Theory of the linewidth of semiconductor lasers," *IEEE J. Quantum Electron.*, vol. QE-18, pp. 259-264, February 1982.
 249. C. Harder, K. Vahala, and A. Yariv, "Measurement of the linewidth enhancement factor α of semiconductor lasers," *Appl. Phys. Lett.*, vol. 42, pp. 328-330, 15 February 1983.
 250. D. Welford and A. Mooradian, "Output power and temperature dependence of the linewidth of single-frequency cw (GaAl)As diode lasers," *Appl. Phys. Lett.*, vol. 40, pp. 865-867, May 1982.
 251. N. K. Dutta, N. A. Olsson, and W. T. Tsang, "Carrier induced refractive index change in AlGaAs quantum well lasers," *Appl. Phys. Lett.*, vol. 45, pp. 836-837, 15 October 1984.
 252. W. W. Chow and D. Depatie, "Carrier-induced refractive-index change in quantum-well lasers," *Optics Lett.*, vol. 13, pp. 303-305, April 1988.
 253. M. Nakamura, K. Aiki, N. Chinone, R. Ito, and J. Umeda, "Longitudinal mode behavior of mode stabilized AlGaAs injection lasers," *J. Appl. Phys.*, vol. 49, pp. 4644-4648, September 1978.
 254. G. P. Agrawal, "Effect of nonlinear gain on single-frequency behavior of semiconductor lasers," *Electron. Lett.*, vol. 22, pp. 696-697, 19 June 1986.
 255. C.-Z. Guo, J.-S. Xie, and F. Shen, "Effects of nonlinear-gain on single longitudinal mode behavior of semiconductor lasers," *IEEE J. Quantum Electron.*, vol. QE-21, pp. 794-803, July 1985.
 256. A. Olsson and C. L. Tang, "Coherent optical interference effects in external-cavity semiconductor lasers," *IEEE J. Quantum Electron.*, vol. QE-17, pp. 1320-1323, August 1981.
 257. J. C. Goodwin and B. K. Garside, "Threshold variations in diode lasers induced by external resonator feedback," *IEEE J. Quantum Electron.*, vol. QE-19, pp. 1492-1495, October 1983.
 258. J. K. Butler, D. E. Ackley, and M. Ettenberg, "Coupled-mode analysis of gain and wavelength oscillation characteristics of diode laser phased arrays," *IEEE J. Quantum Electron.*, vol. QE-21, pp. 458-464, May 1985.
 259. F. A. Jenkins and H. E. White, *Fundamentals of Optics*, 3rd Ed., McGraw-Hill, New York, 1957.
 260. E. Hecht, *Optics*, 2nd ed., Addison-Wesley, Reading Mass., 1987.
 261. C. E. Moeller, P. S. Durkin, and G. C. Dente, "Mapping the injection-lock band of semiconductor lasers," *IEEE J. Quantum Electron.*, vol. 25, pp. 1603-1608, July 1989.
 262. M. Lax, "Quantum noise X. Density-matrix treatment of field and population-difference fluctuations," *Phys. Rev.*, vol. 157, pp. 213-231, 1967.

263. M. Lax and W. H. Louisell, "Quantum noise XII. Density-operator treatment of field and population fluctuations," *Phys. Rev.*, vol. 185, pp. 568-591, 1969.
264. A. Papoulis, *Probability, Random Variables, and Stochastic Processes*, 2nd ed., McGraw-Hill, New York, 1984.
265. M. Sargent, M. O. Scully, and W. E. Lamb, *Laser physics*, Addison-Wesley, Reading, Mass., 1974.
266. C. H. Henry, "Theory of phase noise and power spectrum of a single mode injection laser," *IEEE J. Quantum Electron.*, vol. QE-19, pp. 1391-1397, September 1983.
267. C. H. Henry, "Phase noise in semiconductor lasers," *J. Lightw. Techn.*, vol. LT-4, pp. 298-311, March 1986.
268. K. Petermann, *Laser Diode Modulation and Noise*, Kluwer Academic Publishers, Dordrecht, 1988.
269. H. Olesen, J. H. Osmundsen, and B. Tromborg, "Nonlinear dynamics and spectral behavior for an external cavity laser," *IEEE J. Quantum Electron.*, vol. QE-22, pp. 762-773, June 1986.
270. K. Stubkjaer, M. Asada, S. Arai, and Y. Suematsu, "Spontaneous recombination, gain and refractive index variation for 1.6 μm wavelength InGaAsP/InP lasers," *Japan. J. Appl. Phys.*, vol. 20, pp. 1499-1505, August 1981.
271. I. D. Henning and J. V. Collins, "Measurement of the semiconductor laser linewidth broadening factor," *Electron. Lett.*, vol. 19, pp. 927-929, 27 October 1983.
272. N. K. Dutta, H. Temkin, T. Tanbun-Ek, and R. Logan, "Linewidth enhancement factor for InGaAs/InP strained quantum well lasers," *Appl. Phys. Lett.*, vol. 57, pp. 1390-1391, 1 October 1990.
273. J. Manning and R. Olshansky, "Carrier-induced index change in AlGaAs double-heterostructure lasers," *Electron. Lett.*, vol. 17, pp. 506-507, 1981.
274. K. Stubkjaer, Y. Suematsu, M. Asada, S. Arai, and A. R. Adams, "Measurements of refractive-index variation with free carrier density and temperature for 1.6 μm GaInAs/InP lasers," *Electron. Lett.*, vol. 16, pp. 895-896, 1980.
275. B. W. Hakki and T. L. Paoli, "Gain spectra in GaAs double-heterostructure injection lasers," *J. Appl. Phys.*, vol. 46, pp. 1299-1306, 1975.
276. J. Jacquet, P. Brosson, A. Olivier, A. Perales, A. Bodere, and D. Leclerc. "Carrier-induced differential refractive index in GaInAsP-GaInAs separate confinement multiquantum well lasers," *IEEE Photon. Tech. Lett.*, vol. 2, pp. 620-622, September 1990.
277. C. H. Shin, M. Teshima, and M. Ohtsu, "Novel measurement method of linewidth enhancement factor in semiconductor lasers by optical self-locking," *Electron. Lett.*, vol. 25, pp. 27-28, 5 January 1989.
278. J. H. Osmundsen, B. Tromborg, and H. Olesen, "Experimental investigation of stability properties for a semiconductor laser with optical

- feedback," *Electron. Lett.*, vol. 19, pp. 1068-1070, 8 December 1983.
279. P. Andersson and T. Andersson, "Modulation amplitude dependence of the time-bandwidth product of picosecond pulses from semiconductor lasers," *Tech. Dig. 5th Int. Conf. Integrat. Opt. Optic. Fiber Commun./11th Euro. Conf. Optic. Commun.*, vol. I, pp. 783-786, Venice, Italy, October 1-4 1985.
280. S. E. H. Turley, G. H. B. Thompson, and D. F. Lovelace, "Effect of injection current on dielectric constant of an inbuilt waveguide in twin-transverse-junction stripe lasers," *Electron. Lett.*, vol. 15, pp. 256-257, April 1979.
281. R. Olshansky, C. B. Su, J. Manning, and W. Powazinik, "Measurement of radiative and nonradiative recombination rates in InGaAsP and AlGaAs light sources," *IEEE J. Quantum Electron.*, vol. QE-20, pp. 838-854, August 1984.
282. N. K. Dutta, R. L. Hartman, and W. T. Tsang, "Gain and carrier lifetime measurements in AlGaAs multiquantum well lasers," *IEEE J. Quantum Electron.*, vol. QE-19, pp. 1613-1616, 1983.
283. K. Vahala and A. Yariv, "Semiclassical theory of noise in semiconductor lasers - part I," *IEEE J. Quantum Electron.*, vol. QE-19, pp. 1096-1101, June 1983.
284. R. Adler, "A study of locking phenomena in oscillators," *Proc. IEEE*, vol. 61, pp. 1380-1385, October 1973.

APPENDIX A

This appendix reviews the so-called linewidth enhancement factor, α . Special consideration is devoted to α , due to its importance in the operation of coupled systems of semiconductor lasers. In section A.1, the resonant electric susceptibility in semiconductor lasers is contrasted to that of a two level atomic system. The α parameter describing this phenomenon is then defined and reduced to the form used throughout the body of this thesis. A brief discussion of α follows.

A.1 Resonant Susceptibility

The response of a medium, consisting of a collection of oscillators or atoms, to an electric field is governed by the electric susceptibility. In a linear, isotropic dielectric medium under steady-state conditions, the macroscopic polarization is proportional to the inducing field

$$\mathbf{P} = \epsilon_0 \chi(\omega) \mathbf{E} . \quad (\text{A.1})$$

The proportionality factor, χ , is generally complex and frequency-dependent, due to dispersion in the medium.

In describing a laser transition, it is convenient to express the polarization as the sum of two terms: A resonant polarization \mathbf{P}_r , associated with external pumping, and a second contribution \mathbf{P}_o accounting for any background polarization in the gain medium. The electric displacement can then be written

$$\begin{aligned} \mathbf{D} &= \epsilon_o \mathbf{E} + \mathbf{P}_o + \mathbf{P}_r \\ &= \epsilon_o(1 + \chi_o) \mathbf{E} + \epsilon_o \chi_r \mathbf{E} = \epsilon_o \epsilon \mathbf{E}, \end{aligned} \quad (\text{A.2})$$

where ϵ is the dielectric constant.

The resonant susceptibility, in the simplest case of a two-level atomic system, typical of many gas or solid state lasers, can be found quantum mechanically²²⁹⁻²³¹ or by treating the atoms as a collection of classical oscillators²³². In either case, the result in the resonance approximation ($\omega \approx \omega_o$) has the well known complex Lorentzian form,

$$\chi_r'(\omega) = -\chi_{ro}'' \frac{2(\omega - \omega_o)}{(\Delta\omega/2)^2 + (\omega - \omega_o)^2}, \quad (\text{A.3a})$$

$$\chi_r''(\omega) = -\chi_{ro}'' \frac{\Delta\omega}{(\Delta\omega/2)^2 + (\omega - \omega_o)^2}, \quad (\text{A.3b})$$

where $\chi_r = \chi_r' + i\chi_r''$. $\Delta\omega$ is the FWHM linewidth of the transition, while χ_{ro}'' is a constant giving the peak amplitude of the imaginary amplifying (or absorbing) part of the susceptibility at midband ($\omega = \omega_o$), and depends upon the population inversion density of the two-level system. The real susceptibility, on the other hand, describes refractive index dispersion in the medium. The real and imaginary susceptibilities are fundamentally related by through the

Kramers-Kronig dispersion relation²³³

$$\chi_r'(\omega) = \frac{2}{\pi} P \int_0^{\infty} \frac{\omega' \chi_r''(\omega')}{\omega'^2 - \omega^2} d\omega'. \quad (\text{A.4})$$

Since the imaginary susceptibility given by (A.3b) is an even function about ω_0 , the symmetry properties of this (Hilbert) transform²³⁴ imply that the zero dispersion point of the real susceptibility is centered at ω_0 . Therefore, the index of refraction at the resonance peak remains constant, independent of the level of pumping, in a two-level laser.

Semiconductor lasers differ from gas or other solid state lasers in that radiative transitions occur between energy bands, rather than between the discrete levels of isolated atoms. The population inversion density at a given frequency is then dependent on the density of states with direct transitions between the conduction and valence bands in the semiconductor, where the occupation probability of the bands obeys Fermi-Dirac statistics. Consequently, the gain spectrum of a direct bandgap semiconductor is asymmetric about the gain peak frequency²³⁵⁻²³⁷. It follows, from the Kramers-Kronig relation (A.4), that the real susceptibility must also be asymmetric. More importantly, however, the index dispersion zero is no longer located at the gain peak frequency²³⁸. As the bands fill with free carriers due to current injection, the dispersion zero is found to shift to higher energies at a faster rate than the gain peak. An electric field oscillating at ω_0 therefore experiences an index of refraction lower than that of the unpumped medium. Further, an increase in carrier density is accompanied by a decrease in refractive index at ω_0 .

Free carrier absorption also contributes to the refractive index change with carrier injection in semiconductor lasers. Interaction of the optical field and the free carriers produces a reduction in the index of refraction through the plasma effect²³⁹. However, this reduction is an order of magnitude smaller than that attributed to coupling between the real and imaginary parts of the resonant susceptibility.^{240,241}

A.2 Definition of α

Previously, the fundamental relationships between the real electric susceptibility and index of refraction, and imaginary susceptibility and gain/loss have been referred to. It is straightforward to derive these relationships by defining the complex propagation constant as²⁴²

$$\beta = \beta_0 \tilde{\mu} = \beta_0 \mu - ig/2 \quad (\text{A.5})$$

where μ is the real index of refraction, β_0 is the free-space propagation constant and g is the net gain of the medium. Recalling that $\tilde{\mu} = \sqrt{\tilde{\epsilon}}$, equations (A.2) and (A.5) result in

$$\mu = \mu_0 + \frac{\text{Re}[\tilde{\chi}_r]}{2\mu_0}, \quad (\text{A.6})$$

$$g = -\frac{\beta_0}{\mu_0} \text{Im}[\tilde{\chi}_o + \tilde{\chi}_r]. \quad (\text{A.7})$$

μ_0 is the refractive index in the absence of pumping. Two approximations

have been made in deriving the above equations: First, the gain is considered to be much smaller than the propagation constant in the medium, $g \ll \beta_o$, which is true for typical gains near the lasing threshold. Further, the carrier-induced index of refraction change is assumed to be much smaller than the refractive index of the unpumped gain medium, which is equivalent to $|\text{Re}[\tilde{\chi}_r]| \ll \mu_o$.

Physically, the population inversion, and therefore optical gain, is reflected in the number of electron-hole pairs N in the active layer provided by an external pump current. The gain peak amplitude is known to increase in an approximately linear fashion for small carrier number variations in the vicinity of the lasing threshold, and is often written²³⁶

$$g(N) = \frac{\partial g}{\partial N}(N - N_o) = \left(\frac{\partial g}{\partial N} \right)_{th} \Delta N + g(N_{th}). \quad (\text{A.8})$$

Here, $\frac{\partial g}{\partial N}$ is the differential gain and N_o is the carrier number required to achieve transparency. Variations in carrier number from the threshold value, N_{th} , are denoted by $\Delta N \equiv N - N_{th}$. Similarly, the change in index of refraction in the active layer can be approximated as linear^{237, 240, 243}

$$\mu(N) = \mu_o + \frac{\partial \mu}{\partial N} N = \mu + \left(\frac{\partial \mu}{\partial N} \right)_{th} \Delta N. \quad (\text{A.9})$$

μ is the refractive index at threshold. It is useful to describe the coupling between the real and imaginary parts of the electric susceptibility by a single parameter²³⁸

$$\alpha = \frac{\left[\frac{\partial (\text{Re}[\tilde{\chi}_r])}{\partial N} \right]_{th}}{\left[\frac{\partial (\text{Im}[\tilde{\chi}_r])}{\partial N} \right]_{th}}. \quad (\text{A.10})$$

evaluated at the lasing threshold. Using expressions (A.6) and (A.7) with their associated linear approximations (A.8) and (A.9) in the above definition, α can be written in an equivalent form,

$$\alpha = -2\beta_0 \frac{\partial\mu/\partial N}{\partial g/\partial N}. \quad (\text{A.11})$$

This is the form of α used in the rate equations throughout the body of the thesis. Note that α is positive, since $\partial\mu/\partial N$ is typically negative at semiconductor laser wavelengths.

A.3 Discussion

The concept of the α parameter is a phenomenological approach to describing optical gain in a semiconductor laser. It is based on the very successful approximations that gain and refractive index vary almost linearly with carrier density in a semiconductor laser about its threshold. Values of α for semiconductor lasers operating at the gain peak are typically in the range²⁴⁴ of 2 to 8. Gas and solid-state lasers, in contrast, have $\alpha = 0$ at the gain peak and only small non-zero values when detuned from line center.

Many of the properties unique to semiconductor lasers can be traced to the non-zero value of α . Early recognition of the carrier-dependent refractive index began with the observation of lasing filaments in broad-area devices²⁴⁵ as well as self-focusing and "anti-guiding" effects in gain-guided stripe geometry lasers^{246,247}. As is evident in the body of this thesis, the α parameter greatly

influences the stability and locking properties of slave, self and mutually coupled semiconductor lasers. The α parameter is also of great importance in determination of the linewidth and noise properties of a semiconductor laser²⁴⁸. It shows up, for example, as chirp in AM (amplitude modulated) lasers²⁴⁹. Most of the preceding effects can, and have, been used to estimate α ²⁴⁴.

Although the α parameter is treated as a constant, it does carry a strong dependence on frequency and carrier concentration²³⁸ and reduces with decreasing temperature²⁵⁰. Furthermore, α is significantly dependent upon laser structure. In lasers with a low optical confinement laterally, such as gain-guided lasers, α may be different from the bulk value²⁴⁴. Quantum well lasers also have shown much lower values of α than conventional DH (double heterostructure) lasers, due to their differing density of states^{251,252}. Therefore, the α should be treated as a constant describing only a particular device with a given band gap, structure, threshold current and operating condition. Measurement of α for the experimental lasers used in this thesis is described in Appendix E.

APPENDIX B

Methods to experimentally measure self and cross-coupling coefficients are presented in this appendix. Sections B.2 and B.3, in particular, discuss the means by which the power coupling ratios cited in Chapters 3 and 4 were calibrated.

B.1 Measurement of Coupling Coefficients

In Section 2.2, it was shown how coupling coefficients enter the rate equation model for optically coupled lasers. The coefficients were determined through comparison to the composite resonator description of the coupled system and their evaluation hinged on the ability to theoretically solve for the modes of individual lasers as well as those of the compound resonator. Coupling coefficients, on the other hand, can also be determined experimentally by examining their influence on the stationary solutions of the rate equations describing the coupled system. These solutions specify the equilibrium values of the carrier number $\bar{\Delta n}$ and field amplitude \bar{e} in each laser, the locked phase difference $\Delta\phi_L$ between the lasers and the locked frequency of oscillation of the compound resonator, ω_L .

The variation in carrier number of a mode from its free-running value, for instance, is related to a change in threshold gain through equations (2.1.10), (2.1.15) and (2.3.2) by

$$\overline{\Delta n} = \frac{1}{2} \tau_p v_g \Delta g, \quad (\text{B.1})$$

where Δg is the change in modal gain per unit length. Since gain equals loss at threshold, the coupling coefficients must therefore be determined, in part, by supermode selective losses in the compound resonator. Changes in threshold gain are perhaps most easily measured through the (total) power output of the mode, given by equation (2.1.13), recalling that the carrier number variation and field amplitude in each laser are linked via (2.3.15). *Differences* in threshold gain between the modes of the coupled system will show up in the mode suppression ratio²⁴² between the supermodes. The MSR is often questionable as a calibration tool, however, since nonlinear effects, such as spectral hole-burning and population pulsations, are known²⁵³⁻²⁵⁵ to have an important effect on the relative strength of side modes in a semiconductor laser, especially away from the gain peak.

Similarly, the coupling coefficients can be linked to details of the optical spectrum. The locked frequency of oscillation of the coupled system is an excellent observable for use in calibration due to its straightforward measurement with a Fabry-Perot interferometer or spectrometer. Furthermore, it was shown in Section 2.3 that the locked phase difference $\Delta\phi_L$ between the constituent lasers is a function of detuning. The maximum detuning corresponding to a stationary solution, $\Delta\omega_{LB}$, was found to be profoundly influenced by the ampli-

tude and phase of the coupling coefficient.

Since the stationary solutions follow from a coupled set of nonlinear equations, it may be difficult, if not impossible, to uniquely determine the coupling coefficients from a given equilibrium. Some simplification might be necessary to reduce the the degrees of freedom. For example, if the optical coupling can be turned off momentarily, coupling coefficients can be found from changes in the laser output from its free-running condition. This technique has often been used to infer the coupling level for external cavity devices^{256, 257} with relatively large power coupling levels ($\sim 10\%$) through a threshold current variation.

Often the coupling is symmetric and the lasers are equally pumped. Take, for example, the two mutually coupled lasers considered in Section 2.3. When the lasers are resonantly tuned, the carrier equation (2.3.13) is decoupled from (2.3.14) and (2.3.15), as $\bar{e}_j = \bar{e}_k$. Equation (2.3.13) can then be written

$$\Delta \bar{n} = -\text{Re}[\eta_{sc}] - \cos\Delta\phi_L \text{Re}[\eta_{cc}], \quad (\text{B.2})$$

where $\Delta\phi_L = 0, \pi$. The change in carrier number of a mode from its isolated threshold value, in this case, depends exclusively on the real part of the self and mutual coupling coefficients. In other words, from (B.1), the real part of the coupling coefficient is responsible for the threshold gain of the even and odd modes. This fact has been previously pointed out in reference to evanescently coupled semiconductor laser arrays²⁵⁸, although the role of real and imaginary parts have been switched by convention in the definition of the coupling coefficient. Knowing the real part of the coupling coefficient, it is then possible to determine the imaginary contribution from the optical spectrum using equations (2.3.15) and (2.3.19).

The remainder of this appendix concentrates on the specific longitudinal coupling schemes employed in Chapters 3 and 4 for the study of self and mutual coupling. Due to the flexibility in controlling the amplitude and phase of the optical interaction in these experiments, calibration of coupling coefficients simplifies greatly. It is shown how self and mutual coupling coefficients were determined in these cases exclusively from measurements of the optical spectrum.

B.2 Self-Coupling Calibration

The coupling coefficient describing the self-coupling experiment of Figure 3.2 is given in the steady-state by equation (2.5.23). Here, the cold cavity bandwidth (2.5.22) is found from the diode's longitudinal mode spacing and output mirror reflectivity. Therefore, the magnitude of the coupling coefficient is known upon determination of the power coupling ratio PCR_{sc} given by (2.5.20). The phase of the coupling coefficient, on the other hand, requires precise knowledge of ω_L and τ . Since it is impractical to measure these values experimentally, an indirect method was found to determine ψ_{cc} . By using a piezo translator behind the retro-reflecting mirror, as shown in Figure 3.2, to control the coupling delay on a fine scale, the coupling phase was made variable, independent of the coupling magnitude. Recording the optical spectrum over a full 2π range of phase, ψ_{cc} could then be implied through direct comparison to theory.

In the self-coupling experiment depicted by Figure 3.2, two crossed calcite polarizers, fixed absorption filters and other intervening optics contribute to the attenuation of incident power. The one-way transmission through the external cavity was measured by replacing the retro assembly with a power meter and ratioing to the known power output of the laser. The round-trip power return ratio ϵ_T^4 , was then estimated by doubling this value (in dB). The result, however, gives only a relative measure of the power coupling ratio, as it does not include coupling losses ξ to the guided mode of the semiconductor laser. This is in practice a difficult number to determine. Fortunately, assuming that the coupling losses are independent of polarizer angle,[‡] the losses need only be found at a single coupling level, thereby anchoring the calibration.

The oscillation frequency of a self-coupled laser was found, from (3.1.5), to periodically tune about the isolated value with changes in coupling delay. The extreme deviation in frequency, from equations (3.1.7) and (2.5.20), is

$$\Delta\nu_{\max} = \Delta\nu_{cc} \epsilon_T^2 \xi \sqrt{1 + \alpha^2}, \quad (\text{B.3})$$

where R_{2k} was taken as unity. The power coupling ratio, $\epsilon_T^4 \xi^2$ can then be determined by measuring either the maximum deviation in frequency from the free-running location or the total width of the tuning range, knowing the values of $\Delta\nu_{cc}$ and α from independent measurements. The difference between the measured power return of the coupling junction and the predicted power coupling ratio from frequency extreme measurements gives an estimate of the cou-

[‡] The polarizers used had parallelism between entrance and exit faces to within 5 arc seconds. This guaranteed that the returned spot did not walk around on the laser facet as the polarizer was rotated, changing the overlap with the active area.

pling loss to the guided mode of the laser. Even very weak returned signals $\sim 10^{-7}$ times the lasing output can be accurately calibrated using this method. This is important for locating inadvertent optical feedback sources in many experiments.

The preceding calibration technique may not be useful when the coupling level is sufficiently high to allow multimode operation, yet below the level corresponding to hysteretic tuning behavior (see Chapter 3). In this case the frequency extremes will never be observed experimentally due to noise-induced mode hops. The frequency separation between the modes involved in a hop can be related to the coupling magnitude. This separation is found from equation (3.1.5), which reduces to

$$\Delta\nu_L = \Delta\nu_{\max} \sin \left(\frac{4\pi L_{ext}}{c} \Delta\nu_L \right) \quad (\text{B.4})$$

at the mode hop boundary. Graphically, solutions of (B.4) can be represented by the intersection of the line $\Delta\nu_L/\Delta\nu_{\max}$ with the sinusoidal term, as shown in the inset of Figure B.1. The root at $\Delta\nu_L = 0$ was shown to be dynamically unstable in Chapter 3. Therefore, the mode hops occur between the two outer roots. The frequency separation of these roots is

$$2\Delta\nu_L = \frac{c}{2L_{ext}} - 2x, \quad (\text{B.5})$$

which, assuming $x \ll \frac{c}{4L_{ext}}$, from simple geometrical arguments is straightforwardly derived as

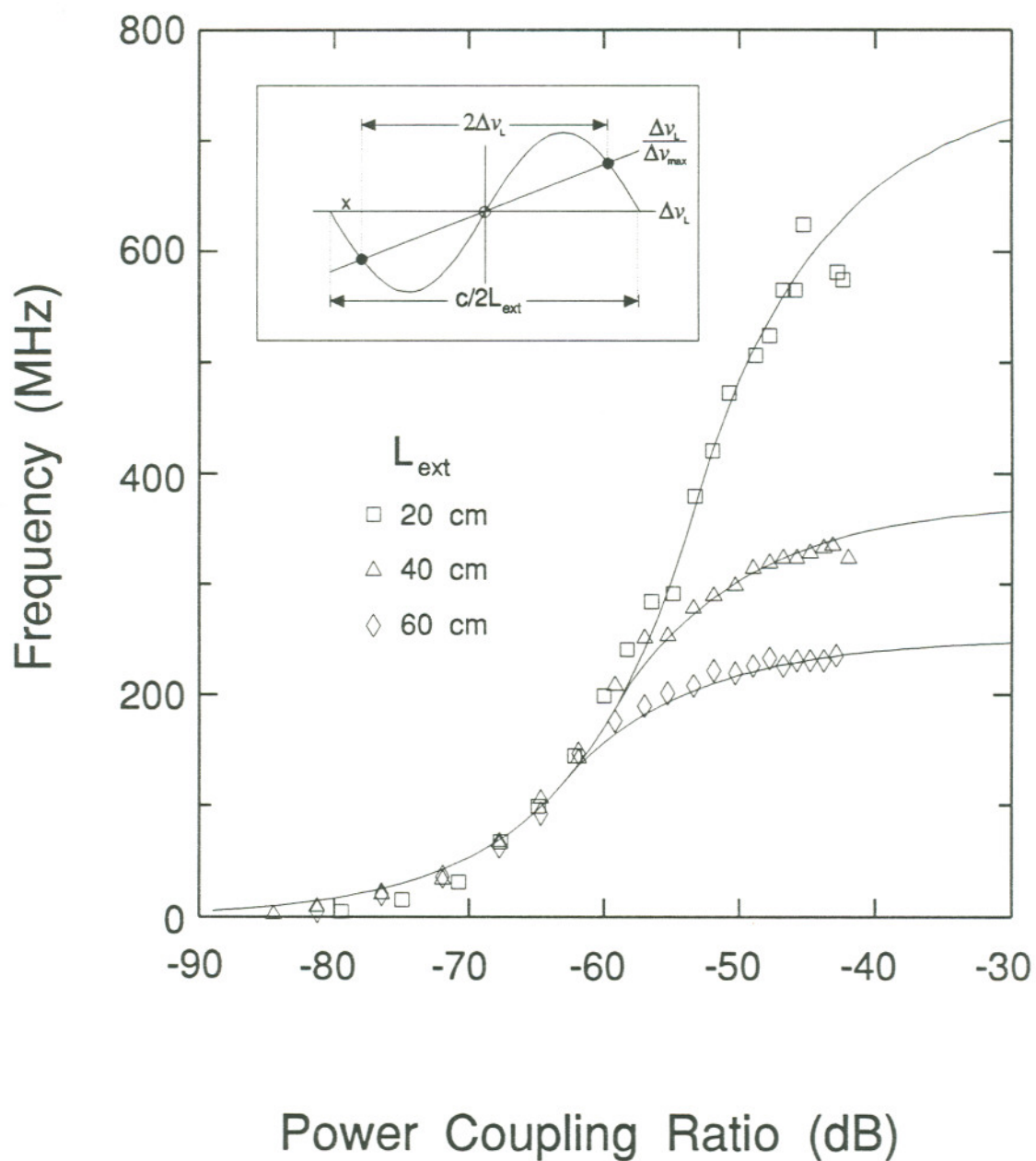


Figure B.1 Power coupling calibration curves for a self-coupled CSP laser. Solid lines are theoretical, symbols experimental. The inset depicts the graphical solution of (B.4).

$$2\Delta\nu_L \approx \frac{c}{2L_{ext} + \frac{c}{4\pi\Delta\nu_{max}}}. \quad (\text{B.6})$$

Recalling from (B.3) that $\Delta\nu_{max}$ is a function of the power coupling ratio, an approximate relation between the hop separation and coupling magnitude has been derived. Again, the difference between the measured power return and that predicted theoretically gives the coupling loss to the lasing mode.

Note that for large coupling levels the mode separation approaches the external cavity resonance spacing, $\frac{c}{2L_{ext}}$. Written in the form (B.6), the mode spacing obviously decreases at lower coupling levels due to an effectively longer laser cavity length. Figure B.1 displays numerically generated coupling calibration curves, along with experimentally measured values for external cavity lengths of 20, 40 and 60 cm respectively. The tuning extreme and mode hop spacing calibration methods merge smoothly together in the transition region from single to multimode behavior. A power coupling loss of $\xi^2 = -3\text{dB}$ was assumed in each case. Experimental data shows excellent agreement with theory.

Data above about - 43 dB, however, could not be collected, due to the onset of dynamic instability. Here, calibration of the self-coupling coefficient by means of fine-scale spectral measurements becomes virtually impossible due to spectral broadening. In this regime, attenuator transmission measurements were relied on to determine the coupling magnitude. By anchoring ξ at a lower coupling level, the relative change in power coupling ratio could be inferred from the $\cos^2\theta$ dependence of the attenuator. All of the above techniques were used

to determine the power coupling ratios listed in Chapter 3.

B.3 Mutual Coupling Calibration

Similar techniques can be employed for mutually coupled semiconductor lasers. In this case, however, multiple modes exist at all coupling levels. Thus, below the onset of hysteretic tuning behavior, calibration of the coupling level was exclusively obtained from mode hops. In Section 4.3, mode hops were shown to occur between the symmetric and asymmetric modes with every half wavelength change in laser separation. The frequency spacing at the mode hop boundary can be found by numerically solving equations (4.1.6) and (4.1.7) at $\bar{\omega}_o \tau = (2m + 1)\pi/2 - \tan^{-1}\alpha$. The mode spacing is found to vary in a fashion similar to Figure B.1, approaching the resonance separation of the cavity formed between the laser output facets at large power coupling ratios. Note that it is sufficient to determine PCR_{cc} in the resonant case, since the coupling magnitude is not expected to change as the lasers are detuned.

When hysteretic tuning was experimentally observed at moderate coupling levels, the maximum deviation in locked frequency from the average isolated value was again used to estimate PCR_{cc} . This value is nearly the same as self-coupling

$$\Delta\nu_{\max} = \Delta\nu_{cc} \epsilon_T \xi \sqrt{1 + \alpha^2},$$

with the power coupling ratio now given by (2.5.21). Power transmission through the coupling junction ϵ_T^2 , which shows up in the cross-coupling

coefficient (2.5.19), was measured by inserting a power meter in place of one diode laser and ratioing the result by the known output of the operating laser. Coupling losses to the guided mode of each laser was then estimated by comparison to theory. Knowledge of ξ allowed calibration curves characterizing the attenuation of the coupling junction to again be used at higher coupling levels, where dynamic instability obscured detailed spectral measurement.

The power coupling ratio, for mutually coupled lasers, can also be found from the maximum locking range of the lasers through equation (4.1.9). This technique proved to be less accurate, however, due to the softness of the lock-band edge discussed in Section 4.4.

APPENDIX C

This appendix deals with the measurement of coherence between mutually coupled lasers. After a brief background, the methodology used in determining visibility from the interference fringe data presented in Chapter 4 is outlined. Several effects present in the experiment which apparently reduce the visibility are analyzed, and methods to separate the actual visibility are introduced. Finally, a derivation is given which allows the visibility to be theoretically calculated from integrated time series of the rate equations.

C.1 Visibility

A single light source is not perfectly coherent, due to its finite bandwidth and finite spatial extent. When attempting to phase-lock a number of oscillators into a spatially coherent extended source, however, the coherence properties of the whole are dependent upon the constancy of the locked phase difference $\Delta\phi_L$ between the individual oscillators. For lasers, spatial coherence effects generally dominate the coherence properties, since the extended source often has a very narrow bandwidth. Fluctuations in the locked phase difference may change with the coupling level, its phase, and the frequency detuning of the

lasers, all of which are allowed to vary in the present experiments. Spontaneous emission and other noise sources also independently contribute to a degradation of the coherence. It is therefore important to have a means to measure the quality of the lock. This can be accomplished experimentally by interfering the laser outputs, thereby generating interference fringes. The (time-averaged) depth of modulation of the fringes gives a measure of the correlation between the sources, or their degree of coherence. The visibility²⁵⁹

$$V = \frac{I_{\max} - I_{\min}}{I_{\max} + I_{\min}}, \quad (\text{C.1})$$

was defined by Michelson as a measure of the modulation depth, where I_{\max} and I_{\min} are the intensities of a maximum and adjacent minimum, respectively, of an interference pattern. In coherence theory, the visibility corresponds to the modulus of the complex degree of coherence²⁶⁰.

C.2 Measuring Visibility

Several factors can contribute to an erroneous measurement of the visibility from interference fringe data. Expression (C.1), for example, assumes a uniform intensity distribution of the incident wavefronts over the region to be evaluated. This approximation can only be made if the spacing of fringes is much smaller than the distance over which an appreciable change in intensity across the wavefront exists. This situation was not easily attained in the experiments of Chapter 4, due to considerations concerning alignment of the diagnos-

tic optics in the setup. At most, several fringes were visible across the entire laser spot, which must be taken into account when quantifying the visibility. When measuring I_{\max} at the peak of a roughly Gaussian-shaped intensity envelope, the apparent value of I_{\min} at the next fringe minimum will be too small, since there is an overall reduction in the intensity of the envelope at that point as well. The following technique was developed to deal with this complication.

Figure C.1 is offered to illustrate the computation of visibility for a typical interference fringe data set. The solid curve in part a) of the figure displays the raw fringe data minus any DC background. The background light was recorded independently, with the interfering beams blocked, directly after each data set was taken. The Fourier transform of the resulting fringe pattern is displayed by the solid curve in Figure C.1 b). Two sizable components are present in the transform: the low frequency intensity envelope and a higher frequency peak corresponding to the interference fringes. Due to the sufficiently large difference in spatial frequency between the two components, the fringes and overall envelope are easily separated in frequency space. These are denoted in part c) by dashed and dot-dashed lines. The absolute-valued inverse transform of each portion is given in Figure C.1 a) by the same line style. Note that a (vector) sum of the parts returns the original fringe pattern, neglecting high frequencies.

It is easily seen that

$$I_{\max} = I_{1\max} + I_{2\max}, \quad (\text{C.2})$$

where $I_{1\max}$ is the intensity recorded at the maximum fringe and $I_{2\max}$ is the

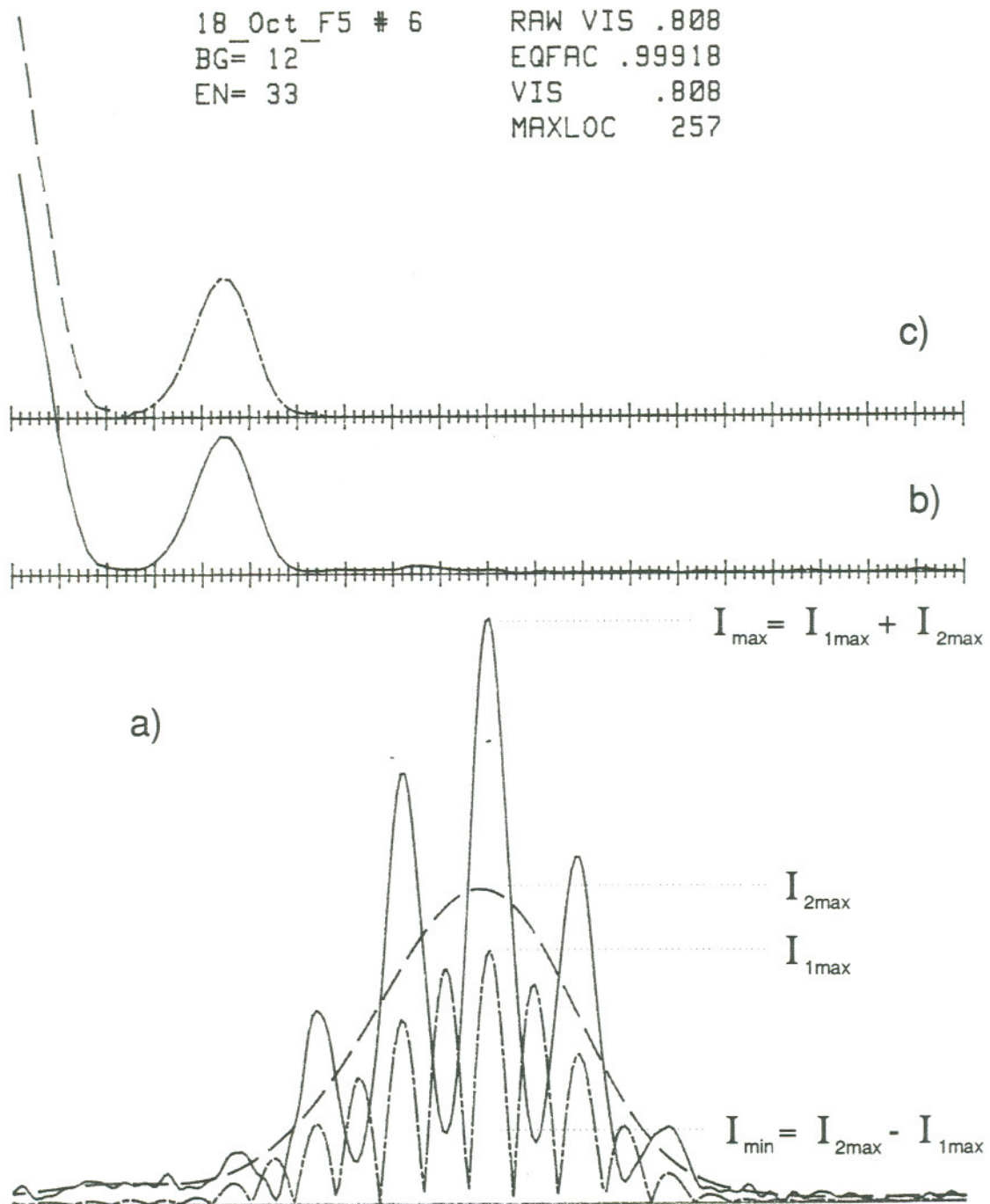


Figure C.1 Fourier transform technique used to extract visibility measurements from interference fringe data.

intensity of the envelope at the same location. If the fringe data was shifted by π before recombining, however, a minimum would be located at a previous maximum and vice versa. Here, at the same point where I_{\max} was determined, I_{\min} can be obtained as

$$I_{\min} = I_{2\max} - I_{1\max}. \quad (C.3)$$

The maximum and minimum intensities needed for the visibility (C.1) are then found at the same point on the envelope, eliminating the problem of non-uniform intensity on the interfering wavefronts. Note that these values need not be measured at the location of the largest fringe maximum; any fringe will do. In reality, this method accomplishes numerically what could also be done experimentally by altering the optical pathlength of one of the interfering beams by a half wavelength in between measurements of I_{\max} and I_{\min} .

Substitution of equations (C.2) and (C.3) into the visibility expression (C.1) gives

$$V = \frac{I_{1\max}}{I_{2\max}}. \quad (C.4)$$

In the example of Figure C.1, the "raw" visibility was determined to be .808. This value may underestimate the true visibility, however, due to an imbalance in intensity between the two interfering wavefronts at the point where the visibility is evaluated. Assuming two perfectly coherent sources, the intensity of a fringe maximum can be written as

$$I_{\max} = I_1 + I_2 + 2\sqrt{I_1 I_2}, \quad (C.5)$$

and a fringe minimum as

$$I_{\min} = I_1 + I_2 - 2\sqrt{I_1 I_2}, \quad (\text{C.6})$$

where I_1 and I_2 are evaluated at the point where the visibility is measured. Substitution into (C.1) and a few lines of algebra leads to

$$V = \frac{2\sqrt{I_1 I_2}}{I_1 + I_2}. \quad (\text{C.7})$$

This is the apparent visibility due to non-equal intensities. Note that when $I_1 = I_2$, the visibility goes to 1 as expected. Experimentally, the interfering wavefronts were individually recorded by opening and closing the appropriate electronic shutters indicated in the optical setup of Figure 4.3. By applying formula (C.7) at the same location where the visibility was measured, the correction factor, in the example of Figure C.1, was found to be negligible at .999. Division of the apparent visibility by this factor thus left its value virtually unchanged.

The contribution of a fraction of incoherent power in the interfering beams, spontaneous emission for example, also reduces visibility. While there is no such thing as truly incoherent radiation, the bandwidth of spontaneous emission in a semiconductor laser is large enough to be considered so in these experiments. The few hundred Å gain width of a semiconductor laser corresponds to a coherence length $\sim 10\mu\text{m}$. In practice, spontaneous emission represents an unavoidable limitation to the coherence of an extended source. In this sense, the measured visibility, including incoherent power, is the important number. In a stability study such as this, however, it is important to distinguish a

reduction in visibility due to spontaneous emission from that caused by poor phase-locking.

The interfering beams in the mutual coupling experiment of Chapter 4 are taken from different locations in the coupling region which were a few cm apart. Further, the spontaneous emission events originate independently in the two laser diodes and are therefore uncorrelated. This power will then create a non-zero baseline for the fringes and reduce the visibility. Consider the calculation of visibility for two interfering wavetrains where the total intensity of each beam is divided into coherent (where path differences are smaller than the coherence length) and incoherent parts (where the opposite is true)

$$I = I_{coh} + I_{incoh}. \quad (C.8)$$

Then the intensity of the fringe maximums and minimums are given by

$$I_{max} = I_{1coh} + I_{2coh} + 2\sqrt{I_{1coh}I_{2coh}} + I_{1incoh} + I_{2incoh}. \quad (C.9)$$

$$I_{min} = I_{1coh} + I_{2coh} - 2\sqrt{I_{1coh}I_{2coh}} + I_{1incoh} + I_{2incoh}. \quad (C.10)$$

The visibility is found from equation (C.1) to be

$$V = \frac{2\sqrt{I_{1coh}I_{2coh}}}{I_{1coh} + I_{2coh} + I_{1incoh} + I_{2incoh}}. \quad (C.11)$$

For equal interfering intensities the above expression can be rewritten as

$$V = \frac{1}{1 + \frac{I_{incoh}}{I_{coh}}}. \quad (C.12)$$

The reduction in visibility depends upon the fraction of incoherent power in the interfering sources. With $I_{incoh} = 0$, the visibility clearly goes to 1. The fraction of spontaneous emission power present in a laser's output can be found from its light versus current characteristic. Since the population inversion clamps at threshold, so must the spontaneous emission rate. For the semiconductor lasers used in the experiments of Chapter 4, spontaneous emission was determined to account for about 3% of the output power - resulting in a maximum visibility of 0.97. Not all of the highly divergent spontaneous emission from the diode laser is collected by the collimation lenses in Figure 4.3, however, slightly increasing this number.

In the course of examining the fringe data, it was found that visibilities exceeding about .9 were seldom seen, regardless of the coupling configuration. For this visibility, equation (C.12) predicts that an incoherent power of $\sim 10\%$ is necessary. The small fraction of spontaneous emission definitely could not account for it. To deduce whether this visibility was truly the limit, or merely an artifact of the optical setup, the mutual coupling experimental arrangement was modified so that a single laser could be interfered in an amplitude-splitting interferometer. This was accomplished by setting the attenuating polarizers for maximum transmission and rotating a single beam-splitter by 90° . Power balance between the two paths was carefully adjusted before generating fringes. The extremely small emitting aperture and narrow frequency bandwidth of a single stripe semiconductor laser was expected to produce fringes with visibility much in excess of 90%. This was not the case experimentally.

Figures C.2 a) and b) show the visibility of self-interference fringes of a single TJS and CSP laser respectively, versus injection current. It is evident

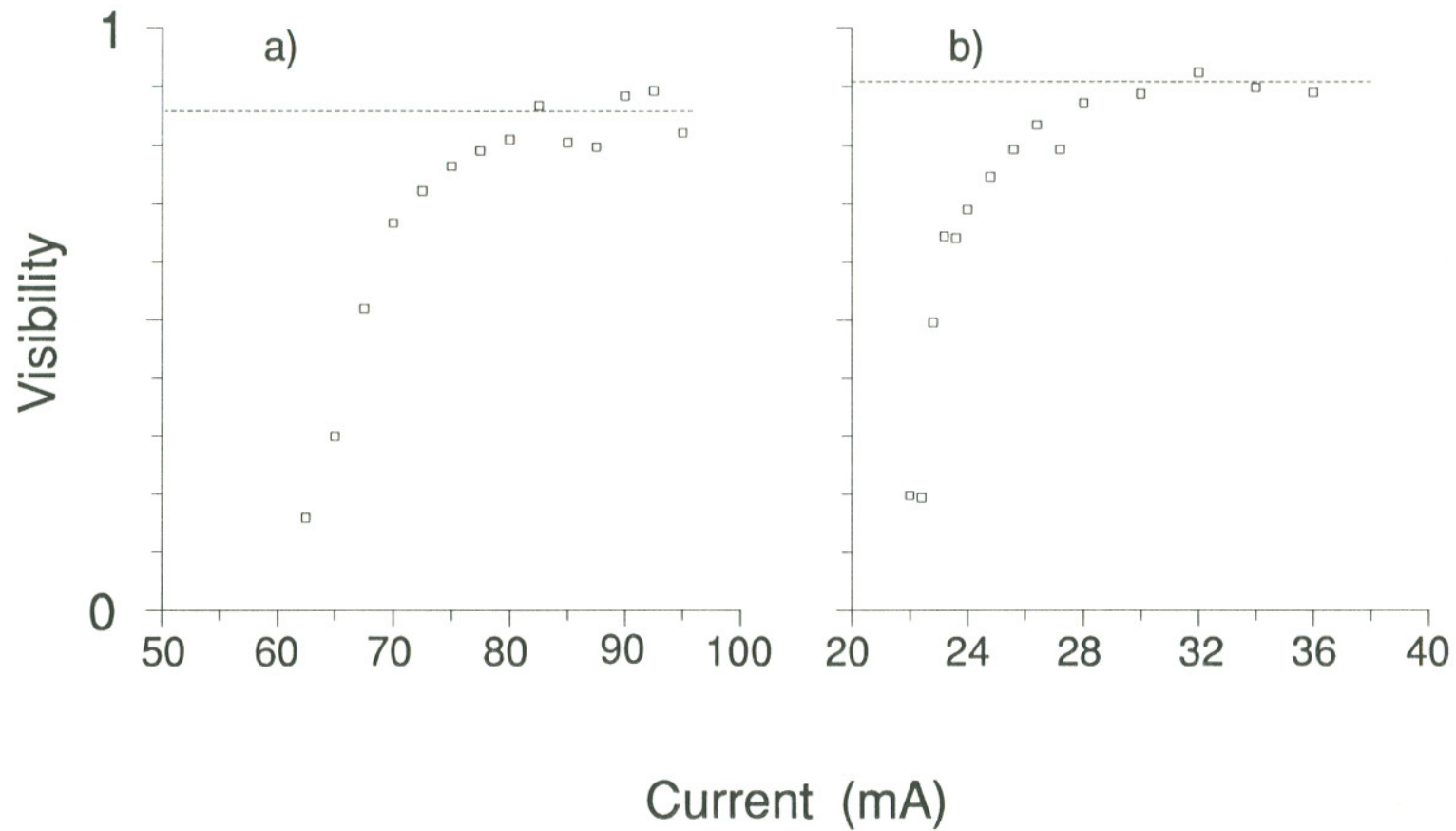


Figure C.2 Visibility versus injection current of a) HLP1400 CSP and b) ML5101a TJS lasers in an amplitude-splitting interferometer.

that visibility is poor just above threshold and approaches the same 90% mark measured in the mutual coupling setup. Near threshold the visibility is expected to be low, since several longitudinal diode modes oscillated with a mode suppression ratio of about 3 at best. The $\sim 3\text{\AA}$ mode separation of these modes corresponds to a coherence length of only a few millimeters. Since path-lengths were not matched to within this tolerance, the contribution of power to the fringes from the modes looked effectively incoherent. Furthermore, spontaneous emission made up a larger fraction of the total output power there. When biased well above threshold, the lasers exhibited primarily single longitudinal mode operation, as measured in Figure 4.24 a), with mode suppression ratios in excess of 50. Figure C.2, however, indicates that the nonlasing modes still comprised a sizable fraction of the total output power. After correcting for spontaneous emission background, equation (C.12) predicts about 6.5 percent of the total power was contained in secondary modes, resulting in a considerable influence on the maximum fringe visibility.

Unfortunately, interfering paths from each laser in the mutual coupling experimental setup were matched only to within $\lesssim 1$ cm, insuring that the coherence length would not be exceeded for spectral features within a 30 GHz bandwidth. Secondary longitudinal modes therefore contributed incoherently to the fringe pattern, resulting in a reduced visibility. In retrospect, a pathlength difference of about $100\mu\text{m}$ should have been employed to guarantee an accurate visibility measurement. Values approaching 97% would have then been measured near the central area of the fringe patterns for optimum coupling.‡ A

‡ This assumes that, in addition to the main mode, secondary longitudinal modes of the coupled lasers are also phase-locked.

correction factor for the incoherent addition of secondary longitudinal modes can be obtained from (C.12) and Figure C.2. Caution must be exercised, however, since the power content of the secondary modes depends sensitively on the injection current well above threshold, as evidenced in Figure C.2. This is due to competition and mode hopping between diode modes, resulting in longitudinal mode distributions with slightly different mode suppression. The correction was not introduced in the experimental results presented in this thesis, unless otherwise stated.

C.3 Visibility From Time Series

Theoretical modeling of phase locking between coupled lasers proceeds from numerical evaluation of noise driven rate equations introduced in Chapter 2 and Appendix D. The numerical simulations result in time series of field amplitude and phase for each laser. To determine the degree to which the lasers are coherent, a relationship must be established between the time series and the time-averaged visibility. This can be accomplished in the following way²⁶¹. Consider the intensity measured by a small detector over some finite time interval much longer than the coherence time, located in a plane where two waves are interfering

$$I = \langle |\tilde{E}(t)|^2 \rangle, \quad (\text{C.13})$$

where the total field is given by

$$\tilde{E}(t) = \tilde{E}_1(t) + \tilde{E}_2(t)e^{i\theta}. \quad (\text{C.14})$$

In this thought experiment, optical pathlengths are considered identical, and a variable phase delay θ has been incorporated into the optical path of laser 2 to move fringes across the detector. From expressions (C.13) and (C.14), the intensity can be written

$$I(\theta) = \langle |\tilde{E}_1(t)|^2 \rangle + \langle |\tilde{E}_2(t)|^2 \rangle + \frac{1}{T} \int_0^T [\tilde{E}_1(t)\tilde{E}_2^*(t)e^{-i\theta} + \tilde{E}_1^*(t)\tilde{E}_2(t)e^{i\theta}] dt. \quad (\text{C.15})$$

To compute the visibility, the maximum and minimum time-average intensities are needed. These are moved onto the detector at some θ found from

$$\frac{dI}{d\theta} = 0 = \frac{1}{T} \int_0^T [-ie^{-i\theta}\tilde{E}_1\tilde{E}_2^* + ie^{i\theta}\tilde{E}_1^*\tilde{E}_2] dt. \quad (\text{C.16})$$

Simplification leads to expressions for θ in terms of the incident fields

$$e^{i\theta} = \left(\frac{\langle \tilde{E}_1\tilde{E}_2^* \rangle}{\langle \tilde{E}_1^*\tilde{E}_2 \rangle} \right)^{1/2}, \quad e^{-i\theta} = \left(\frac{\langle \tilde{E}_1^*\tilde{E}_2 \rangle}{\langle \tilde{E}_1\tilde{E}_2^* \rangle} \right)^{1/2}. \quad (\text{C.17})$$

Substitution into equation (C.15) then gives the maximum and minimum intensities

$$I_{\max} = I_1 + I_2 + 2\sqrt{\langle \tilde{E}_1\tilde{E}_2^* \rangle \langle \tilde{E}_1^*\tilde{E}_2 \rangle}, \quad (\text{C.18})$$

$$I_{\min} = I_1 + I_2 - 2\sqrt{\langle \tilde{E}_1\tilde{E}_2^* \rangle \langle \tilde{E}_1^*\tilde{E}_2 \rangle}. \quad (\text{C.19})$$

I_1 and I_2 are the intensities of the individual interfering waves. The above can

be substituted into the definition of visibility (C.1), giving

$$V = \frac{2\sqrt{\langle \tilde{E}_1 \tilde{E}_2^* \rangle \langle \tilde{E}_1^* \tilde{E}_2 \rangle}}{I_1 + I_2}. \quad (\text{C.20})$$

Finally, if the complex field amplitudes are written as

$$\tilde{E}_1(t) = E_1(t)e^{i\phi_1(t)}, \quad \tilde{E}_2(t) = E_2(t)e^{i\phi_2(t)}, \quad (\text{C.21})$$

it is easily derived that

$$\langle \tilde{E}_1 \tilde{E}_2^* \rangle \langle \tilde{E}_1^* \tilde{E}_2 \rangle = C^2 + S^2, \quad (\text{C.22})$$

where

$$C = \frac{1}{T} \int_0^T E_1(t) E_2(t) \cos \Delta\phi(t) dt \quad (\text{C.23})$$

$$S = \frac{1}{T} \int_0^T E_1(t) E_2(t) \sin \Delta\phi(t) dt. \quad (\text{C.24})$$

The general expression for the visibility as calculated from time averages of the numerical time series for field and phase can then be written

$$V = \frac{2\sqrt{C^2 + S^2}}{I_1 + I_2}. \quad (\text{C.25})$$

APPENDIX D

This appendix discusses the application of Langevin noise sources in the stochastic rate equations. To begin, a brief background of the use and properties of Langevin noise terms is presented. A procedure is outlined to numerically simulate the noise forces arising from spontaneous emission. In section D.2, phase noise is independently considered. A noise source is derived for use in numerical integration of the phase equation (F.2). Numerical simulations of Brownian motion are presented to substantiate that the Langevin noise source does indeed give the desired linewidth.

D.1 Stochastic Rate Equations

The single-mode rate equations for an isolated semiconductor laser may be written in a stochastic form^{262, 263} by including Langevin noise sources to account for the incoherent addition of many random fluctuations due to spontaneous emission events (F_E, F_ϕ), and shot noise (F_N) associated with the discrete nature of carriers

$$\dot{E}(t) = \frac{1}{2} \frac{\partial G}{\partial N} \Delta N(t) E(t) + \frac{R_{sp}}{2E(t)} + F_E(t) \quad (\text{D.1})$$

$$\dot{\phi}(t) = \frac{1}{2}\alpha \frac{\partial G}{\partial N} \Delta N(t) + F_{\phi}(t) \quad (\text{D.2})$$

$$\Delta \dot{N}(t) = \Delta J - \frac{\Delta N(t)}{\tau_s} - \left(\frac{\partial G}{\partial N} \Delta N(t) + \frac{1}{\tau_p} \right) E^2(t) + F_N(t). \quad (\text{D.3})$$

R_{sp} is the average rate of spontaneously emitted photons entering the lasing mode. The field amplitude $E(t)$ is normalized such that its square gives the photon number in the cavity. The deterministic part of the Langevin equations, where $F_i(t)=0$, describes completely the time evolution of the system given a set of three initial conditions $X(t=0)$ for the dynamic variables. Each $F_i(t)$ is a random, rapidly varying force with a zero ensemble average,

$$\langle F_i(t) \rangle = 0. \quad (\text{D.4})$$

It is assumed that the Langevin sources portraying spontaneous emission superimpose *incoherently*, implying that the correlation times of the forces are much shorter than the smallest response time of the deterministic equation. In this case, delta function correlations may be employed

$$\langle F_i(t) F_j(t') \rangle = 2D_{ij} \delta(t-t'), \quad (\text{D.5})$$

corresponding to a white noise source. This is the so-called Markoffian assumption²⁶⁴. The D_{ij} 's are constants expressing the magnitude of the fluctuating forces. They can, in general, be related to the second moments of a Fokker-Planck equation^{264, 265} describing the time evolution of the probability density for the dynamic variables in equations (D.1)-(D.3). The second moment is responsible for the diffusion or spreading of the distribution in time; hence the

name *diffusion coefficient* for D_{ij} . The most important ones are given by^{248, 262}

$$D_{\phi\phi} = \frac{R_{sp}}{4E_o^2}, \quad D_{EE} = \frac{R_{sp}}{4}, \quad D_{E\phi} = 0. \quad (\text{D.6})$$

Carrier fluctuations due to shot noise, described by the Langevin source $F_N(t)$, produce a negligible effect on phase noise²⁶⁶ and therefore may be ignored. The strength of the fluctuating forces depend on the photon number and, of course, the spontaneous emission rate.

The Langevin forces arising from spontaneous emission can also be written as a sum of all spontaneous events occurring at a time t ²⁴⁸

$$F_E(t) = \sum_i \cos\theta_i \delta(t-t_i) \quad (\text{D.7})$$

$$F_\phi(t) = \sum_i \frac{1}{E(t)} \sin\theta_i \delta(t-t_i) \quad (\text{D.8})$$

where θ_i is the phase angle of the i th spontaneous photon. For the purpose of numerical integration of the rate equations, it is necessary to determine a form for F_E and F_ϕ within an integration step Δt . Let there be k spontaneous emission events in an interval Δt . The total changes ΔE in field amplitude and $\Delta\phi$ in phase are then

$$\Delta E = \sum_{i=1}^k \cos\theta_i \quad (\text{D.9})$$

and

$$\Delta\phi = \frac{1}{E_o} \sum_{i=1}^k \sin\theta_i. \quad (\text{D.10})$$

On average there will be $\langle k \rangle = R_{sp} \Delta t$ spontaneously emitted photons in the interval Δt . The average spontaneous emission rate R_{sp} at the lasing frequency is related to the stimulated emission rate through²⁶⁷

$$R_{sp} = n_{sp} G(N), \quad (\text{D.11})$$

where n_{sp} is the inversion factor. Since $G(N) = 1/\tau_p$ in steady-state above threshold, an estimate of the spontaneous emission rate can be determined from $R_{sp} = \frac{n_{sp}}{\tau_p}$. With $n_{sp} \sim 2.5$ ²⁶⁸, there are typically ~ 25 photons emitted in a 10 ps integration step. If k is assumed to be Poisson distributed, it has been shown²⁶⁹ that for $\langle k \rangle \gg 1$, the probability distributions for ΔE and $\Delta \phi$ are approximately Gaussian with zero mean and standard deviations

$$\sigma_{\Delta E} = \left(\frac{\langle k \rangle}{2} \right)^{1/2} \quad (\text{D.12})$$

and

$$\sigma_{\Delta \phi} = \sigma_{\Delta E} / E_o. \quad (\text{D.13})$$

Therefore, the Langevin terms can be numerically simulated in each time interval as

$$F_E = \frac{\Delta E}{\Delta t} = \left(\frac{R_{sp}}{2\Delta t} \right)^{1/2} X, \quad (\text{D.14})$$

$$F_\phi = \frac{\Delta \phi}{\Delta t} = \left(\frac{R_{sp}}{2\Delta t} \right)^{1/2} \frac{1}{E_o} Y. \quad (\text{D.15})$$

X and Y are Gaussian random variables with standard deviations of one.

The above procedure to numerically simulate the Langevin terms associated with spontaneous emission is dependent upon knowledge of R_{sp} , which is difficult to accurately determine. Its value was set by numerically integrating the rate equations (D.1)-(D.3), requiring that the FWHM of the central peak in the field power spectrum match the experimentally observed lasing linewidth. It was found, for example, that a spontaneous emission rate $R_{sp} = 3 \times 10^{12} s^{-1}$ is appropriate to produce the 12 MHz linewidth of the HLP1400 CSP laser. Spontaneous emission is often described in terms of the so-called spontaneous emission factor β_{sp} ²⁴². For the CSP parameters indicated in Table E.1, the above spontaneous recombination rate is equivalent to $\beta_{sp} = 9.2 \times 10^{-6}$. Very long time series were necessary to obtain adequate resolution and to average out the noisy spectrum for this parameter fit.

D.2 Numerical Simulation of Phase Noise

Appendix F derives an approximate phase equation (F.2), which was used extensively in Chapters 3 and 4. The noise source (F.3) which accompanies this equation might also be modeled using the procedure outlined in Section D.1. However, the phase noise can also be analytically related to the natural laser linewidth. In the absence of optical coupling, (F.2) is simply

$$\dot{\phi}(t) = F(t). \quad (D.16)$$

This is the equation for Brownian motion (or a Wiener process) of the phase

$\phi(t)$. When $\bar{e}_j \approx e_o$, where e_o is the isolated field amplitude, (F.3) can be taken as the Langevin source responsible for the natural linewidth of the laser. Note that the last term in (F.3), arising from the average spontaneous emission rate r_{sp} , merely produces a constant frequency shift in the lasing field, and is unimportant for the remainder of this discussion.

Consider the spectral density function $S_E(\omega)$ of the complex field amplitude,

$$E(t) = E(t)e^{i[\omega_o t + \phi(t)]}, \quad (\text{D.17})$$

since this is what is measured in the Fabry-Perot spectral data of Chapters 3 and 4. The Wiener-Khintchine theorem²⁶⁴ states that $S_E(\omega)$ is given by the Fourier transform of the field autocorrelation

$$S_E(\omega) = \int_{-\infty}^{\infty} R(\tau)e^{-i\omega\tau}d\tau, \quad (\text{D.18})$$

where $R(\tau) = \langle E(t)E(t+\tau) \rangle$. Using (D.17), the autocorrelation is straightforwardly shown to be²³⁵

$$R(\tau) = \frac{\langle E_o^2 \rangle}{4} e^{-i\omega_o\tau} \langle e^{i[\phi(t+\tau) - \phi(t)]} \rangle + c.c. \quad (\text{D.19})$$

keeping only slowly varying terms and assuming the field amplitude is constant as was done in deriving equation (F.2). The expectation value

$$\langle e^{-i\Delta\phi(t,\tau)} \rangle = \int_{-\infty}^{\infty} e^{-i\Delta\phi(t,\tau)} \rho(\Delta\phi) d(\Delta\phi), \quad (\text{D.20})$$

where $\rho(\Delta\phi)$ is the density function of the random variable

$\Delta\phi(t,\tau) \equiv \phi(t) - \phi(t+\tau)$. The phase fluctuations due to spontaneous emission execute a Brownian motion assuming any value between $(0,2\pi)$ with equal probability. In the limit of a large number of spontaneous emission events the density function of $\Delta\phi(t,\tau)$ will be normally distributed²⁶⁴ with zero mean and variance $\langle(\Delta\phi)^2\rangle$ such that

$$\rho(\Delta\phi) = \frac{1}{\sqrt{2\pi\langle(\Delta\phi)^2\rangle}} e^{-\Delta\phi^2/2\langle(\Delta\phi)^2\rangle}. \quad (\text{D.21})$$

Equation (D.20) can be expanded as

$$\begin{aligned} \langle e^{-i\Delta\phi} \rangle &= 1 - i\langle\Delta\phi\rangle - \frac{1}{2}\langle(\Delta\phi)^2\rangle + \dots \\ &+ \langle \frac{(-i)^n}{n!} (\Delta\phi)^n \rangle + \dots \end{aligned} \quad (\text{D.22})$$

Since $\Delta\phi$ will be positive as often as negative, its ensemble average $\langle\Delta\phi\rangle=0$. Furthermore, *all* the odd moments will be zero, since their density (D.21) is an even function. The even moments of a Gaussian distributed random variable are given by

$$\langle(\Delta\phi)^{2n}\rangle = 1\cdot3\cdot5\cdots(2n-1) \left(\langle(\Delta\phi)^2\rangle\right)^n. \quad (\text{D.23})$$

Evaluation of the expectations in equation (D.22) then results in

$$\langle e^{-i\Delta\phi} \rangle = \sum_{k=0}^{\infty} \frac{(-1)^k}{k!} \left(\frac{\langle(\Delta\phi)^2\rangle}{2} \right)^k = e^{-\langle(\Delta\phi)^2\rangle/2}. \quad (\text{D.24})$$

The field spectral density (D.18) can now be evaluated after specifying $\langle(\Delta\phi)^2\rangle$. Returning to equation (D.16), its discrete form can be written

$$\lim_{\Delta t \rightarrow 0} \frac{\phi(t+\Delta t) - \phi(t)}{\Delta t} = F(t). \quad (\text{D.25})$$

After a time $\tau = N\Delta t$, keeping in mind the limit in (D.25), the total phase variation is the sum of N contributions

$$\Delta\phi(t, \tau) = - \sum_{k=1}^N F(k\Delta t)\Delta t. \quad (\text{D.26})$$

The mean squared variation in the phase difference is then

$$\langle (\Delta\phi)^2 \rangle = \sum_{k=1}^N \sum_{k'=1}^N F(k\Delta t)F(k'\Delta t)(\Delta t)^2. \quad (\text{D.27})$$

The discrete form of the autocorrelation of a Langevin source, given by equation (D.5) is

$$\langle F(k\Delta t)F(k'\Delta t) \rangle = 2D\delta_{k,k'}. \quad (\text{D.28})$$

This is only valid, in light of the limit imposed in equation (D.25), if the correlation time of the noise source is much shorter than the time step Δt . This is the case under the Markoffian assumption. Therefore, equation (D.27) reduces to

$$\langle (\Delta\phi)^2 \rangle = \sum_{k=1}^N 2D(\Delta t)^2 = 2D\tau\Delta t. \quad (\text{D.29})$$

The above merely states that the mean squared coordinate of a system undergoing Brownian motion increases linearly with total elapsed time τ . Equation (D.29) can now be substituted into (D.19) and the Fourier integral transform (D.18) evaluated. The spectral field density is found to be a simple Lorentzian

$$S_E(\omega) \sim \frac{\langle E_o^2 \rangle}{(D\Delta t)^2 + (\omega - \omega_o)^2} \quad (\text{D.30})$$

centered on the angular frequency ω_o with a FWHM $\Delta\omega^o = 2D\Delta t$. Therefore, the coefficient

$$D = \frac{\pi\Delta\nu^o}{\Delta t}. \quad (\text{D.31})$$

So the diffusion coefficient of the overall Langevin noise source $F(t)$, not surprisingly, is directly related to the linewidth of the lasing mode. This allows a very accurate determination of the noise level from an experimentally measured linewidth. By inspection, $F(t)$ can finally be defined as

$$F(t) = \left(\frac{2\pi\Delta\nu_o}{\Delta t} \right)^{\frac{1}{2}} X(t), \quad (\text{D.32})$$

in which the random variable $X(t)$ is normally distributed and describes a stochastic process where

$$\langle X(t)X(t') \rangle = \delta(t-t'). \quad (\text{D.33})$$

Figure D.1 displays the Fourier transform of the complex field amplitude given by equation (D.17), where $E(t)$ is assumed constant and fluctuations in phase $\phi(t)$ are supplied through numerical integration of equation (D.16) using (D.32) as the Langevin source. The line shapes appear Lorentzian with full width at half maximums closely matching the specified values.

The Gaussian distributed random variables, necessary to numerically handle the stochastic noise sources in the laser rate equations, can be derived in

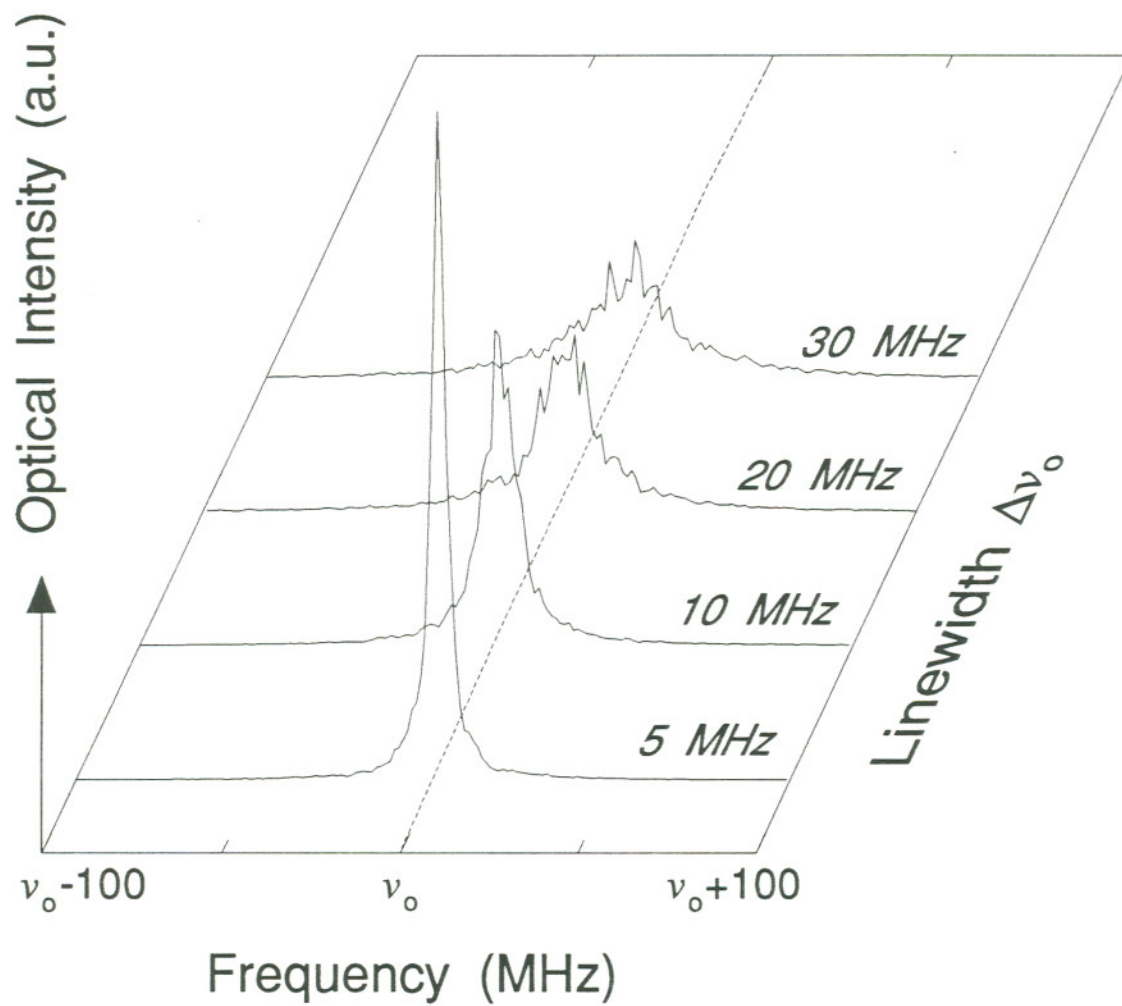


Figure D.1 Numerically simulated natural linewidth of a semiconductor laser, obtained by integrating the phase rate equation (F.2) with the Langevin noise source (D.32).

terms of uniformly distributed random variables in the following way. Consider *two* jointly normal random variables x, y and the transformations

$$z = e^{-(x^2+y^2)/2\sigma^2} \quad (\text{D.34})$$

$$\theta = \tan^{-1} \frac{y}{x}. \quad (\text{D.35})$$

Note that z is confined to the range $(0,1)$ and θ ranges over $(0,2\pi)$. Under the inverse transformations, the normal random variables are then given by

$$x = \sqrt{-2\sigma^2 \ln z} \cos \theta \quad (\text{D.36})$$

$$y = \sqrt{-2\sigma^2 \ln z} \sin \theta. \quad (\text{D.37})$$

It will be shown that z and θ are uniformly distributed. The joint density function of z and θ is given by²⁶⁴

$$f_{z\theta} = \frac{f_{xy}(\sqrt{-2\sigma^2 \ln z} \cos \theta, \sqrt{-2\sigma^2 \ln z} \sin \theta)}{|J(x, y)|}, \quad (\text{D.38})$$

where the Jacobian of the transformation is given by

$$J(x, y) = \begin{vmatrix} \frac{\delta x}{\delta z} & \frac{\delta x}{\delta \theta} \\ \frac{\delta y}{\delta z} & \frac{\delta y}{\delta \theta} \end{vmatrix}^{-1} = -\frac{z}{\sigma^2}. \quad (\text{D.39})$$

The joint density function is then

$$f_{z\theta} = \frac{1}{2\pi}, \quad (\text{D.40})$$

a constant. Hence, z, θ are jointly uniformly distributed over their respective intervals. If x, y are independent random variables, then so are z, θ . So (D.36) and (D.37) give two independent, normally distributed random variables given two uniformly distributed random variables over $(0,1)$ and $(0,2\pi)$. This procedure was used to generate the numerical results in Figure D.1.

APPENDIX E

This appendix discusses the measurement of parameters needed for numerical modeling of the rate equations for self and mutual coupling. Experiments to determine the necessary parameters are explained for the two experimental semiconductor lasers used in Chapters 3 and 4.

E.1 Parameter Measurements

Measurement of parameters is important so that a reasonably accurate comparison between computer modeling, based on the coherent rate equations, and the experimental results can be presented. An exhaustive survey need not be undertaken, however, as the number of necessary parameters in the reduced form of the rate equations is quite small ($\Delta\nu_D, \alpha, \frac{\partial G}{\partial N}, \tau_p$ and τ_s). This is possible since the rate equations are written in terms of photon and carrier *numbers*, rather than densities, per optical *mode*, so that the active volume and confinement factor are unnecessary. The four different experiments carried out to determine the parameters are now described.

Longitudinal mode spectra: The values of several important device characteristics can be determined from the longitudinal mode spectra of a semiconductor laser both above and below threshold. For example, a standard technique for experimentally determining the value of α in a given laser is through the simultaneous measurement of wavelength shift and modal gain change with injection current below threshold²⁷⁰⁻²⁷². This can be seen by writing expression (A.11) in terms of quantities which are directly measurable from the emission spectrum. Below threshold, a change in the index of refraction of the active layer, $d\mu$, can be determined from the wavelength shift of a longitudinal mode with current through^{273,274}

$$d\mu = \frac{\mu_g}{\Gamma\lambda} d\lambda, \quad (\text{E.1})$$

where μ_g is the effective group index. Further, the material gain g at a given carrier density can be found in terms of the modal gain $g_m \equiv \Gamma g$, by measuring the intensity modulation of the spontaneous emission spectrum below threshold as²⁷⁵

$$g_m = \frac{1}{L_D} \ln \left(\frac{r^{1/2} - 1}{r^{1/2} + 1} \right) + \alpha_t. \quad (\text{E.2})$$

r is the ratio of an intensity maximum to the intensity of the adjacent minimum at a particular wavelength in the spontaneous spectrum. α_t is the total loss per unit length in the cavity. Substitution of (E.1) and (E.2) into equation (A.11), eliminating the carrier number N in favor of current, gives

$$\alpha = \frac{2\pi}{\Delta\lambda} \frac{d\lambda/dI}{d(g_m L_D)/dI}. \quad (\text{E.3})$$

$\Delta\lambda = \frac{\lambda^2}{2\mu_g L_D}$ is the longitudinal mode spacing of the resonator.

The longitudinal mode spectra were measured on a 1.25 m SPEX spectrometer as a function of current. The entire exit plane of the spectrometer was imaged onto a CCD array and subsequently digitized for analysis. An IR polarizer was inserted in front of the lasers to discriminate against sizable TM mode contributions to the spontaneous spectrum below threshold, as this would lead to an underestimate of the modal gain in equation (E.2). Operating near $1.5 I_{th}$ at room temperature, the lasing wavelength of the Hitachi HLP1400 CSP laser was 831 nm, while the Mitsubishi ML5101a lased at 818 nm. Their longitudinal mode spacings above threshold were 2.82 \AA (123 GHz) and 2.58 \AA (116 GHz) respectively.

The sub-threshold wavelength and gain shift measurements were carried out CW, as an accurate assessment of the pulsed injection current was not realizable with the available equipment, due to the relatively low thresholds of these devices. Figures E.1 and E.2 display the resulting variations of $d\lambda$ and $dg_m L_D$ with current in each device. The wavelength is observed to shift to shorter values in an approximately linear fashion with increasing current, due to a decreasing index of refraction in the active region with increasing carrier density. Upon reaching threshold, the carrier density clamps and the resonator modes return to longer wavelengths due to heating. The shift above threshold is also very linear with respect to current. Therefore, the reduction in the slope $d\lambda/dI$ below threshold can be corrected for thermal effects using the slope above threshold²⁷⁶. The corrected $d\lambda/dI$ for the CSP laser was $-0.19 \text{ \AA} / \text{mA}$ while the TJS data resulted in $-0.31 \text{ \AA} / \text{mA}$. With $dg_m L_D/dI$ values of 0.14 (CSP)

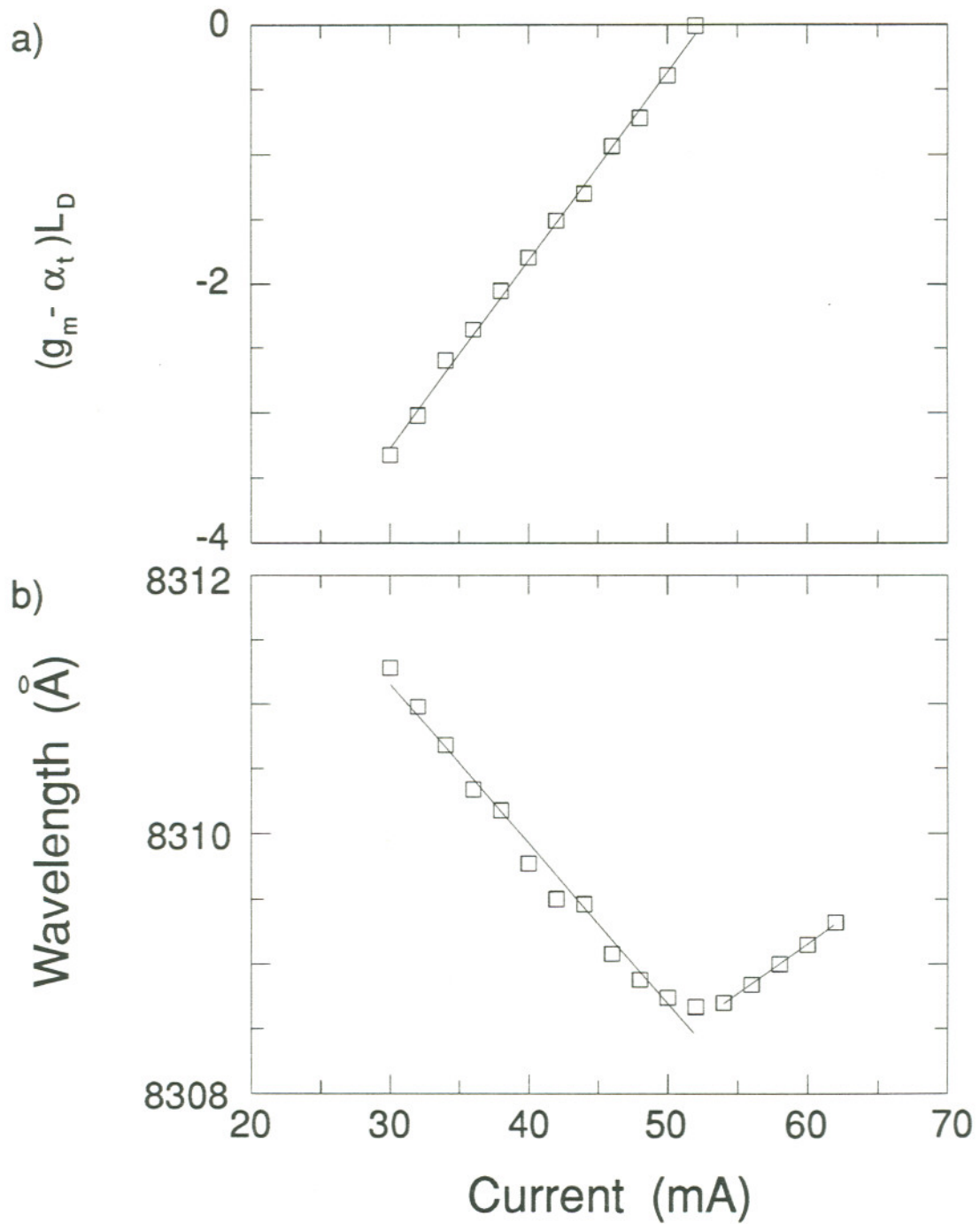


Figure E.1 Modal a) gain change and b) wavelength shift of a HLP1400 CSP laser diode versus injection current below and just above threshold.

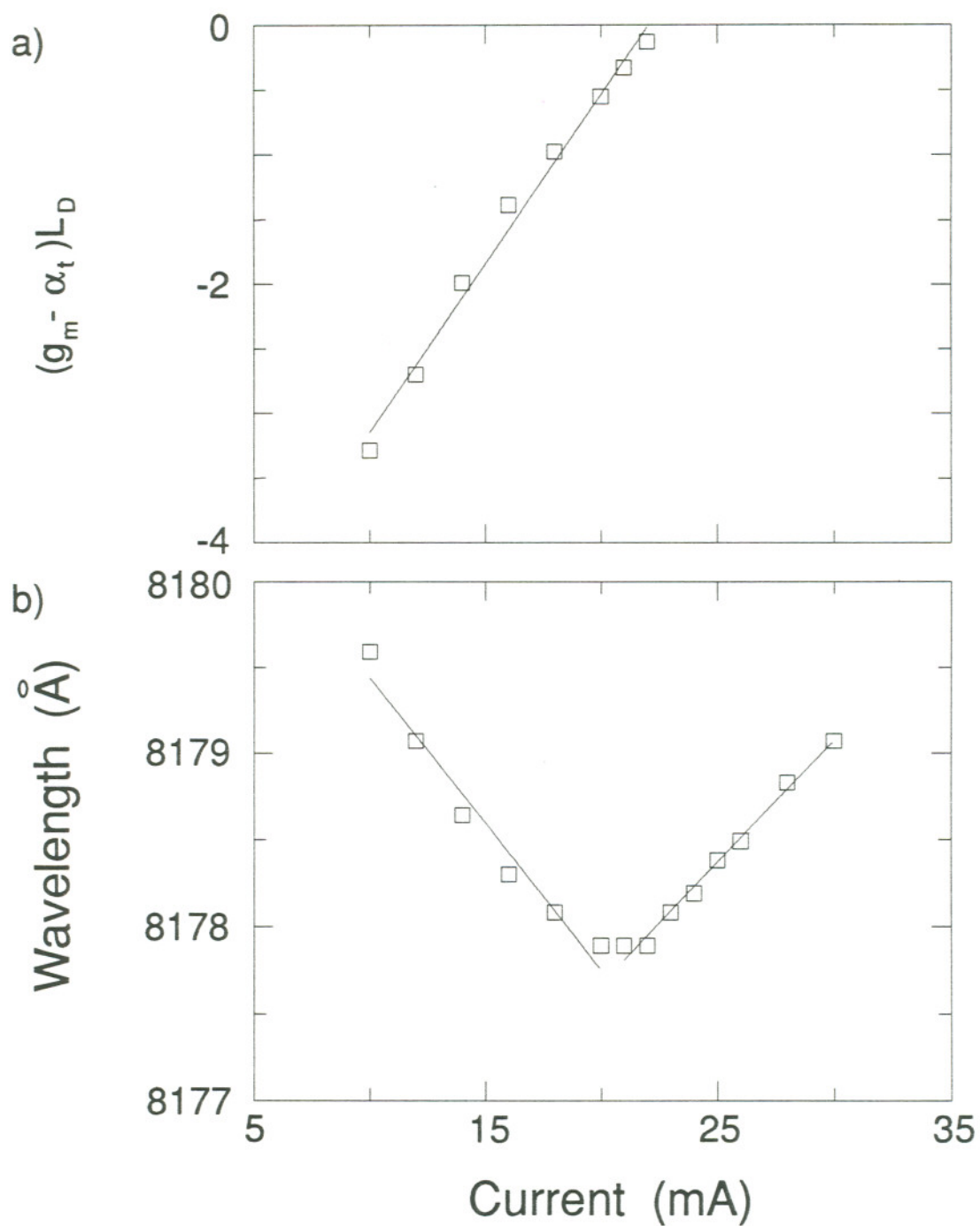


Figure E.2 Modal a) gain change and b) wavelength shift of a ML5101a TJS laser diode versus injection current below and just above threshold.

and 0.28 (TJS) measured in Figures E.1 a) and E.2 a), α parameter values of 3.0 ± 0.3 for the CSP and 2.7 ± 0.3 for the TJS laser were calculated. There have been several past reports of α measurements on AlGaAs CSP lasers using a variety of techniques^{271,277-279}. Typical values range from 2.5 to 4. Even less of a consensus has been reached in the relatively few reports for AlGaAs TJS lasers^{250,279,280}, with results scattered from 3.8 to 8.3.

Light versus current characteristics: The single stripe, index guided lasers used in the experiments of Chapters 3 and 4 could provide power outputs in excess of 10 mW CW when driven to about 2 times threshold. Figure E.3 displays the light-current characteristics of both lasers. The threshold of the HLP1400 laser was about 52 mA with $dP/dI = .21 W/A$, whereas the ML5101a had a much lower threshold of 22 mA with a slope $dP/dI = .47 W/A$. An important parameter which can be determined from this data is the photon lifetime τ_p in the laser resonator. The photon lifetime is defined as

$$\frac{1}{\tau_p} = v_g \alpha_t = v_g (\alpha_{mir} + \alpha_{int}), \quad (E.4)$$

where α_{mir} is the loss out of the resonator due to finite facet power reflectivities R_1 and R_2 , while α_{int} is the loss from internal scattering, absorption, etc. The total loss, α_t , can be related to the external differential quantum efficiency through²⁴²

$$\eta_d = \eta_i \frac{\alpha_{mir}}{\alpha_t} = \eta_i \frac{\alpha_{mir}}{v_g \tau_p}. \quad (E.5)$$

However, this efficiency is also directly proportional to the (measurable) slope

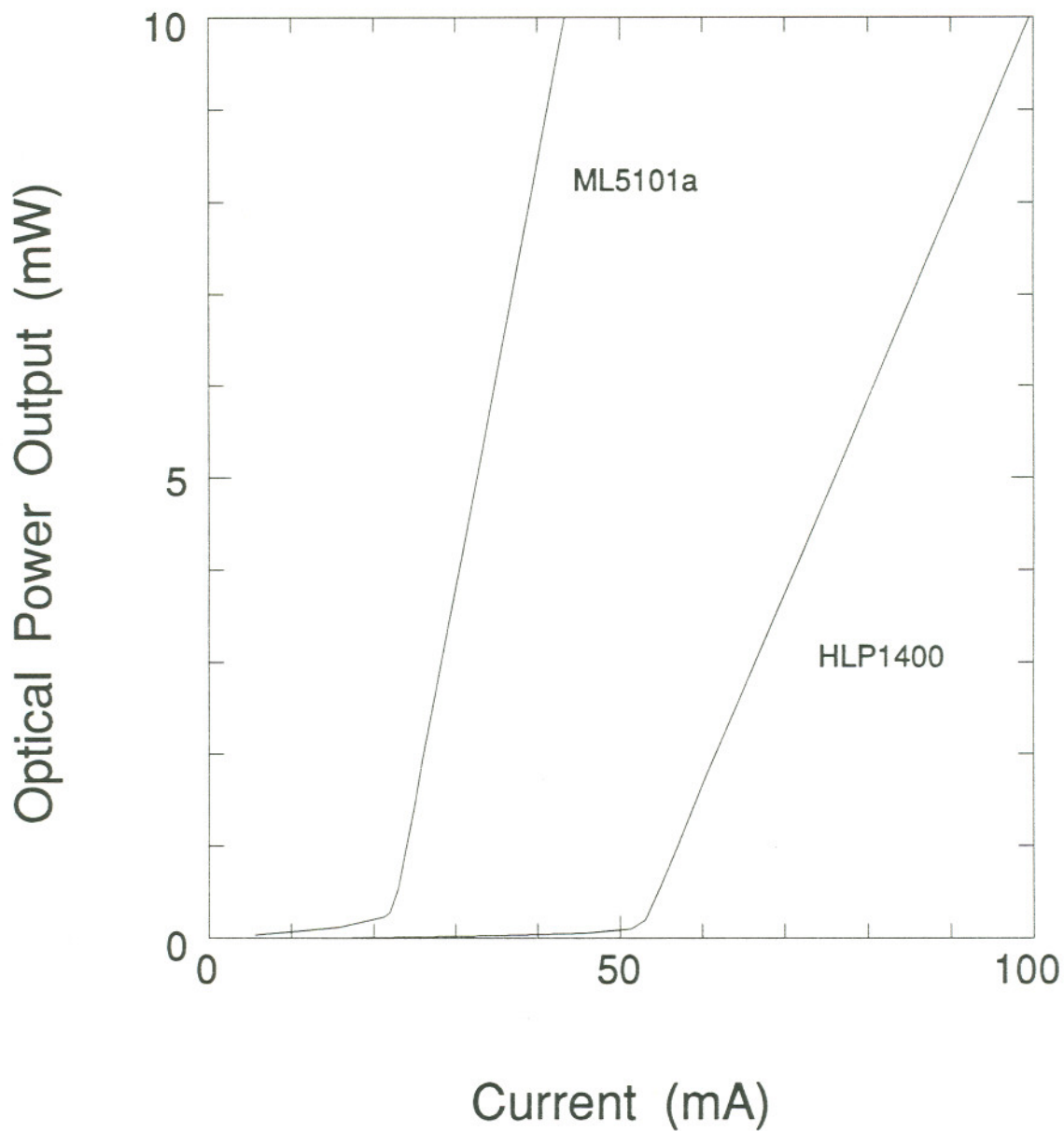


Figure E.3 Light versus current characteristics of the experimental semiconductor diode lasers.

efficiency²⁴²

$$\eta_d = \eta_i \frac{q}{\zeta h \nu} \frac{dP}{dI}, \quad (\text{E.6})$$

with²⁶⁸

$$\zeta = \frac{(1-R_2)\sqrt{R_1}}{(\sqrt{R_1} + \sqrt{R_2})(1 - \sqrt{R_1 R_2})} \quad (\text{E.7})$$

accounting for the fraction of power emitted from the front facet. (E.5) and (E.6) together give an expression for the photon lifetime in terms of measurable

$$\tau_p = \frac{q}{\alpha_{mir} v_g \zeta h \nu} \cdot \frac{dP}{dI}. \quad (\text{E.8})$$

The mirror loss/group velocity product is given by

$$\alpha_{mir} v_g = \Delta \nu_D \ln \left(\frac{1}{R_1 R_2} \right), \quad (\text{E.9})$$

where $\Delta \nu_D$ is the longitudinal Fabry-Perot mode spacing of the diode laser. The facets of the HLP1400 laser were uncoated, other than passivation, whereas the ML5101a device, according to the manufacturer, was coated to make $R_1 = .6$ and $R_2 = .1$. Substitution of the appropriate parameters results in photon lifetimes of 1.0 ps and 1.1 ps, respectively.

Optical delay measurements: The carrier lifetime τ_c can be determined from the turn-on time delay of a pulsed semiconductor laser.^{281,282} The carrier

lifetime is in general dependent upon the number of carriers. It can be modeled as

$$\frac{1}{\tau_s} = A + BN + CN^2, \quad (\text{E.10})$$

where the coefficient A accounts for non-radiative recombination at defects or traps, BN describes bimolecular recombination, and CN^2 is the contribution from Auger recombination. If τ_s is approximated as a constant, the carrier rate equation may be integrated analytically, given a current step from a bias I_o below threshold to some I above threshold. The carrier number is found to build up to its threshold value in a time²⁴¹

$$\tau_d(I) = \tau_s \ln \left(\frac{I - I_o}{I - I_{th}} \right). \quad (\text{E.11})$$

Thus, the carrier lifetime can be found experimentally by measuring the time delay between a current pulse and the onset of lasing at various current levels.

An approximately 1 ns risetime current pulse was used to pulse the lasers from zero bias, while the resulting optical pulse was detected with a fast PIN photodiode. Figure E.4 displays the time delay, relative to an arbitrary time t_o , versus the current pulse amplitude. The slopes of a linear fit to each data set result in carrier lifetimes of 1.4 ns for the HLP1400 laser and 1.7 ns for the ML5101a.

Relaxation resonance measurements: The well known relaxation resonance between photons and carriers in a semiconductor laser can be written²³⁵

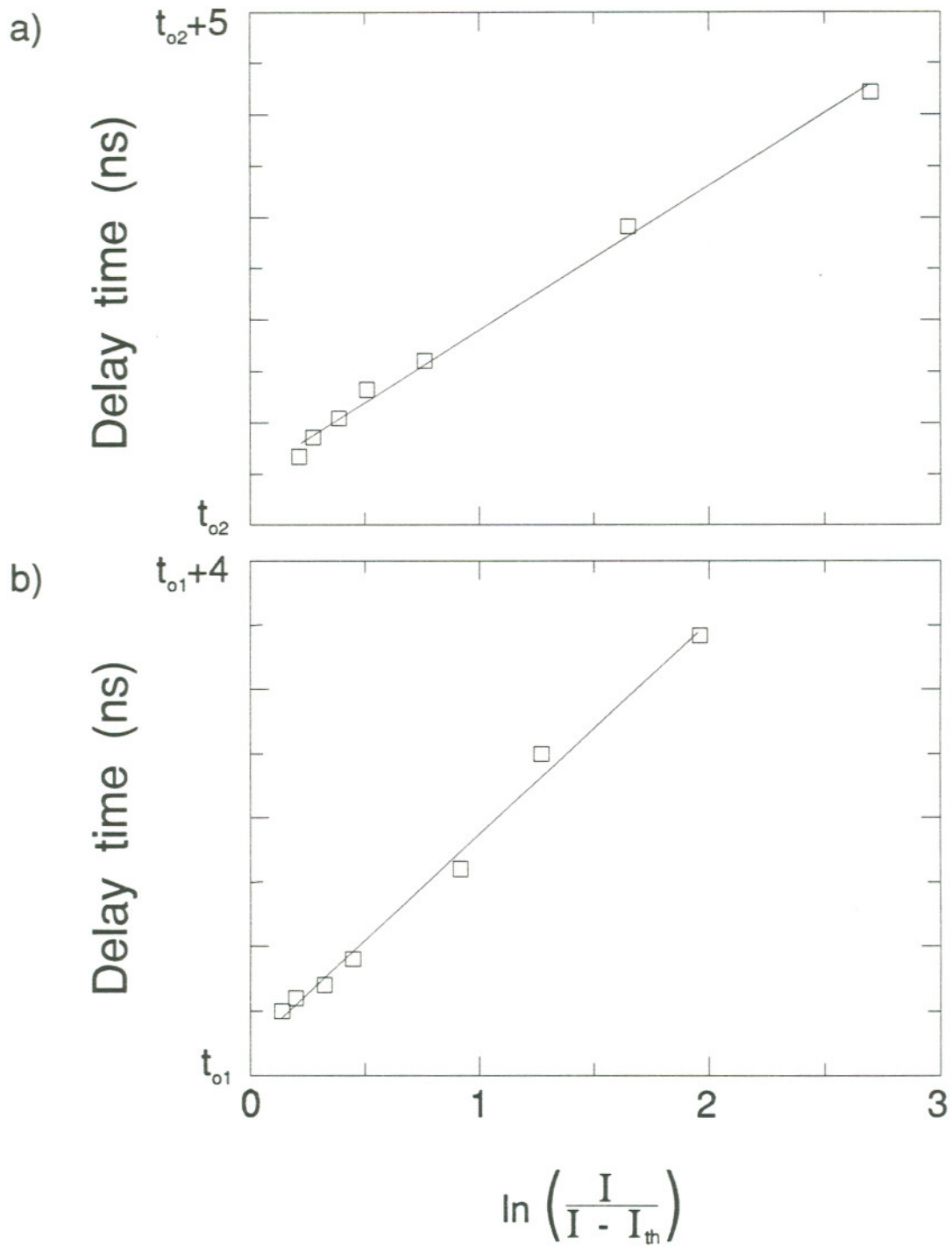


Figure E.4 Turn-on delay time versus injection current for a) HLP1400 CSP and b) ML5101a TJS diode lasers.

$$\omega_R^2 = \frac{1 + \tau_p N_o \partial G / \partial N}{\tau_s \tau_p} \left(\frac{I}{I_{th}} - 1 \right), \quad (\text{E.12})$$

from small signal analysis of the rate equations. However, the gain=loss condition above threshold requires that

$$N_{th} - N_o = \frac{1}{\tau_p \partial G / \partial N}. \quad (\text{E.13})$$

Further, the threshold carrier density is

$$\frac{N_{th}}{V} = \frac{\tau_s I_{th}}{qV}, \quad (\text{E.14})$$

where q is the electronic charge and V is the volume of the active region. Substituting (E.13) and (E.14) into (E.12), eliminating N in favor of current gives

$$\omega_R^2 = \frac{v_g}{\tau_s} \left(\frac{dg_m}{dI} \right) (I - I_{th}). \quad (\text{E.15})$$

So the relaxation resonance frequency at a specific current level can be related to the previously measured carrier lifetime and differential modal gain with respect to current. The length of each laser was measured in an SEM to be 300 μm . From the longitudinal mode spacing, a group index n_g of 4.1 was calculated for the HLP1400 and 4.3 for the ML5101a. These numbers give relaxation resonance frequencies of 4.8 GHz and 3.8 GHz, respectively. These values are in reasonable agreement with the experimentally observed values of about 5.1 GHz and 3.9 GHz, respectively. Any discrepancy must be attributed to either an erroneous measurement of τ_s or dg_m/dI , since the values used for v_g , I and I_{th} in equation (E.15) are beyond doubt due to their straightforward measurements.

The carrier lifetime is the most suspect, since its measurement assumes the risetime of the current pulse is much shorter than τ_c , and further, that the risetime remains constant with pulse amplitude. Neither of these assumptions were precisely true in these experiments. A value of 1.3 ns was adopted for numerical calculations involving the CSP laser to insure the relaxation resonance frequency matched experiment so that direct comparisons could be made.

Table E.1 is offered as a compilation of the above experimental measurements for each laser. Only those parameters which are necessary for the numerical model are given. Listed in the first half of the table are the directly measurable quantities followed by useful, although redundant, parameters.

Parameter	Symbol	HLP1400	ML5101a	Units
Cavity length	L_D	300	300	μm
Rear facet reflectivity	R_1	0.32	0.6	
Front facet reflectivity	R_2	0.32	0.1	
Lasing wavelength	λ	831	818	nm
Mode spacing	$\Delta\nu_D$	123	116	GHz
Threshold current	I_{th}	52	22	mA
Slope efficiency	dP/dI	0.21	0.47	W/A
Linewidth	$\Delta\nu^o$	12	18	MHz
Resonance frequency	ν_R	5	3.8	GHz
Modal gain derivative	dg_m/dI	4.7×10^5	9.3×10^5	$\text{m}^{-1}\text{A}^{-1}$
Carrier lifetime	τ_s	1.3	1.7	ns
Photon lifetime	τ_p	1.0	1.1	ps
Antiguinding parameter	α	3.0	2.7	
Group velocity	v_g	7.4×10^7	7.0×10^7	m/s
Transparency carrier number	N_o	2.0×10^8	8.8×10^7	
Cold cavity bandwidth	$\Delta\nu_{cc}$	23.6	52.5	GHz

Table E.1 Compilation of parameters characterizing the experimental semiconductor lasers at an operating bias of $1.7 I_{th}$.

APPENDIX F

This appendix derives an approximate form of the coupled rate equations (2.3.6) and (2.3.7).

Consider a coupled system of lasers operating in a state where field amplitude fluctuations can be ignored, $e_j(t) = \bar{e}_j$. The field rate equation (2.3.6), including noise, then reduces to

$$\begin{aligned} \Delta n_j(\hat{t}) = & -\text{Re}[\bar{\eta}_{jj}] - \frac{r_{sp}}{2\bar{e}_j^2} - \frac{F_e(\hat{t})}{\bar{e}_j} \\ & - \eta_{jk} \frac{\bar{e}_k}{\bar{e}_j} \cos[\tau_p \Delta\omega_{oj} \hat{t} + \phi_k(\hat{t}) - \phi_j(\hat{t}) + \psi_{jk}]. \end{aligned} \quad (\text{F.1})$$

This expression can now be substituted into the phase rate equation (2.3.7), leaving

$$\begin{aligned} \dot{\phi}_j(\hat{t}) = & \eta_{jj} \sqrt{1+\alpha^2} \sin(\psi_{jj} - \tan^{-1}\alpha) - \alpha \frac{r_{sp}}{2\bar{e}_j^2} + F(\hat{t}) \\ & + \eta_{jk} \frac{\bar{e}_k}{\bar{e}_j} \sqrt{1+\alpha^2} \sin[\tau_p \Delta\omega_{oj} \hat{t} + \phi_k(\hat{t}) - \phi_j(\hat{t}) + \psi_{jk} - \tan^{-1}\alpha], \end{aligned} \quad (\text{F.2})$$

where

$$F(\hat{t}) = F_{\phi}(\hat{t}) - \alpha \frac{F_{\epsilon}(\hat{t})}{\bar{\epsilon}_j} \quad (\text{F.3})$$

is defined as an overall Langevin noise source.

The assumption of constant field amplitude results in a neglect of carrier dynamics, which are responsible for relaxation resonance sidebands present in the field power spectrum²⁶⁶. Normally, an amplitude fluctuation contributes a delayed phase fluctuation, through α , and leads to damped relaxation oscillations. In the limit of large damping, however, the relaxations die out rapidly, resulting in reduced sidebands. The response of carriers to fluctuations in the intensity can then be considered instantaneous, and the temporal response of the laser is well described by a constant field amplitude and a phase given by equation (F.2).

An instantaneous response is equivalent to stating that only frequencies $\omega \ll \omega_R$ contribute significantly to the power spectrum²⁸³, where ω_R is the relaxation resonance frequency. This is the same approximation introduced by Adler²⁸⁴ in his classic paper on injection locking of oscillators. The resulting phase equation, in that work, is often referred to as the Adler equation. (F.2) can then be considered an Adler-like equation for the phase in a mutually coupled system. It is used heavily in Chapters 3 and 4 to model transient behavior.

APPENDIX G

This appendix lists the source codes of several computer programs used for numerical solutions throughout this dissertation.

The first, *ocop.for* solves the full nonlinear rate equations for two mutually coupled diode lasers with arbitrary coupling delay. This program was used heavily in Chapter 4 to simulate optical spectra and visibility during overcoupling. A very similar program was used to model coherence collapsed spectra in Chapter 3.

Several spectral simulations for coupled operation below the onset of coherence collapse or overcoupling were also compared to experiment in Chapters 3 and 4. Stationary solutions, in these chapters, were calculated with the program *detsols.for*. Although written for two coupled lasers, steady-state solutions for the self-coupled case were also obtained, as discussed in Section 4.1. Optical spectra were generated with variations on the program *hop.for*, which integrates the Adler-like phase equation (3.1.10).

The η -plane stability plots displayed in Chapter 2 were generated with the program *hurwitz.for*.

```

program ocop
c This program integrates the rate equations (2.3.8), (4.1.1)
c and (4.1.2) describing the time evolution of two mutually
c coupled lasers with an arbitrary time delay.
c Integration is performed using the NAG routine d02ebf,
c a variable-order, variable-step Gear method.
c The user must supply an input file ocop.prm containing
c the necessary input parameters. Output consists of two files
c x*.dat and y*.dat containing time series of the field amplitudes
c and phases for lasers x and y, respectively.
c
integer iw,ifail,mped,ir,n
double precision w(3,21),y(3),x(3)
double precision tol,t0,tmax,tstep,tstart,tstop,tval

c
character*7 suffix
character*60 charline
integer ndelay,i,l,nmax,nthrow,fskip,fout,sskip,sout
real z1,z2,z3,z4
double precision dnsp,q,spamp,rsp,e0,redkap,kapnl,detun
double precision c,db,dgdi,ld,lext,n0,pi,dnul,ith,tm
double precision r,taup,taus,xthresh,tau,eps,dvcc,vg
double precision xdelay,ydelay,eta,pstn,delrho,sigma,alpha
double precision omegar,frac,phsdiff0

c
common/blk1/ xdelay(2,1000),ydelay(2,1000),
& z1,z2,z3,z4,spamp,rsp,e0
common/blk2/ eta,pstn,delrho,sigma,alpha,redkap,detun
common/blk3/ ndelay
common/blk4/ tstep,l,taup
common/blk5/ nthrow,nskip,ncount
external fcnx,fcny,outdat,pedervx,pedervy

c
*** constants
c
c = 3.d8
q = 1.6e-19
pi = 3.1415927

c
input parameters

```

```

open(1,file='ocop.prm',status='old')
read(1,*) charline,suffix / output file suffix
read(1,*) charline,alpha / alpha parameter
read(1,*) charline,db / coupling level, db
read(1,*) charline,detun / detuning, Hz
read(1,*) charline,dgdi / differential gain, m-1 mA-1
read(1,*) charline,dnsp / inversion factor
read(1,*) charline,dnul / mode spacing, Hz
read(1,*) charline,dpdi / slope efficiency, W/A
read(1,*) charline,ith / threshold current, A
read(1,*) charline,kapnl / nonlinear gain coef, W-1
read(1,*) charline,ld / diode laser length
read(1,*) charline,lext / laser separation, m
read(1,*) charline,nmax / number of iterations
read(1,*) charline,fskip / pts to skip between output
read(1,*) charline,sskip / pts to skip, screen output
read(1,*) charline,nthrow / # pts to throw away at start
read(1,*) charline,pstn / piston phase, rads
read(1,*) charline,r / facet power reflectivity
read(1,*) charline,taup / photon lifetime, s
read(1,*) charline,taus / carrier lifetime, s
read(1,*) charline,tval / integration time step, s
read(1,*) charline,xthresh / bias times threshold
read(1,*) charline,phsdiff0 / initial phase difference
close(1)

c
c
*** compute higher level params
tstep = tval/taup
fout = nthrow + 1
tmax = (nmax + nthrow)*tstep
sigma = taus/taup
vg = 2.*dnul*ld
n0 = .5*(vg*taup*ith*dgdi-1.)
delrho = (.5 + n0)*(xthresh-1.)
tau = lext/c
eps = 10** (db/20.)
dvcc = dnul*(1-r)/2./pi/dsqrt(r)
detun = detun*taup
eta = 2*pi*taup*dvcc*eps

```

```

cc = eta/taup*tau*dsqrt(1 + alpha*alpha)
ndelay = int(10*tau/(tstep*taup) + 0.5)/10.
spamp = dsqrt(vg*q*dgdi*dnspl/tstep)/2.
rsp = vg*q*dgdi*dnspl/2.
e0 = dsqrt(delrho)
redkap = 2*kapnl/taup*dpci/vg/dgdi

c
c initialize random # generator
call seed(9151)

c
c *** set up the integrater parameters
n = 3
tol = 1.d-12
ir = 0
mped = 1
iw = 21
ifail = 0
l = 0

c
c *** open output files
open(1,file='y//suffx//'.dat')
open(2,file='x//suffx//'.dat')

c
c *** initial values
y(1) = e0
y(2) = 0.
y(3) = 0.
x(1) = e0
x(2) = phsdiff0
x(3) = 0.

c
c *** fill delayed arrays
do 100 i = 1,ndelay
    ydelay(1,i) = y(1)
    ydelay(2,i) = 0.
    xdelay(1,i) = x(1)
    xdelay(2,i) = phsdiff0
100 continue
c

```

```

c
c *** main integration loop
c
c *** output integrated values
c
199 if ((l .eq. fout) .and. (l .gt. nthrow)) then
    tm = snl(tstop*taup*1.d9)
    write(1,1000) tm,snl(y(1)),snl(y(2))
    write(2,1000) tm,snl(x(1)),snl(x(2))
    fout = fout + fskip
endif

c
c *** output to screen
c
if (l .eq. sout) then
    print *,tm,y(1),y(2)
    sout = sout + sskip
endif

c
c *** shift the delayed array
do 200 i = ndelay,1,-1
    ydelay(1,i+1) = ydelay(1,i)
    ydelay(2,i+1) = ydelay(2,i)
    xdelay(1,i+1) = xdelay(1,i)
    xdelay(2,i+1) = xdelay(2,i)
200 continue

c
c *** store the newest delayed data
ydelay(1,1) = y(1)
ydelay(2,1) = y(2)
xdelay(1,1) = x(1)
xdelay(2,1) = x(2)

c
c *** get four gaussian distributed random numbers
c *** for next time interval
call gaus(z1,z2)
call gaus(z3,z4)

c
c *** set the next output time
tstart = l*tstep
t0 = tstart
l = l + 1

```

```

tstop = l*tstep
c
c *** integrate laser y rate equations
call d02ebf(t0,tstop,n,y,tol,ir,fcny,mped,pedervy,
&          outdat,w,iw,ifail)
c
c *** integrate laser x rate equations
t0 = tstart
call d02ebf(t0,tstop,n,x,tol,ir,fcnx,mped,pedervx,
&          outdat,w,iw,ifail)
c
if (tstop .lt. tmax) goto 199
close (1)
close (2)
1000 format(1x,f6.2,1x,f5.3,1x,f10.3)
stop
end

c *** function to output data
subroutine outdat(tstop,y)
integer l
double precision tstop,y(3),tstep,taup
common/blk4/ tstep,l,taup
tstop = tstop + tstep
return
end

c *** function to evaluate difeq
subroutine fcny(t,y,yprime)
integer ndelay
real z1,z2,z3,z4
double precision t,y(3),yprime(3),spamp,rs,e0,gnl,detun
double precision xdelay,ydelay,eta,pstn
double precision delrho,sigma,alpha,redkap
common/blk1/ xdelay(2,1000),ydelay(2,1000),
&          z1,z2,z3,z4,spamp,rs,e0
common/blk2/ eta,pstn,delrho,sigma,alpha,redkap,detun
common/blk3/ ndelay

```

```

c *** evaluate reduced rate equations:
c *** field laser 1
gnl = 1-redkap*y(1)*y(1)
yprime(1) = ((2.*y(3)+1.)*gnl - 1.)*y(1)/2.
&          + rsp/2./y(1) + spamp*z1
&          + eta*dcos(pstn + detun*t + y(2)-xdelay(2,ndelay))
&          *xdelay(1,ndelay)
c
c *** phase laser 1
yprime(2) = alpha*y(3) + spamp*z2/e0
&          - eta*dsin(pstn + detun*t + y(2)-xdelay(2,ndelay))
&          *xdelay(1,ndelay)/y(1)
c
c *** carrier density laser 1
yprime(3) = (delrho-y(3) - (2*y(3) + 1)*gnl*y(1)*y(1))/sigma
c
return
end

c *** function to evaluate difeq
subroutine fcnx(t,x,xprime)
integer ndelay
real z1,z2,z3,z4
double precision t,x(3),xprime(3),spamp,rs,e0,gnl,detun
double precision xdelay,ydelay,eta,pstn,delrho
double precision sigma,alpha,redkap
common/blk1/ xdelay(2,1000),ydelay(2,1000),
&          z1,z2,z3,z4,spamp,rs,e0
common/blk2/ eta,pstn,delrho,sigma,alpha,redkap,detun
common/blk3/ ndelay
c
c *** evaluate reduced rate equations:
c *** field laser 2
gnl = 1-redkap*x(1)*x(1)
xprime(1) = ((2.*x(3)+1.)*gnl - 1.)*x(1)/2.
&          + rsp/2./x(1) + spamp*z3
&          + eta*dcos(pstn-detun*t + x(2)-ydelay(2,ndelay))
&          *ydelay(1,ndelay)
c

```

```

c      *** phase laser 2
      xprime(2) = alpha*x(3) + spamp*z4/e0
      &      - eta*dsin(pstn-detun*t + x(2)-ydelay(2,ndelay))
      &      *ydelay(1,ndelay)/x(1)
c
c      *** carrier density laser 2
      xprime(3) = (delrho-x(3) -(2*x(3) + 1)*gnl*x(1)*x(1))/sigma
c
      return
      end
c
      *** Jacobian routine laser y
      subroutine pedervy(t,y,pwy)
      double precision t,y(3),pwy(3,3)
      integer ndelay
      real z1,z2,z3,z4
      double precision xdelay,ydelay,eta,pstn,delrho,ycube,detun
      double precision sigma,alpha,spamp,rs,e0,redkap
      common/blk1/ xdelay(2,1000),ydelay(2,1000),
      &      z1,z2,z3,z4,spamp,rs,e0
      common/blk2/ eta,pstn,delrho,sigma,alpha,redkap,detun
      common/blk3/ ndelay
c
      *** equations of laser 1
      ycube = y(1)*y(1)*y(1)
      pwy(1,1) = y(3) - 3.*redkap*y(3)*y(1)*y(1)
      &      - 3./2.*redkap*y(1)*y(1) - rsp/2./y(1)/y(1)
      &      pwy(1,2) = -eta*dsin(pstn + detun*t + y(2)-xdelay(2,ndelay))
      &      *xdelay(1,ndelay)
      pwy(1,3) = y(1) - redkap*ycube
      pwy(2,1) = eta*dsin(pstn + detun*t + y(2)-xdelay(2,ndelay))
      &      *xdelay(1,ndelay)/y(1)/y(1)
      &      pwy(2,2) = -eta*dcos(pstn + detun*t + y(2)-xdelay(2,ndelay))
      &      *xdelay(1,ndelay)/y(1)
      pwy(2,3) = alpha
      pwy(3,1) = -4.*y(3)*y(1)/sigma
      &      + 8.*redkap*y(3)*ycube/sigma
      &      - 2.*y(1)/sigma + 4.*redkap*ycube/sigma
      pwy(3,2) = 0

```

```

      pwy(3,3) = -1/sigma - 2*y(1)*y(1)/sigma
      &      + 2.*redkap*ycube*y(1)/sigma
c
      return
      end
c
      *** Jacobian routine laser x
      subroutine pedervx(t,x,pwx)
      double precision t,x(3),pwx(3,3)
      integer ndelay
      real z1,z2,z3,z4
      double precision xdelay,ydelay,eta,pstn,delrho,xcube,detun
      double precision sigma,alpha,spamp,rs,e0,redkap
      common/blk1/ xdelay(2,1000),ydelay(2,1000),
      &      z1,z2,z3,z4,spamp,rs,e0
      common/blk2/ eta,pstn,delrho,sigma,alpha,redkap,detun
      common/blk3/ ndelay
c
      *** equations of laser 2
      xcube = x(1)*x(1)*x(1)
      pwx(1,1) = x(3) - 3.*redkap*x(3)*x(1)*x(1)
      &      - 3./2.*redkap*x(1)*x(1) - rsp/2./x(1)/x(1)
      &      pwx(1,2) = -eta*dsin(pstn-detun*t + x(2)-ydelay(2,ndelay))
      &      *ydelay(1,ndelay)
      pwx(1,3) = x(1) - redkap*xcube
      pwx(2,1) = eta*dsin(pstn-detun*t + x(2)-ydelay(2,ndelay))
      &      *ydelay(1,ndelay)/x(1)/x(1)
      &      pwx(2,2) = -eta*dcos(pstn-detun*t + x(2)-ydelay(2,ndelay))
      &      *ydelay(1,ndelay)/x(1)
      &      pwx(2,3) = alpha
      &      pwx(3,1) = -4.*x(3)*x(1)/sigma
      &      + 8.*redkap*x(3)*xcube/sigma
      &      - 2.*x(1)/sigma + 4.*redkap*xcube/sigma
      pwx(3,2) = 0
      pwx(3,3) = -1/sigma - 2*x(1)*x(1)/sigma
      &      + 2.*redkap*xcube*x(1)/sigma
c
      return
      end

```

```

subroutine gaus(z1,z2)
c This subroutine generates a gaussian distributed
c random variable. (actually 2).
c
d = 6.283185307
10 call random(u1)
if (u1 .eq. 0.0) goto 10
call random(u2)
thb = d*u2
rb = sqrt(-2.*alog(u1))
z1 = rb*sin(thb)
z2 = rb*cos(thb)
return
end

```

program **detsols**

```

c This program solves equations (4.1.6) and (4.1.7) for the
c modes of two identical, mutually coupled lasers with arbitrary
c coupling delay and detuning. The NAG routine c05pbf, a
c modified Powell hybrid method for solving N nonlinear equations
c in N unknowns, is called. The user must supply the file det.inp
c containing the necessary input parameters. Output consists of
c two files ctuns*.dat and ctunu*.dat containing the stable and
c unstable mode frequencies versus piston, respectively. Stability
c of the solutions is checked by solving the stability criterion
c (4.1.19).

```

```

double precision tol,fvec(2),fjac(2,2),wa(15),x(2)
integer ifail,n,ldfjac,lwa
external fcn

```

```

character*1 chnum
integer pp,f
logical stabcrit
double precision alpha,kappa,pstn0,db,cc,s
double precision detun,tau,dvcc,pcr,piston
double precision pstep,delfrq,lastroot,roots(10)
common /blk1/ alpha,cc,piston,detun

```

```

pi = 3.1415927
pstep = pi/10.

```

```

c *** read parameters
open(1,file='det.inp',status='old')
read(1,*) alpha,db,detun,dvcc,tau,phsdiff0
close(1)

```

```

print *,'enter set number'
read *,chnum

```

```

c *** calculate higher level parameters
pcr = 10**(db/10.)
kappa = 2*pi*dvcc*sqrt(pcr)
cc = kappa*tau*sqrt(1+alpha*alpha)

```

```

pstn0 = pi/2.-datan(alpha)
detun = 2.*pi*detun*tau

c   *** open output files
open(1,file='ctuns'//chnum//'.dat')
open(2,file='ctunu'//chnum//'.dat')

c   *** nag setup
n = 2
ifail = 1
tol = 1.e-9
ldfjac = 2

c   *** loop through pistons
do 900 pp = 0,40
piston = pp*pstep + pstn0
numroots = 0

c   *** search freq dimension for roots
do 800 f = -10,10

c   *** initial estimates
x(1) = phsdiff0
x(2) = f*cc/10.

c   *** find roots
ifail = 1
call c05pbf(fcn,n,x,fvec,fjac,ldfjac,tol,wa,lwa,ifail)

c   *** check if root found
if (ifail .eq. 0) then
c   *** if no previous roots
      if (numroots .eq. 0) then
          roots(1) = x(2)
          numroots = 1
c   *** evaluate stability
          if (stabcrit(x)) then
              write(2,999) x(2)/2./pi/tau*1.e-6,piston
          else

```

```

              write(1,999) x(2)/2./pi/tau*1.e-6,piston
          endif
          iflag = 1
          goto 800
      endif
c   *** compare to previous roots
do 500 i = 1,numroots
      if (dabs(x(2)-roots(i)) .lt. 1.e-4) goto 800
500  continue

c   *** if no match, output it
c   *** check stability
      if (stabcrit(x)) then
          write(2,999) x(2)/2./pi/tau*1.e-6,piston
      else
          write(1,999) x(2)/2./pi/tau*1.e-6,piston
      endif
      iflag = 1
      numroots = numroots + 1
      roots(numroots) = x(2)
    endif

800  continue
900  continue
close(1)
close(2)
999  format(1x,e13.6,5x,e13.6)
stop
end

c   *** subroutine to evaluate equations or jacobian
subroutine fcn(n,x,fvec,fjac,ldfjac,iflag)
integer iflag,ldfjac,n
double precision fjac(ldfjac,n),fvec(n),x(n)

double precision alpha,cc,piston,detun
common /blk1/ alpha,cc,piston,detun

```

```

c      *** evaluate equations at current x values
      if (iflag .eq. 1) then
        fvec(1) = detun-2*cc*dsin(x(1))*dcos(x(2)
&          + piston + datan(alpha))
        fvec(2) = x(2)
&          + cc*dcos(x(1))*dsin(x(2) + piston + datan(alpha))
      endif

C      *** evaluate jacobian
      if (iflag .eq. 2) then
        fjac(1,1) = -2*cc*dcos(x(1))*dcos(x(2) + piston + datan(alpha))
        fjac(1,2) = 2*cc*dsin(x(1))*dsin(x(2) + piston + datan(alpha))
        fjac(2,1) = -cc*dsin(x(1))*dsin(x(2) + piston + datan(alpha))
        fjac(2,2) = 1 + cc*dcos(x(1))*dcos(x(2) + piston + datan(alpha))
      endif
      return
      end

c      *** subroutine to evaluate stability
      logical function stabcrit(x)
      double precision x(2)
      double precision cj,ck,s,s0,diff
      double precision alpha,piston,cc,detun,lhs,rhs
      integer oldflag,newflag
      common /blk1/ alpha,cc,piston,detun

      stabcrit = .false.
c      *** initially evaluate equation (4.1.19)
      cj = cc*dcos(x(2) + piston-x(1) + datan(alpha))
      ck = cc*dcos(x(2) + piston + x(1) + datan(alpha))
      csum = cj + ck
      s0 = -(csum)/2. + dsqrt(csum*csum + 4*dabs(cj*ck))/2.
      lhs = -cj*ck*(1-dexp(-2*s0))
      rhs = s0*s0 + (cj + ck)*s0
      diff = lhs-rhs
      if (diff .lt. 0) then
        oldflag = -1
      else
        oldflag = 1

```

```

      endif
c      *** look for change of sign to indicate root in right half
c      *** of complex plane - unstable!
      do 100 s = s0,s0/100.,-s0/100.
        lhs = -cj*ck*(1-dexp(-2*s))
        rhs = s*s + (cj + ck)*s
        diff = lhs-rhs
        if (diff .lt. 0) then
          newflag = -1
        else
          newflag = 1
        endif
c      *** root has been found - unstable solution.
        if (oldflag .ne. newflag) then
          stabcrit = .true.
          goto 200
        endif
100    continue
200    return
      end

```

```

c      program hurwitz
c      This program locates stability boundaries in
c      the plane of the complex coupling coefficient
c      for two mutually coupled lasers with no coupling delay
c      using the hurwitz criterion and equation (2.4.16).
c      This produces three boundaries, which are
c      output in files hur*.dat. The fourth criterion
c      (2.4.15) is also tested.

```

```

character*1 sufx
logical stab1old,stab1new,stab2old,stab2new
logical stab3old,stab3new,stab4,origin
real alpha,phscc,sigma,delrho,sqtalp,omegar0
real gamma0,cphscc,cphsalp,etacc,delnbar,gamma
real etasc,phssc,cphssc
real a1,a2,a3,omegar,mag,magval
real stormag(1000),storphs(1000)
integer mode,count

```

```

pi = 3.1415927
count = 0

```

```

c      *** parameters
alpha = 3.
mode = 1
sigma = 1500.
delrho = 0.67
etasc = 0.
phssc = 0.

```

```

print *, 'what file suffix? (one char)'
read *, sufx
open(1, file = 'hur1'//sufx//'.dat')
open(2, file = 'hur2'//sufx//'.dat')
open(3, file = 'hur3'//sufx//'.dat')
open(4, file = 'hur4'//sufx//'.dat')

```

```

c      *** calculate higher level parameters
sqtalp = sqrt(1 + alpha*alpha)

```

```

omegar0 = 2*delrho/sigma
gamma0 = (1. + 2.*delrho)/2./sigma

c      *** loop through 2 pi coupling phase
do 900 phscc = 0,2*pi,.01

cphscc = cos(phscc)
cphssc = cos(phssc)
cphsalp = cos(phscc-atan(alpha))
stab4 = .true.
origin = .true.

c      *** search radially for a boundary, -60 db up
do 500 mag = -6.,0.,.01
etacc = 10.**mag

c      *** evaluate (2.4.15)
delnbar = - etacc*cphscc*mode - etacc*cphssc
if (-delnbar .ge. 0.5) then
    if (stab4) then
        magval = mag + 6.
        write(4,999) magval*cos(phscc),magval*sin(phscc)
        stab4 = .false.
    endif
c      *** if unstable, don't bother with other criteria
    goto 500
endif

gamma = gamma0/(1 + 2*delnbar)
omegar = omegar0-2.*delnbar/sigma

c      *** hurwitz matrices
a1 = 4.*etacc*cphscc*mode + 2.*gamma
a2 = 4.*etacc*etacc
&      + omegar + 8.*gamma*etacc*cphscc*mode
a3 = 8.*gamma*etacc*etacc
&      + 2.*omegar*etacc*mode*sqtalp*cphsalp

c      *** check stability - first condition

```

```

stab1new = .true.
if (a1 .lt. 0.) stab1new = .false.
if (origin) then
  stab1old = stab1new
else
  if (stab1old .neqv. stab1new) then
    magval = mag + 6.
    write(1,999) magval*cos(phscc),magval*sin(phscc)
    stab1old = stab1new
  endif
endif
c   *** second condition
stab2new = .true.
if (a3 .lt. 0.) stab2new = .false.
if (origin) then
  stab2old = stab2new
else
  if (stab2old .neqv. stab2new) then
    magval = mag + 6.
    write(2,999) magval*cos(phscc),magval*sin(phscc)
    stab2old = stab2new
  endif
endif
c   *** third condition
stab3new = .true.
if ((a1*a2-a3) .lt. 0.) stab3new = .false.
if (origin) then
  stab3old = stab3new
  origin = .false.
else
  if (stab3old .neqv. stab3new) then
    magval = mag + 6.
    if (stab3old) then
      write(3,999) magval*cos(phscc),magval*sin(phscc)
    else
      stormag(count) = magval
      storphs(count) = phscc

```

```

          count = count + 1
        endif
        stab3old = stab3new
      endif
    endif
500  continue
900  continue

999  format(1x,f13.6,5x,f13.6)
      close (1)
      close (2)
      close (3)
      close (4)
      end

```

```

program hop
c   This program integrates the approximate phase
c   equation (3.1.10) for a self-coupled laser with
c   arbitrary coupling delay. The user may select
c   to output the phase time series, the optical
c   spectrum or a spectrally-resolved time series
c   showing mode hops. Spontaneous emission
c   noise sources are included. The Cooley-Tukey FFT
c   subroutine four1 is called, but not included here.

dimension x(-100:20000),spec(-1000:1000)
complex freq(20000)
character basename*4,cnum*2
logical timflag,specflag,hopflag
integer pfb,nfft,nmax,next,n,i,cycle,uplimit,sgnfac
integer numffts,n1,n2,nstep,tens,ones,nlim
real alpha,pi,dvnat,dvcc,tau,fpres,dt,beta,pstn,normfac
real gam,ep2,calp,www,z1,z2,apodiz
real nmax2,denom,tmax,frqlim,hoptime

c   *** parameters & constants
pi = 3.1415927
alpha = 3.           / alpha parameter
dvnat = 12.e6        / natural linewidth
dvcc = 27.e9         / cold cavity HBW
tau = 2.666e-9       / coupling delay
fpres = 1.e6         / resolution of Fabry-Perot
dt = .1e-9           / time step
tmax = 500.e-6       / total integration time
lwfrq = 0.e6         / frequency window to
hifrq = 200.e6       / integrate over
frqlim = 200.e6      / max frequency output
pfb = -54.           / power fb ratio, dB
timflag = .false.
specflag = .false.
hopflag = .true.
basename = "hopa"
nstep = 10

```

c

```

beta = atan(alpha)
pstn = pi - beta
normfac = 2.*pi*dvcc
gam = sqrt(dvnat/(normfac*dvcc*dt))
nfft = int(-log(fpres*dt)/log(2.) + 0.5)
fpres = 1/(2.**nfft*dt)
nmax = 1/(fpres*dt)
next = int(tau/dt + 0.5)
numffts = int(tmax/(dt*nmax) + 0.5)
nmax2 = nmax*nmax
n1 = nmax/2 + nmax*dt*lwfrq
n2 = nmax/2 + nmax*dt*hifrq
nlim = nmax*dt*frqlim
ep2 = 10.**(pfb/20.)
calp = sqrt(1. + alpha*alpha)*ep2

c   *** initialize random # generator
z1 = random(9151)

c   *** open the output files
tens = int(-pfb/10.)
ones = -pfb-tens*10
cnum = char(tens + 48)//char(ones + 48)
if (timflag) open(1,file = basename//cnum//'tim.dat')
if (specflag) open(2,file = basename//cnum//'spec.dat')
if (hopflag) open(3,file = basename//cnum//'.dat')

c   *** zero the phase and frequency arrays
do 10 i = -100,20000
    x(i) = 0.
10 continue
do 20 i = -1000,1000
    spec(i) = 0.
20 continue

c   *** integrate the time series of phase for one cycle length
do 500 cycle = 1,numffts
    print *, " cycle = ",cycle

```

```

c   *** Huen's method
      uplimit = nmax - 1
      do 100 n = 0,uplimit
          www = (x(n)-x(n-next))*normfac
c   *** get a gaussian distributed random number
          call gaus(z1,z2)
c   *** initial approximation
      x(n+1) = -(calp*sin(www + pstn + beta)
&         + gam*z1)*dt + x(n)
c   *** integrated value
      www = (x(n+1)-x(n+1-next))*normfac
      x(n+1) = (x(n) + x(n+1))/2. -
&         (calp*sin(www + pstn + beta) + gam*z1)*dt/2.
100   continue
c   *** print out the time series
      if (timflag) then
          tstrt = (cycle-1)*dt*nmax
          do 125 i = 1,nmax,nstep
              write(1,999) (tstrt + i*dt)/1.e-6,normfac*x(i)
125   continue
          endif
c   *** fill the FFT freq array - shift and apodize
      denom = float(nmax)
      sgnfac = 1
      do 150 i = 1,nmax
          sgnfac = -sgnfac
          apodiz = sin(i*pi/denom)
          freq(i) = cexp(cmplx(0.,-normfac*x(i)))*sgnfac*apodiz
150   continue
c   *** FFT the data
      call four1(freq,nmax,1)
c   *** output the hop time series

```

```

      if (hopflag) then
          hoptime = 0.
          do 200 i = n1,n2
              hoptime = freq(i)*conjg(freq(i))/nmax2 + hoptime
200   continue
          write(3,999) cycle/fpres/1.e-6,hoptime
          endif
c   *** 'integrate' the frequency spectrum
      if (specflag) then
          do 250 i = -nlim,nlim
              spec(i) = freq(nmax/2 + i)
&                 *conjg(freq(nmax/2 + i))/nmax2 + spec(i)
250   continue
          endif
c   *** store time delayed data at start of phase array
      x(0) = x(nmax)
      do 300 i = 1,next
          x(-i) = x(nmax-i)
300   continue
500   continue
c   *** output the frequency spectrum
      if (specflag) then
          do 550 i = -nlim,nlim
              write(2,999) i/float(nmax)/dt/1.e6,spec(i)
550   continue
          endif
999   format(1x,e12.5,1x,e12.5)
      if (timflag) close(1)
      if (specflag) close(2)
      if (hopflag) close(3)
      stop
      end

```

VITA

David J. Bossert was born in Minot, North Dakota on May 24, 1964. He received the B.S. degree (Maxima Cum Laude, Distinction) in physics from the University of Portland, Portland, Oregon in May, 1986.

In September 1986, he entered the Ph.D. program at the Oregon Graduate Institute. Since May, 1989 the author has held an Air Force Graduate Fellowship. He spent the summers of 1989-90 researching the stability of coupled semiconductor lasers at the Pilot branch of the Air Force Phillips Laboratory.